4-20-2015

Spectroscopy of States with Ion-Pair Character Near Rb(5s)+Rb(4d)

Marco Ascoli
University of Connecticut - Storrs, marco.ascoli@uconn.edu

Spectroscopy of States with Ion-Pair Character Near Rb(5s)+Rb(4d)

Marco Ascoli, Ph.D.

University of Connecticut, 2015

Molecular and Rydberg physics have separately enjoyed, in the last decade or so, an enormous expansion due to the application of laser cooling techniques that allow control and resolution previously unattainable. One field that lies at the intersection has not yet benefited from this development: heavy Rydberg states. In this experimental work, I investigated the possibility of ion pair production in ultracold rubidium through configuration mixing.

Spectroscopy of States with Ion-Pair Character Near Rb(5s)+Rb(4d)

Marco Ascoli

Laurea, Universitá di Pisa, 2001

M.S., University of Connecticut, 2009

A Dissertation

Submitted in Partial Fullfilment of the

Requirements for the Degree of

Doctor of Philosophy

at the

University of Connecticut

2015

APPROVAL PAGE

Doctor of Philosophy Dissertation

Spectroscopy of States with Ion-Pair Character Near Rb(5s)+Rb(4d)

Presented by

Marco Ascoli,

Major Advisor

Phillip Gould

Associate Advisor

Robin Côté

Associate Advisor

William Stwalley

University of Connecticut

2015

TABLE OF CONTENTS

1. Background 1

1.1 Introduction to Diatomic Molecules 4

1.1.1 Hamiltonian for a molecule 4

1.1.2 Born-Oppenheimer approximation 5

1.1.3 Schrödinger equation for nuclear motion 5

1.1.4 Quantized motion in a diatomic molecule 7

1.1.5 Radiative transitions in molecules 10

1.2 Electronic Transitions and the Franck-Condon Principle 11

1.2.1 Symmetry 16

1.2.2 Gerade-Ungerade Symmetry 17

1.2.3 Selection rules 26

1.3 Ion-Pair and Heavy Rydberg States 27

1.4 Recent Results 30

2. Experiment 33

2.1 General Scheme 33

2.1.1 Ion-pair and covalent character 33

2.1.2 Goal: Search for near degeneracy of gerade and ungerade states below the Rb(5s)+Rb(4d) limit: $3^1\Sigma_g^+$ and $2^1\Sigma_u^+$ 34

2.1.3 General Scheme 37

2.2 Components 43
2.2.1 Ultracold environment 44
2.2.2 Fabry-Perot lock 45
2.2.3 Pulsed lasers for REMPI 47
2.2.4 Laser mixing, stabilization of power 48
2.2.5 Wavemeter WA-4500 49
2.2.6 Ion detection using ToF selection 50
2.2.7 Noise sources and their evaluation 53

3. Introduction to spectrum assignment 65
3.1 What is an assignment anyway? 65
3.2 Data: Common features 70
3.2.1 Data collection 70
3.2.2 Data format 71
3.2.3 Error 73
3.3 Ground-State pattern 74
3.4 Excited-State pattern 75

4. Analysis of $X^1\Sigma_g^+ \rightarrow 2^1\Sigma_u^+$ spectrum 80
4.1 Ground-state pattern matching 80
4.2 Excited-state identification 81
4.3 Use of LEVEL 8.0 83

4.4 Comparison with Y. Huang's work 83

5. Analysis of $a(1)^3\Sigma_u^+ \rightarrow 3^1\Sigma_g^+$, $2^3\Pi_g$ spectra 86

5.1 Ground-state pattern matching 87

5.2 Excited-state identification 88

5.3 Comparison with Ye Huang's work 94

5.4 Overview of $a^3\Sigma_u^+$ spectrum 100

6. Conclusions 105

6.1 Findings summary 105

6.2 R-transfer 106

6.3 Configuration mixing 107

6.3.1 DC Stark mixing 107

6.3.2 Laser mixing 114

A. Notes on fitting methods 119

A.1 General Nonlinear fit 119

A.2 Bi-square fitting 123

A.2.1 Least square fitting 124

A.2.2 Bi-Square iteration 124

B. Table of assigned transitions of the $2^1\Sigma_u^+$ state from the $X^1\Sigma_g^+$. 127

C. Table of assigned transitions of the $3^1\Sigma_g$ state from the $a^3\Sigma_u^+$ state 138

D. Table of assigned transitions of the A series of the $2^3\Pi_g$ state from the $a^3\Sigma_u^+$ state 146

E. Table of assigned transitions of the B series of the $2^3\Pi_g$ state from the $a^3\Sigma_u^+$ state 154

F. Table of assigned transitions of the C series of the $2^3\Pi_g$ state from the $a^3\Sigma_u^+$ state 161

G. The $X^1\Sigma_g^+ \rightarrow 2^1\Sigma_u^+$ spectrum plots and assignments. 167

H. The $a^3\Sigma_u^+ \rightarrow 2^3\Pi_g$ and $3^1\Sigma_g^+$ spectrum plots and assignments. . 203

Bibliography 266

LIST OF FIGURES

1.1 Molecular potential energy (PEC) curve of a diatomic molecule . . . 7

1.2 Qualitative implications of the Franck-Condon principle 12

1.3 Spherical and polar coordinates for describing the orbitals 18

1.4 Probability amplitudes for a square well 20

1.5 Probability distributions for a square well 23

1.6 Wavefunctions of both gerade (left) and ungerade (right) symmetry for each electron. 24

1.7 The sum of wavefunctions of both gerade and ungerade symmetry for each electron (left) and the resulting square of the amplitude (probability density) (right) 25

1.8 A subset of Rb_2 covalent potentials and the Coulomb potential dissociating to the $Rb^+ + Rb^-$ ion pair (dashed line), derived from [14]. The negative and positive ion polarizability corrections (important at short-range) have been included in the Coulomb curve [15,16]. . 30

2.1 A subset of Rb_2 singlet covalent potentials and the Coulomb potential dissociating to the $Rb^+ + Rb^-$ ion pair (dashed line), derived from [14]. The negative and positive ion polarizability corrections (important at short-range) have been included in the Coulomb curve [15,16]. Highlighted in red, green, and blue are the shelf states with manifest ion-pair branches. 35

2.2 General scheme for spectroscopy of an ungerade-symmetry shelf state: PA followed by spontaneous emission (SE) into the gerade-symmetry ground state $X^1\Sigma_g^+$; subsequent excitation with a pulsed laser ($\tau \sim 10\,ns$) to the energy region of interest ($\sim 17000 - 18000\,cm^{-1}$), and quasi simultaneous ionization with an auxiliary pulsed detection laser. 36

2.3 General scheme for spectroscopy of a gerade-symmetry $3^1\Sigma_g^+$ shelf state 39

2.4 REMPI ion signal of PA using the $0_g^- - 1^3\Sigma_g^+$ state which dissociates to $5S + 5P_{1/2}$. Shown are PA detunings of $\Delta_{PA} = -69\,cm^{-1}$, $-43\ cm^{-1}$, and $-17\ cm^{-1}$ below the atomic asymptote. $\Delta_{PA} = -69\,cm^{-1}$ has been used for state preparation into the $a^3\Sigma_u^+$ state throughout this study. The natural decay $1^3\Sigma_g^+ \rightarrow a^3\Sigma_u^+$ seems to afford a good compromise between spectroscopic resolution of the target states populated while their long range extension provides a favorable FCF for the ion-pair branch of the shelf state. 41

2.5 Resonant-Coupling photoassociation 42
2.6 Schematic representation of the experimental apparatus, more details of the detection region are shown separately in Figure 2.8 43
2.7 Representation of servo loop for average power stabilization of pulsed dye laser. 49
2.8 Schematic representation of time of flight dynamics 51
2.9 TOF oscilloscope trace 52
2.10 Example of frequency axis smoothing: (a) Raw spectrum, no smoothing applied. The granular nature of the wavemeter reading bins the spectrum in too large intervals. (b) The spectrum as a function of its recording index ($\sim$ time). Comparison with (a) highlights a loss of resolution. (c) Raw wavemeter readings vs recording index and polynomial smoothing of the same spectral interval as in (a) and (b). (d) End result of the frequency smoothing procedure where the granularity present in (a) has been removed. 54
2.11 Wavemeter Burleigh WA-4500 manual, specification page 56
2.12 Typical result of the smoothing procedure, which in addition to smoothing, returns an evenly resampled scan. 58

2.13 Schematic representation of two spectra. (left) the convolution product yields directly θ, but the measurements may not be compatible if the areas of likelihood do not overlap. (center) Renormalizing the spectra allows the areas of likelihood to overlap, (right) allowing the evaluation of χ^2 60

2.14 Shown are two overlapping scans, 2013-06-04\scan 14 and 2013-06-14\scan3, taken 10 days apart, with visibly different linewidths for the two scans. On top are the unshifted data, while for the bottom the two scans are aligned by up-shifting Plot 2 by $\sim +0.27\,cm^{-1}$. . 62

2.15 The two functionals considered for alignment (χ^2 and $cos(\theta)$) are shown in the case of the scans of Fig. 2.14, 2013-06-04\scan 14 and 2013-06-14\scan3, along with their combination $(1 - cos(\theta))\chi^2$; it has to be noted that χ^2 and $cos(\theta)$ do not completely agree with each other and that their combination offers a compromise. In this example a shift of $\sim 0.27\,cm^{-1}$ is optimal. 64

3.1 With a given level structure, transitions from multiple ground-state levels to multiple excited levels are well recognizable with a proper labeling (left). Once sorted by transition frequency (energy), it is apparent how the relative splittings of the ground-state and excited-state levels come into play: the orange lines are almost completely grouped together, while the blue lines are interleaved with other transitions (right). 66

3.2 Spectrum with color labeling (top). These are the same transitions of Fig. 3.1(bottom) vs frequency. Only the color coding helps in picking out the presence of a repeating pattern. 67

3.3 Top: Spectrum of Fig. 3.2 without color labeling, showing an apparent lack of regularity. Center: Using the ground-state pattern (the differences of ground-state levels) it is possible to regain a first layer of labeling, assigning the ground-state quantum numbers v" (bottom). 68

3.4 Interval search method 77

4.1 Optimal v' assignment with respect to *ab initio* PECs for the $2^1\Sigma_u^+$ state 82

4.2 Accuracy evaluation by comparison with previous measurement by Huang et al. 84

4.3 $\Delta G_{v'+\frac{1}{2}}$ vs frequency for $2^1\Sigma_u^+$: this work in red, Huang's work in blue. 85

5.1 Differences between theoretical and experimental energies for the $2^3\Pi_g$ state of the series A, as labelled by Huang, as a function of v' shift. The plots represent the three closest choices of v' shift to have a constant energy difference between *ab initio* theory and experiment. A zero slope is the optimal v'$_{shift} = 1$ which corresponds to an offset of -1.20 cm^{-1} and a standard deviation of 0.69 cm^{-1}. 89

5.2 Differences between theoretical and experimental energies for the $2^3\Pi_g$ state of the series B, as labelled by Huang, as a function of v' shift. The plots represent the three closest choices of v' shift to have a constant energy difference between *ab initio* theory and experiment. A zero slope is the optimal v'$_{shift} = 1$ which corresponds to an offset of -8.95 cm^{-1} and a standard deviation of 0.35 cm^{-1}. 90

5.3 Differences between theoretical and experimental energies for the $2^3\Pi_g$ state of the series C, as labeled by Huang, as a function of v' shift. The plots represent the three closest choices of v' shift to have a constant energy difference between *ab initio* theory and experiment. A zero slope is the optimal v'$_{shift} = 0$ which corresponds to an offset of -157.90 cm^{-1} and a standard deviation of 0.31 cm^{-1}. 91

5.4 Difference between *ab initio* and optimal v' assignment for the $2^3\Pi_g$ state, series A, B, C 92

5.5 Difference between *ab initio* predictions and optimal v' assignment for the $3^1\Sigma_g^+$ state 93

5.6 The methods for frequency measurement between this work and Huang's have been radically different. Nonetheless the agreement is well within the expected experimental error for the excited levels that were assigned by both Huang and this work. 95

5.7 Comparison of the spectrum between Huang and this work 96

5.8 Comparison of $\Delta G_{v'+\frac{1}{2}}$ for the $2^3\Pi_g$ states vs. v' for the present work and the work of Ye Huang (YH). 97

5.9 Comparison of $\Delta G_{v'+\frac{1}{2}}$ for $2^3\Pi_g$ states vs. $E_{v'}$ for the present work and the work of Ye Huang (YH). 98

5.10 $\Delta G_{v'+\frac{1}{2}}$ for the $3^1\Sigma_g^+$ state vs. v' for this work (■), YH work (♦) and theory (▼). These results are somewhat surprising as there seems to be a perturbation starting in the vicinity of v'$\sim$ 50, where Huang has also investigated, terminating near v'$\sim$ 100, only to deviate substantially from the *ab initio* predictions near v'$\sim$ 120. This last phenomenon is more apparent in Fig. 5.5. 99

5.11 Top: The spectrum excited from the $a^3\Sigma_u^+$ state - black, Spectrum fitting results - red. Bottom four plots: FCF simulation for the indicated state - black, Spectrum fitting results for the indicated state - red 101

5.12 Spectrum sample from 16360 cm^{-1} to 16675 cm^{-1} (top) and from 16670 cm^{-1} to 16985 cm^{-1} 102

5.13 Spectrum sample from 16980 cm^{-1} to 17295 cm^{-1} (top) and from 17290 cm^{-1} to 17605 cm^{-1} 103

5.14 Spectrum sample from 17600 cm^{-1} to 17915 cm^{-1} (top) and from 17910 cm^{-1} to $\sim$18200 cm^{-1} 104

6.1 Nearest-neighbor energy difference of $2^3\Pi_g$ - $3^1\Sigma_g^+$ level pairs: this difference is very susceptible to error: each series has an error of $\sim 0.5\,cm^{-1}$ and a relative shift of $\sim 0.7\,cm^{-1}$ can significantly change which specific level is closest. Highlighted between the red horizontal lines are all candidates with a nearest neighbor closer than 1 cm^{-1}. 109

6.2 Polarizability 112

6.3 Depletion REMPI scheme 113

6.4 Depletion REMPI spectrum 114

6.5 Mixing strategies for $2^1\Sigma_u^+ \leftrightarrow 3^1\Sigma_g^+$ 115

6.6 FCF Intensity Graph for $2^1\Sigma_u^+ \leftrightarrow 3^1\Sigma_g^+$ 117

6.7 QCL operating temperature 118

A.1 Representation of LS fitting applicability condition 123

A.2 Bisquare weighting function with unitary median 125

A.3 flow diagram of bi-square fitting 126

LIST OF TABLES

1.1 Selected properties of Rydberg 3

1.2 Selection Rules for Electronic Transitions in Diatomic Molecules. Here Λ is the projection of the total angular momentum on the intrenuclear axis and S is the total spin. 26

1.3 Selection Rules for Electronic Transitions in Diatomic Molecules . . . 27

2.1 Laser dyes used and their corresponding wavelength ranges 48

6.1 Table of v' assignment shift of the $2^3\Pi_g$ states. 106

6.2 Table of nearest-neighbor energy difference of the two states: $2^1\Sigma_g^+$ and $3^1\Sigma_g^+$. Only the pairs with $\Delta E < 1\ cm^{-1}$ are shown. On the left side of each row is the level of lower energy of the pair, while on the right side is the level of higher energy. Each series has an error of $\sim 0.5\, cm^{-1}$ and a relative shift of $\sim 0.7\, cm^{-1}$ (combined error) which can significantly change which specific level is closest. . . . 109

Chapter 1

Background

Rydberg atoms, with their rich internal structure and extreme properties, have been a focus of atomic physics for more than a century. In the last decade the physics of Rydberg gases was combined with laser cooling techniques, allowing the investigation of very cold or ultracold systems with controllable, strong interactions and negligible thermal motion.

One of the roots of specific interest in this kind of system is the universality of the dynamics: electronic Rydberg systems can be made out of virtually any species of atom by exciting one single outer electron. If the excitation reaches a high enough level, the system can be described by a hydrogen-atom-like Hamiltonian; this happens when the "electron" is displaced far enough from the positive core that the core can be approximated to a good degree by a point particle. In that case, the system obeys the hydrogen-atom Schrödinger equation:

$$\left(-\hbar^2\frac{\nabla^2}{2m^*} - \frac{1}{4\pi\epsilon_0}\frac{e^2}{r}\right)\Psi = E\Psi \tag{1.1}$$

where Ψ is the electron wavefunction, $m^* = m_e M_{core}/(M_{core} + m_e)$ is the reduced mass, and r is the distance between the electron and the core. For the case of hydrogen, the solution of this equation is a textbook case with energy levels $E_n = -h\,c\,R_\infty \dfrac{m^*}{m_e\,n^2}$, and wavefunctions given by the product of Laguerre polynomials and associated spherical harmonics, $\Psi_{n,l,m}(r,\theta,\phi) = \chi_{n,l}(r)Y_l^m(\theta,\phi)$. Here R_∞ is the Rydberg constant, n is the principal quantum number, l is the angular momentum quantum number, and m is the projection of l. This leads to the scaling laws reported in table I. Note that for extending this treatment to other systems, the Rydberg constant $R_\infty = m_e e^4/(8\epsilon_0^2 h^3 c)$ is a universal constant independent of the nuclear mass, but the reduced mass m^* depends on the details of the system considered.

For alkali atoms the solutions must be found numerically but, for high n, they resemble hydrogenic wavefunctions. The most notable correction is a phase shift in the long-range radial wavefunction, which results in the replacement of the principal quantum number n by the effective quantum number $n^* = (n - \delta_{n,l,j})$ in the hydrogenic formulas (e.g. for the binding energy) [1,2], where $\delta_{n,l,j}$ is the quantum defect.

The system's exaggerated properties, listed in Table 1.1, are attractive for possible quantum computing applications, such as fast quantum logic gates, long-range two-qubit gates, collective encoding of multiqubit registers, implementation of robust light-atom quantum interfaces, and the potential for simulating quantum

Quantity	n dependence	Value for Rb 60d[3]
Binding energy	n^{-2}	$4\ meV \sim 30\ cm^{-1}$
Ionizing field	n^{-4}	$40\ V/cm$
Energy spacing	n^{-3}	$30\ GHz$
Orbital radius	n^2	$6000\ a_0$
Dipole moment $\lvert\langle nD\lvert er\rvert nF\rangle\rvert$	n^2	$5000\ ea_0$
Radiative lifetime	n^3	$200\ \mu s$
Polarizability	n^7	$50\ GHz/(V/cm)^2$

Table 1.1: Selected properties of Rydberg atoms and their principal quantum number dependence. For complex atoms, where core penetration is important, the principal quantum number n has to be replaced by $n^* = (n - \delta_{n,l,j})$. The numerical values for Rb have been rescaled from [3].

many-body physics [4]. Also long-range interactions can mediate collective phenomena, and low binding energies can be exploited for studying ultracold plasma dynamics as well. [83]

1.1 Introduction to Diatomic Molecules

1.1.1 Hamiltonian for a molecule

Consider the time-independent Schrödinger equation for a molecule:

$$H_{mol}\Psi_{mol} = E_{total}\Psi_{mol} \tag{1.2}$$

where the Hamiltonian H_{mol} is given by:

$$H_{mol} = -\frac{\hbar^2}{2m}\sum_i \nabla_i^2 - \sum_A \frac{\hbar^2}{2M_A}\nabla_A^2 + V\big(\vec{R},\vec{r}\big) \tag{1.3}$$

Here, i, m, and $\vec{r}$ refer to electrons, and A, M_A, and $\vec{R}$ to nuclei. The potential energy, $V\big(\vec{R},\vec{r}\big)$ can be written as:

$$V\big(\vec{R},\vec{r}\big) = -\sum_{A,i}\frac{Z_A e^2}{4\pi\epsilon_0 r_{Ai}} + \sum_{A>B}\frac{Z_A Z_B e^2}{4\pi\epsilon_0|R_A - R_B|} + \sum_{i>j}\frac{e^2}{4\pi\epsilon_0 r_{ij}} \tag{1.4}$$

We assume that the wavefunction of the system is separable and can be written as:

$$\Psi_{mol}\big(\vec{r}_i,\vec{R}_A\big) = \psi_{el}\big(\vec{r}_i;\vec{R}\big)\eta_{nuc}\big(\vec{R}\big) \tag{1.5}$$

where $\psi_{el}\big(\vec{r}_i;\vec{R}\big)$ is assumed to be calculable for a particular R. Then:

$$\nabla_i^2[\psi_{el}\big(\vec{r}_i;\vec{R}\big)\eta_{nuc}\big(\vec{R}\big)] = \eta_{nuc}\big(\vec{R}\big)\nabla_i^2\psi_{el}\big(\vec{r}_i;\vec{R}\big) \tag{1.6}$$

$$\nabla_A^2[\psi_{el}\eta_{nuc}\big(\vec{R}\big)] = \psi_{el}\nabla_A^2\eta_{nuc} + 2\Big(\nabla_A\psi_{el}\Big)\Big(\nabla_A\eta_{nuc}\Big) + \nabla_A^2\psi_{el} \tag{1.7}$$

In this case, the Schrödinger equation cannot be solved analytically. To overcome this difficulty, the Born-Oppenheimer approximation is normally adopted, which takes advantage of the great difference in mass between electrons and nuclei.

1.1.2 Born-Oppenheimer approximation

Even the simplest molecule, H_2^+, consists of three particles, and its Schrödinger equation cannot be solved analytically, so the Born-Oppenheimer approximation is normally adopted. Because they are much lighter, the electrons can respond almost instantaneously to displacement of the nuclei. Therefore, instead of trying to solve the Schrödinger equation for all the particles simultaneously, we regard the nuclei as fixed in position, so $\nabla_A \psi_{el} \sim 0$, i.e. in Eq. 1.6:

$$\nabla_A^2 \psi_{el} \eta_{nuc}(\vec{R}) = \psi_{el} \nabla_A^2 \eta_{nuc} \tag{1.8}$$

1.1.3 Schrödinger equation for nuclear motion

Using the results of the previous two sections (1.1.1 and 1.1.2), the Schrödinger equation can be written as:

$$\begin{aligned} H_{mol}\Psi_{mol} = \eta_{nuc} \left\{ -\frac{\hbar^2}{2m} \sum_i \nabla_i^2 + \sum_{i>j} \frac{e^2}{4\pi\epsilon_0 r_{ij}} - \sum_{A,i} \frac{Z_A e^2}{4\pi\epsilon_0 r_{Ai}} \right\} \psi_{el} + \\ \psi_{el} \left\{ \sum_{A>B} \frac{Z_A Z_B e^2}{4\pi\epsilon_0 |R_A - R_B|} - \sum_A \frac{\hbar^2}{2M_A} \nabla_A^2 \right\} \eta_{nuc} = E_{total} \Psi_{mol} \end{aligned} \tag{1.9}$$

The Schrödinger equation for the electrons can be written separately as:

$$\left\{ -\frac{\hbar^2}{2m} \sum_i \nabla_i^2 + \sum_{i>j} \frac{e^2}{4\pi\epsilon_0 r_{ij}} - \sum_{A,i} \frac{Z_A e^2}{4\pi\epsilon_0 r_{Ai}} \right\} \psi_{el}(\vec{r}_i; \vec{R}) = E_{el} \psi_{el}(\vec{r}_i; \vec{R}) \tag{1.10}$$

and solved, considering a static electric potential arising from the nuclei in a particular arrangement, R. The result, E_{el}, can be inserted into Eq. 1.9, resulting in a wave equation for the nuclear motion:

$$\left\{ -\sum_{A} \frac{\hbar^2}{2M_A} \nabla_A^2 + \sum_{A>B} \frac{Z_A Z_B e^2}{4\pi\epsilon_0 |R_A - R_B|} + E_{el}\big(\vec{R}\big) \right\} \eta_{nuc} = E_{total} \eta_{nuc} \tag{1.11}$$

Equation 1.11 is a Schrödinger equation with a potential energy:

$$V\big(\vec{R}\big) = \sum_{A>B} \frac{Z_A Z_B e^2}{4\pi\epsilon_0 |R_A - R_B|} + E_{el}\big(\vec{R}\big) \tag{1.12}$$

where:

$$\sum_{A>B} \frac{Z_A Z_B e^2}{4\pi\epsilon_0 |R_A - R_B|} \tag{1.13}$$

represents nuclear repulsion, and $E_{el}\big(\vec{R}\big)$, the chemical binding. Different arrangements of nuclei may then be adopted and the calculation repeated. The set of solutions so obtained allows construction of the molecular potential energy curve (PEC) of a diatomic molecule, as shown in Fig. 1.1.

This holds true for molecules in a normal covalent configuration. For ion-pair or heavy Rydberg molecules the electrons are bound and localized to an atomic ion, making this approximation of scarce significance: while the electrons' motion is still much faster than that of the nuclei, the main interaction remains Coulombic between the positive core and the negative ion (e.g. Rb^+ and Rb^-, respectively). While the solutions to the heavy Rydberg problem are easier than the covalent case, the cases where the covalent and ionic configurations are in

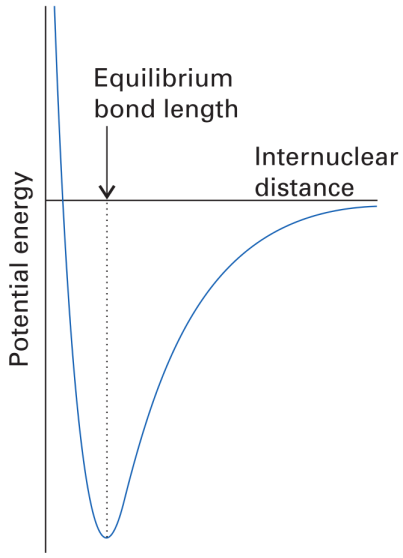

Fig. 1.1: Molecular potential energy (PEC) curve of a diatomic molecule

principle good descriptions of the molecular state give rise to the questions this thesis tries to answer.

1.1.4 Quantized motion in a diatomic molecule

The molecular wave equation for nuclear motion, Eq. 1.11, accounts for both the vibrational and rotational motion of the molecule. For a diatomic molecule, if one transforms to the center-of-mass system and uses the reduced mass:

$$\mu = \frac{M_A M_B}{M_A + M_B} \tag{1.14}$$

then, inserting Eq. 1.12 into Eq. 1.11, the equation of motion becomes:

$$-\frac{\hbar^2}{\mu}\Delta_{\vec{R}}\eta_{nuc} + V\left(\vec{R}\right)\eta_{nuc} = E_{total}\eta_{nuc} \tag{1.15}$$

with:

$$\Delta_{\vec{R}} = \frac{1}{R^2}\frac{\partial}{\partial R}\left(R^2\frac{\partial}{\partial R}\right) + \frac{1}{R^2 sin\theta}\frac{\partial}{\partial\theta}\left(sin\theta\frac{\partial}{\partial\theta}\right) + \frac{1}{R^2 sin\theta}\frac{\partial^2}{\partial\phi^2}. \tag{1.16}$$

The angular part of Eq. 1.16:

$$\vec{N} = \frac{1}{R^2 sin\theta}\frac{\partial}{\partial\theta}\left(sin\theta\frac{\partial}{\partial\theta}\right) + \frac{1}{R^2 sin\theta}\frac{\partial^2}{\partial\phi^2}$$

is well known, with solutions:

$$\vec{N}^2|N,M> \;=\; \hbar^2 N(N+1)|N,M> \tag{1.17}$$

$$N_z|N,M> \;=\; \hbar M|N,M> \tag{1.18}$$

with rotational quantum number $N = 0, 1, 2, 3, \cdots$ and $M = -N, -N+1, \cdots, N$, and angular wavefunctions:

$$|N,M> \;=\; Y_{NM}\big(\theta,\phi\big). \tag{1.19}$$

Hence the wavefunction of the molecule can be expressed as:

$$\eta_{nuc}\big(R,\theta,\phi\big) \;=\; \frac{\chi\big(R\big)}{R}Y_{NM}\big(\theta,\phi\big). \tag{1.20}$$

The molecular Schrödinger equation can be reduced to:

$$\left[-\frac{\hbar^2}{2\mu}\frac{\partial^2}{\partial R^2} + \frac{\hbar^2 N(N+1))}{2\mu R^2} + V\big(R\big)\right]\chi\big(R\big) = E_{vib,rot}\chi\big(R\big). \tag{1.21}$$

Refs. [67] [68] have a compact but more extensive treatment.

In a quantum system, a molecular system in our case, there are particles that interact through a potential. Their motion is then described by the Schrödinger

(wave) equation 1.1.1. Under certain simplifying conditions (where the potential does not vary quickly) it is possible to apply an approximate method for solving the motion with a method that is helpful in picturing the physics: the semi-classical or WKB method. A good introduction is found in [54], and here we report a brief summary. From eq. 1.21 we have that given a certain electronic and rotational state, the nuclear motion is described by a 1D 2^{nd}-order differential equation:

$$-\frac{\hbar^2}{2\mu}\frac{d^2\phi(q)}{dq^2} + U(q)\phi(q) = E\phi(q). \tag{1.22}$$

with the replacement $U(R) = \frac{\hbar^2 N(N+1))}{2\mu R^2} + V(R)$ and q for R with respect to eq. 1.21. Suppose that the potential is growing sufficiently fast as $q \to \infty$ so that the classical particle motion is confined; then the momentum will be given by

$$p(q) = \pm\sqrt{2\mu(E - U(q))}\,, \quad p(q) = \hbar k(q) \tag{1.23}$$

and eq. 1.22 becomes

$$\phi''(q) + k^2(q)\phi(q) = E\,\phi(q) \tag{1.24}$$

With a trial function: $\phi = A(q)e^{\frac{i}{\hbar}S(q)}$, with $A(q), S(q) \in \Re$ the previous equation can be split into real and imaginary parts:

$$S(q)^2 = p(q)^2 + \hbar^2\tfrac{A''(q)}{A(q)} \tag{1.25}$$

$$S''(q)A(q) + 2S'(q)A'(q) = \tfrac{1}{A(q)}\frac{d(S'(q)A(q)^2)}{dq} \tag{1.26}$$

The semiclassical method drops $\frac{A''(q)}{A(q)}$ by assuming: $p(q)^2 + \hbar^2\frac{A''(q)}{A(q)} \sim p(q)^2$ or $\hbar^2\frac{A''(q)}{A(q)} \ll p(q)^2 = (\hbar k(q))^2$. With this assumption, eqs. 1.25 and 1.26 turns into

the solution:

$$S(x, x_1, E) = \int_{x_1}^{x} p(q)dq \tag{1.27}$$

$$A(x) = \frac{C}{\sqrt{p(x)}} \tag{1.28}$$

where C is determined by the initial conditions. Putting everything together:

$$\phi\big(x\big) = \frac{C}{\sqrt{p(x)}} e^{\frac{i}{\hbar}S(x,x_1,E)} \tag{1.29}$$

At this point the WKB quantization condition follows by demanding that the wavefunction computed after a complete period be single-valued; in practice this means that the phase satisfies:

$$\frac{i}{\hbar}S(x_2, x_1, E) = \frac{i}{\hbar}\int_{x_1}^{x_2} p(q)dq = \pi\big(n + \frac{1}{2}\big) \tag{1.30}$$

where x_2 and x_2 are the classical turning points. This quantization, schematically presented in fig. 1.2 (right), is the quantization recorded in this study by examination of molecular spectra..

1.1.5 Radiative transitions in molecules

The dipole moment in a molecule can be expressed in terms of electronic and nuclear dipole moments:

$$\mu = \mu_e + \mu_N \tag{1.31}$$

and the molecular wavefunction as:

$$\Psi_{mol}\big(\vec{r}_i, \vec{R}_A\big) = \psi_{el}\big(\vec{r}_i; \vec{R}\big)\psi_{vib}\big(\vec{R}\big). \tag{1.32}$$

where the vibrational wavefunction is given by $\psi_{vib}(\vec{R}) = \eta_{nuc}(R, \theta, \phi)$.

Considering the dipole transition between two states:

$$\mu_{if} = \int \Psi'_{mol} \mu \Psi''_{mol} d\tau \tag{1.33}$$

results in two different types of transitions, electronic transitions given as:

$$\int \left(\int \psi'_{el} \mu_e \psi''_{el} d\vec{r} \right) \psi'_{vib} \psi''_{vib} d\vec{R} \tag{1.34}$$

and rovibrational transitions:

$$\int \psi'_{el} \psi''_{el} d\vec{r} \int \psi'_{vib} \mu_N \psi''_{vib} d\vec{R}. \tag{1.35}$$

1.2 Electronic Transitions and the Franck-Condon Principle

Whenever an electronic transition occurs in a molecule the nuclei are subjected to a change in Coulombic force as a result of the redistribution of electronic charge. In other words, the molecular potential energy surface, which governs nuclear motion, changes as the electronic state changes during the transition. As a result, the nuclei respond by breaking into more vigorous vibration and the absorption spectrum shows a structure characteristic of the vibrational energy levels of the molecule. Simultaneous electronic and vibrational transitions are known as vibronic transitions.

The Franck-Condon principle

Because nuclear masses are so much larger than the mass of an electron, an electronic transition occurs within a stationary nuclear framework. As a result, the

nuclear locations remain unchanged during the actual transition, but then readjust once the electrons have adopted their final distribution.

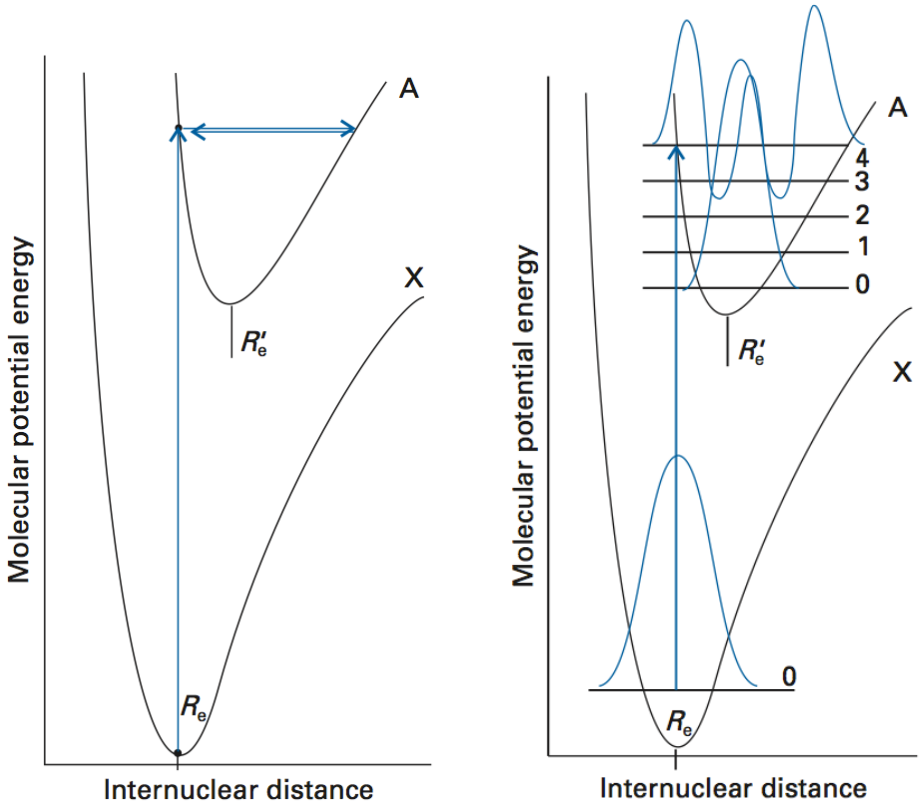

Fig. 1.2: Left: The classical basis of the Franck-Condon principle in which the molecule makes a vertical transition that terminates at the turning point of the excited state. The nuclei neither change their locations nor accelerate while the electronic transition is in progress. Right: The quantum mechanical version of the Franck-Condon principle. The molecule makes a transition from the ground vibrational state to the state with a vibrational wavefunction that most strongly resembles the initial vibrational wavefunction [48].

The qualitative implications of this principle, called the Franck-Condon principle, are illustrated in Fig. 1.2(left), which shows two molecular potential

energy curves for two electronic states of a diatomic molecule. We shall confine our attention to the fundamental progression, with the transitions starting in the ground vibrational state of the lower electronic state. Classically, the transition occurs when the internuclear separation is equal to the equilibrium bond length R_e of the lower electronic state, when the nuclei are stationary, and that internuclear separation and state of motion are preserved during the transition. As a result, the transition terminates where a vertical line cuts through the upper molecular potential energy curve. At the point of intersection, the excited molecule is at a turning point in its vibration, so the nuclei are momentarily stationary, and the internuclear separation is the same as it was initially. Such a transition is called vertical. Once the electronic transition is complete, however, the molecule begins to vibrate with an energy corresponding to the intersection.

The quantum mechanical description of the process echoes the classical description as shown in Fig. 1.2(right). Qualitatively, the transition is most likely to occur from the ground vibrational state of the lower electronic state to the vibrational state that it most resembles in the upper electronic state. That way, the vibrational wavefunction undergoes the least change, which corresponds to the preservation of the dynamical state of the nuclei as required by the Franck-Condon principle. The vibrational state with a wavefunction that most resembles the original bell-shaped Gaussian of the vibrational ground state is one with a peak immediately above the ground state, that is a wavefunction with large am-

plitude at R_e. In the illustration, this wavefunction corresponds to an energy level that lies in much the same position as in the vertical transition of the classical description.

The justification of the quantum mechanical description is based on the evaluation of the electric dipole transition moment between the ground vibronic state $|\epsilon\nu\rangle$ and the upper vibronic state $|\epsilon'\nu'\rangle$. In a molecule, the electric dipole moment operator depends on the locations and charges of the electrons, $\boldsymbol{r}_i$ and $-e$, and the locations and charges of the nuclei, which we denote $\boldsymbol{R}_s$ and $Z_s e$, respectively:

$$\boldsymbol{\mu} = -e\sum_i \boldsymbol{r}_i + e\sum_s Z_s \boldsymbol{R}_s = \boldsymbol{\mu}_e + \boldsymbol{\mu}_N \tag{1.36}$$

Within the Born-Oppenheimer approximation (Section 1.1.2), the vibronic state $|\epsilon\nu\rangle$ is described by the wavefunction $\Psi_\epsilon(\boldsymbol{r};\boldsymbol{R})\Psi_{\nu(\boldsymbol{R})}$, where $\boldsymbol{r}$ and $\boldsymbol{R}$ denote, respectively, the electronic and nuclear coordinates collectively. Note that the electronic wavefunction depends parametrically on the nuclear coordinates (that is, there is a different electronic wavefunction for each nuclear arrangement). The transition moment is therefore:

$$\begin{aligned}\langle\epsilon'\nu'|\boldsymbol{\mu}|\epsilon\nu\rangle = & \int \Psi^*_{\epsilon'}(\boldsymbol{r};\boldsymbol{R})\Psi^*_{\nu'}(\boldsymbol{R})(\boldsymbol{\mu}_e+\boldsymbol{\mu}_N)\Psi_\epsilon(\boldsymbol{r};\boldsymbol{R})\Psi_\nu(\boldsymbol{R})d\tau_e d\tau_N \\ & = \int \Psi^*_{\nu'}(\boldsymbol{R})\{\int \Psi^*_{\epsilon'}(\boldsymbol{r};\boldsymbol{R})\boldsymbol{\mu}_e\Psi_\epsilon(\boldsymbol{r};\boldsymbol{R})d\tau_e\}\Psi_\nu(\boldsymbol{R})d\tau_N \\ & + \int \Psi^*_{\nu'}(\boldsymbol{R})\boldsymbol{\mu}_N\{\int \Psi^*_{\epsilon'}(\boldsymbol{r};\boldsymbol{R})\Psi_\epsilon(\boldsymbol{r};\boldsymbol{R})d\tau_e\}\Psi_\nu(\boldsymbol{R})d\tau_N\end{aligned} \tag{1.37}$$

The integral over the electron coordinates in the final term is zero because the

electronic states are orthogonal to one another for each selected value of $\boldsymbol{R}$. The integral over the electron coordinates in the remaining integral is the electric dipole moment for the transition when the nuclei have coordinates $\boldsymbol{R}$. To a reasonable first approximation,[1] this transition moment is independent of the locations of the nuclei so long as they are not displaced by a large amount from equilibrium, and so the integral may be approximated by a constant $\boldsymbol{\mu}_{\epsilon'\epsilon}$. Therefore, the overall electric dipole transition moment is

$$\langle \epsilon'\nu'|\boldsymbol{\mu}|\epsilon\nu\rangle = \boldsymbol{\mu}_{\epsilon'\epsilon}\int \Psi^*_{\nu'}(\boldsymbol{R})\Psi_{\nu}(\boldsymbol{R})d\tau_N = \boldsymbol{\mu}_{\epsilon'\epsilon}S(\nu',\nu) \tag{1.38}$$

where

$$S(\nu',\nu) = \int \Psi^*_{\nu'}(\boldsymbol{R})\Psi_{\nu}(\boldsymbol{R})d\tau_N \tag{1.39}$$

is the overlap integral (the square of which is the Franck-Condon factor) between the two vibrational states in their respective electronic states. The electric dipole transition moment is therefore largest between vibrational states that have the greatest overlap. This is the quantitative version of the previous qualitative discussion, where we looked for the upper vibrational state that had a local bell-shaped region above the Gaussian function of the ground vibrational state of the lower electronic state. Significant values of the overlap integral $S(\nu',\nu)$ are generally found for a progression of vibrational states ν' rather than for a single value of ν', so transitions occur with varying probabilities to all of them. Thus, a

[1] In more rigorous treatments, this transition moment must be considered a function of $\boldsymbol{R}$.

progression of vibrational transitions is observed in the electronic spectrum. The relative intensities of the lines are proportional to the square of the electric dipole transition moments and hence to the Franck-Condon factors, $|S(\nu', \nu)|^2$.

1.2.1 Symmetry

Spin: singlet and triplet

An ion-pair molecule is composed of ions, which implies that the negative ion (whose electronic wavefunction should be fundamentally unperturbed by the molecular bond) has a well determined spin state. For all alkali atoms, the negative ion arises from a form of anti-correlation between the two electronic wavefunctions in an S type orbital [52]. In an alkali-alkali ion-pair molecule, the positive ion is closed-shell, so the total spin state is completely determined by the negative ion spin state. Therefore this is a case of a system with two spin-1/2 particles. Measured on a given axis, each particle can be either spin up or spin down. This gives the system a basis of four state vectors:

$$|\uparrow,\uparrow\rangle\,,\ \ |\uparrow,\downarrow\rangle\,,\ \ |\downarrow,\uparrow\rangle\,,\ \ |\downarrow,\downarrow\rangle \tag{1.40}$$

The total spin and its projection onto a defined axis can be computed using the rules for adding angular momentum in quantum mechanics using the Clebsch-Gordan coefficients. In general

$$|s, m\rangle = \sum_{m_1+m_2=m} C^{s_1\, s_2\, s}_{m_1\, m_2\, m}\, |s_1,\, m_1\rangle\, |s_2,\, m_2\rangle \tag{1.41}$$

Substituting our four basis states, where s_1, $s_2 = \frac{1}{2}$ and m_1, $m_2 = +\frac{1}{2}$, $-\frac{1}{2}$ we find three states with total spin $s = 1$ (triplet state):

$$\left.\begin{aligned} |1,1\rangle &= |\uparrow,\uparrow\rangle \\ |1,0\rangle &= \frac{1}{\sqrt{2}}(|\uparrow,\downarrow\rangle + |\downarrow,\uparrow\rangle) \\ |1,-1\rangle &= |\downarrow,\downarrow\rangle \end{aligned}\right\} \text{Triplet} \tag{1.42}$$

and one state with total spin $s = 0$ (singlet state):

$$\left.\begin{aligned} |0,0\rangle &= \frac{1}{\sqrt{2}}(|\uparrow,\downarrow\rangle - |\downarrow,\uparrow\rangle) \end{aligned}\right\} \text{Singlet} \tag{1.43}$$

The ground state of this negative ion is a singlet state (eq. 1.43). Therefore the molecule of interest will also be in this spin state.

1.2.2 Gerade-Ungerade Symmetry

The following section contains an overview of the principles of gerade-ungerade symmetry. A more complete description can be found in [47].

For homonuclear diatomic molecules there is an additional symmetry to be considered: the exchange of the nuclei leaves the molecule apparently unchanged. The operation of exchanging the nuclei can be geometrically seen as a reflection of all other coordinates (other than nuclear) in the plane orthogonal to the internuclear axis at the centerpoint between the nuclei.

The potential field of a nucleus in an atom is spherically symmetric, depending only on the distance between the nucleus and the electron. Consequently the

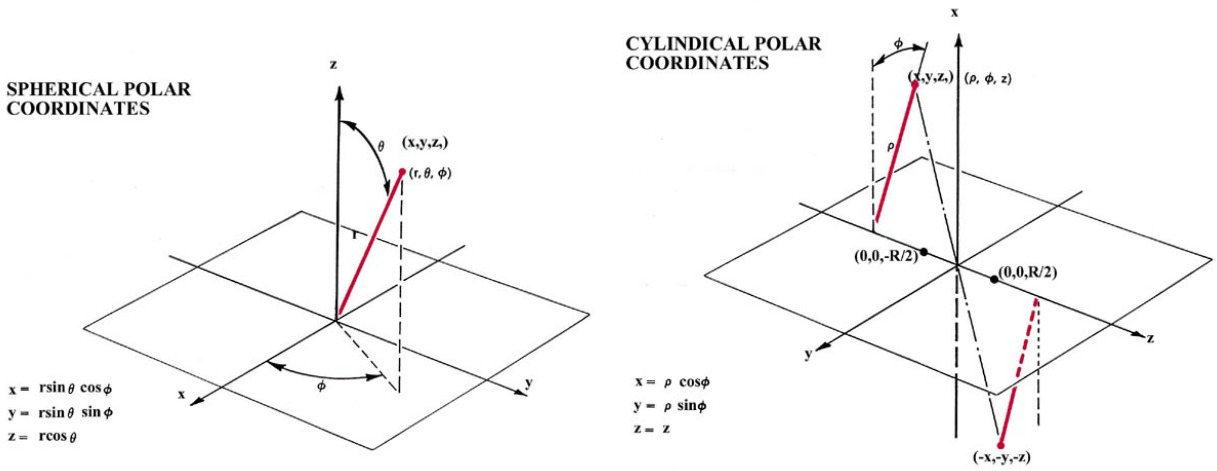

Fig. 1.3: The relationships of spherical polar and cylindrical polar coordinate systems to the Cartesian axes x, y and z. The inversion operation transforms the point (x, y, z) into the point $(-x, -y, -z)$ [47].

spatial symmetries of atomic orbitals are completely determined by the angular momentum quantum numbers l and m. When spherical polar coordinates rather than Cartesian coordinates are used to describe the orbitals, Fig. 1.3 (left), the dependence of the orbitals on the angles θ and ϕ is determined by their angular momentum quantum numbers.

Only the radial dependence (the dependence of the orbital on the coordinate r, the distance between the nucleus and the electron) differs between orbitals with the same l and m values but different values of n.

The potential field of the nuclei in a linear molecule possesses cylindrical symmetry. In terms of a cylindrical coordinate system, Fig. 1.3 (right), the single angular momentum quantum number l determines the dependence of the

molecular orbitals on the angle ϕ, a dependence determining the symmetry of the orbital for a rotation about the internuclear axis. The dependence of the molecular orbitals on ρ and θ is left undetermined.

The forms of the orbitals are not as fully determined by the angular momentum quantum numbers in a molecule as they are in an atom. However, we may further characterize and label the orbitals for a molecular system by taking advantage of the symmetry possessed by the molecule. The symmetry of the potential field in which an electron moves imposes restrictions on the possible forms of the orbitals. This is a very general result.

In order to exemplify the concept more easily let's consider the analogous problem in a 1-D square well potential, where the eigenstates have wavefunctions with a very simple form easily interpretable by eye. Shifting the origin of the x-axis in Fig. 1.4 to the mid-point of the line, changes the values of the coordinates of the two end points from 0 and L to $-L/2$ and $+L/2$ respectively. Next let us denote by the symbol $\boldsymbol{R}$ the operation of reflection through the origin, an operation which replaces each value of x by $-x$. For example, the end points $x = -L/2$ and $x = +L/2$ are interchanged by the reflection operator $\boldsymbol{R}$.

The first point to note about the operation of reflection is that its application leaves the physical system itself unchanged. The potential in which the electron moves is completely symmetric with respect to the x-axis. The reflection operator simply interchanges the two halves of the line, leaving the system unchanged. The

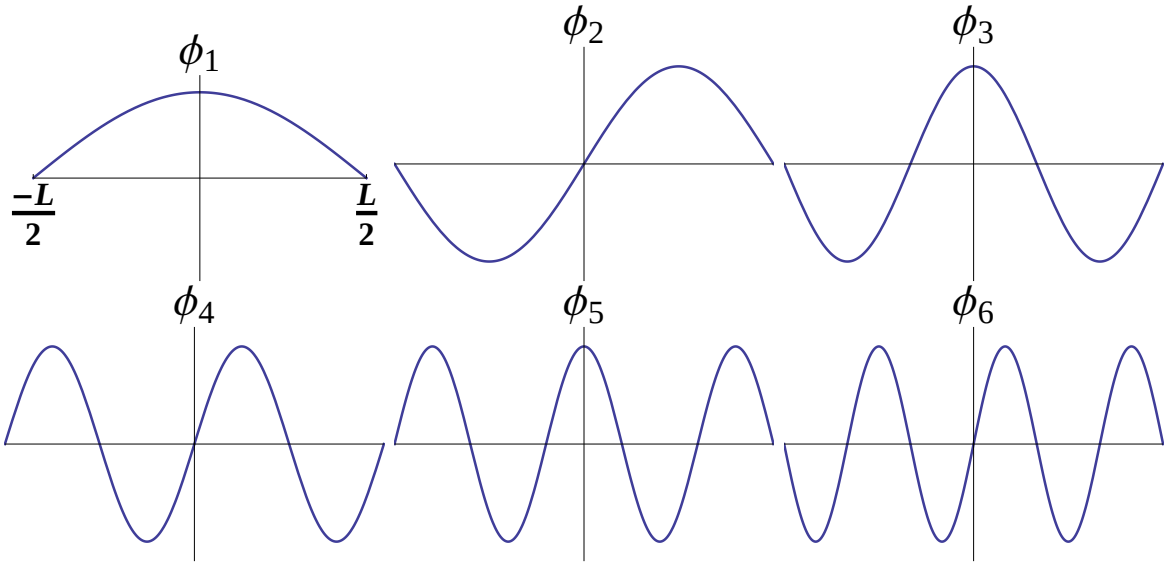

Fig. 1.4: The first six probability amplitudes $\Psi_n(x)$ for an electron moving on a line of length L. Note the $\Psi_n(x)$ may be negative for certain values of x. The $\Psi_n(x)$ are squared to obtain the probability distribution functions $P_n(x)$, which are positive for all values of x. Wherever $\Psi_n(x)$ crosses the x-axis and changes sign, a node appears in the corresponding $P_n(x)$ [47].

potential is said to be invariant to the operation of reflection through the origin.

What is the effect of $\boldsymbol{R}$ on the wavefunctions or orbitals shown if Fig. 1.4? When $\boldsymbol{R}$ operates on $\Psi_1(x)$ (that is, when $\Psi_1(x)$ is reflected through the origin) the result is to change $\Psi_1(x)$ into itself:

$$\boldsymbol{R}\Psi_1(x) = \Psi_1(-x) = (+\mathbf{1})\Psi_1(x) \tag{1.44}$$

The reflected function $\Psi_1(-x) = \Psi_1(x)$.

The result of operating on $\Psi_1(x)$ with the operator $\boldsymbol{R}$ is to leave the function unchanged. $\Psi_1(x)$ is said to be symmetric with respect to a reflection through the origin. The operation of $\boldsymbol{R}$ on $\Psi_2(x)$ yields a different result:

$$\boldsymbol{R}\Psi_2(x) = \Psi_2(-x) = (-\mathbf{1})\Psi_2(x) \tag{1.45}$$

The reflection of $\Psi_2(x)$ through the mid-point changes its sign: the reflected function $\Psi_2(-x)$ is the negative of the original function $\Psi_2(x)$. Such a function is said to be antisymmetric with respect to a reflection at the origin. Every orbital for this system is either symmetric (those with odd n values) or antisymmetric (those with even n values) with respect to the symmetry operation of reflection.

Any orbital which was neither symmetric nor antisymmetric but was instead simply unsymmetrical with respect to reflection would, when squared, yield an unsymmetrical probability distribution. An unsymmetrical probability distribution implies that the electron is more likely to be found on one half of the x-axis than on the other.

This is a physically unacceptable result for a covalent bond since there are no forces acting on the electron which would favor one end of the line over the other. Only orbitals which are either symmetric or antisymmetric yield density distributions which properly reflect the symmetry of the system shown in Fig. 1.5, that is, density distributions which are themselves symmetrical with respect to reflection at the mid-point of the line. Thus we conclude that the only wavefunctions resulting in physically acceptable probability distributions are those which are either symmetrical or antisymmetrical with respect to any symmetry operation which changes the physical system into itself.

The action of the inversion operator on the nuclear coordinates simply interchanges one nucleus for the other. Since the nuclei possess identical charges, the nuclear framework is left unchanged and the potential exerted by the nuclei is invariant to the operation of inversion. Thus every molecular orbital for a homonuclear covalent molecule must be either symmetric or antisymmetric with respect to the inversion operator. Orbitals which are left unchanged by the operation of inversion (are symmetric) are labelled with a subscript g, while those which undergo a change in sign (are antisymmetric) are labelled u. The symbols g and u come from the German words "gerade" and "ungerade" meaning "even" and "odd", respectively.

For a heavy Rydberg system the physical picture is somewhat in disagreement with the discussion above: in this ionic bonding the valence electrons are

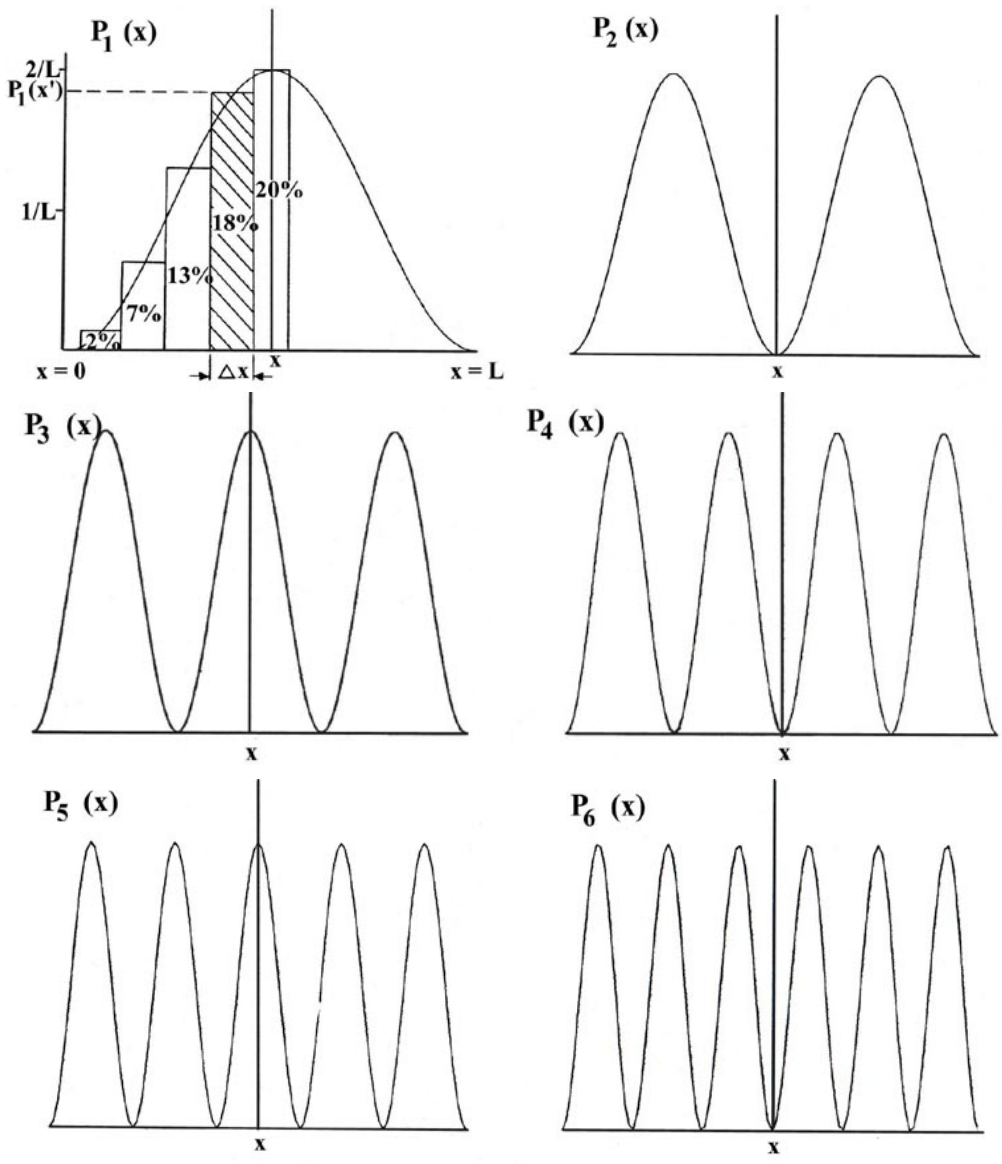

Fig. 1.5: Probability distributions $P_n(x)$ for an electron confined to move on a line of fixed length L in the quantum levels with $n = 1, 2, ..., 6$. The area of each rectangle shown in the figure for $P_1(x)$ equals the probability that the electron is in the particular segment of the line Δx forming the base of the rectangle. The percentage shown in each rectangle is the percentage probability that the electron is in that segment. The total probability that the electron is somewhere on the line is given by the total area under the $P_1(x)$ curve, that is, by the sum of each small element of area $P_1(x)\Delta x$ for each segment Δx. This total area is made to equal unity for every $P_n(x)$ curve by expressing the values of $P_n(x)$ in units of (1/L). Thus by definition a probability of one denotes a certainty.

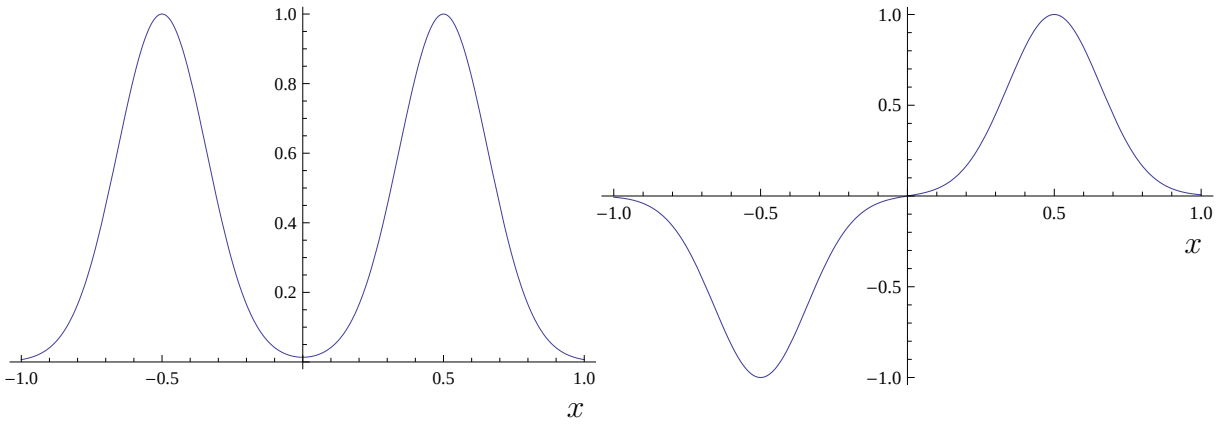

Fig. 1.6: Wavefunctions of both gerade (left) and ungerade (right) symmetry for each electron.

both localized onto one nucleus (Rb^-) while the other (Rb^+) is left stripped of one electron. This is only possible by breaking the gerade-ungerade symmetry, i.e., the wavefunctions describing the heavy Rydberg molecule must be a sum of functions of both gerade and ungerade symmetry. Summing the wavefunctions of both gerade and ungerade symmetry for each electron, as shown in 1.6, we can obtain a total wavefunction whose amplitude squared (probability density) is localized on one nucleus, as shown in 1.7.

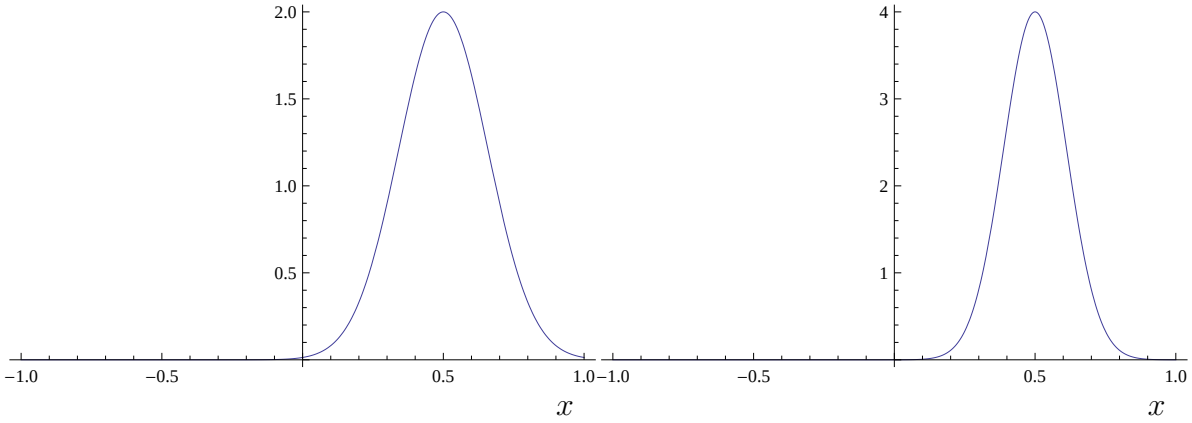

Fig. 1.7: The sum of wavefunctions of both gerade and ungerade symmetry for each electron (left) and the resulting square of the amplitude (probability density) (right)

Allowed Transitions	Examples
$\Delta\Lambda = 0, \pm 1$	$\Sigma \leftrightarrow \Sigma$, $\Pi \leftrightarrow \Pi$, $\Sigma \leftrightarrow \Pi$, $\Delta \leftrightarrow \Pi$
$\Delta S = 0$	${}^1\Sigma \leftrightarrow {}^1\Sigma$, ${}^3\Pi \leftrightarrow {}^3\Pi$, ${}^1\Sigma \leftrightarrow {}^1\Pi$, ${}^3\Sigma \leftrightarrow {}^3\Pi$
$+ \leftrightarrow +$	$\Sigma^+ \leftrightarrow \Sigma^+$
$- \leftrightarrow -$	$\Sigma^- \leftrightarrow \Sigma^-$
$g \leftrightarrow u$	$\Sigma_g^+ \leftrightarrow \Sigma_u^+$, $\Sigma_g \leftrightarrow \Pi_u$

Table 1.2: Selection Rules for Electronic Transitions in Diatomic Molecules. Here Λ is the projection of the total angular momentum on the internuclear axis and S is the total spin.

1.2.3 Selection rules

Section 1.1.5 shows how selection rules come about: integrals can be rigorously zero, for instance if the two states involved have the same parity, a dipole transition is strictly forbidden (since it is a representation of the work done by the electric field $\vec{E}\,.\,\vec{r} = Ez$). The selection rules for optical transitions between different electronic states of a diatomic molecule are shown in Tables 1.2 and 1.3. It is to be noted that in molecular systems the richness of interactions and the wide variety of approximations (cases) bring about a large number of exceptions that often violate strict rules. In our case the spin-orbit interaction allows us to violate the $\Delta S = 0$ rule [43]. If we consider, for completeness, the rotational states as well, it is required that the total angular momentum of photon and molecule remains constant. In general, the selection rules for the total angular momentum J are as

Electron Transition	Allowed transitions	Name
$\Sigma \leftrightarrow \Sigma$	$\Delta J = -1$	P branch
	$\Delta J = 1$	R branch
all others	$\Delta J = -1$	P branch
	$\Delta J = 1$	R branch
	$\Delta J = 0$	Q branch

Table 1.3: Selection Rules for Electronic Transitions in Diatomic Molecules

follows: $\Delta J = 0, \pm 1$. However, for $\Sigma \leftrightarrow \Sigma$ transitions the $\Delta J = 0$ transition is forbidden.

1.3 Ion-Pair and Heavy Rydberg States

In 1988 Pan and Mies [5] theoretically predicted (using as an example LiI), that for potential curves with an ionic long-range form, the vibrational progression near the dissociation limit approaches a Rydberg-like series. In LiI and similar alkali halides, the alkali valence electron is transferred to the halogen (forming a halide negative ion); this charge configuration at sufficiently large distances can be thought of as a Rydberg pseudo-atom with a massive pseudo-electron: the negative ion. Heavy Rydberg formation requires that at least one of the species supports a stable negative ion.

Starting from molecular beams of diatomic molecules or in a vapor cell,

heavy Rydbergs and production of free ion pairs have been observed [6–12]. Heavy Rydberg states or negative ions have not yet been detected in an ultracold environment.

Heavy-Rydberg states (pseudo-atoms) bear strong similarities to electronic Rydberg systems. The main differences are:

* The pseudo-electron is about as massive as the positive core.

* There are significant perturbations due to interactions with covalent configurations of the molecule.

The theoretical framework for heavy Rydberg molecules [11] can be developed in terms of mass scaling with respect to the reduced mass of the system. Electronic Rydberg physics (for which $m^*/M_e \approx 1$ for all atoms and molecules, except exotic species such as positronium and muonium) can be applied in a straightforward manner. However, heavy Rydberg states, with atomic ions as both the positive and negative particles, give a >1000-fold increase in the Rydberg constant even in the lightest of elements.

This implies that the principal quantum number n^* (or vibrational number ν, for molecular systems) corresponding to a given binding energy is increased by a factor $\chi = \sqrt{m^*/m_e}$ relative to an electronic Rydberg system. Since n^* is much larger for these states, the accessible values of angular momentum $l(0 \leq l < n-1)$ are much larger. An electronic Rydberg state bound by ~ 30 cm$^{-1}(n \sim 60)$ has

the same energy as $n^* \sim 17000$ of a Rb_2 ion pair or $n^* \sim 1800$ of an H_2 ion-pair state. The level density follows the scaling but is increased by a factor χ.

When the interatomic spacing is large, the interactions between the atomic ions in an ion-pair molecule are predominantly due to the Coulomb potential ($V(r) \sim 1/r$). This potential does, however, couple to covalent molecular states at short-range [13,14] which gives rise to avoided crossings that have been predicted [17] and observed [18] as shelf states, which support wavefunctions of mixed covalent-ionic nature (see Figure 1.8). The strength of this coupling varies according to Equation 1.46, which diminishes exponentially at large distances [13,19], and where A and B are constants depending on the specific alkali atomic state.

$$V_{covalent-ionic} = Ar^{\frac{1}{B}-1}e^{-Br} \tag{1.46}$$

Even at short-range, the ion-pair potential curve has an effect on molecular structure; however, the interactions are more complicated (e.g. multi-configuration mixing and centrifugal barriers due to angular momentum become more important); this can explain negative ion observations when some molecular channels are excited [8].

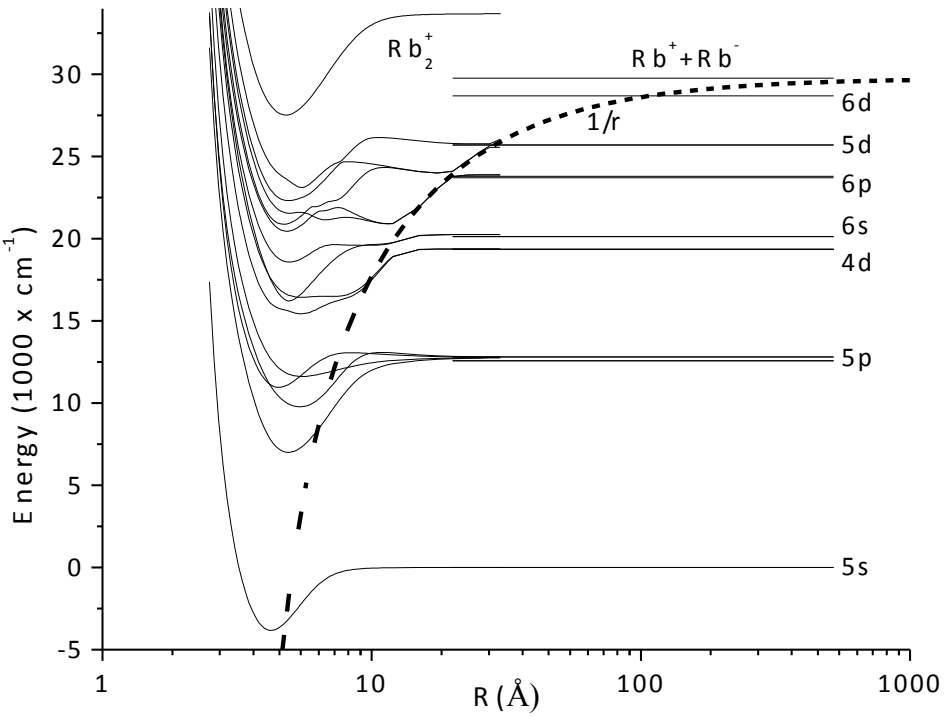

Fig. 1.8: A subset of Rb_2 covalent potentials and the Coulomb potential dissociating to the $Rb^+ + Rb^-$ ion pair (dashed line), derived from [14]. The negative and positive ion polarizability corrections (important at short-range) have been included in the Coulomb curve [15,16].

1.4 Recent Results

Heavy Rydberg states have been observed in a variety of molecular species, and some dynamics have been studied [11]. The excitation mechanism of these states is not clear, and studies done in Edinburgh on ICl [20] and on I_2 [21] are aimed at determining excitation pathways. Vibrational levels in ICl have been followed up to v=360, where the vibrational spacings begin to take on Rydberg characteristics [46].

Many groups, as described in [22–26], are involved in the search for a clean ion-pair system and the development of related methods. Still, to our knowledge, few efforts are directed toward the ultracold regime.

In the past decade several methods have been used to form unresolved superpositions of heavy Rydberg atoms and to show that they can be stable against rapid dissociation. Hepburn's group found compelling indirect evidence for long-lived vibrational Rydberg states in O_2 by using delayed pulsed field dissociation to produce $O^+ + O^-$, [6] and went on to use similar approaches to measure the dissociation energy of HCl [7] and other species. [26]

Ubachs and coworkers have observed strong temporal oscillations in wave packets of Stark-split vibrational Rydberg states of H_2 and HF, excited by nanosecond pulsed lasers and detected using pulsed-field dissociation. [9,10] The same group recently published a very useful review on heavy Rydberg states, with an emphasis on $H^+ + H^-$ [11].

There are numerous unanswered questions regarding the stability of heavy Rydberg states, and interlinked with them is the question of whether individual levels or degenerate groups of levels can be spectroscopically resolved. A good discussion of some of these issues appears in Ref. [11]. Unconditional stability occurs only when the centrifugal barrier $J(J+1)/2R^2$ is so large that there is no penetration into the region of avoided crossings with low-n molecular Rydberg states, nor of Rb^+ into the extended Rb^- wavefunction. [51] In the case of Rb_2 this

requires $n \sim 1500$. However, some of the strongest decay channels are suppressed more easily than this because of the angular momentum barriers that build up in the covalent potentials. This begins at J=23 in H_2, although in Rb_2 the higher reduced mass requires larger J values. Even J=23 seems like a preposterous amount of angular momentum, and is not attainable in zero-field electric dipole excitation. However, for states within a few hundred cm^{-1} of the Rb^++Rb^- limit, angular momentum mixing by electric fields of even a few hundred mV/cm is extensive, relaxing the usual selection rules. In H_2, Suits and Ubachs attribute most of the long-lived heavy Rydberg states to just such high-J levels. The measured lifetimes are typically hundreds of ns in H_2, but much longer in other species ($\sim 2\,\mu s$ in H^++F^-, [10] and $< 5\,\mu s$ in new work on the K^++SF_6^- system [50]).

Chapter 2

Experiment

2.1 General Scheme

2.1.1 Ion-pair and covalent character

In the previous chapter the fundamental traits of covalent and ionic character have been outlined. The most relevant point of their description can be summarized by the consideration that while a covalent state has a definite gerade or ungerade symmetry, an ionic state must have *both* gerade and ungerade components within its wavefunction:

$$\begin{aligned} \Psi_{cov} &= \psi_g \text{ or } \psi_u \\ \Psi_{IP} &= \psi_u^{'} + \psi_g^{''} \end{aligned} \tag{2.1}$$

with the subscripts (cov), (IP), (u), and (g) indicating that the wavefunctions have covalent, ionic character, and are of ungerade, gerade symmetry, respectively. Of course the second of Eq. 2.1 gives a necessary condition only. With current ultracold techniques it is possible to produce only covalent molecular states since the ultracold neutral atomic sample (of separate atoms) composes a continuum

of colliding atom pairs whose states have either gerade or ungerade symmetry. In order to attain ionic character a charge transfer has to be performed between two atoms, which in principle can be performed in at least two ways:

- at long range, when the electronic wavefunctions normally do not overlap, by exciting one electron to a Rydberg state. This electron can be displaced far from its original nucleus and thus be subsequently attached onto the second atom. This possibility is not experimentally investigated in this thesis.

- at short-range, when the electronic wavefunctions do overlap, by creating a wavepacket of both symmetries, which in itself requires a violation of regular molecular transition selection rules. This could be achieved through the introduction of an ad-hoc perturbation in the molecular Hamiltonian exploiting appropriate near degeneracies in the covalent molecular structure.

The second item of this list is the frame in which this thesis is developed.

2.1.2 Goal: Search for near degeneracy of gerade and ungerade states below the Rb(5s)+Rb(4d) limit: $3^1\Sigma_g^+$ and $2^1\Sigma_u^+$

In order to explore such a pathway to ion-pair molecules, a detailed knowledge of the relevant level structures is needed. In covalent molecules the influence of the ionic configuration is clearly discernible in Fig. 2.1. Among the highlighted electronic states (which are the prime candidates in this pathway), our choice to investigate the states asymptotically approaching the Rb(5s)+Rb(4d) limit

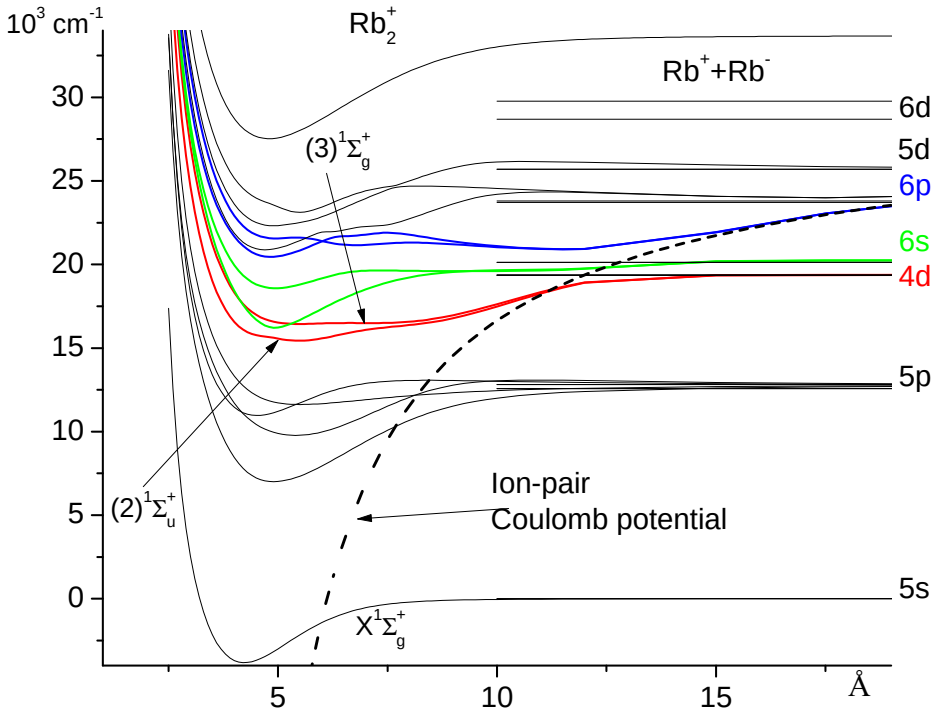

Fig. 2.1: A subset of Rb_2 singlet covalent potentials and the Coulomb potential dissociating to the $Rb^+ + Rb^-$ ion pair (dashed line), derived from [14]. The negative and positive ion polarizability corrections (important at short-range) have been included in the Coulomb curve [15,16]. Highlighted in red, green, and blue are the shelf states with manifest ion-pair branches.

is purely technical: starting with ground-state vibrational levels just below the Rb(5s)+Rb(5s) asymptote, it is possible to use convenient dyes for laser excitation. In addition, a previous study performed by Y. Huang [43] had already mapped out part of the potentials up to almost 17000 cm^{-1}.

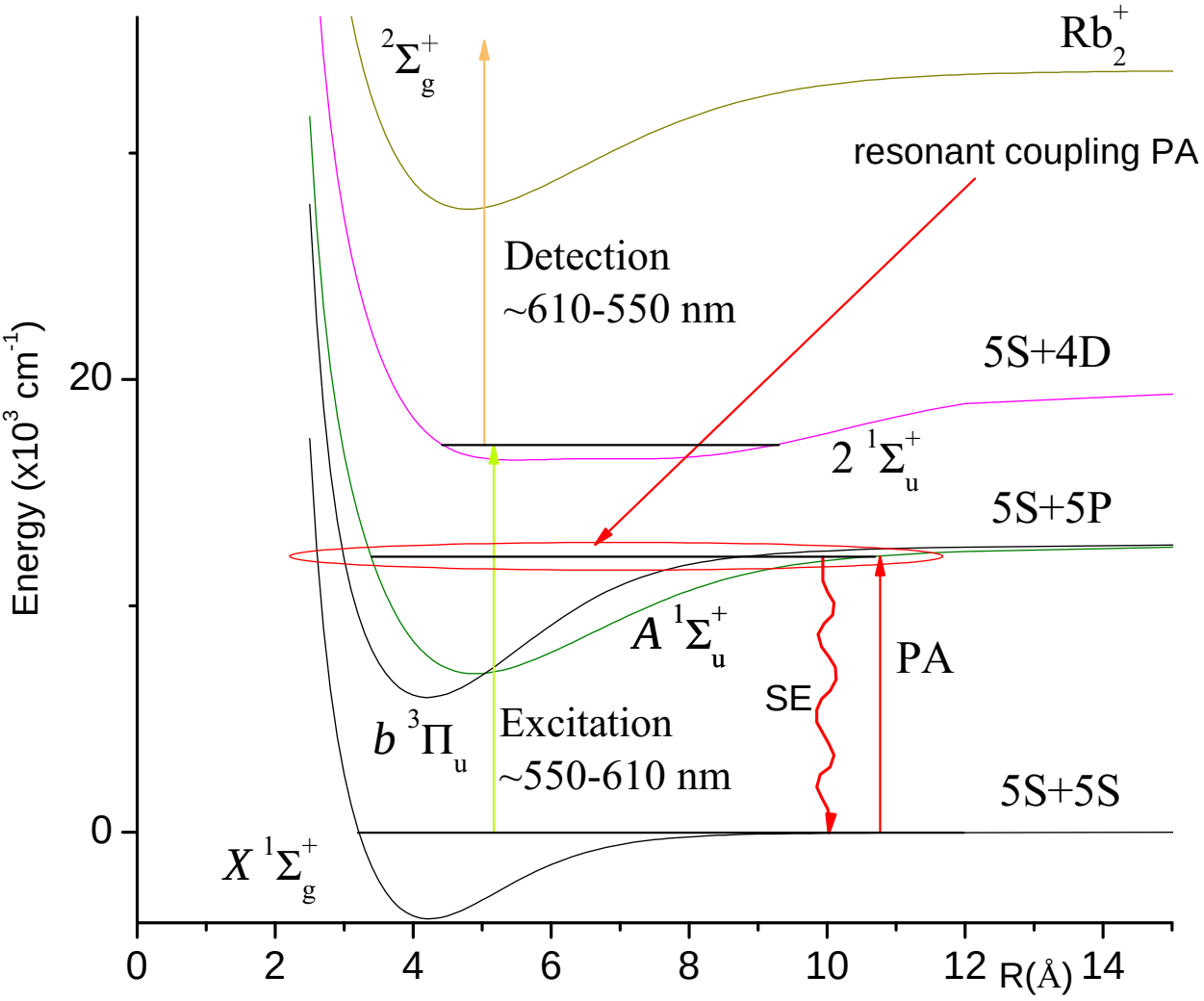

Fig. 2.2: General scheme for spectroscopy of an ungerade-symmetry shelf state: PA followed by spontaneous emission (SE) into the gerade-symmetry ground state $X^1\Sigma_g^+$; subsequent excitation with a pulsed laser ($\tau \sim 10\,ns$) to the energy region of interest ($\sim 17000 - 18000\,cm^{-1}$), and quasi simultaneous ionization with an auxiliary pulsed detection laser.

2.1.3 General Scheme

In view of the fact that only states of gerade or ungerade symmetry, as opposed to a superposition, can be prepared directly from an ultracold continuum, it is necessary to:

* first prepare a sample of a given symmetry. This is achieved by photoassociation (PA) and subsequent spontaneous emission.

* excite the sample to the spectral region of interest, which is done by pulsed laser excitation.

* selectively ionize the excited sample for detection.

The last two items of this list are known as Resonance-Enhanced Multi-Photon Ionization (REMPI) in which exciting simultaneously (or almost simultaneously) a transition to the ion-continuum is vastly more efficient if performed through a resonant intermediate level. This substantially becomes a powerful tool to selectively detect states above a certain energy level dictated by the photon's energy and the ionization threshold. In our case, the intermediate states are of primary interest and we perform their spectroscopy using this ionization detection. Avoiding as much as possible the excitation of unwanted electronic states is a factual requirement; otherwise the resulting spectrum may be too crowded for interpretation. This can be done in two ways:

* by photoassociation of states with the most favorable Franck-Condon factors (FCFs) to the states of interest.

* by controlling the pulse energy of the exciting laser, we can avoid strong saturation of the transitions to the electronic states of interest and minimize excitation to unwanted electronic states.

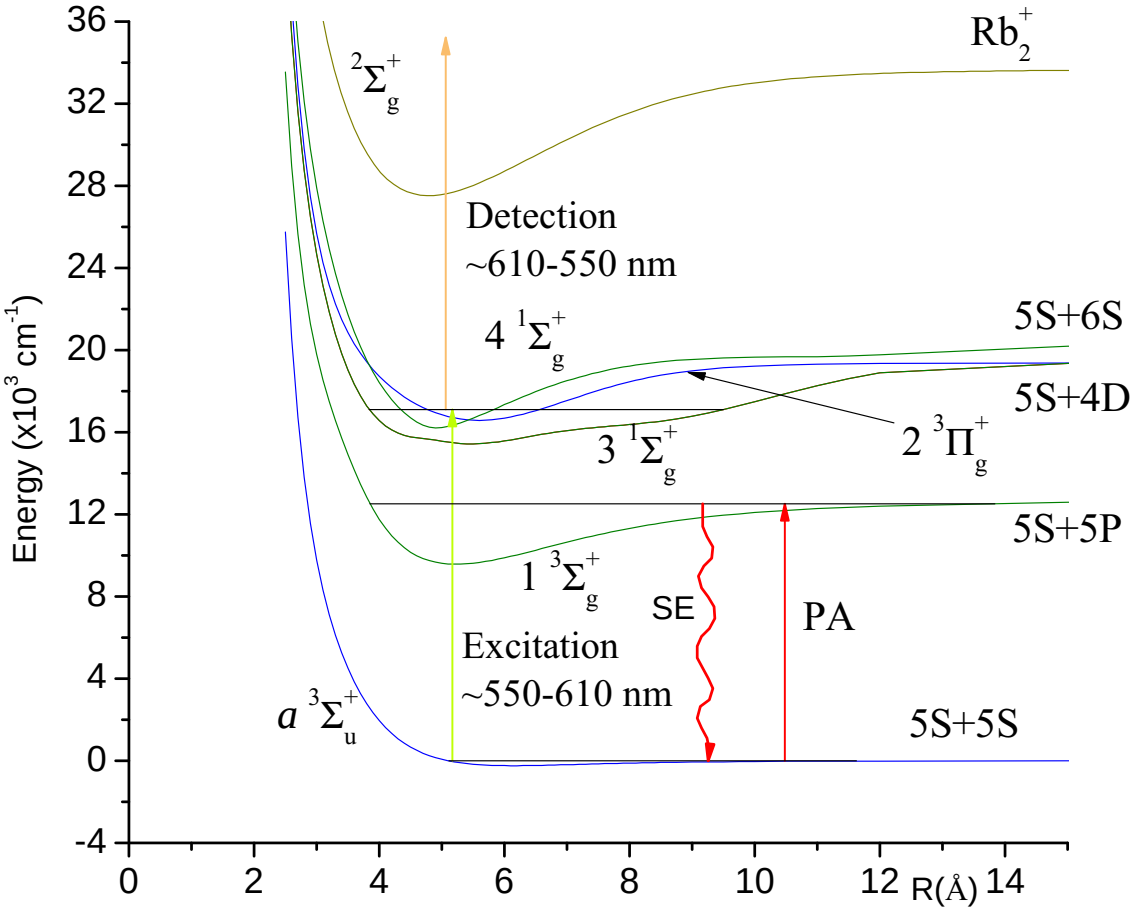

Fig. 2.3: General scheme for spectroscopy of a gerade-symmetry shelf state: PA followed by spontaneous emission (SE) into the ungerade-symmetry metastable state $a^3\Sigma_u^+$; subsequent excitation with a pulsed laser ($\tau \sim 10\,ns$) to the energy region of interest ($\sim 17000 - 18000\,cm^{-1}$); and quasi simultaneous ionization with an auxiliary pulsed laser. Note that the metastable $a^3\Sigma_u^+$ state used here offers the promise of vertical outer turning point alignment with the levels of the $3^1\Sigma_g^+$ state. Transitions to this singlet state, which are nominally spin forbidden, are allowed by spin orbit coupling [43], but with reduced probability. The inner turning points for the $2^3\Pi_g$ (spin allowed) and $(4)^1\Sigma_g^+$ (spin forbidden) state also have reasonable overlap, leading to finite FCFs. Considering these factors, the presence of transitions belonging to the $2^3\Pi_g$ state can be expected in this excitation spectrum.

State preparation: photoassociation

Photoassociation (PA) is a technique in which a pair of atoms in the ground-state continuum approach each other with a given kinetic energy E (which is small for ultracold atoms) in the presence of a radiation field $\hbar\omega$; if the laser field is chosen appropriately, that is $E + \hbar\omega = E_{v',J'}$, then the following reaction is possible:

$$\mathrm{Rb}(5s) + \mathrm{Rb}(5s) + E + \hbar\omega \rightarrow \mathrm{Rb}_2(^{2S+1}\Lambda^{+/-}_{u/g};\, v',\, J') \tag{2.2}$$

where S, Λ, v', and J' are the total electron spin, the projection of the angular momentum on the internuclear axis, the vibrational quantum number, and the rotational quantum number, respectively. Naturally the molecular production rate depends greatly on details of the target excited state: after photoassociation, decay to the continuum is still important, and accurate studies are key in these situations in order to accumulate ground-state bound molecules. For the purpose of this work, Y. Huang [43] and H. K. Pechkis [53] have already paved the way in this direction, with a detailed description of the procedure. The parameters utilized in this work are shown in Fig. 2.4, taken from [43], for preparing barely-bound levels in the lowest-lying metastable state (a $^3\Sigma_u^+$), and Fig. 2.5, taken from [53], for preparing barely-bound molecules in the electronic ground state (X $^1\Sigma_g^+$). In the latter case, comparisons of experimental detection laser scans for different PA detunings show the effects of resonant coupling between a long-range state and a short-range state. The emission of such a resonantly-coupled excited state has

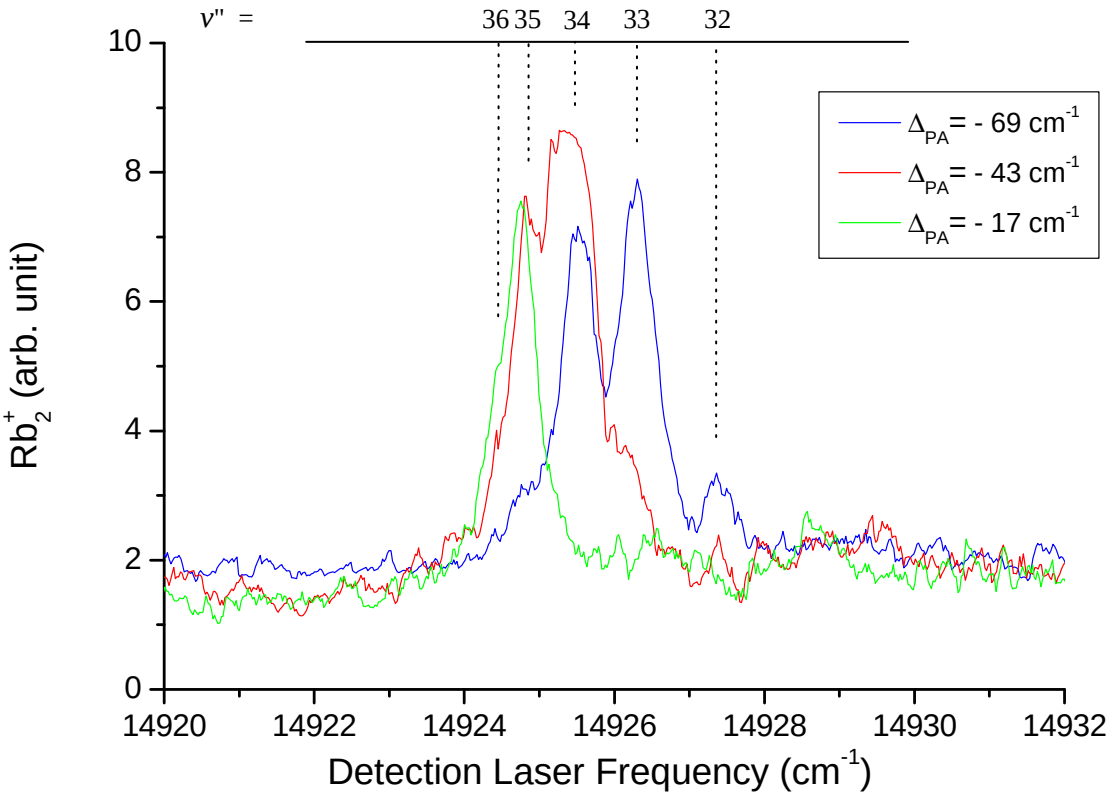

Fig. 2.4: REMPI ion signal of PA using the $0_g^- - 1^3\Sigma_g^+$ state which dissociates to $5S + 5P_{1/2}$. Shown are PA detunings of $\Delta_{PA} = -69\,cm^{-1}$, $-43\ cm^{-1}$, and $-17\ cm^{-1}$ below the atomic asymptote. $\Delta_{PA} = -69\,cm^{-1}$ has been used for state preparation into the $a^3\Sigma_u^+$ state throughout this study. The natural decay $1^3\Sigma_g^+ \rightarrow a^3\Sigma_u^+$ seems to afford a good compromise between spectroscopic resolution of the target states populated while their long range extension provides a favorable FCF for the ion-pair branch of the shelf state.

a bimodal vibrational probability distribution, with one peak at long range which enhances the photoassociation rate, and another at shorter range which enhances radiative decay into relatively deeply-bound levels of the ground electronic state.

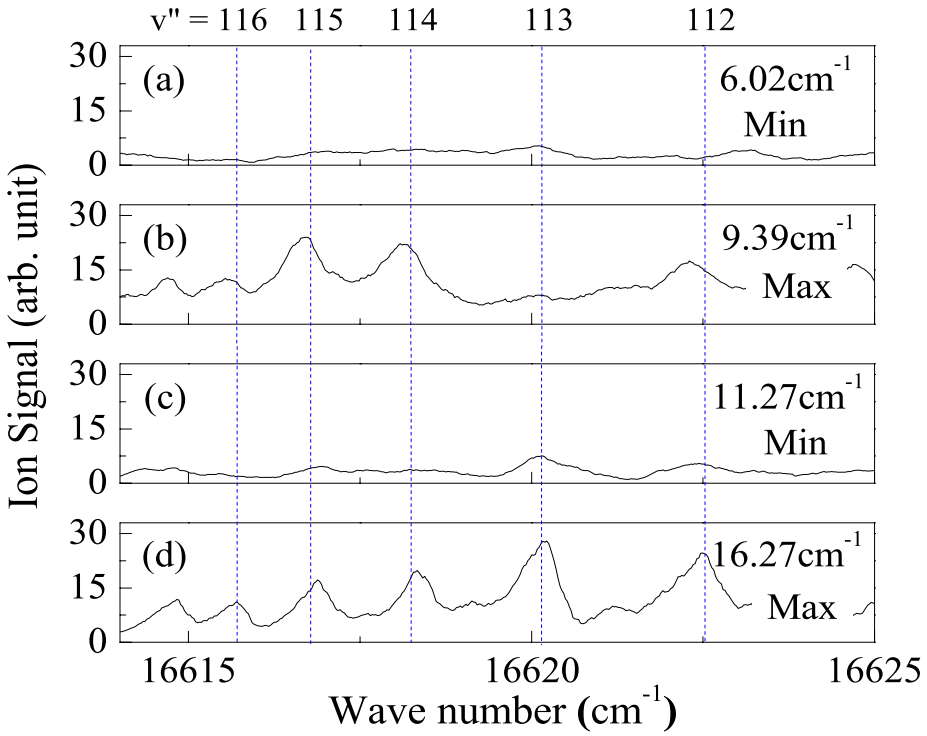

Fig. 2.5: Comparison of experimental detection laser scans for PA detunings corresponding to the minimum and maximum effects of resonant coupling: PA to an excited state with emission that has a bimodal vibrational probability distribution, with one peak at long range to enhance the photoassociation rate, and another at shorter range to enhance radiative decay into deeply-bound levels of the ground electronic state. Here [53] spin-orbit perturbations between the pair of 0_u^+ states, $0_u^+(P_{1/2})$ and $0_u^+(P_{3/2})$, in the region below the $5S_{1/2} + 5P_{1/2}$ limit, have been studied. Subsequent radiative decay produces high vibrational levels of the ground state, $X^1\Sigma_g^+$. Shown are ionization signals for PA binding energies relative to $5S_{1/2} + 5P_{1/2}$ of (a) $6.02\,cm^{-1}$ (Min), (b) $9.39\,cm^{-1}$ (Max), (c) $11.27\,cm^{-1}$ (Min), and (d) $16.27\,cm^{-1}$ (Max). For easy comparison, the vibrational levels v" are marked by vertical lines. Case (b) has been used in this thesis, promising a good trade off between spectroscopic resolution of the target states populated and favorable FCFs to the ion-pair branch of the shelf state.

2.2 Components

The basic layout of the apparatus has been used repeatedly over the last decade or so in various experiments [55] [56] [43]. In light of this fact we restrict ourselves to the description of the components and working regime specific to the particular series of measurements described in this thesis.

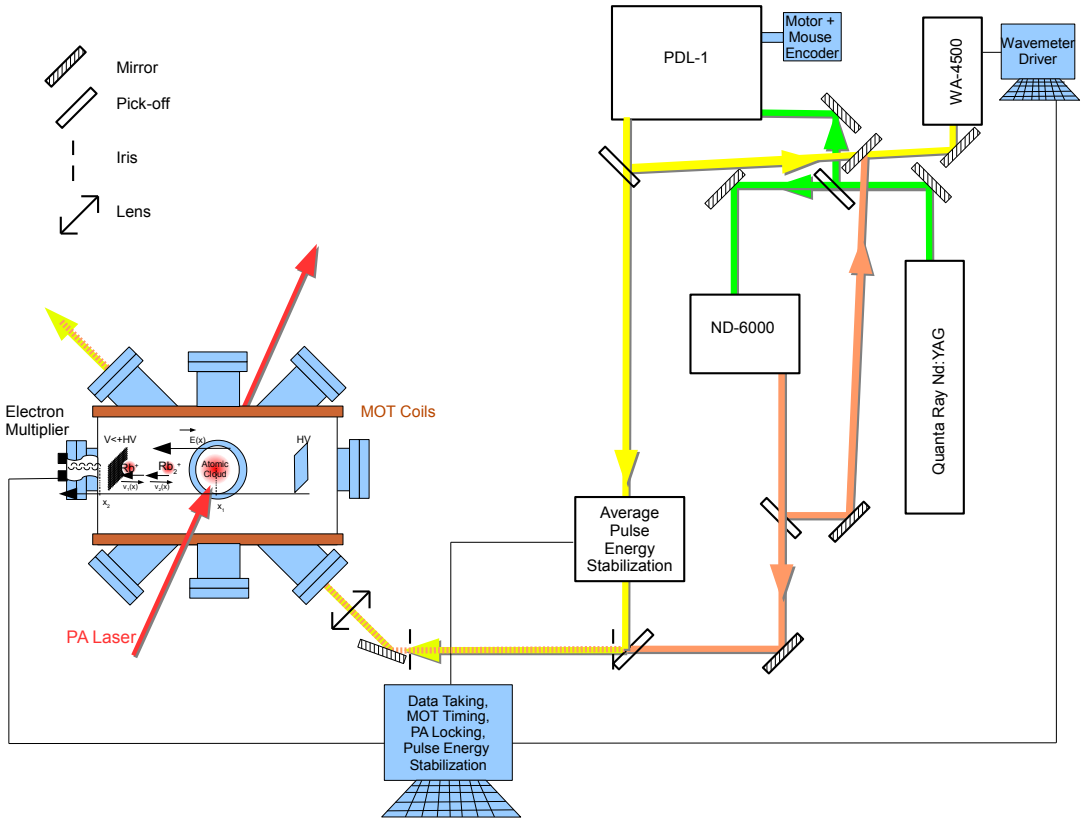

Fig. 2.6: Schematic representation of the experimental apparatus, more details of the detection region are shown separately in Figure 2.8

2.2.1 Ultracold environment

The basic apparatus in which the experiment is run is a vapor-cell MOT (Magneto-Optical Trap) [57]. Substantially, the slow tail of the room-temperature Boltzmann distribution of Rb vapor feels a viscous force due to nearly resonant, red-detuned counter-propagating laser beams; the presence of a quadrupole magnetic field introduces a position-dependent, spring-like, restoring force. The sum of the forces from three orthogonal pairs of counter-propagating beams slows down and collects Rb atoms in a small region of nearly zero magnetic field. MOTs have been described extensively in the literature; a good starting reference is Metcalf's "Laser cooling and trapping" [58]. The relevant parameters routinely used are: a quasi-Gaussian atomic cloud, in a pancake shape, composed of $\sim 10^7$ atoms with a peak density of $10^{11}\, atoms/cm^3$, and geometrical FWHM of $\sim 0.7\, mm$ along x- and y- axes, and $\sim 0.35\, mm$ along the z-axis.

The production of diatomic molecules is achieved via photoassociation (PA), where a CW laser connects the quasibound free-atom population (typically spread over a 2 MHz band) to a bound excited electronic molecular state. The spontaneous decay from the excited level populates a number of levels in either the electronic ground state $X^1\Sigma_g^+$, or the metastable $a^3\Sigma_u^+$ triplet state (or both if the upper state does not have u-g symmetry). In particular the PA laser requires a certain power (typically near 1 W) and frequency stability, both short-term and long-term. For this a Coherent $899-29$ Ti:Sapphire laser was employed. Its

short-term stability (linewidth $< 700\,kHz$ RMS) is quite good. Using an external Fabry-Perot cavity stabilized to a MOT laser (locked to a Rb $5s - 5p$ transition) gives an overall long-term stability better than 2 MHz/day with respect to the reference.

2.2.2 Fabry-Perot lock

The Fabry-Perot lock is used for long-term stabilization of the apparent frequency difference of the PA laser with respect to the reference laser (one of the MOT lasers). It is a fairly standard Labview software lock: A Fabry-Perot interferometer with a free spectral range (FSR) of 2 GHz is scanned at $\sim 20\,Hz$ with a sawtooth wave produced by a microcontroller [59] [60]. On the optical input side of the interferometer, the orthogonally polarized reference (REF) and PA lasers are combined through a Polarizing Beam Splitter (PBS). After transmission through the cavity, the two beams are separated by another PBS and sent to separate photodiodes. On a PC with a National Instruments (NI) card, 2 analog-to-digital converters (ADCs) are set to acquire synchronously with the generated scan, while one of the digital-to-analog converters (DACs) is set up as a feedback line to the PA laser frequency. An internal routine is used to determine the frequency difference between the peak patterns of the two channels. During the sawtooth modulation the piezo transducer is ramped for a time T_0. The center-part of this time interval (approximately $(\frac{1}{6}\,T_0,\ \frac{5}{6}\,T_0)$ has a linear rela-

tionship with cavity mirror displacement, while the "edges" show deviations from linearity due to ferroelectric hysteresis. Considering only the linear region, the time difference between two successive peak centers of the REF, combined with the specified cavity Free Spectral Range (FSR), gives the time to frequency conversion. The apparent frequency offset between the REF laser and the PA laser is then determined by measuring the time difference between chosen peaks in the two acquisition channels. This way the apparent frequency difference between the two lasers can be locked using the DAC feedback line to the PA laser.

There are, however, some non-standard features: Initially, long-term operation has been limited by the time the REF laser would remain locked to a saturated absorption feature in a Rb cell. While reacquiring lock on this laser is a relatively quick procedure, it is a much more involved operation to re-acquire lock on the PA line. To prevent actively driving the 899-29 (which has a good short-term stability) away from the PA line, the feedback routine is frozen if the apparent frequency difference between the two interference patterns is more than 10 MHz from the setpoint. This fail-safe feature enables extension of the stability of the PA laser well beyond the stability of the MOT lasers; however, it does not protect fully against 899-29 mode hops, which can only be recognized by comparison with the MOT status.

2.2.3 Pulsed lasers for REMPI

Two pulsed dye lasers are employed to perform Resonance-Enhanced Multi-Photon Ionization (REMPI). Once the initial state preparation has been achieved through PA, a pulsed laser (L1) is used to excite molecular levels in the spectral region of interest, between $16200\,cm^{-1}$ and $18400\,cm^{-1}$, with the power chosen to keep power broadening to a minimum, while the other (L2) is used at a higher power to photoionize the excited molecular state, creating a molecular ion, which is subsequently detected through time-of-flight mass spectroscopy (TOFMS). It turns out that in order to efficiently excite and ionize molecules, the two photons' frequencies are both contained in the region of interest mentioned above, so care has been taken in keeping L2 tuned away from any molecular transition. The lasers used for this purpose are commercially available: Spectra Physics/Quanta Ray PDL-1, and Continuum ND-6000, both pumped by a doubled Nd:YAG (Spectra Physics Quanta Ray). The linewidths of both lasers are $\leq 0.1\,cm^{-1}$. Either one of these lasers has been employed as L1 or L2 depending on convenience. As shown in Table 2.1, a number of dyes (and also dye mixtures) have been used to cover the required wavelength ranges. The recipes used for dye solutions have been based on the Lambdachrome laser dye guide [61], the articles there cited, and our own historical recipes. In particular the use of Pyrromethene (PM) dyes has been key in efficiently covering the shorter wavelengths, almost up to the pump laser (Nd:YAG, 2^{nd} harmonic at 532 nm) limit.

Dye	Range Low End (cm^{-1})	Range High End (cm^{-1})
R6G (LC 5900)	∼17100	∼18000
R610 (LC 6100)	∼16150	∼17100
R640 (LC 6400)	∼15100	∼16300
PM 556 (LC 5560)	∼17000	∼18300
PM 567 (LC 5670)	∼16900	∼18200

Table 2.1: Laser dyes used and their corresponding wavelength ranges

2.2.4 Laser mixing, stabilization of power

To keep power broadening to a minimum, and more importantly nearly constant, the output power for L1 has been stabilized using a Polarizing Beam Splitter (PBS) downstream from a motorized half-wave plate. A Labview servo routine has been used to keep the power reaching the chamber constant during the scan. This stabilization is particularly important near the edges of the operating range of a dye where the power output drops. Depending on frequency and dye performance L1 and L2 are overlapped on the molecular cloud with different procedures.

With power to spare, one laser is reflected off a thick etalon while the other is transmitted through the same flat, allowing co-propagation into all subsequent optics. With some dyes, the use of a flat for reflection was found to be the limiting

element. In order to extend the operation of L1 as far as possible, it has sometimes been necessary to directly align each individual laser onto the molecular cloud, by introducing a small angle between the two converging beams.

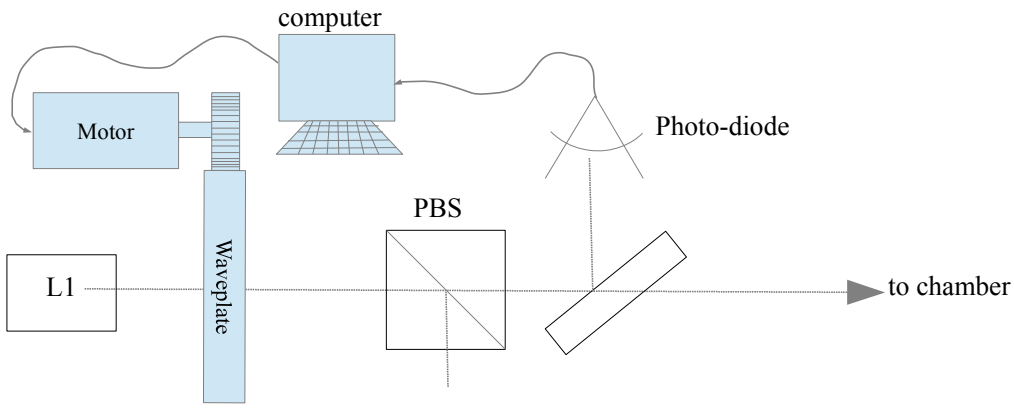

Fig. 2.7: Representation of servo loop for average power stabilization of pulsed dye laser.

2.2.5 Wavemeter WA-4500

All spectra have been recorded with the aid of a commercial wavemeter, Burleigh WA-4500, with a specified maximum accuracy of $\sim 0.02\,cm^{-1}$. This value is to be considered carefully: in the absence of lineshape asymmetry and other spectral irregularities, this is the accuracy value that can be expected. This pulsed wavemeter utilizes the resolving power of two etalons for the precise determination of the wavelength. The accuracy depends on comparing peak locations in the unknown laser spectrum with a built-in HeNe reference laser. The major error

is in determining the interference order of the unknown laser, and results in an error that takes the value of an integer multiple of the FSR. In the case of two etalons being used, the error will be the sum (or difference) of integer multiples of FSRs of the two etalons. The absolute accuracy is ultimately determined by the reference HeNe laser.

While in the many hours of data collection this wavemeter has performed up to expectations, there have been a few cases in which order determination has been an issue; in these cases a simple shift has been sufficient to restore the correct wavelength assignment. In addition, data runs have been taken by overlapping separate scans, allowing alignment of different segments of the spectrum, yielding a spectrum that could be calibrated by two reference points, the atomic transitions from $5p_{3/2} \rightarrow 7d_{3/2}$ and $7d_{5/2}$.

2.2.6 Ion detection using ToF selection

REMPI produces, along with the molecular ions of interest, atomic ions, electrons etc... In order to capture only the relevant signal, it is possible to separate species by mass: the laser pulses produce within a $10\,ns$ time window all the species in the presence of an applied electric field.

Immediately, all ions start their drift, accelerating according to their mass and charge. Positive ions are directed toward the detector (an ETP discrete dynode electron multiplier, ETP model 14150), while any negative charges are

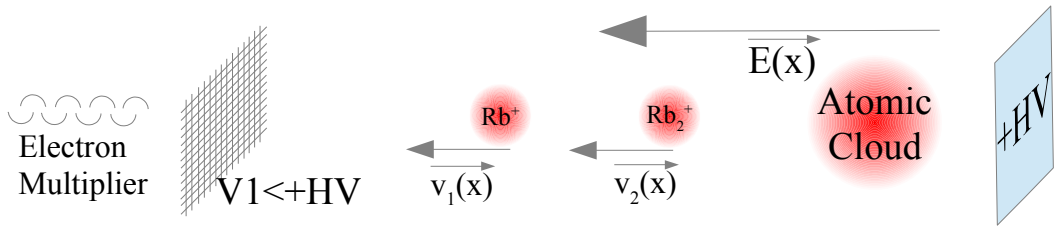

Fig. 2.8: Schematic representation of time of flight dynamics

driven into the HV plate. The time of arrival τ can be estimated. Consider the kinetic energy, $T = \frac{1}{2}mv^2$. By isolating v:

$$\frac{\mathrm{dx}}{\mathrm{dt}} = v(x) = \sqrt{\frac{2qV(x)}{m}} \tag{2.3}$$

we can integrate to get τ:

$$\tau = \int_{t_1}^{t_2} dt = \int_{x_1}^{x_2} \frac{1}{v(x)} dx = \int_{x_1}^{x_2} \sqrt{\frac{m}{2qV(x)}} dx = \eta_0 \sqrt{\frac{m}{q}} \tag{2.4}$$

Where η_0 is the result of the integral independent from q and m, and depends only on the shape of the potential $V(x)$.

Fig. 2.9 represents a typical TOF ion signal. Specifically to be noted are:

- $t \sim 0$: the Light Pulse: photoelectrons are generated directly inside the electron-multiplier by stray photons coming from the pulsed lasers.

- Following the Light Pulse is a saturation tail. This is due to nonlinear effects and finite recovery time in the detector and its electronics becoming

important with larger ion signals. In particular, it is noticeable how this tail imparts a sloping background within the Rb^+ time window.

- $t \sim 4.5\,\mu s$: Although the Atomic Signal is not large enough to show a saturation tail in this figure, when present, it introduces systematics and noise into the molecular ion signal.

- $t \sim 6.3\,\mu s$: Molecular Signal

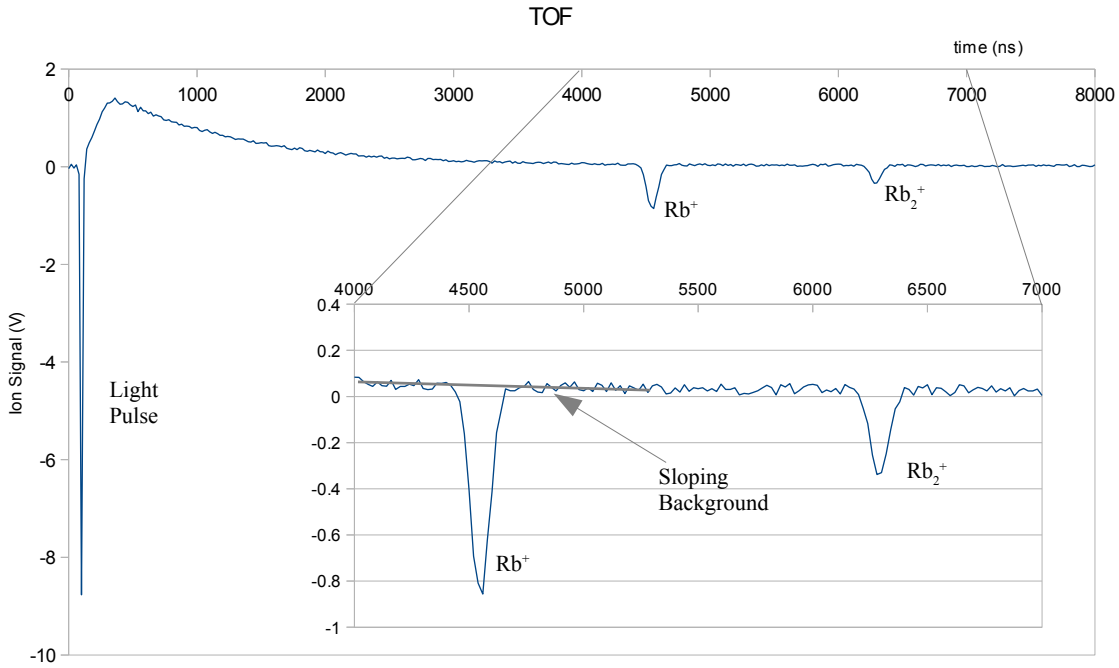

Fig. 2.9: TOF oscilloscope trace

These peaks are the result of the superposition of individual ion peaks that reach the detector in the time window determined by the TOF mechanics; their

pulse area is subject, in the most optimistic scenario, to Poissonian statistical fluctuations.

Given the presence of leakage of the saturation tail into the following channels, very small signals are better detected by subtracting the background baseline. Using boxcar averagers for measuring both the ion channel (either Rb^+ or Rb_2^+) pulse area and the background level immediately preceding it, we can obtain just the baseline-free ion signal by taking their difference. Other schemes using different integration window widths around the ion peak have been investigated but they have yielded a lower signal-to-noise ratio.

2.2.7 Noise sources and their evaluation

The overall spectrum is composed of several intervals pieced together; the way this is achieved in turn gives the final error evaluation. We'll start with the processing of a single scan, then proceed to the overlapping of neighboring scans.

X-Axis

The wavemeter's finest etalon (etalon B) was borderline usable due to the laser linewidth being comparable to the etalon's measurable linewidth of $0.05\,cm^{-1}$. Only etalon A of the WA-4500 was of practical use; this led to a relatively granular reading of the frequency giving a fictitious loss of accuracy. This can be observed in Fig. 2.10 where the same spectral feature is presented as a function of the

recorded wavenumber (a) and time index (b). It is to be noted that what seem to be vertical fluctuations in Fig. 2.10 (a) show as a smooth frequency dependence in Fig. 2.10 (b). Considering that the continuous scanning of the laser was monotonic in time and that the sampling rate was higher than what the resolution of the etalon could discriminate, this is not surprising.

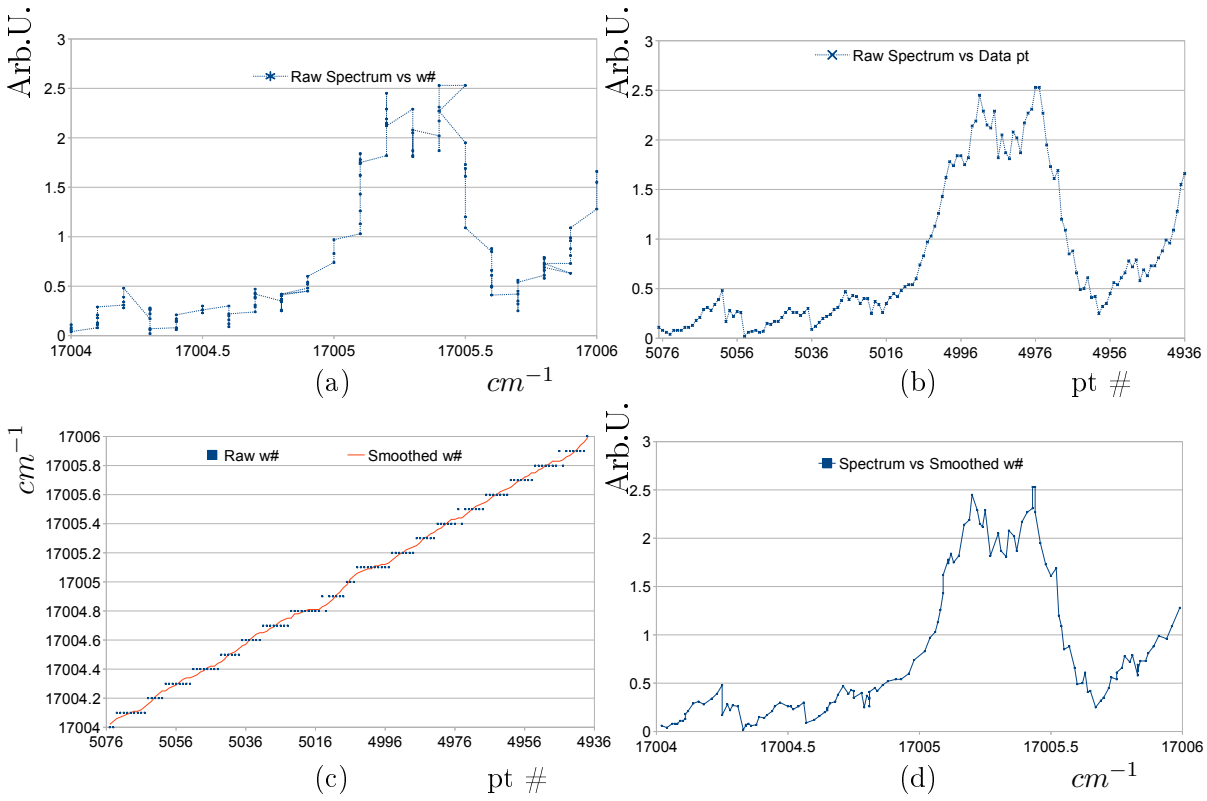

Fig. 2.10: Example of frequency axis smoothing: (a) Raw spectrum, no smoothing applied. The granular nature of the wavemeter reading bins the spectrum in too large intervals. (b) The spectrum as a function of its recording index ($\sim$ time). Comparison with (a) highlights a loss of resolution. (c) Raw wavemeter readings vs recording index and polynomial smoothing of the same spectral interval as in (a) and (b). (d) End result of the frequency smoothing procedure where the granularity present in (a) has been removed.

A local fitting procedure was used to reduce granularity and the expected relative frequency reading error: a 2^{nd}-order polynomial fit was applied on a 17 point sample around every single data point shown in Fig. 2.10 (c). An example of the result is shown in Fig. 2.10 (d): the spectrum vs. frequency closely resembles the same spectrum vs. time index, effectively regaining a relative resolution on the order of the laser linewidth $\sim 0.05\,cm^{-1}$. This process lends itself to determining the fluctuations around the smoothed data points, yielding a standard deviation for the frequency measurement of $\sim 0.03\,cm^{-1}$, if evaluated on a large enough interval. The exclusive use of Etalon A has effectively reduced the absolute accuracy, downgrading the WA-4500 to a WA-4000 (Fig. 2.11), whose accuracy should be considered $\sim 1.0\,cm^{-1}$. In the later subsections we'll see how a higher absolute accuracy can be regained.

Y-axis

The channels collected by the boxcar averagers result in a differential signal. Systematics are mostly eliminated, but the signal is still subject to statistical fluctuations from all channels/components involved. These fluctuations partly depend on the size of the signal itself (in the best case scenario being the result of a form of particle counting) so the error can show a wavelength dependent behavior. Given a data set, $\{x_i,\, y_i\}$ with $i = 0, 1, .., N$, consider a single point, of index j. As in the previous subsection, we take an interval of points around j, say $k = j - n_1 ... j + n_2$.

11. Specifications

Model	WA-5000	WA-5500	WA-4000	WA-4500
Wavelength Range	190-680 nm		400-1100 nm	
Accuracy	± 3.3 cm^{-1} (0.03nm @ 300nm)	± 0.2 cm^{-1} (0.002 nm @ 300nm)	± 1.0 cm^{-1} (0.06nm @ 800nm)	± 0.02 cm^{-1} (0.001 nm @ 800nm)
Spectral Resolution (Etalon A)	8.3 cm^{-1} (250 GHz)	8.3 cm^{-1} (250 GHz)	2.5 cm^{-1} (75 GHz)	2.5 cm^{-1} (75 GHz)
(Etalon B)	N/A	0.33 cm^{-1} (10 GHz)	N/A	0.05 cm^{-1} (1.5 GHz)
Maximum Linewidth (Etalon A)	30 cm^{-1} (900 GHz)	30 cm^{-1} (900 GHz)	15 cm^{-1} (450 GHz)	15 cm^{-1} (450 GHz)
(Etalon B)	N/A	1.5 cm^{-1} (45 GHz)	N/A	0.3 cm^{-1} (9 GHz)
Input Requirements Beam Acceptance Spatial Mode Quality Energy/Power	1 mm dia. Any collimated beam Pulsed: 5 μJ min (1 mJ max) CW: 50 μW min (10 mW max)		1 mm dia. Any collimated beam Pulsed: 1 μJ min (1 mJ max) CW:10 μW min (10 mW max)	
Pulse Duration	> 2 psec		> 2 psec	
External Gate Duration Separation	100 μsec minimum, 50 msec maximum 25 msec minimum			
Update Rate	Wavelength Display Only: > 5 Hz Wavelength and Spectral Display: > 1 Hz			
Dimensions **Weight** **Beam Height** **Power**	420 x 270 x 200 mm 14 Kg 165 mm ± 6 mm (adjustable) 110-120 / 220-240 VAC, 50 / 60 Hz, 40 W typical			
Computer Requirements	12 MHz PC or compatible with 80286 or higher processor, 1 MB RAM, (2MB RAM preferred) Hard disk, Floppy drive for 1.2 MB, 5.25" disk, or 1.44 MB, 3.5" disk Full-sized expansion slot, EGA or VGA monitor and graphics adapter card (VGA preferred) Operating system MS-DOS® 3.3 or higher Strongly recommended: Math co-processor and mouse			
Interfacing	RS-232 (serial port) Printer (parallel port) IEEE-488 (interface card required)			

Fig. 2.11: Wavemeter Burleigh WA-4500 manual, specification page

On this subset we apply polynomial fitting with a function $f(x)$. In particular we obtain the value $f(x_j)$ that we take as the best approximation of the spectrum at the point x_j. We then repeat this process for all possible values of j, that is $J = 0, 1, .., N$. One advantage of this fitting procedure compared to performing a moving average smoothing is that linewidths are nearly unaffected.

In addition this method is useful for evaluating the statistical error. The error on a single data point is difficult to evaluate, but the statistical error on a set of values collected can be readily calculated in a similar manner. After having determined the smoothed spectrum $\{x_i,\, f(x_i)\}$ of our data $\{x_i,\, y_i\}$, the Y-axis error can be then estimated by the statistical deviation from the fit using at least 6 points around the point considered, x_j:

$$\sigma_j^2 = \sum_{k=j-n_1}^{j+n_2} \frac{y_k - f(x_k)}{n_1 + n_2} \tag{2.5}$$

and then repeating for all values of $J = 0, 1, .., N$.

To summarize:

- from $\{x_i,\, y_i\}$ we obtain, from an iterated local procedure, $\{x_i,\, f(x_i)\}$;

- from $\{x_i,\, y_i\}$ and $\{x_i,\, f(x_i)\}$ we obtain, from an iterated local procedure, $\{x_i,\, \sigma_i\}$;

The values of n_1 and n_2 are chosen to:

- be above a certain minimum, $n_1 + n_2 > 5$

- cover a minimum wavenumber interval $\Delta x > 0.3\, cm^{-1}$

- be asymmetric in the case of the extremities of the scan.

In the end this gives an estimate of the resulting expected deviation from an-

other measurement of the same spectrum, considering the fitted value $f(x_i)$ as the closest approximation to the "true" value.

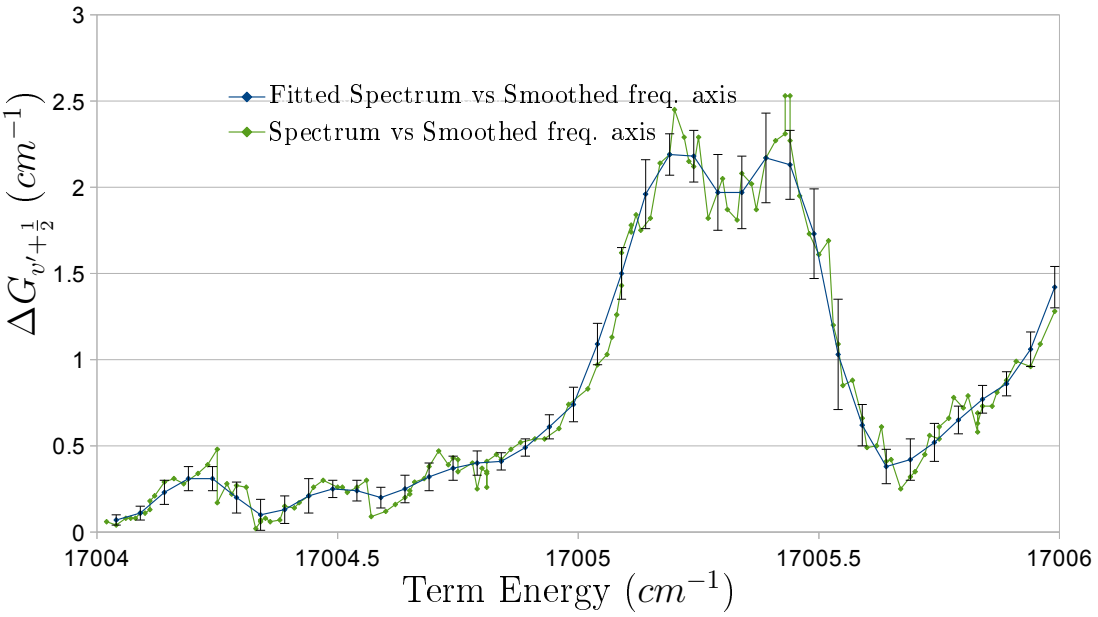

Fig. 2.12: Typical result of the smoothing procedure, which in addition to smoothing, returns an evenly resampled scan.

For a single scan we finally get $\{x_i,\ f(x_i), \sigma_i\}$ while throughout the whole scan we have a relative frequency error of $\sim 0.03\, cm^{-1}$.

Piecing together scans

To align separate scans that overlap in a certain region, one tool is the convolution product. Consider two spectra $f(x)$ and $g(x)$. Just like functions, they form a vector space and the convolution product does nothing else than measure the

cosine between the two argument-vectors multiplied by their norm:

$$\| f \| \| g \| cos(\theta(x_0)) = \int_{x_1}^{x_2} f(x)g(x - x_0)dx. \tag{2.6}$$

where the norm is $\| f \| = \int_{x_1}^{x_2} f(x)f(x)dx$ and x_0 is a shift. It is apparent that if $f(x) = g(x - x_0)$ then $\theta(x_0) = 0$.

When $f(x) \sim g(x)$ then there's a value of x_0 for which $cos(\theta(x_0))$ takes an extremal value. There is an additional caveat that our functions are numerical, discrete in nature, so that the integrals are replaced by sums:

$$\begin{aligned} \| f \| \| g \| cos(\theta_{n_0}) &= \sum_{i=n_1}^{n_2} f(x_i)g(x_{i-n_0})\Delta x \\ \| f \| &= \sum_{i=n_1}^{n_2} f(x_i)f(x_i)\Delta x \end{aligned} \tag{2.7}$$

which is formally identical to the dot product of two vectors in a space of dimension $(n_2 - n_1)$. The convolution product is in fact the dot product between two functions that have a shift in their index $(i \rightarrow (i - n_0))$, and functions are indeed vectors. Picturing vectors of finite dimension helps in laying out the problem and finding the solution:

There are **two** vectors, which always have one (and only one) 2D plane that contains them both; we can reduce our problem to a 2D picture!

This allows the two spectra to have slightly different parameters (for instance different linewidths), but does not take into account how significant they are, i.e. whether the S/N ratio is large or small. Fig. 2.13 (left) represents two spectra in the 2D plane they determine. Their errors determine areas of likelihood around

them.

We need to find how tolerant we ought to be in finding an extremal value of $cos(\theta)$. In general one considers that two measurements are compatible when they agree within their error. Given the measurement $a_1 \pm \delta a_1$ and $a_2 \pm \delta a_2$ they are compatible if:

$$\frac{(a_1 - a_2)}{\sqrt{(\delta a_1^2 + \delta a_2^2)}} < 1 \tag{2.8}$$

This requires that a_1 and a_2 are measured with the same units. Our spectra are measured with arbitrary units that can change depending on instrumental amplification and fine differences in the experimental conditions. One has to rescale!

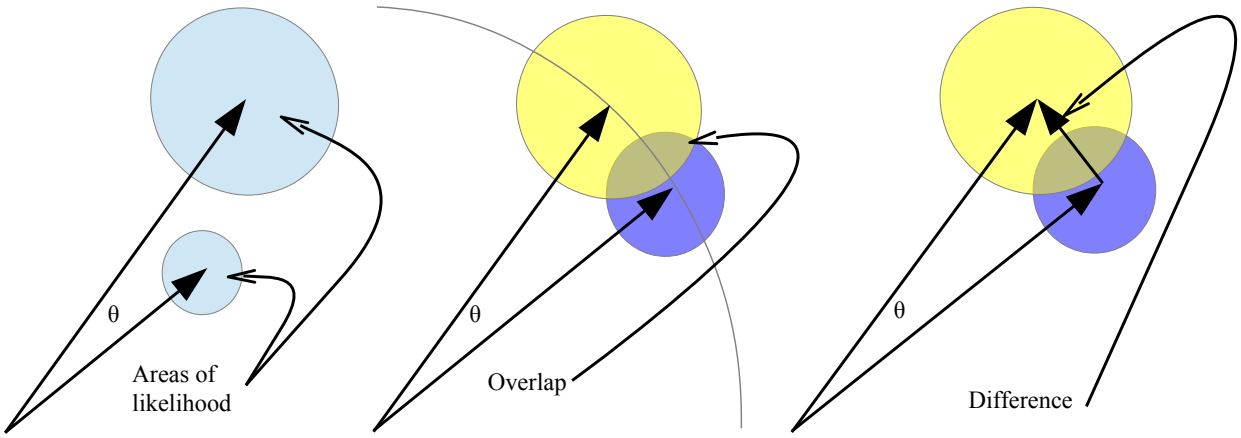

Fig. 2.13: Schematic representation of two spectra. (left) the convolution product yields directly θ, but the measurements may not be compatible if the areas of likelihood do not overlap. (center) Renormalizing the spectra allows the areas of likelihood to overlap, (right) allowing the evaluation of χ^2

Once normalized, the errors of $f(x)$ and $g(x)$ must be rescaled, which is

represented in Fig. 2.13 (center),

$$\begin{aligned} \boldsymbol{v} &= \left\{ \frac{f_i}{\parallel f \parallel} \right\}_{i=0\ldots n-1} ; \boldsymbol{u} = \left\{ \frac{g_j}{\parallel g \parallel} \right\}_{J=j_0\ldots j_0+n-1} \\ \boldsymbol{\delta v} &= \left\{ \frac{\delta f_i}{\parallel f \parallel} \right\}_{i=0\ldots n-1} ; \boldsymbol{\delta u} = \left\{ \frac{\delta g_j}{\parallel g \parallel} \right\}_{J=j_0\ldots j_0+n-1} \end{aligned} \tag{2.9}$$

To account for uncertainty of the spectrum we can use χ^2 that is the natural extension of eq. 2.8 to a series of measurements:

$$\chi^2 = \frac{1}{n} \sum \frac{(v_i - u_i)^2}{(\delta v_i^2 + \delta u_i^2)} \tag{2.10}$$

These two functionals, χ^2 and the convolution product, are not dependent on each other. While θ could be a right angle, corresponding to linearly independent vectors, with an appropriate uncertainty ($S/N \sim 2$) we could have $\chi^2 < 1$. Conversely, a large S/N ratio can lead to $\theta \sim 0$ while χ^2 can be large.

A reasonable way of taking into account both measures is to consider the product $(1 - cos(\theta))\chi^2$. The minimization of this combined functional has some issues only far away from a reasonable frequency shift, that in any case should be always smaller than the absolute accuracy. An excerpt of the result of this procedure is shown in Fig. 2.14 where a magnified area of two scans is shown before and after alignment, with the actual adjustment $\sim 0.27\, cm^{-1}$

The behavior of the functionals shows, as can be expected, extrema well pronounced in the relevant region of possible shifts, and secondary extrema not representing any particular significance beyond casual sporadic alignment of spectral features. This is evident in Fig. 2.15. Nevertheless, the assessment of the

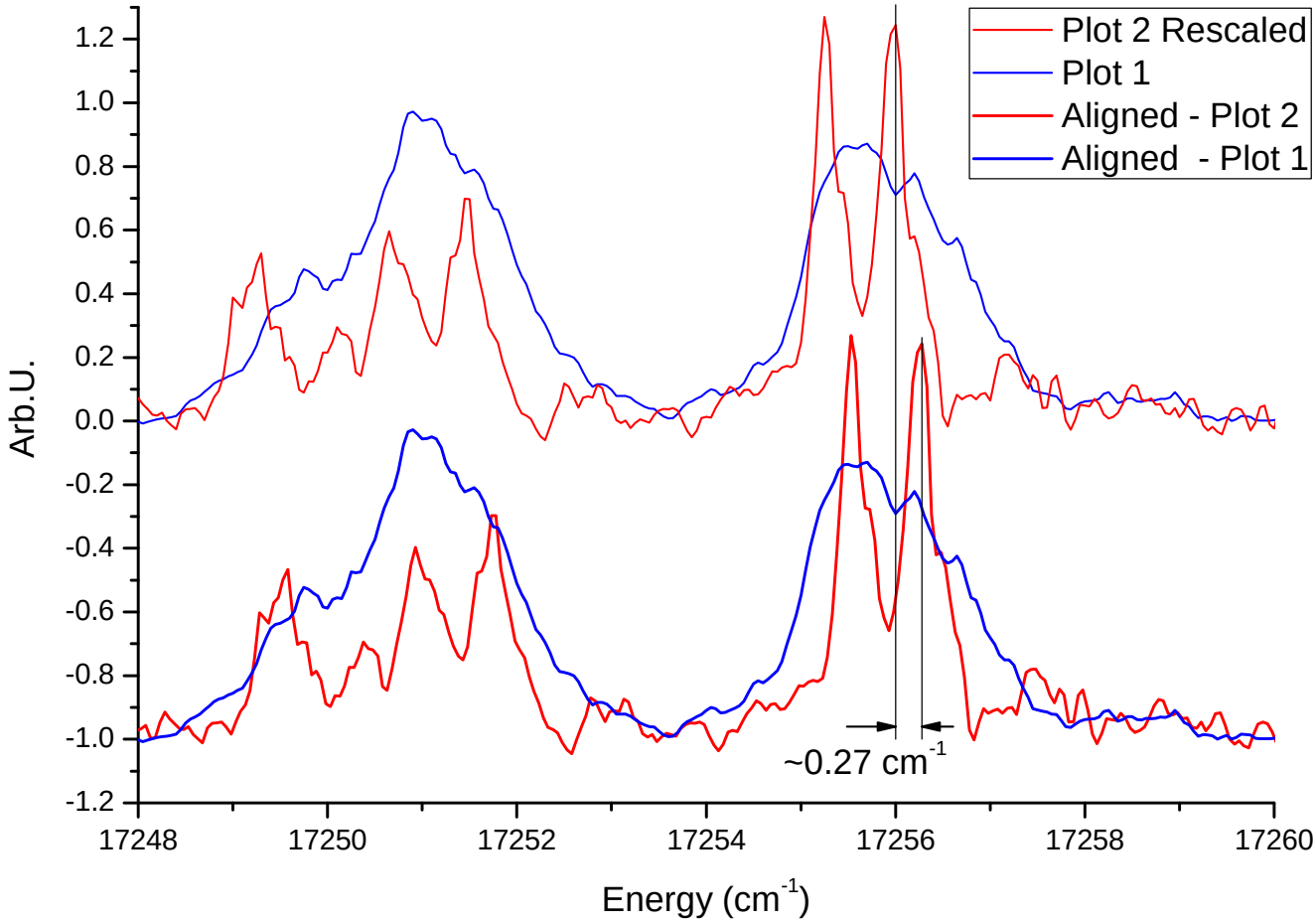

Fig. 2.14: Shown are two overlapping scans, 2013-06-04\scan 14 and 2013-06-14\scan3, taken 10 days apart, with visibly different linewidths for the two scans. On top are the unshifted data, while for the bottom the two scans are aligned by up-shifting Plot 2 by $\sim +0.27\,cm^{-1}$.

error in this process is of interest since it is repeated for all links in the alignment chain. While it is possible to propagate the error from the initial measurement through the whole process, it is more interesting to determine the relevant figures: the algorithm is based on spectra with a $S/N \sim 10 - 100$ and a variable width $\sim 1\, cm^{-1}$ on relevant features. This substantially sets the limit on how well these spectra can be aligned: the center of each feature can be determined with an uncertainty of $\sim \frac{FWHM}{(S/N)}$. So for each alignment in the chain we can expect an additional error $\delta_\nu \sim \frac{1}{30}\ cm^{-1} = 0.03\ cm^{-1}$. We can expect these errors to accumulate, in quadrature along the spectral chain, where every scan is linked to the next. The final solid spectrum will have a maximum error $\Delta \sim \sqrt{n}\delta_\nu$ where n is the number of scans employed in the whole spectrum.

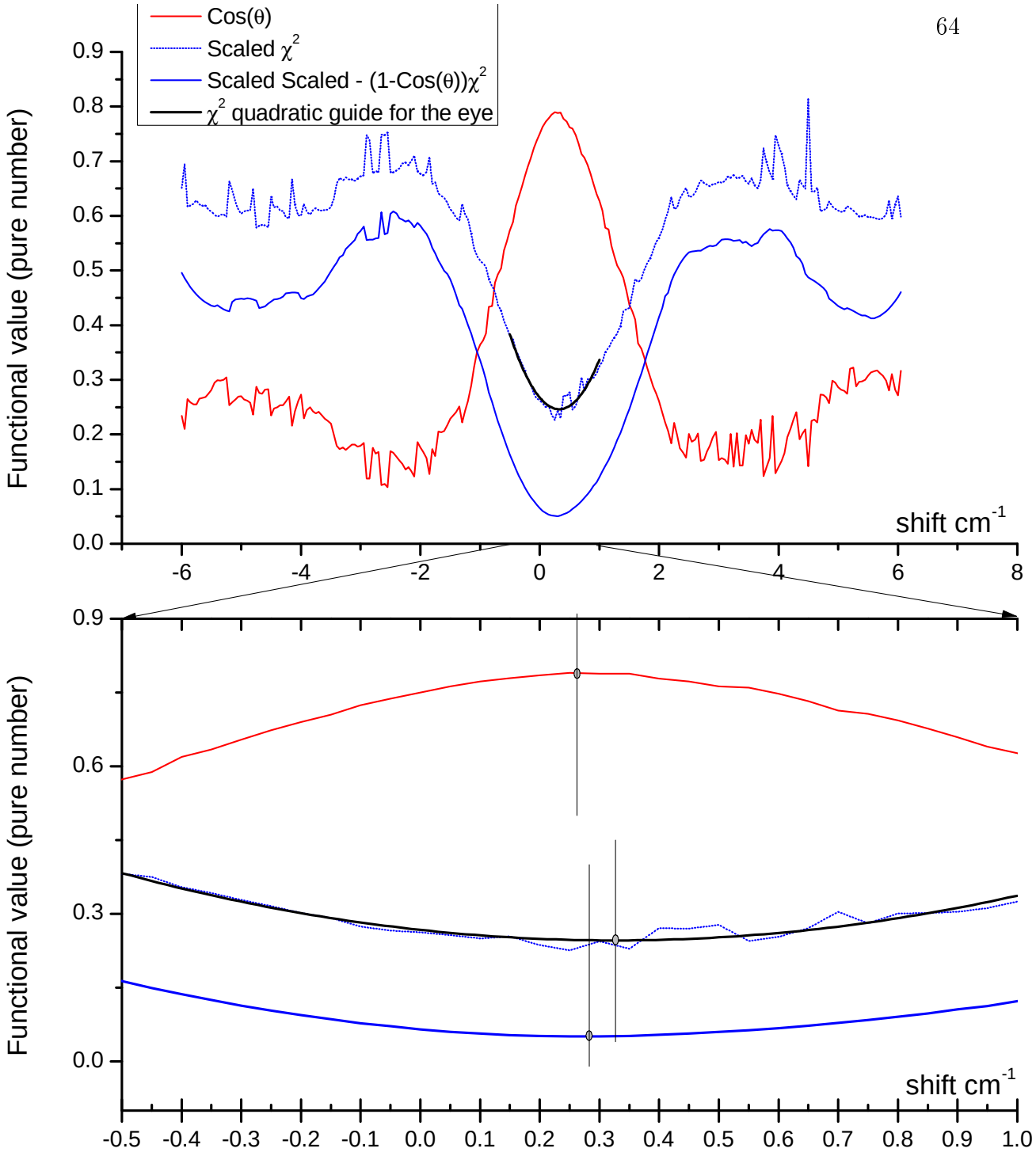

Fig. 2.15: The two functionals considered for alignment (χ^2 and $cos(\theta)$) are shown in the case of the scans of Fig. 2.14, 2013-06-04\scan 14 and 2013-06-14\scan3, along with their combination $(1-cos(\theta))\chi^2$; it has to be noted that χ^2 and $cos(\theta)$ do not completely agree with each other and that their combination offers a compromise. In this example a shift of $\sim 0.27\, cm^{-1}$ is optimal.

Chapter 3

Introduction to spectrum assignment

3.1 What is an assignment anyway?

Spectral structure can be quite complicated and its complexity depends strongly on the system examined. In this section we introduce the nature of the assignment problem, and some strategies to tackle it.

A spectral assignment is a correspondence between a set of quantum numbers and the recorded spectrum whose features bear the properties of system examined: the transitions involve an upper and a lower state and the spectral feature energies are given by $T_{v',v"} = E_{v'} - E_{v"}$, where $E_{v'}$, $E_{v"}$ indicate the energy level of the upper and lower states respectively. v' and $v"$ in general could be sets of quantum numbers for the upper and lower states. In this study we are concerned only with vibrational transitions, since the laser linewidth does not allow rotational resolution. Vibrational transitions do not have strict selection rules, but line strengths are determined by Frank-Condon factors.

In principle there are more than two electronic states that contribute to

the spectrum, making it necessary to use additional information beyond the spectroscopic data to assign all quantum numbers. Transitions from multiple v" to a single v' are possible, actually useful, and have been the main mechanism for primary pattern recognition in this thesis.

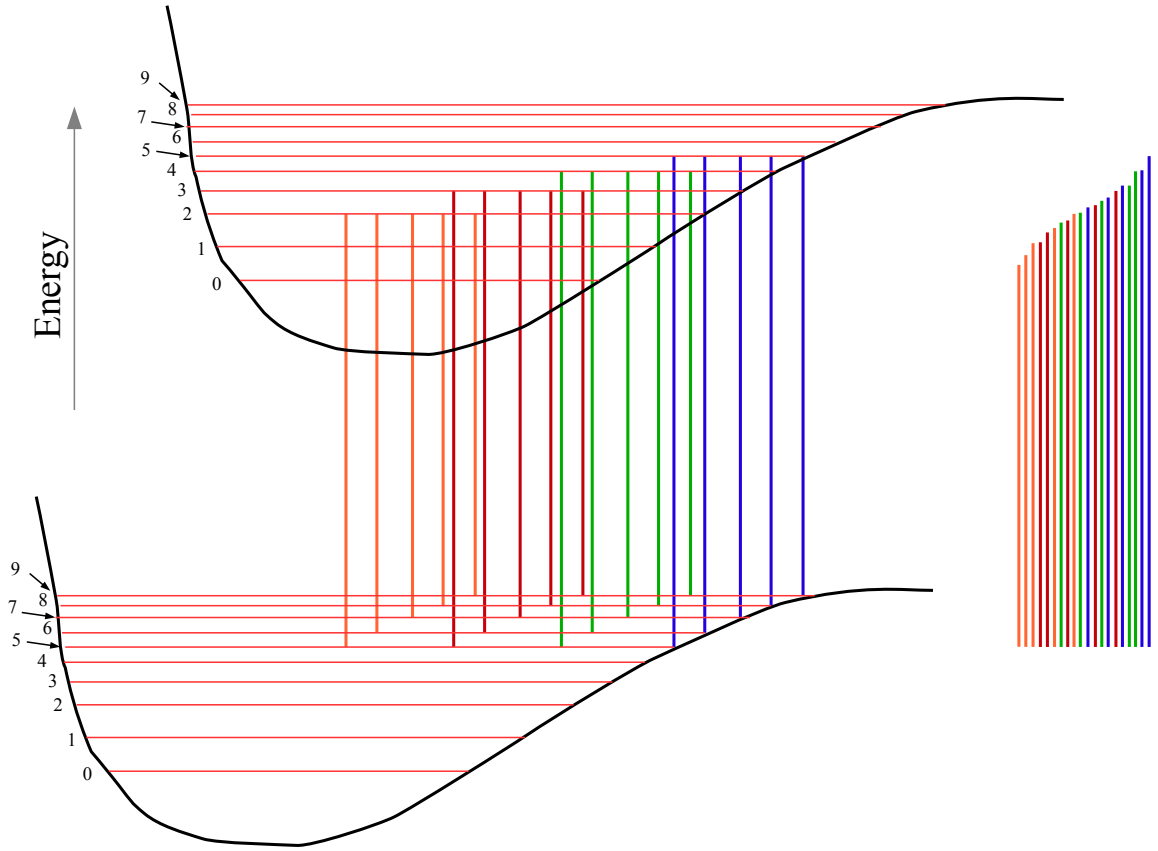

Fig. 3.1: With a given level structure, transitions from multiple ground-state levels to multiple excited levels are well recognizable with a proper labeling (left). Once sorted by transition frequency (energy), it is apparent how the relative splittings of the ground-state and excited-state levels come into play: the orange lines are almost completely grouped together, while the blue lines are interleaved with other transitions (right).

In Fig. 3.1 it is shown how a ground-state pattern that spans a range smaller that the excited-state spacing yields a spectrum that is sorted by excited state

quantum number. Of course this is increasingly difficult to achieve with multiple excited electronic states, which effectively reduces the level spacing.

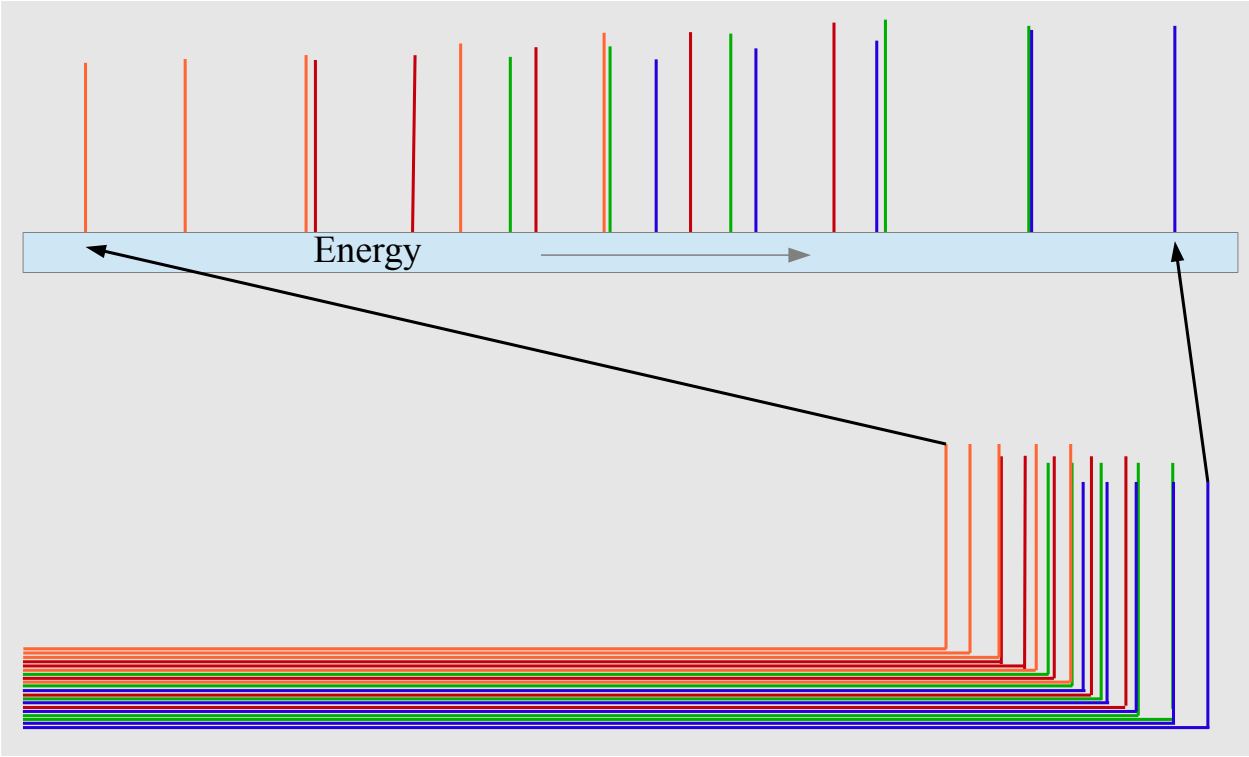

Fig. 3.2: Spectrum with color labeling (top). These are the same transitions of Fig. 3.1(bottom) vs frequency. Only the color coding helps in picking out the presence of a repeating pattern.

Fig. 3.2 shows a set of labeled spectral lines, where overlap, or near overlap, further complicates interpretation. Only an accurate frequency axis allows recognition of ground-state patterns (Fig. 3.3).

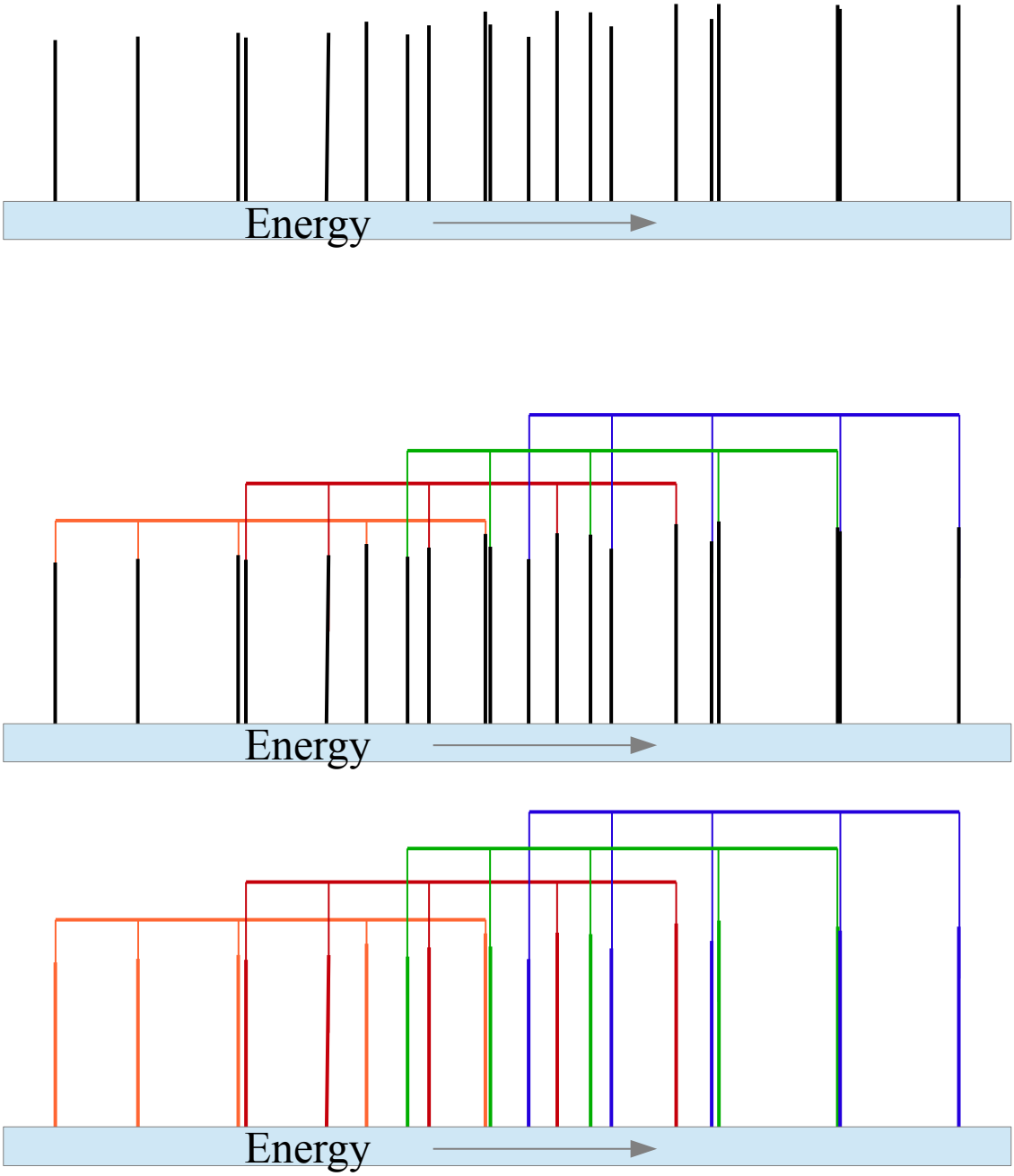

Fig. 3.3: Top: Spectrum of Fig. 3.2 without color labeling, showing an apparent lack of regularity. Center: Using the ground-state pattern (the differences of ground-state levels) it is possible to regain a first layer of labeling, assigning the ground-state quantum numbers v" (bottom).

Once excited levels are determined we need to assign quantum numbers. If

additional electronic states are involved, those numbers have to be assigned too: theoretical *ab initio* PECs guide us in determining the overall behavior of the excited series. This entails making the hypothesis that a small subset of excited levels has already determined labels, and subsequently testing by finding matches to a large fraction of the $\{E_v\}$ series. Line shapes can aid hypothesis making. We illustrated an assignment method that goes from local to global:

- Initially some local relationship within the spectrum has to be approximately known. In our case this is the ground-state level energies, and the spread of the initial state preparation: only a few of the highest levels were populated which makes it a somewhat easier case. This allows us to determine upper-state levels.

- Once the excited levels are known, a global behavior for each electronic state is expected, giving the possibility of hypothesis testing for a subset of determined levels. In our case, *ab initio* potentials guide us.

In a certain sense it resembles a large sudoku game: by some means there is a limited number of fixed points that have to be determined, the initially assigned cells. Once they are determined, only the relationships between the cells, both the local ones within a sub-square and the remote ones within a row and column, solve the whole puzzle.

There are other ways of approaching the problem, not utilized in this thesis. Instead of knowing some local relationship well, one can exploit a global property

of, for instance, an electronic state, to discern it from others. For example: Ω doublets and their susceptibility to electric fields with a DC Stark modulation. Resolution of rotational structure can also help. A more elaborate technique, Extended Cross Correlation (XCC), has been used in R. Field's group at MIT with this basic idea [69]: "spectra are used to decode each other without any knowledge of or assumptions about the patterns that are sought".

3.2 Data: Common features

3.2.1 Data collection

Data have been taken in separate scans at different times, some consecutively, and some within weeks.

This has an impact on the calibration of the wavemeter data used: relative readings (within a short time) should be consistent within 0.1 cm^{-1} (as mentioned previously, Etalon A was used); on a longer timescale, the absolute accuracy whenever specifically checked has varied by ~ 0.5 cm^{-1}, which is consistent with a specification of 1.0 cm^{-1}.

Using the recorded spectrum itself, separate scans have been aligned by maximizing a functional composed by the convolution product of overlapping features and their χ^2. Only three of the scans used did not overlap since they were taken consecutively within minutes of the end of the previous scan. This should still guarantee the short-term consistency of the energy scale. In addition, one of

these three scans has, within the background channel, features corresponding to atomic transitions ($5p_{3/2}$ to $7d_{3/2}$ and $7d_{5/2}$) which allows the absolute calibration of the whole spectrum to be improved.

As for the ordinate axis, the spectrum amplitude, care as been taken to adjust the scale of each individual scan so to have a consistent peak amplitude scale throughout the spectrum. This is done by making overlapping features of different scans to have the same amplitude.

3.2.2 Data format

Data have been collected with a variety of channels that has changed over time. This is due to addressing experimental issues found to be restricting factors on the acquisition speed or quality of the data. Below is the complete list of channels ever recorded, but not all data have all channels. In a post-recording phase, all useful data have been written to a compact file format easily accessible with our own Labview program.

1- Index

2- 1^{st} step laser frequency cm^{-1}

3- Rb^{+} boxcar-averaged channel, 30 shots @ 10 Hz.

4- Rb_2^{+} boxcar-averaged channel, 30 shots @ 10 Hz.

5- Rb_2^+ boxcar-averaged channel, 30 shots @ 10 Hz - this is a TOF window just preceding the arrival of the Rb_2^+ cloud, for background subtraction.

6- 1^{st} step laser average power - using Gentec pyroelectric detector, amplified with a homebuilt amplifier and measured with an oscilloscope.

7- 2^{nd} step laser average power - using thermoelectric detector.

8- Time, ms from last data line

9- MOT fluorescence

10- 2^{nd} step laser frequency cm^{-1}

During post-processing, this information has been reduced into a Labview binary file with extension XDF for each preparation state. It is organized as an array of clusters that contains all original data (all the scans of possible relevance), in addition to a few "headers" such as original file, recording date, comments if applicable, calibration information and the resulting smoothed spectrum. Each element of the array, a cluster, has all the information relative to one scan. A subset of this array as been selected and merged into a single spectrum. This spectrum is conveniently stored in a Labview VI for easy consultation, and is also saved as a text file.

3.2.3 Error

Polynomial smoothing has been applied to reduce the granularity of the energy axis (the resolution is only 0.1 cm^{-1}), but observation of the raw spectra shows clearly that this is only a limitation of the wavemeter and not the stability of the scanning pulsed dye laser. Dealing with this granularity is also discussed in section 2.2.7.

For each data point a surrounding interval is chosen. On this reduced stretch of data a bi-square polynomial fit (which is briefly introduced in appendix A.2.2) is applied and the resulting value at the point considered is taken as the smoothed data point. This allows us to evaluate the error by either considering the standard deviation of the difference between the bi-square fit and the raw data, or by evaluating the FWHM of the distribution of the difference between smoothed data points and raw data.

The same procedure has been applied to the amplitude, leading to a statistical evaluation of the Y axis error. This yields typical values of $\frac{\delta_Y}{Y} \sim 0.05$ in amplitude, or $S/N \sim 20$, and an uncertainty of $\sim 0.03\ cm^{-1}$ on the energy scale. Considering this reduced error on the X axis we find a limitation: common fitting methods are usually developed under the assumption that the only uncertainty that actually counts is along the Y axis, thus they minimize some version of χ^2. This condition is mathematically stated:

$$\Delta x_i \frac{df}{dx} \mid_{x_i} << \Delta y_i \tag{3.1}$$

Normalizing if a transition line swings an amplitude of 1 in a stretch $\sim 0.5\ cm^{-1}$, this leads to χ^2-based applicability condition which is not met.

$$0.03\ cm^{-1}\frac{1}{0.5\ cm^{-1}} << 0.05 \tag{3.2}$$

This means that regular fitting methods are in certain cases bound to fail. A short discussion of this condition can be found in appendix A.

Instead of developing an ad hoc fitting procedure I opted for a human assisted process.

3.3 Ground-State pattern

It is to be noted that this step is only possible due to accurate and tested knowledge of the ground-state energy levels; key in this have been Tiemann's PEC [45] and the supporting work. A preliminary pattern recognition has been done by printing a 10 ft roll (taped letter size prints) of the spectrum. With the aid of a ground-state "stick spectrum" transparency (assembled using Tiemann's PEC [45] and equipped with appropriate holes and openings for notations), it was possible to determine a vast part of the spectrum (acronym SX) resulting from excitation from the $X^1\Sigma_g^+$ state. The same procedure was tried for the spectrum recorded starting from the $a^3\Sigma_u^+$ state (acronym SA). However, no more than plausible hypotheses were made due to congestion and linewidth limitations.

To precisely determine excited-state levels, fitting was applied with a human assisted process (see previous section 3.2.3): using the ground-state level spacing,

manually match each feature with a Gaussian pattern, fit, and accept or reject the fit based on graphical evaluation.

For SX the procedure was relatively efficient determining about 100 excited level energies. For SA frequent merging features have slowed down the process by requiring careful lineshape evaluation, finding more than 250 excited levels.

3.4 Excited-State pattern

In this step we have used *ab initio* PECs, Koch's PECs [49], which have no guarantee of accuracy *a priori*. Nevertheless, for certain cases, namely for the $2^1\Sigma_u^+$ state, they have proven to be accurate beyond expectations. Theoretical prediction of an electronic state structure guides us in selecting those excited states that meaningfully correlate to each other over a large spectral distance. "Meaningfully" here is the key word. If we find a set of excited levels that fits the physical model, we have something to work on for additional confirmation.

For spectrum SX the search has been very limited since with a tolerance very close to the experimental error almost all spectral lines were assigned to $2^1\Sigma_u^+$. The remaining lines are too few for a confident assignment to another electronic state.

In spectrum SA we searched for each electronic state's theoretical levels prediction using a correlation with a variable tolerance and an overall shift in the following manner.

Let $\{Z_i\}$ be the experimentally determined excited level set, and $\{E_v\}$ the theoretical prediction. By assuming that the zero-order error on the prediction is a rigid shift of all levels together we consider the set of energy intervals $I_v = [E_v + X - \delta_v, E_v + X + \delta_v]$ with X an unknown energy shift and δ_v an arbitrarily chosen tolerance. Calling δZ the energy uncertainty (due to measurement), δ_v is bound by the relations

$$\delta Z \leq \delta_v < \frac{Min(E_v - E_{v-1} : E_{v+1} - E_v)}{2} \tag{3.3}$$

If δ_v were larger than the upper bound, then the union of intervals would cover the whole energy region. By counting the number N of intervals that contain at least an excited level Z_i we obtain an integer function $N(X, \delta_v)$ that, depending on the choice of δ_v, oscillates as a function of X and reaches an absolute maximum for a value X_0. This is the best guess for finer testing. Each counted interval could contain more than one excited level Z_i in which case a choice has to be made with a guiding principle: renaming E'_v the selected Z_i in the interval I_v, the graph of $\Delta G_{v'+\frac{1}{2}}(v) = E'_{v+1} - E'_v$ (and its extensions for missing v's) has to be smooth but certainly as continuous as possible with experimental data. This first set of E'_v can also be used to find additional excited levels, which are a confirmation, among minor spectral features (lower S/N ratio) that may have been ignored in the first round of ground-state pattern recognition.

What can be expected from this kind of method can be explored heuristically:

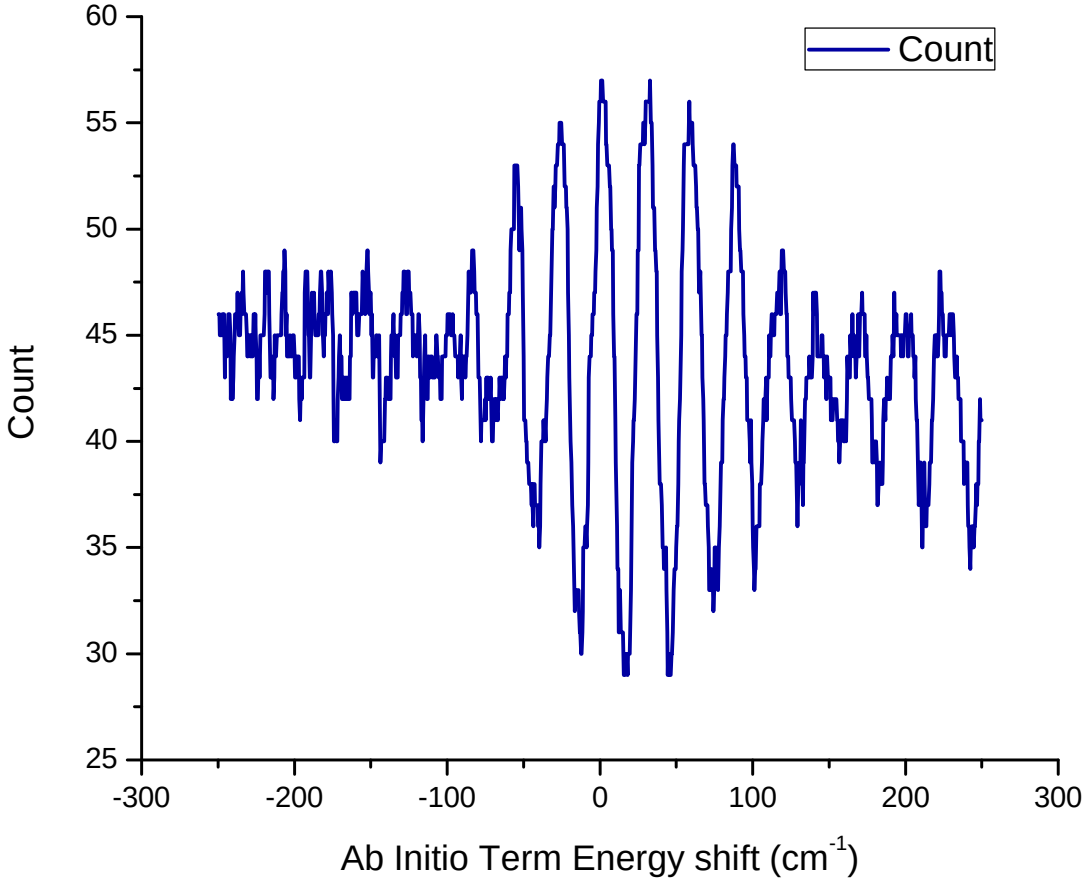

Fig. 3.4: The candidate-counting procedure described in detail in the text produces an interference-like pattern as a function of term energy shift: shown is the search results for $2^3\Pi_g$ with $\delta_v \sim 3$. Considering that $\Delta G_{v'+\frac{1}{2}} \sim 30\,cm^{-1}$, the total spectrum range is $\sim 2000\,cm^{-1}$ and the total number of unassigned excited levels is ~ 250 a background average of ~ 50 with a random fluctuation of ~ 7 is reasonable (left-hand side). In addition a revival can be observed on the right-hand side of the frequency scale; this is due to the presence of 3 series of excited levels belonging to the same potential, but shifted with respect to one another of $\sim 8\,cm^{-1}$ and $\sim 150\,cm^{-1}$. The merging of the interference patterns gives the beat-note-like behavior.

- For values of X away from any correlation we should find an average N count due to accidental alignment and fluctuations around the average should be of the order of $\sqrt{N}$ (the square root of the count).

- When a correlation appears then the fluctuations will not be evenly distributed as a function of frequency shift, in fact they will be periodic with a period close to $\Delta G_{v'+\frac{1}{2}}$

On a large enough spectral range accidental counting can be expected to average

$$N \sim \frac{n}{L} \sum_{v} 2\delta_v \tag{3.4}$$

with n being the total number excited levels within the spectrum and L the spectrum length. This is a background.

When fully correlated to a subset of k levels, the background drops to

$$N \sim \frac{n-k}{L} \sum_{v} 2\delta_v \tag{3.5}$$

a periodic modulation of amplitude k and fringe distance of $\sim \Delta G_{v'+\frac{1}{2}}$. The transition from the two cases is determined largely by the $\Delta G_{v'+\frac{1}{2}}$ behavior as a function of v' in the width of the interference-like pattern, and by δ_v in the fringe contrast. A example of this behavior is shown in Fig. 3.4.

As a side note: if the value of the background in eq. 3.4 approaches the number of intervals at our disposal (i.e. the number of vibrational levels within the spectral range of the state searched) this method may not yield significant results. In fact this limit is an upper bound and a coincidental integer ratio between (or

nearly integer) $\Delta G_{v'+\frac{1}{2}}$ of different electronic states could, in principle, generate false hypotheses or completely destroy any interference-like pattern.

Chapter 4

Analysis of $X^1\Sigma_g^+ \rightarrow 2^1\Sigma_u^+$ spectrum

This chapter contains a summary of the assignment results for the excitation spectrum from the $X^1\Sigma_g^+$ state to the $2^1\Sigma_u^+$ state.

In Sections 4.1 and 4.2 are outlined differences in the assignment procedure for this spectrum compared to that outlined in the previous chapter. The latter section contains also a comparison with the final v' assignment with respect to *ab initio* PECs for the $2^1\Sigma_u^+$ state.

Overall the assignment appears solid, and an amplitude deviation from expected values, which can be observed in detail in Appendix G, is discussed in chapter 6.

In Section 4.4 the frequency calibration has been compared to previous measurements performed in the lower end of the spectral region.

4.1 Ground-state pattern matching

Four attempts at ground-state pattern matching have been performed:

* Human-assisted matching by comparing a Gaussian pattern from levels generated by Tiemann's PEC [45]. This determined a set of almost 100 excited levels.

* A few additional candidates have been added by directly comparing theoretical predictions for the $2^1\Sigma_u^+$ state to the excited levels of the previously determined set by interpolating the experimental $\Delta G_{v'+\frac{1}{2}}$ vs v'.

* Fitting with a "rigid ground-state pattern" (i.e. Gaussian pattern for levels from v'=110 to 118 with the only free parameters being amplitude and standard deviation). Transitions too weak (small amplitude compared to noise) or too wide (too large standard deviation) have been rejected.

* A final round of manual adjustment has been necessary since the fitting procedure occasionally diverged from reasonable solutions: some peaks have become too wide or too small due to various spectral peculiarities such as the presence of a transition to another state.

4.2 Excited-state identification

The identification of a ground-state pattern can lead to the isolation of an excited state which does not necessarily belong to the $2^1\Sigma_u^+$ state. Previously Y. Huang *et al.* [43] have assigned this spectrum up to $\sim 17100\,cm^{-1}$. Preliminary v' quantum numbers were readily assigned to this entire series by exploiting $\Delta G_{v'+\frac{1}{2}}$ continuity.

Using the Potential Energy Curve (PEC) of the $2^1\Sigma_u^+$ state calculated by Tomza *et al.* [49], excited-state energies have been calculated with the aid of LEVEL 8.0 [44]. Systematically assigning a shift to the preliminary vibrational quantum number v' and expecting a flat distribution of the differences between theoretical and experimental energies leads to the determination of an effective correspondence between theoretical and experimental excited-state energies. Figure 4.1 shows the result of such differences.

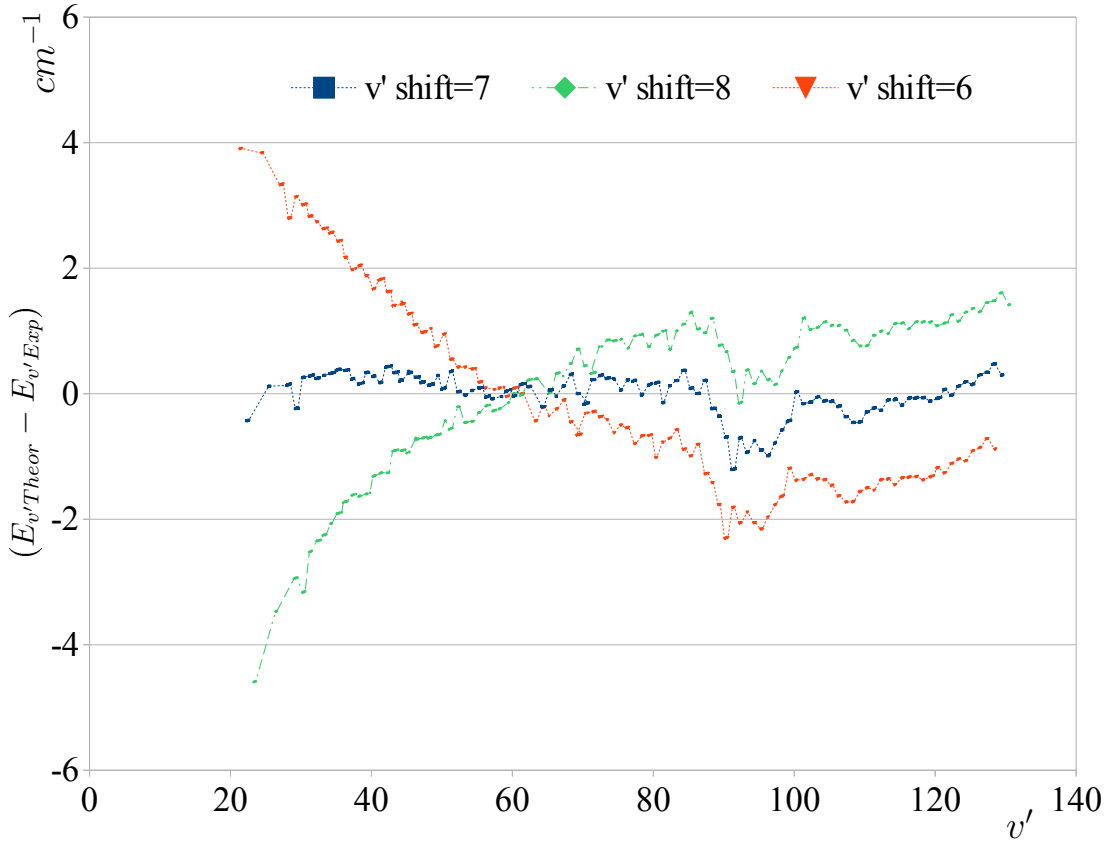

Fig. 4.1: Difference $E_{v'\,Theor} - E_{v'\,Exp}$ between the expected *ab initio* theoretical levels and the experimentally assigned levels of the $2^1\Sigma_u^+$ state as a function of the v' shift. A zero slope is the optimal v'$_{shift} = 7$ to which corresponds an offset of 102 cm^{-1}.

4.3 Use of LEVEL 8.0

The calculation of level energies, transition energies, and Franck-Condon Factors (FCFs) has been performed, using the potential of Tiemann *et al.* [45] for the $X^1\Sigma_g^+$ ground state and the potentials of Tomza *et al.* [49] for the excited-state PECs, employing the LEVEL 8.0 software developed by LeRoy [44]. In particular, in Fig. 4.1 a divergence of theoretical and experimental spectra around v'$\sim$ 90 is noticeable, which is not consistent with experimental error. A local deviation from the theoretical PEC could explain such a discrepancy. The spectrum plotted in Appendix G shows a simulated spectrum using a fixed linewidth and scaled FCF amplitudes in addition to the optimal matching assignment. It shows a very good correlation between line amplitudes of the simulation and the data collected, except in localized areas.

4.4 Comparison with Y. Huang's work

Y. Huang's work [43] (p.162-3) was calibrated using several atomic transitions, all located below 16456.95 cm^{-1}. The present spectrum has an absolute accuracy of ~ 0.5 cm^{-1}. In addition, it has been calibrated with atomic transitions ($5p_{3/2}$ to $7d_{3/2}$ and $7d_{5/2}$) at 17465cm^{-1}, off scale on the right-hand side of the range. Without any other adjustment, the discrepancy with Huang's assigned excited energy levels, Fig. 4.2, is well within expected values.

The two assignments are in very good agreement, as shown in Fig. 4.3.

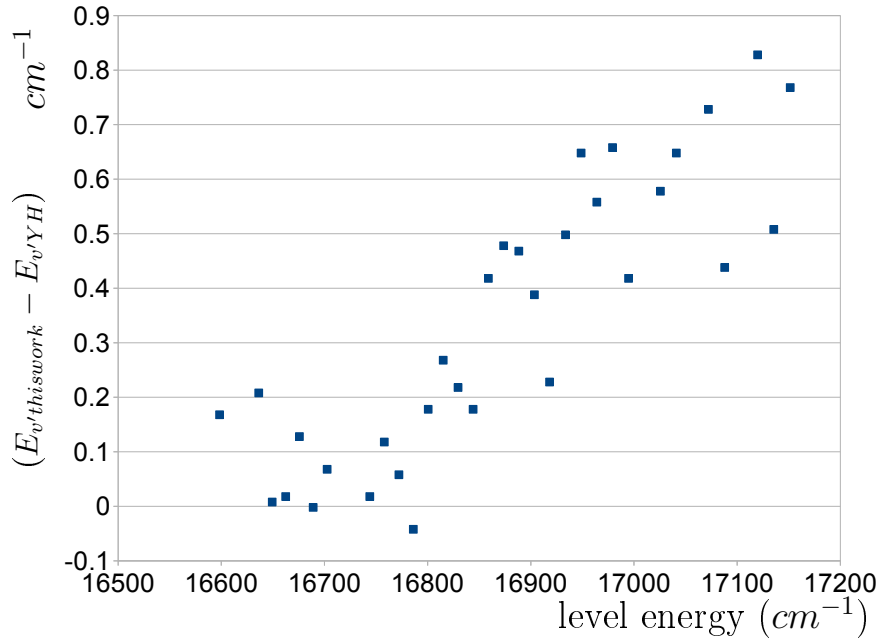

Fig. 4.2: Deviation from data of Y. Huang (YH) versus frequency [43]. A larger tolerance is to be expected in Huang's spectrum on the right-hand side of the range: in Huang's work the calibration of the frequency axis has been done by extrapolation on the right-hand side since all atomic transitions for calibration were offscale on the left side, below 16456.95 cm^{-1}.

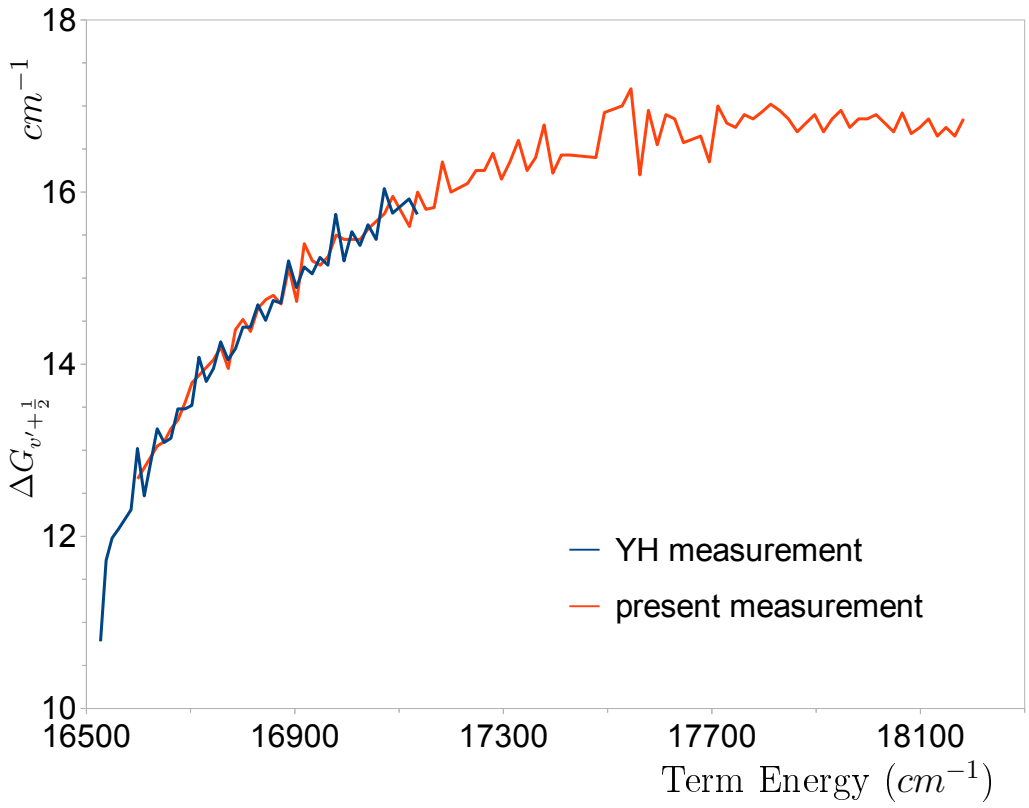

Fig. 4.3: $\Delta G_{v'+\frac{1}{2}}$ vs frequency for $2^1\Sigma_u^+$: this work in red, Huang's work in blue.

Chapter 5

Analysis of $a(1)^3\Sigma_u^+ \rightarrow 3^1\Sigma_g^+$, $2^3\Pi_g$ spectra

This chapter contains a summary of the assignment results for the excitation spectrum from the $a^3\Sigma_u^+$ state.

In Sections 5.1 and 5.2 differences are outlined in the assignment procedure for this spectrum compared to that described in the previous chapter. The latter section contains also a comparison of the final v' assignment with respect to *ab initio* PECs for the $3^1\Sigma_g^+$ state and the three series of the $2^3\Pi_g$ state.

In Section 5.3 the frequency calibration is compared to previous measurements performed in the lower end of the spectral region. The agreement is as good as for the spectrum excited from the $X^1\Sigma_g^+$ state.

Section 5.4 briefly discusses the anomalies arising in this assignment. Overall the assignment appears good, and frequency deviations (which can be observed in detail in Appendix H) from expected values is discussed in chapter 6.

5.1 Ground-state pattern matching

The spectrum resulting from excitation from the $a^3\Sigma_u^+$ state, denoted as the SA spectrum, shows many more excited levels. In addition, the initial states are less tightly bound and thus more closely spaced than the levels of the $X^1\Sigma_g^+$ state. This means the repeating ground-state features merge due to linewidth limitations. Accidental overlapping transitions further increase the complexity of the procedure. This means that lineshape interpretation is much more involved, and necessary for a meaningful assignment. As in the previous chapter, common fitting procedures sometimes fail to yield meaningful results as discussed in Sec. 3.2.3 and in appendix A. Overall, several rounds of interpretation and adjustment were required in order to converge:

- Human assisted matching by comparing a Gaussian pattern from levels generated by Tiemann's potential [45]. This determined more than 250 excited levels, which turned out to belong mainly to $3^1\Sigma_g^+$ and $2^3\Pi_g$. It is important to remark here that this first set was not readily interpretable: using the experimental frequency error ($\sim 0.5\, cm^{-1}$) as a tolerance, *ab initio* predictions did not determine quantum number assignments for a reasonable overall PEC shift.

- Correlation search, described in Sec. 3.4, with a tolerance higher than the experimental error, generated hypotheses for the $3^1\Sigma_g^+$ and the $2^3\Pi_g$ states.

- Using these excited-state hypotheses, a few other candidates were added by

interpolating and extrapolating the experimental $\Delta G_{v'+\frac{1}{2}}$ vs v'. For the $3^1\Sigma_g^+$ state in particular, this added a final set of excited levels that departed from the theoretical predictions substantially, with a level spacing reduced by $\sim 1\,cm^{-1}$ with respect to theory. Figs. 5.8 and 5.5 show this behavior for $v' \geq 120$. For completeness Fig. 5.9 shows the same information vs. excited level energy.

- Fitting with a "rigid ground-state pattern" (i.e. Gaussian pattern for levels from 30 to 39 of the ground-state with the only free parameters being amplitude and width). Transitions too weak (small amplitude compared to noise) or too wide (too large standard deviation) have been rejected.

5.2 Excited-state identification

Previously, Y. Huang *et al.* [43] have partially assigned a spectrum up to $\sim 16640\,cm^{-1}$. Using the Potential Energy Curves (PECs) of the $3^1\Sigma_g^+$ and $2^3\Pi_g$ from Tomza *et al.* [49], we have calculated excited-state energies with the aid of LEVEL 8.0 [44].

Systematically assigning a shift to the preliminary vibrational quantum number v' and selecting a flat distribution of the differences between theoretical and experimental energies leads to the determination of the correspondence between theoretical and experimental excited-state energies. Figures 5.1, 5.2, and 5.3 show the results of such differences. It is relevant to notice that the v' shifts that appear to be most appropriate for the series A, B, C are not all the same

value as for Y. Huang's work.

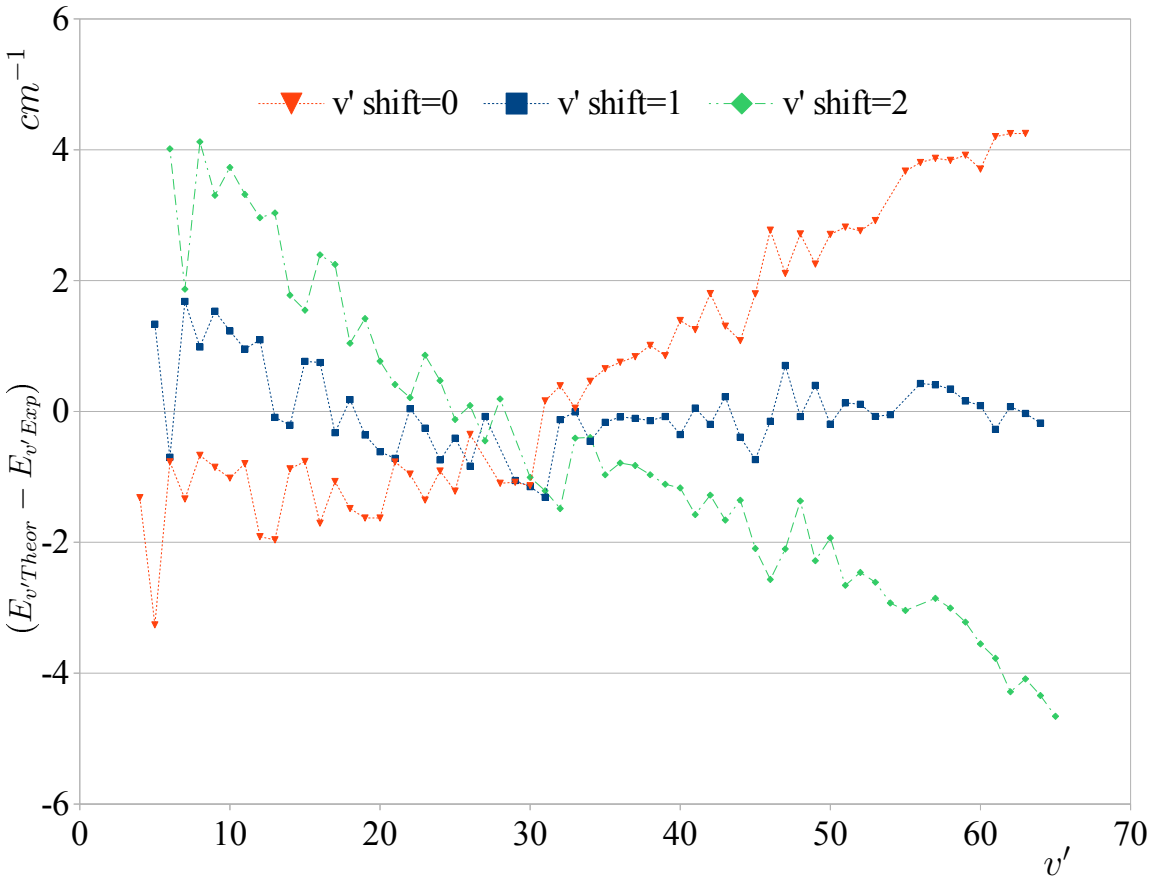

Fig. 5.1: Differences between theoretical and experimental energies for the $2^3\Pi_g$ state of the series A, as labelled by Huang, as a function of v' shift. The plots represent the three closest choices of v' shift to have a constant energy difference between *ab initio* theory and experiment. A zero slope is the optimal v'$_{shift} = 1$ which corresponds to an offset of -1.20 cm^{-1} and a standard deviation of 0.69 cm^{-1}.

For series B and C there is good agreement with *ab initio* PEC evaluations at the optimal v_{shift} with standard deviations of 0.35 cm^{-1} and 0.31 cm^{-1}, respectively. For series A the standard deviation is instead 0.69 cm^{-1}. Observing

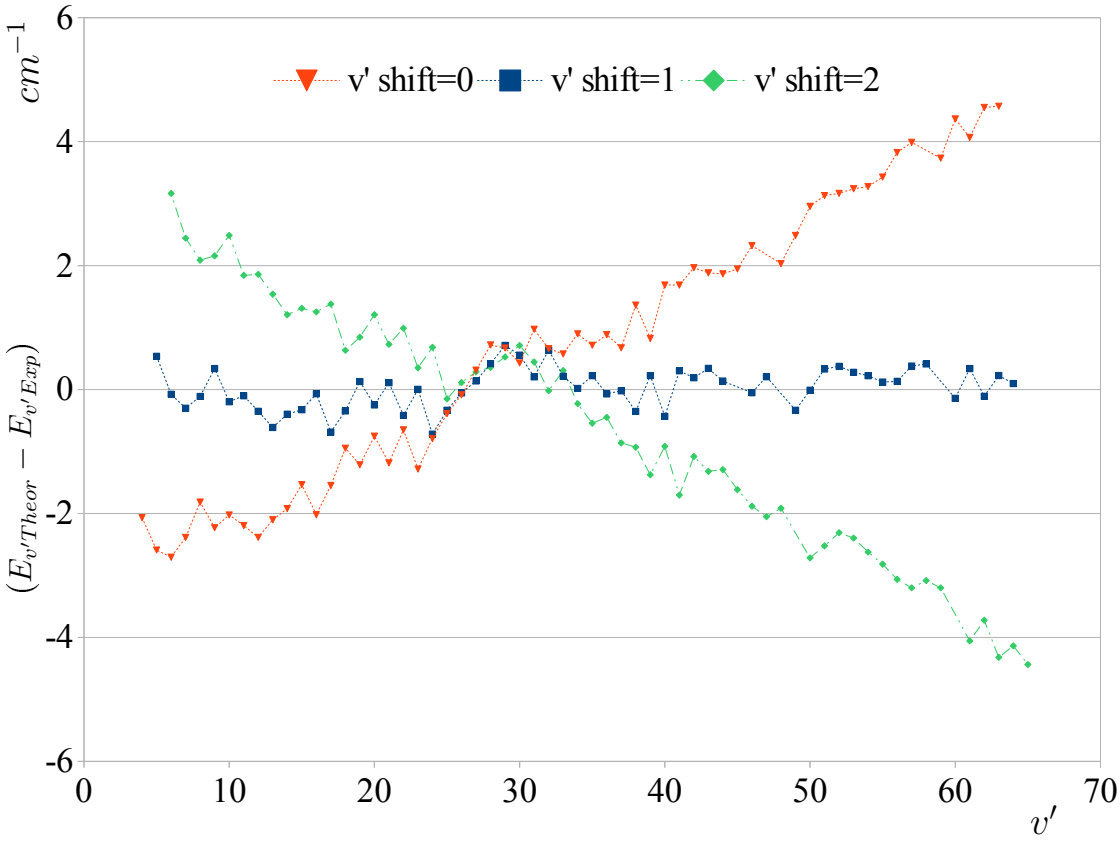

Fig. 5.2: Differences between theoretical and experimental energies for the $2^3\Pi_g$ state of the series B, as labelled by Huang, as a function of v' shift. The plots represent the three closest choices of v' shift to have a constant energy difference between *ab initio* theory and experiment. A zero slope is the optimal v'$_{shift} = 1$ which corresponds to an offset of -8.95 cm^{-1} and a standard deviation of 0.35 cm^{-1}.

$(E_{v'Theor} - E_{v'Exp})$ for series A, it is relevant to notice that agreement with *ab initio* PEC evaluations is quite acceptable for $v' > 30$, but there seem to be substantial perturbations below this threshold (which is near a term energy of 17200 cm^{-1}).

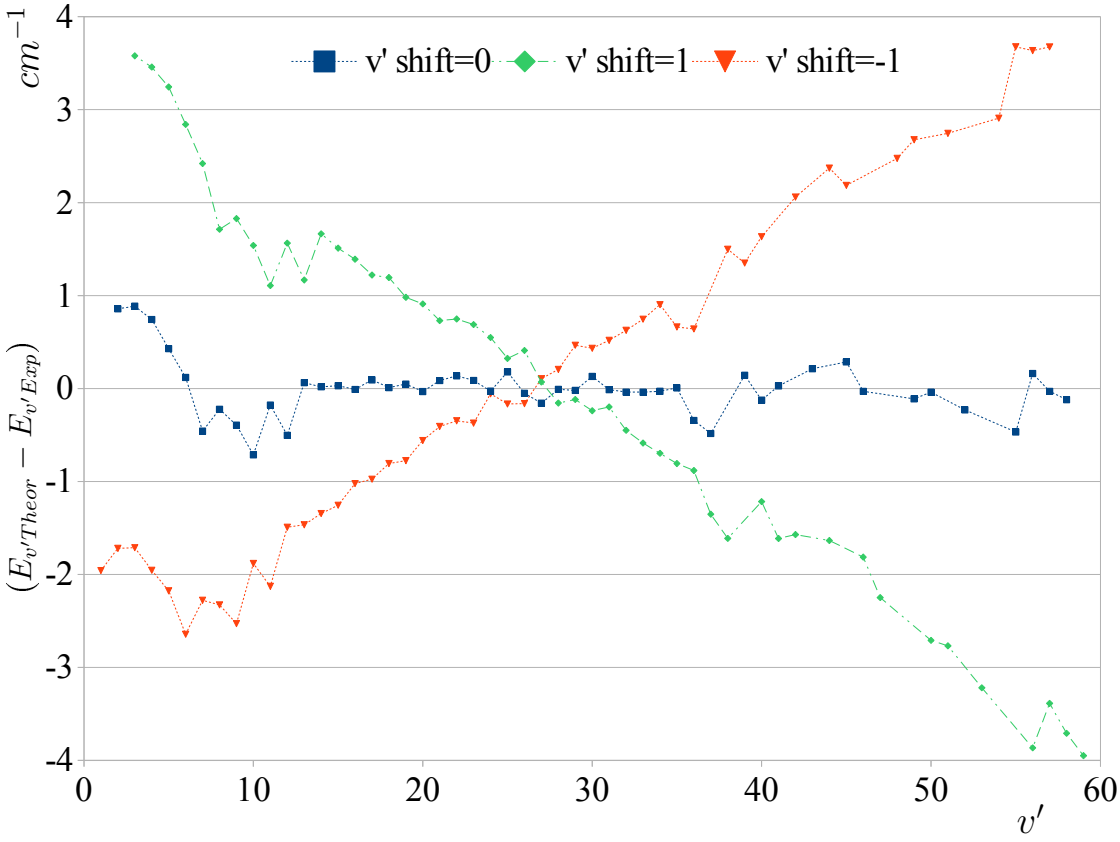

Fig. 5.3: Differences between theoretical and experimental energies for the $2^3\Pi_g$ state of the series C, as labeled by Huang, as a function of v' shift. The plots represent the three closest choices of v' shift to have a constant energy difference between *ab initio* theory and experiment. A zero slope is the optimal v'$_{shift} = 0$ which corresponds to an offset of -157.90 cm^{-1} and a standard deviation of 0.31 cm^{-1}.

Fig. 5.4 shows the $(E_{v'Theor} - E_{v'Exp})$ deviations at the optimal v_{shift} for all three series as functions of both of v' and frequency. Fig. 5.5 presents $(E_{v'Exp} - E_{v'Theor})$ for the $3^1\Sigma_g^+$ levels which shows large perturbations from *ab initio* predictions in the reduced sample of $v' < 120$ and a clear systematic deviation

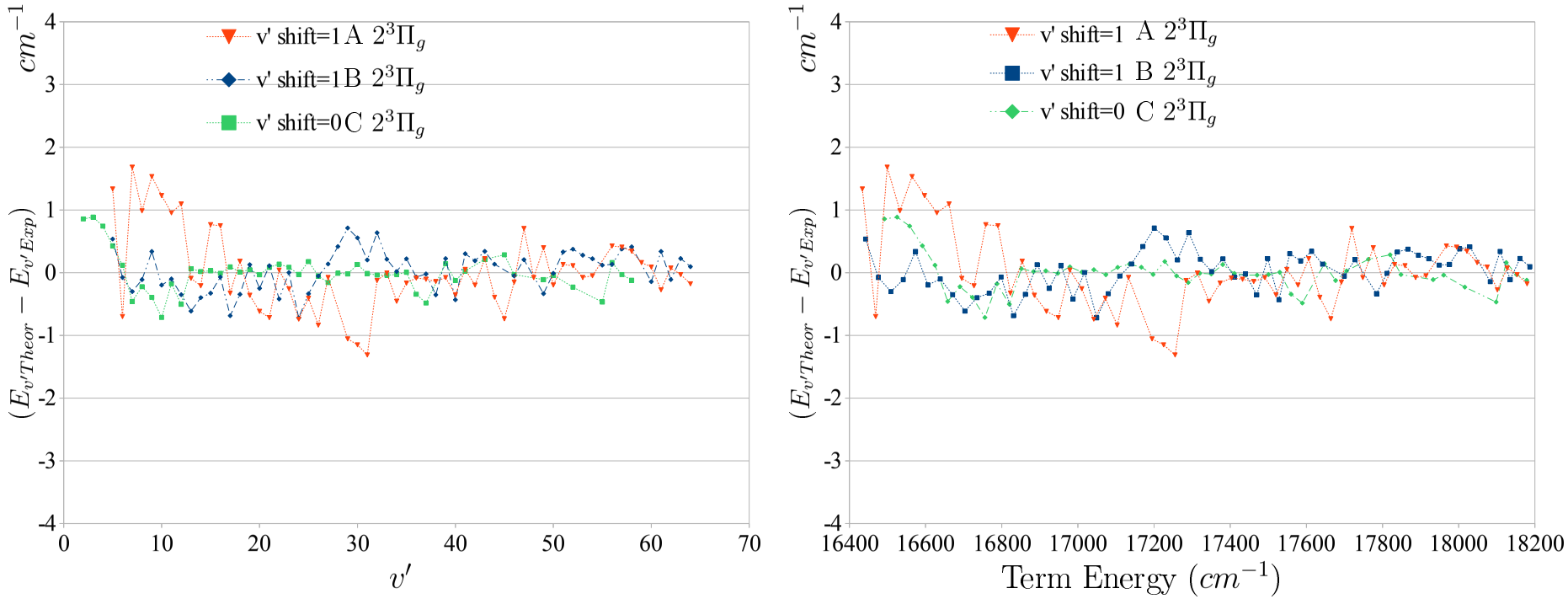

Fig. 5.4: Differences between theoretical and experimental energies for the $2^3\Pi_g$ state, series A, B, C (as labelled by Huang) as functions of v' (left) and $E_{v'}$ (right). The plots represent the v' shifts chosen to have a constant energy difference between *ab initio* theory and experiment (See Figs. 5.1, 5.2, and 5.3). It is interesting to note that series B and C (green and blue) have the same behavior for $v' \lesssim 10$, but this correlation is lost at higher v'. While series B and C maintain a fairly regular behavior (in reasonable agreement with experimental error), series A has large perturbations not explicable by experimental uncertainty.

for $v' > 120$.

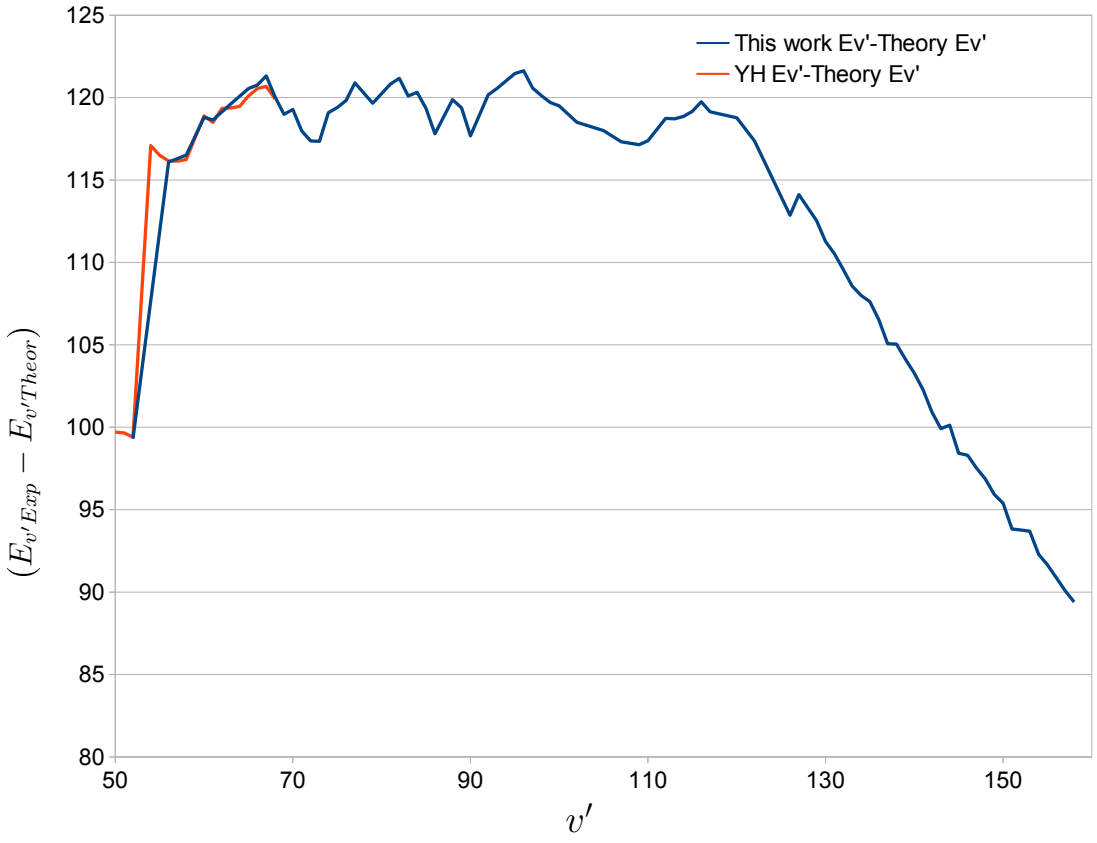

Fig. 5.5: Difference of Huang's excited levels for the $3^1\Sigma_g^+$ state as well as this work's levels, with respect to *ab initio* predictions of Tomza *et al.* vs vibrational quantum number v'. Optimally this graph would show a horizontal line. The offset from *ab initio* predictions is -119.20 cm^{-1} with a standard deviation of 1.50 cm^{-1} when the sample considered is reduced to $v' < 120$. The deviations from a regular behavior could be explained by a correlation with some other electronic state (such as the $2^1\Sigma_u^+$ state).

5.3 Comparison with Ye Huang's work

Ye Huang's work [43] (p.163) was calibrated using several atomic transitions, which all lie below 16456.95 cm^{-1}.

The present spectrum has an absolute accuracy of $\sim 0.5\ cm^{-1}$. In addition it has been calibrated with atomic transitions ($5p_{3/2}$ to $7d_{3/2}$ and $7d_{5/2}$) near $17465\,cm^{-1}$. Without any other adjustment, the discrepancy with Huang's tentative assignment of excited energy levels, shown in Figure 5.6, is well within expected values.

A direct comparison of the spectra recorded in Huang's work and this work in the overlapping region shows very good agreement, see Fig. 5.7. It is noticeable that the efforts in this work to reduce linewidth by controlling the irradiance of the 1^{st} laser, the excitation step, have yielded good results, resolving features previously unresolved by Huang.

At the end of this section, Figs. 5.8, 5.9, and 5.10 present the traditional $\Delta G_{v'+\frac{1}{2}}$ plots.

As expected from the previous graphs (Figs. 5.1 - 5.4, series B and C of the $2^3\Pi_g$ state have a more regular behavior than series A. The theoretical plots are computed on the unshifted energy scale, which has no effect on the $\Delta G_{v'+\frac{1}{2}}$ values in Fig. 5.8. In Fig. 5.9 for series C, there is instead an evident offset that emphasizes well the rather large energy shift that it appears to have.

The $\Delta G_{v'+\frac{1}{2}}$ values for the $3^1\Sigma_g^+$ state 5.10 shows an interesting transition

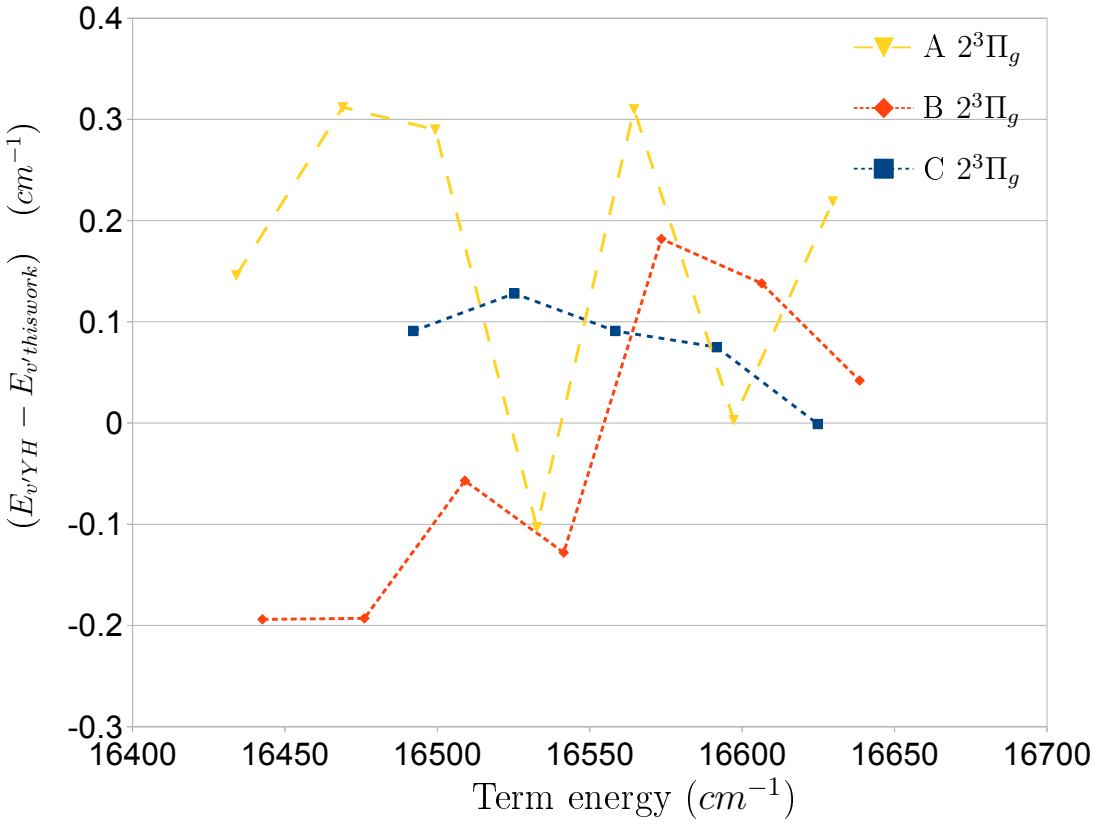

Fig. 5.6: The methods for frequency measurement between this work and Huang's have been radically different. Nonetheless the agreement is well within the expected experimental error for the excited levels that were assigned by both Huang and this work.

from an unperturbed region (recorded by Huang) up to $v' \sim 50$ to a perturbed region up to $v' \sim 100$, after which there is a regular region vs v' but with values constantly below the *ab initio* calculations.

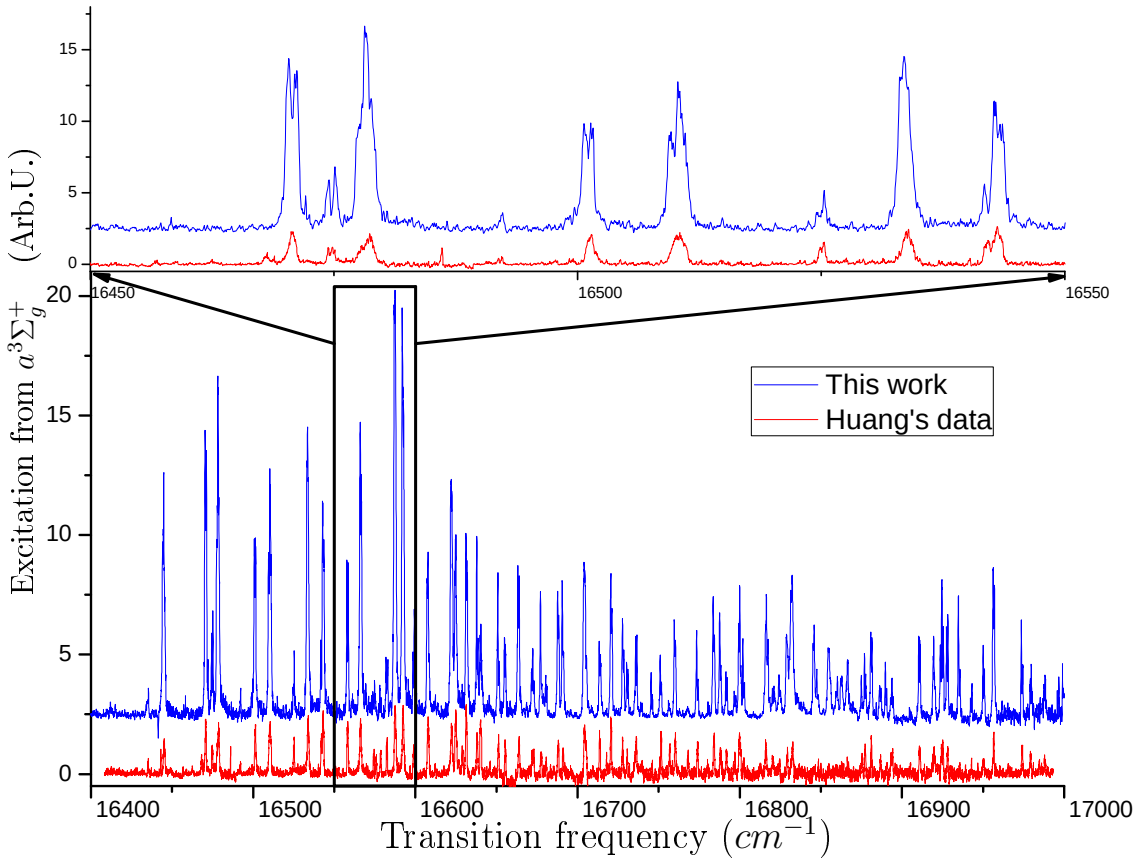

Fig. 5.7: Comparison between Huang (red) and this work (blue) of overlapping spectra starting from the $a^3\Sigma_u^+$ state. There are minor differences in signal-to-noise ratio and resolution which may be due to different control of the exciting irradiance, see section 2.2.4. The overall frequency agreement appears to be excellent. Note: Huang's data has been conditioned to fit in the graph, an over all background has been subtracted, and the amplitude has been rescaled to facilitate comparison.

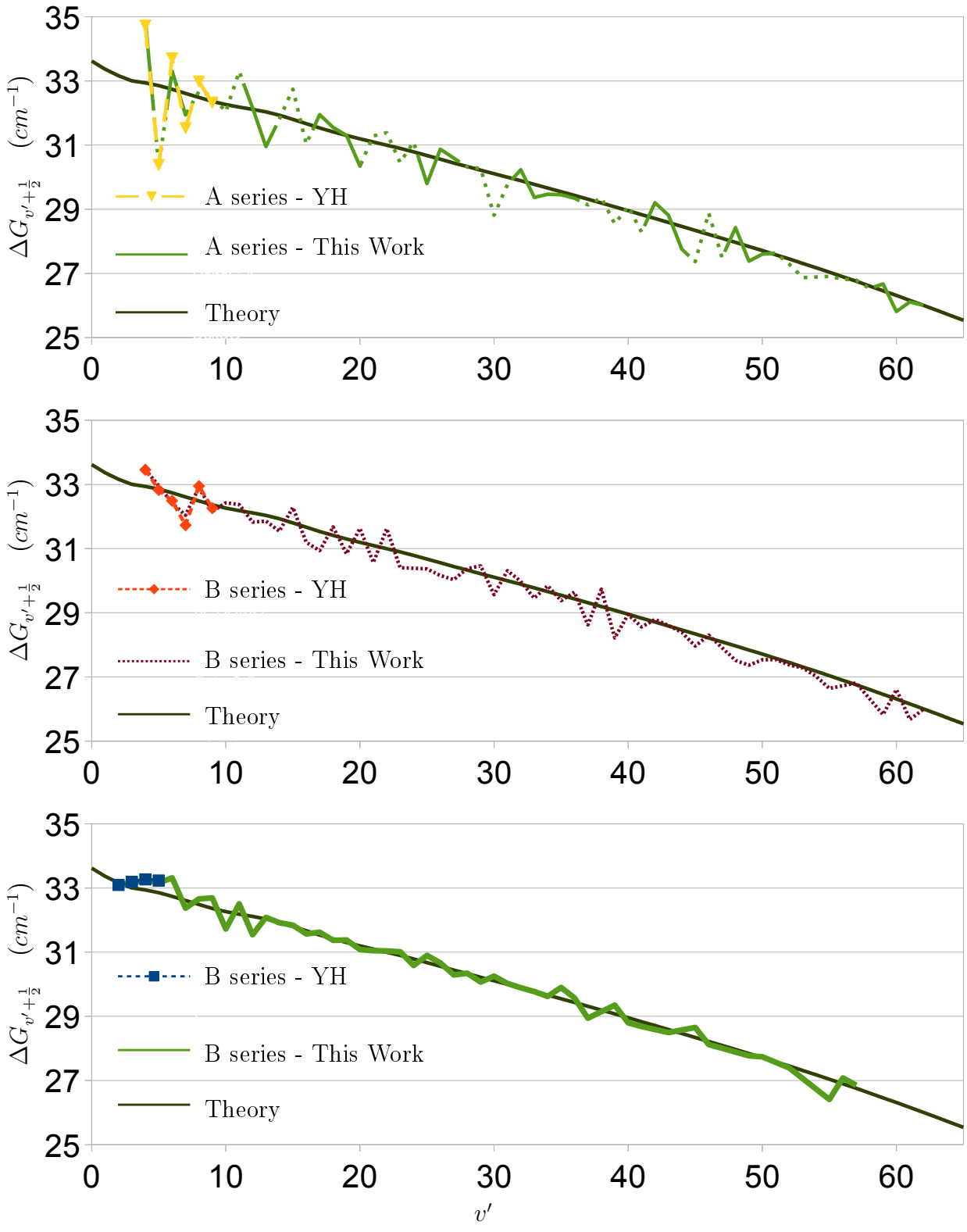

Fig. 5.8: Comparison of $\Delta G_{v'+\frac{1}{2}}$ for the $2^3\Pi_g$ states vs. v' for the present work and the work of Ye Huang (YH).

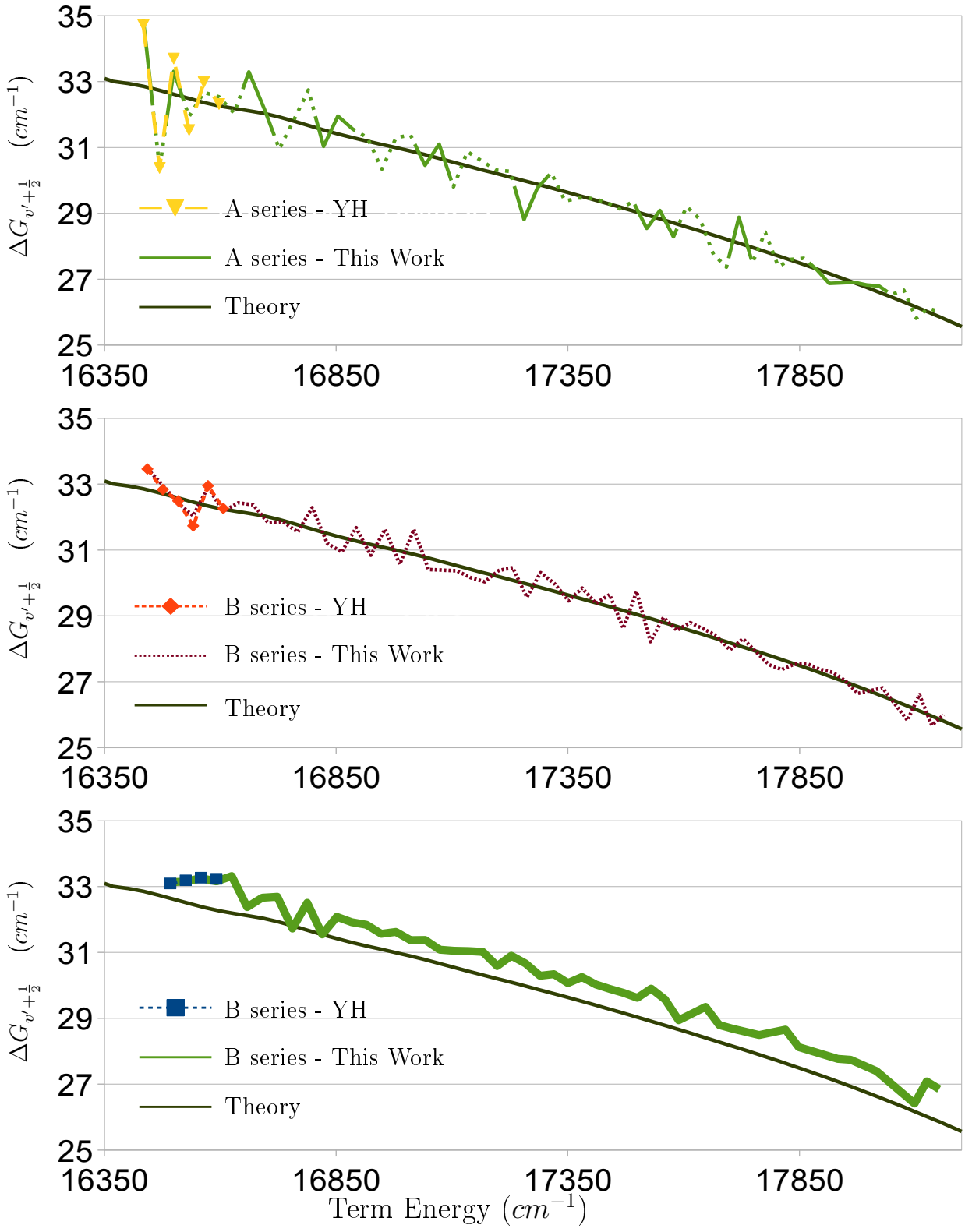

Fig. 5.9: Comparison of $\Delta G_{v'+\frac{1}{2}}$ for $2^3\Pi_g$ states vs. $E_{v'}$ for the present work and the work of Ye Huang (YH).

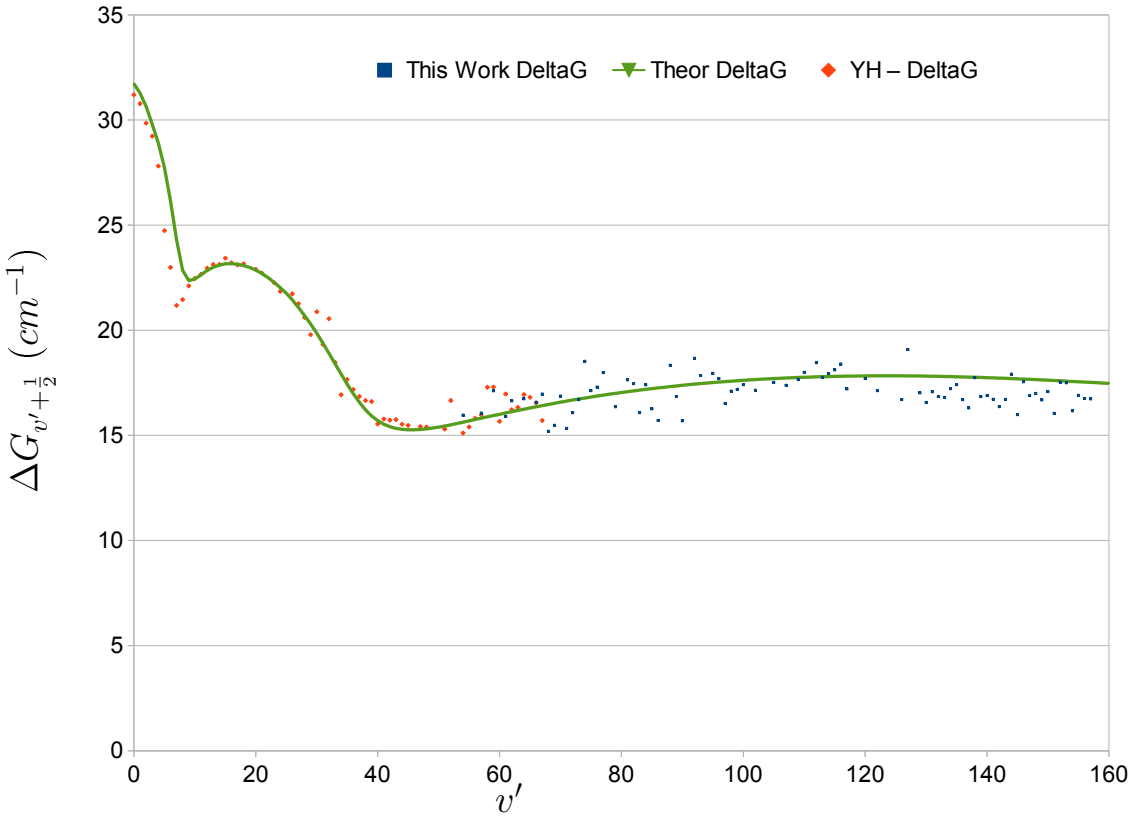

Fig. 5.10: $\Delta G_{v'+\frac{1}{2}}$ for the $3^1\Sigma_g^+$ state vs. v' for this work (■), YH work (♦) and theory (▼). These results are somewhat surprising as there seems to be a perturbation starting in the vicinity of v'$\sim$ 50, where Huang has also investigated, terminating near v'$\sim$ 100, only to deviate substantially from the *ab initio* predictions near v'$\sim$ 120. This last phenomenon is more apparent in Fig. 5.5.

5.4 Overview of $a^3\Sigma_u^+$ spectrum

The spectrum resulting from excitation from the $a^3\Sigma_u^+$ state shows several anomalies with respect to frequency: relatively large scatter with respect to *ab initio* predictions for many assigned states; a lower $\Delta G_{v'+\frac{1}{2}}$ for $v' \gtrsim 120$ for the $3^1\Sigma_g^+$ state; and a large asymmetry in the splitting of the three series of the $2^3\Pi_g$ state. Figure 5.11 presents a condensed overview of the data, fitted spectrum, and its decomposition into single electronic state assigned components (from the fitting results). The single electronic state components themselves are represented alongside their corresponding FCF simulations: the simulations assign to the calculated transition energies (line position), the experimentally found linewidth and an amplitude equal to the FCF scaled up by a factor 4000. All the anomalies mentioned above are observable, especially in the single component plots. It is interesting to note that the FCF simulations and the electronic state component amplitudes have similar behavior vs frequency, which indicates that the experimental assignment has good correlation to the *ab initio* potentials used for the calculation [49].

Figures 5.12, 5.13, and 5.14 are meant to give an overview of the SA spectrum and the levels identified in the assignment. On top are the v' labels. For each v' the vertical line marks the excited level energy. Descending closer to the x-axis, the horizontal plateau shows the binding of the leading ground-state feature, the descending secondary vertical line marks the leading transition. Expanded views of the spectrum and tables of assigned levels are given in the appendices.

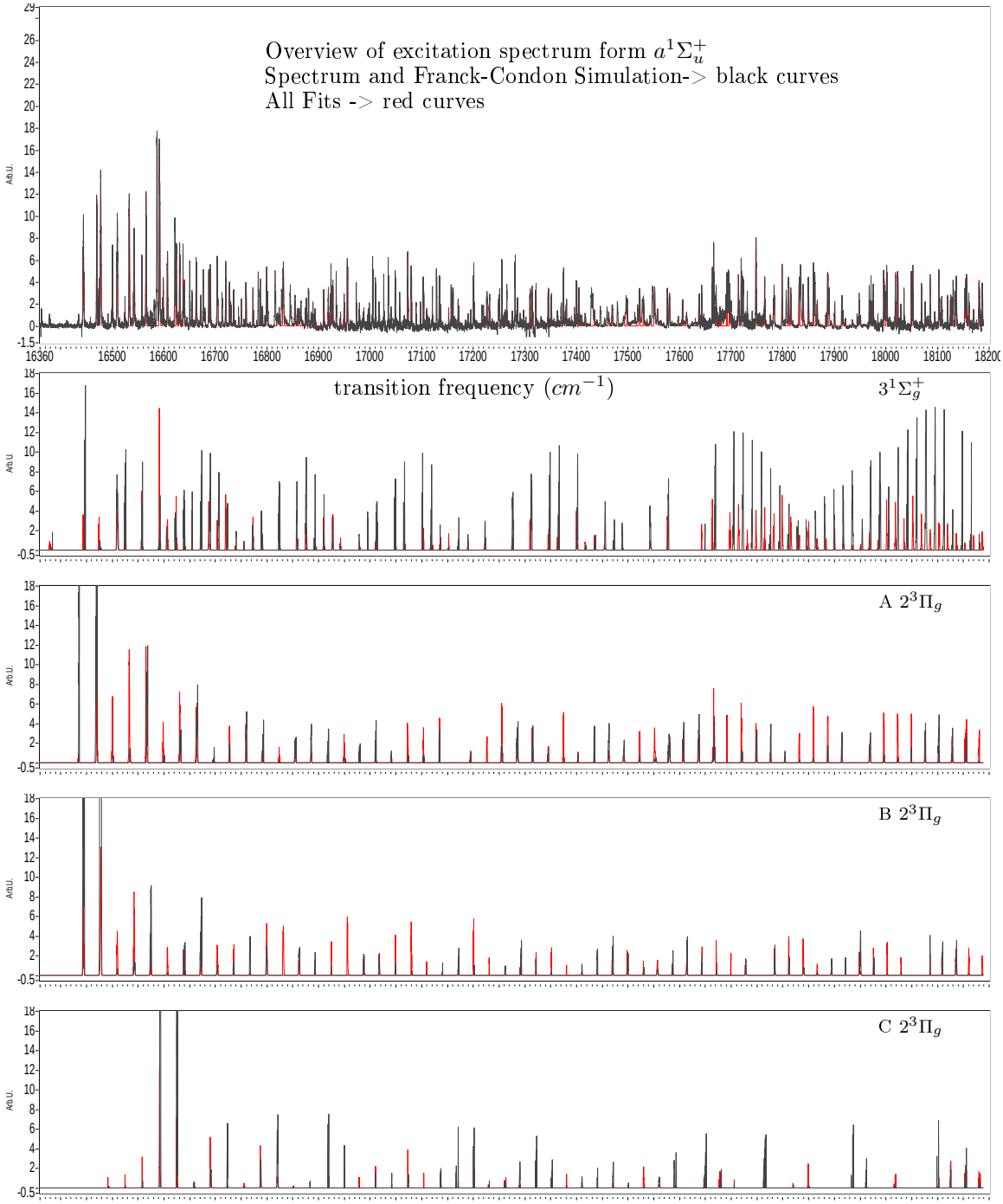

Fig. 5.11: Top: The spectrum excited from the $a^3\Sigma_u^+$ state - black, Spectrum fitting results - red. Bottom four plots: FCF simulation for the indicated state - black, Spectrum fitting results for the indicated state - red

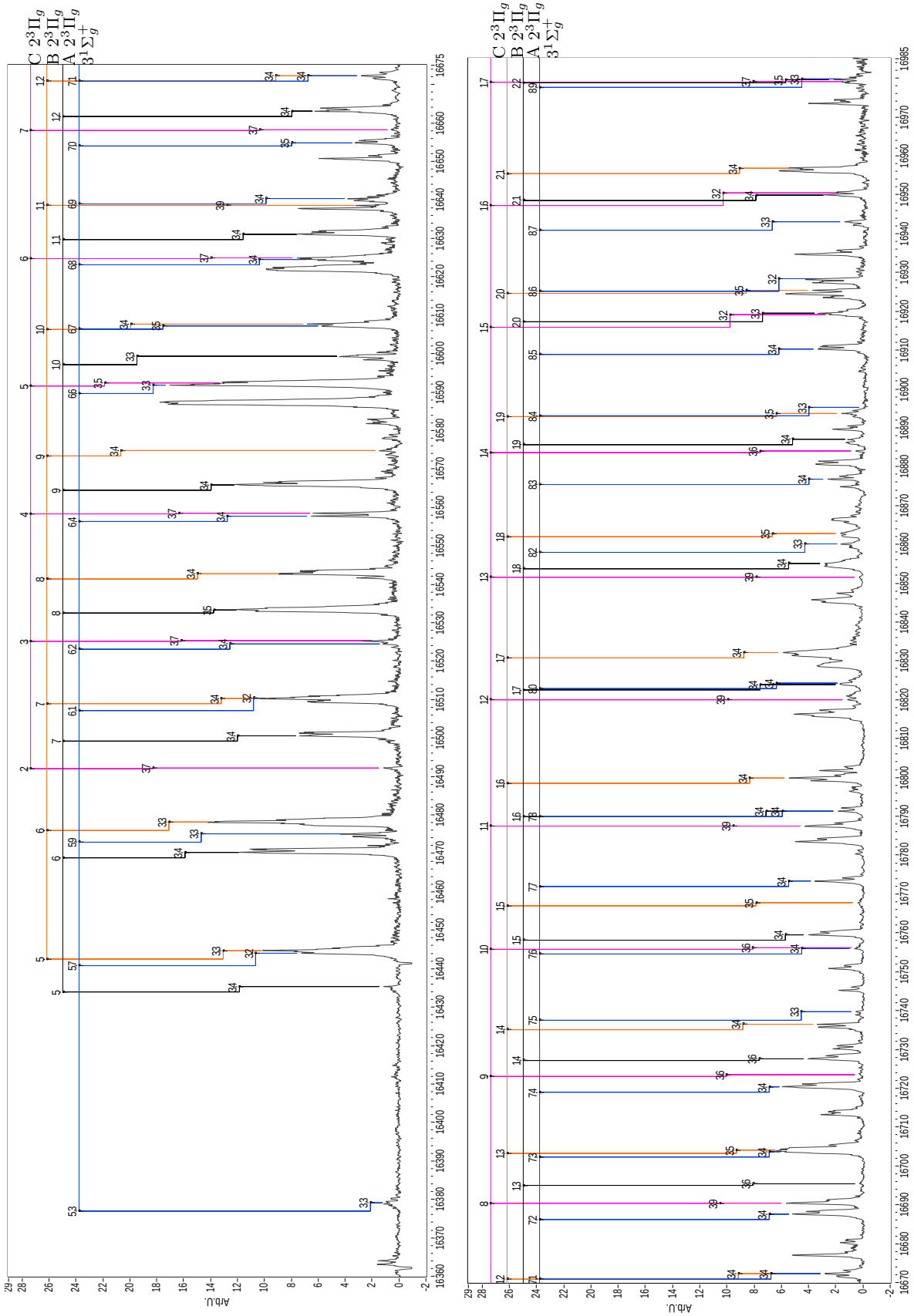

Fig. 5.12: Spectrum sample from 16360 cm^{-1} to 16675 cm^{-1} (top) and from 16670 cm^{-1} to 16985 cm^{-1}

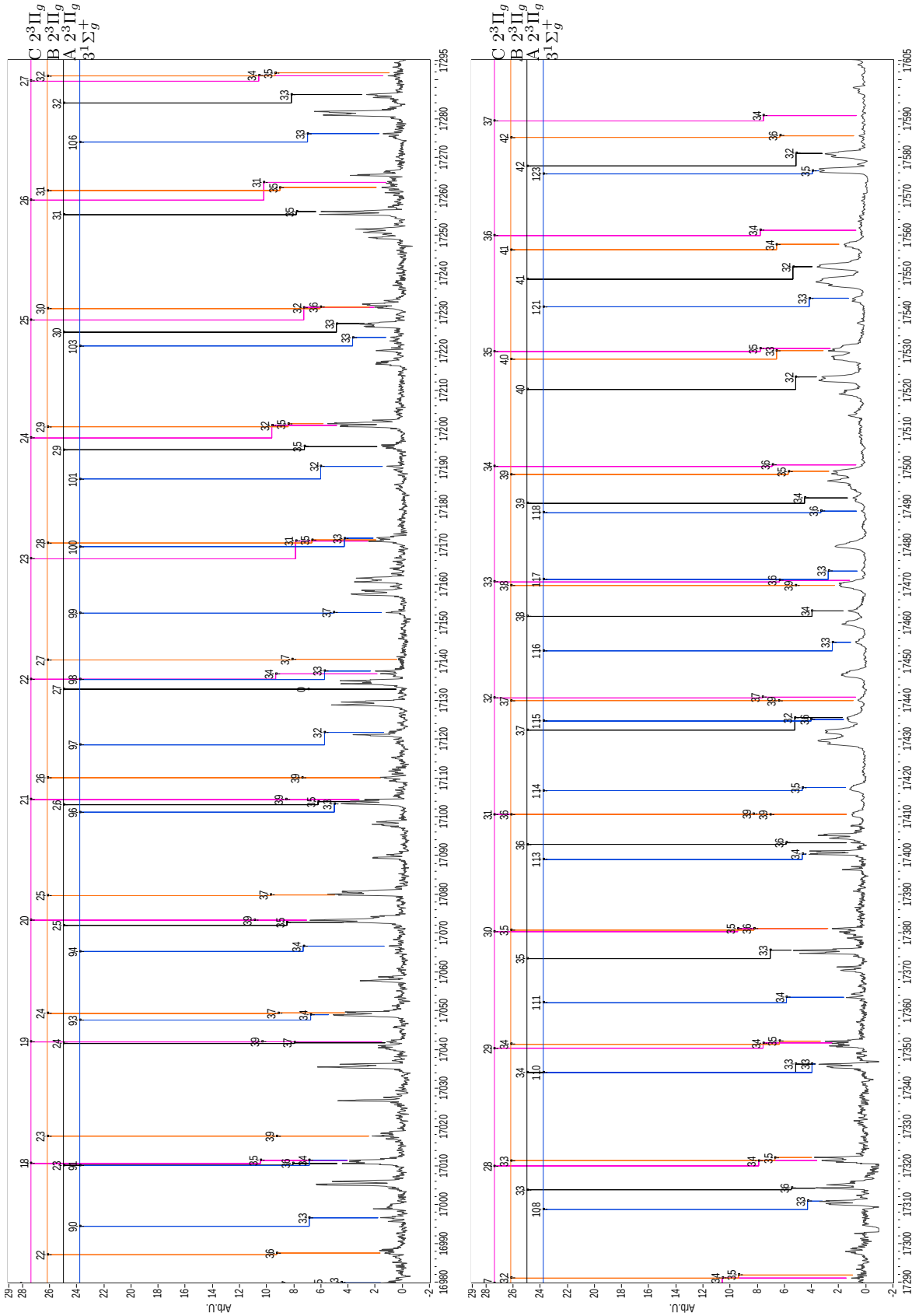

Fig. 5.13: Spectrum sample from 16980 cm^{-1} to 17295 cm^{-1} (top) and from 17290 cm^{-1} to 17605 cm^{-1}

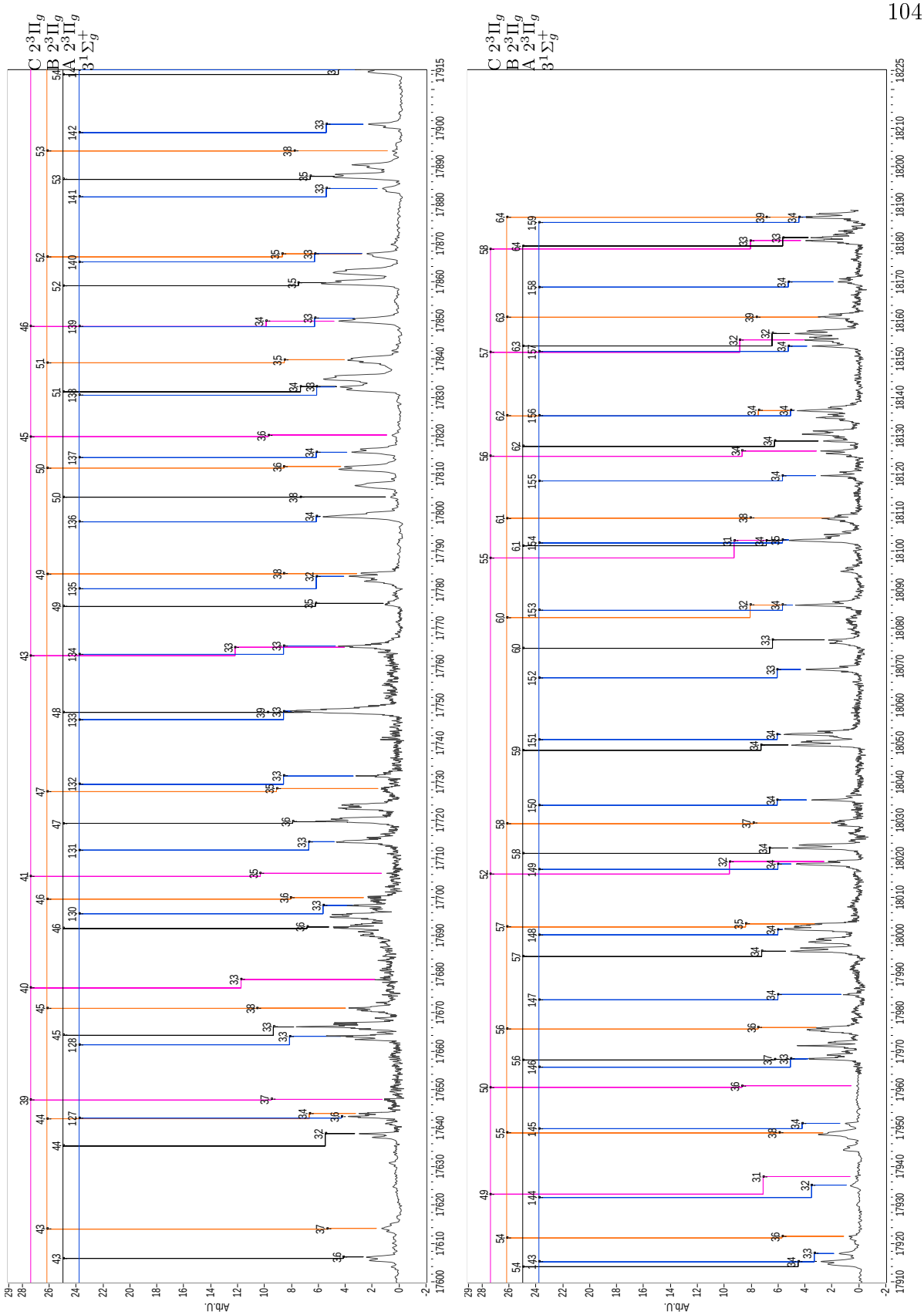

Fig. 5.14: Spectrum sample from 17600 cm^{-1} to 17915 cm^{-1} (top) and from 17910 cm^{-1} to ~18200 cm^{-1}

Chapter 6

Conclusions

6.1 Findings summary

As pointed out in the previous chapter, the $2^3\Pi_g$ and the $3^1\Sigma_g^+$ states seem to be significantly perturbed by some interaction not taken into account by current *ab initio* potentials. The agreement of FCF simulations and the results of the spectral assignment appears to be good, having overall amplitude behavior consistent with their corresponding state.

Previously assigned vibrational quantum numbers for the levels of the $2^3\Pi_g$ states may need revision when taking into account the larger progression of excited levels identified by the present work, and comparing to the present *ab initio* PECs. Series A and B have a v' shift of $+2$ with respect to Huang, while series C has the same optimal v' assigment as Huang [43]. This implies a relative shift between these three series with respect to Huang's work. Table 6.1 gives the apparent correspondence with the *ab initio* PEC of Tomza *et al.* and the corresponding v' values for YH work. Series A, B, and C of the $2^3\Pi_g$ state are different components

State	$E_{v'}$ (cm^{-1})	This work v'	YH v'	Δ v'	Relative energy shift (cm^{-1})
A	16442.60	5	3	2	0
B	16434.05	5	3	2	7.75
C	16492.11	2	2	0	148.95

Table 6.1: Table of v' assignment shift of the $2^3\Pi_g$ states.

of Ω (the projection of the total angular momentum along the internuclear axis); in our calculations any **R**-dependent contribution of Ω is not accounted for.

There is an interesting correlation involving the $3^1\Sigma_g^+$ state: the energy at which it begins to experience perturbations is approximately where the minimum of the $2^3\Pi_g$ state is located.

We have measured and assigned a large fraction of the vibrational levels of the $2^1\Sigma_u^+$ and $3^1\Sigma_g^+$ states which was the principal goal of this experiment.

In the following sections are outlined some of the possibilities that the spectroscopic knowledge acquired in this study opens.

6.2 R-transfer

Hypothesizing a real correlation between $3^1\Sigma_g^+$ perturbations and the beginning of the $2^3\Pi_g$ spectrum, this could be an extremely interesting condition that lends itself to application for population R-transfer. This transfer utilizes a wavefunction with a multi-modal distribution, i.e. significant amplitude at both short and long range, to implement schemes for manipulating population distributions or production rates. This is similar to the basic idea of Pechkis *et al.* [53] and and

Ban *et al.* [19]. Incidentally reference [19] involves a coupling between $^1\Sigma_g^+$ and $^3\Pi_g$ states at longer range (and higher energy along the ion-pair curve). The difference of this specific case, with respect to other models, is in flexibility: with a coupling between excited states extended over such a wide range of energy (or R), it could be possible to choose the excited level to target a specific ground-state level.

6.3 Configuration mixing

The designation of opposite parity (u/g symmetry) for the shelf-state singlets $2^1\Sigma_u^+$ and $3^1\Sigma_g^+$ can lend itself to many purposes given the unusual radial extension of these potentials, but undoubtedly the most attractive implication is the possibility of controlling the mixing of u/g symmetry, thus being able to manipulate the permanent electric dipole moment (in the molecular reference frame) of a homonuclear molecule!

We will explore two ways to achieve mixing between these states.

6.3.1 DC Stark mixing

This study has determined with an absolute uncertainty of $\sim 0.5\ cm^{-1}$ a relatively large fraction of the vibrational states of the $2^1\Sigma_u^+$ and $3^1\Sigma_g^+$ states. Comparing the two spectra leads us to the narrowing of candidate states for wavefunction engineering. Fig. 6.1 shows the energy difference between nearest-neighbor vibra-

tional levels of opposite gerade and ungerade symmetry.

Table 6.2 reports all the candidate pairs of levels that fall between the red lines in Fig. 6.1. To be noticed is that a few level pairs fall closer than $0.1\,cm^{-1}$ and that the order in which the levels of the $2^1\Sigma_u^+$ and $3^1\Sigma_g^+$ states appear in frequency alternates often, so that a relative shift may increase some differences, but will decrease others.

State	v'_{low}	Ev'_{low} (cm^{-1})	State	v'_{high}	Ev'_{high} (cm^{-1})	ΔE
$3^1\Sigma_g^+$	67	16623.44	$2^1\Sigma_u^+$	23	16624.00	0.56
$3^1\Sigma_g^+$	72	16702.39	$2^1\Sigma_u^+$	29	16702.58	0.19
$3^1\Sigma_g^+$	76	16772.04	$2^1\Sigma_u^+$	34	16772.18	0.14
$3^1\Sigma_g^+$	81	16858.03	$2^1\Sigma_u^+$	40	16858.83	0.81
$3^1\Sigma_g^+$	89	16994.48	$2^1\Sigma_u^+$	49	16994.68	0.20
$2^1\Sigma_u^+$	50	17010.13	$3^1\Sigma_g^+$	90	17010.17	0.04
$3^1\Sigma_g^+$	96	17118.95	$2^1\Sigma_u^+$	57	17119.83	0.88
$2^1\Sigma_u^+$	58	17135.43	$3^1\Sigma_g^+$	97	17135.47	0.04
$2^1\Sigma_u^+$	72	17361.80	$3^1\Sigma_g^+$	110	17362.13	0.33
$3^1\Sigma_g^+$	124	17611.63	$2^1\Sigma_u^+$	87	17611.68	0.05
$2^1\Sigma_u^+$	88	17628.58	$3^1\Sigma_g^+$	125	17629.52	0.94
$3^1\Sigma_g^+$	127	17661.74	$2^1\Sigma_u^+$	90	17662.04	0.30
$3^1\Sigma_g^+$	128	17678.54	$2^1\Sigma_u^+$	91	17678.58	0.04
$2^1\Sigma_u^+$	92	17695.23	$3^1\Sigma_g^+$	129	17695.80	0.57
$2^1\Sigma_u^+$	93	17711.58	$3^1\Sigma_g^+$	130	17712.37	0.79
$2^1\Sigma_u^+$	94	17728.58	$3^1\Sigma_g^+$	131	17729.44	0.86
$2^1\Sigma_u^+$	95	17745.38	$3^1\Sigma_g^+$	132	17746.29	0.91
$2^1\Sigma_u^+$	96	17762.13	$3^1\Sigma_g^+$	133	17763.09	0.96
$2^1\Sigma_u^+$	100	17829.83	$3^1\Sigma_g^+$	137	17830.72	0.89

State	v'_{low}	Ev'_{low} (cm^{-1})	State	v'_{high}	Ev'_{high} (cm^{-1})	ΔE

Table 6.2: Table of nearest-neighbor energy difference of the two states: $2^1\Sigma_g^+$ and $3^1\Sigma_g^+$. Only the pairs with $\Delta E < 1\ cm^{-1}$ are shown. On the left side of each row is the level of lower energy of the pair, while on the right side is the level of higher energy. Each series has an error of $\sim 0.5\,cm^{-1}$ and a relative shift of $\sim 0.7\,cm^{-1}$ (combined error) which can significantly change which specific level is closest.

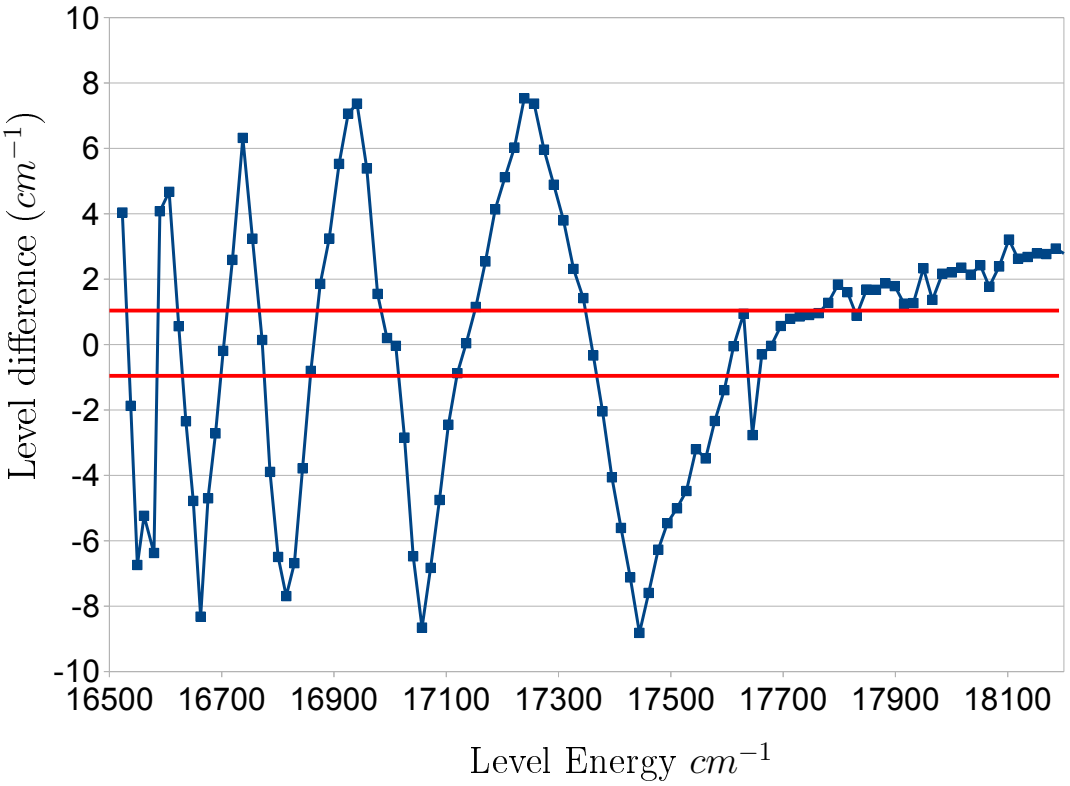

Fig. 6.1: Nearest-neighbor energy difference of $2^3\Pi_g$ - $3^1\Sigma_g^+$ level pairs: this difference is very susceptible to error: each series has an error of $\sim 0.5\,cm^{-1}$ and a relative shift of $\sim 0.7\,cm^{-1}$ can significantly change which specific level is closest. Highlighted between the red horizontal lines are all candidates with a nearest neighbor closer than 1 cm^{-1}.

Our initial motivation was to find out how close to degeneracy these two

states are in order to explore the possibility of mixing states of opposite gerade-ungerade symmetry. For a relative shift between the two spectra, all differences will be displaced either positively or negatively depending on their position on the curve: a way of picturing this is to think that it is the curve that is displaced but not the x-coordinates of the points in Fig. 6.1. Since there are 19 pairs closer than 1 cm^{-1}, there is a reasonable probability of a pair with $\Delta E < 0.1\ cm^{-1}$. We will take this as a characteristic value for the energy separation.

As mentioned in Sec. 2.1.1, introducing an ad-hoc perturbation can produce the desired mixing of gerade-ungerade symmetry. Here we follow closely [71] [eq 10-12, p.253 and following].

Given two states ψ_1^0 and ψ_2^0 of unperturbed energy W_1^0 and W_2^0 that are sufficiently close in energy that $\delta = W_1^0 - W_2^0$ is much less than any other energy difference between these two levels and any third level, in the presence of an electric field F, the wavefunctions can be written:

$$\psi_1 = a(F)\psi_1^0 + b(F)\psi_2^0 \tag{6.1}$$

$$\psi_2 = -b(F)\psi_1^0 + a(F)\psi_2^0 \tag{6.2}$$

where $a(F)$ and $b(F)$ depend on the the molecular static dipole moment.

Here we need to consider carefully the meaning of this dipole moment. What we are exploring is the work done by the electric field on the molecule, which means that $\mu = \mu_e + \mu_N$ much like outlined in Eq.1.37. While the nuclear component μ_N is zero, the electronic component has the two excited electronic wavefunctions

of opposite symmetry separated in energy by a fraction of a cm^{-1}, with a radial extension on the order of the nuclear separation ($\sim 20\,a_0$). Leaving the matrix element indicated as $F\,\mu_{12}$ the energy displacement due to the perturbation is

$$W = \frac{W_1^0 + W_2^0}{2} \pm \left[\left(\frac{W_1^0 - W_2^0}{2}\right)^2 + (F\,\mu_{12})^2\right]^{\frac{1}{2}} \tag{6.3}$$

and the wavefunction admixture turns out to be:

$$a = \sqrt{\frac{\sqrt{\delta^2+(2\,F\,\mu_{12})^2}+\delta}{2\sqrt{\delta^2+(2\,F\,\mu_{12})^2}}} = \sqrt{\frac{\sqrt{1+x^2}+1}{2\sqrt{1+x^2}}} \tag{6.4}$$

$$b = \sqrt{\frac{\sqrt{\delta^2+(2\,F\,\mu_{12})^2}-\delta}{2\sqrt{\delta^2+(2\,F\,\mu_{12})^2}}} = \sqrt{\frac{\sqrt{1+x^2}-1}{2\sqrt{1+x^2}}} \tag{6.5}$$

with $x = \frac{2\,F\,\mu_{12}}{\delta}$. This treatment allows the evaluation of both the quadratic and linear regimes which are expected for the case of a "smooth" passage from homonuclear-covalent to (pseudo-heteronuclear) ionic bond.

This requires the evaluation of $F\,\mu_{12}$ with the molecular wavefunctions of candidate states, which is beyond the scope of the present work and, to the best of our knowledge, has not been published. The overall calculation is nontrivial, and it cannot be done here. A general trend has to be stressed: a larger the nuclear separation, lends to a more polarizable molecule.

Nevertheless, as a crude estimate, we can approximate the molecular static polarizability with the closest value in the literature. Tomza *et al.* have calculated the static polarizability for the $1^1\Sigma_u^+$ state of Rb_2 (Fig. 6.2 reports the relevant information).

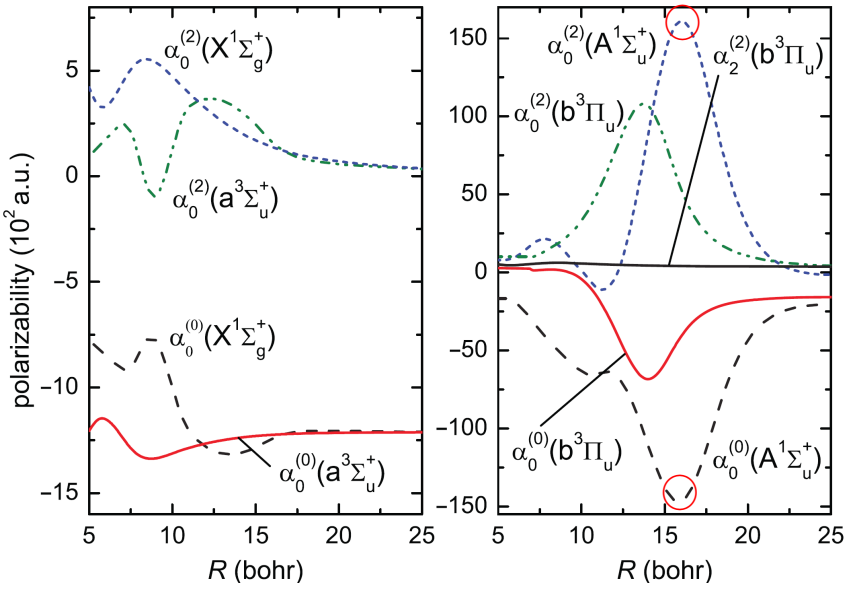

Fig. 6.2: Electric dipole polarizability for the $X(1)^1\Sigma_g^+$ ground state and $a(1)^3\Sigma_u^+$ lowest triplet states(left) and the $A^1\Sigma_u^+$ first excited singlet state and $b^3\Pi_u$ first excited triplet state (right) from [49]. The two red circles mark the reference values for the polarizability in atomic units.

Taking the polarizability as $\alpha_0 \sim\ 15000 a.u. \rightarrow\ 2.35 \times 10^{-37}$ S.I.

and using $\delta\ \sim\ 3\,GHz$ we have

$$\frac{F\,\mu_{12}}{\delta} = \frac{F^2\,\alpha_0}{\delta} \sim\ 1\ \Rightarrow\ F = 28000\,\frac{V}{cm} \tag{6.6}$$

This is an order of magnitude estimate, but it provides some experimental hope: with an electric field of $F\ \simeq\ 7.1\,\frac{kV}{cm}$ the mixture would have a ψ_2^0 component with $b^2 \simeq 0.1\%$ which, with electric field modulation and synchronous detection, could be detectable in a restricted spectral region. In order to pursue this mixing experimentally, gerade/ungerade energy differences would have to be measured more accurately. This would require higher spectral resolution and as well as better frequency calibration. One way of acheiving this is simply replacing the

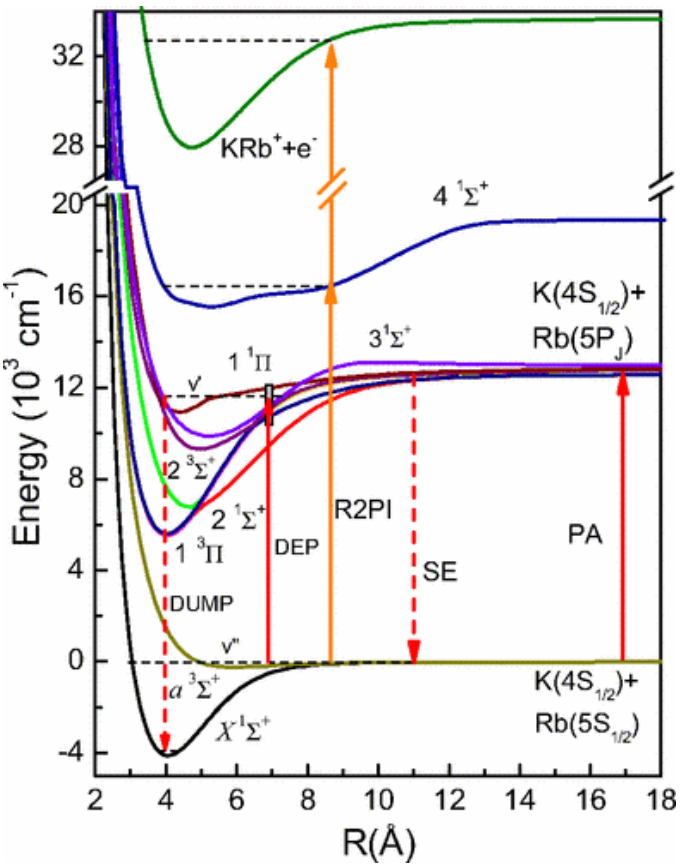

Fig. 6.3: CW depletion REMPI scheme from [85]. In the our case the spectroscopy laser would be the CW laser marked DEP, that gives a depletion signal using the transitions $a(1)^3\Sigma_u^+ \rightarrow 3^1\Sigma_g^+$ or $X(1)^1\Sigma_g^+ \rightarrow 2^1\Sigma_u^+$ in the region 16000 to 18000 cm^{-1} , while the 2-photon (1 color) REMPI laser can be chosen independently.

pulsed dye laser used for excitation in our experimental scheme with a pulse-amplified system where a seeding CW laser is amplified in a capillary cell. These kinds of systems are capable of linewidths $\delta\nu < 0.01\,cm^{-1}$ (in fact they can be Fourier limited). A good alternative is the use of a depletion REMPI scheme which has achieved CW resolution in KRb in the work of Wang *et al.* [85]. Figures 6.3 and 6.4 give more details about this scheme. Large static fields would need to be

applied to the molecular sample during the spectroscopy in order to induce mixing. Heavy Rydberg molecules should result, given good control over the stray electric fields. An alternative method, once the states' energy difference is known to a higher accuracy, is the use of long wavelength (IR, microwave) radiative transitions to induce mixing.

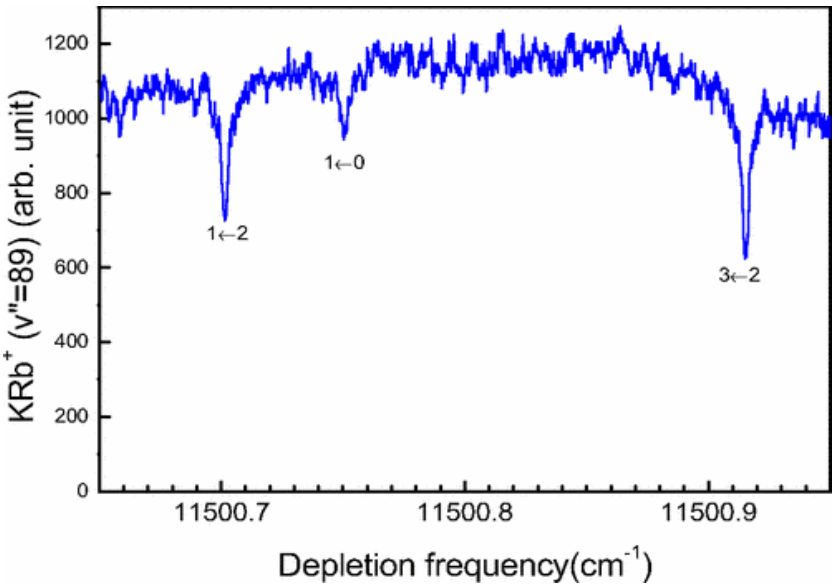

Fig. 6.4: CW depletion REMPI spectrum from [85]. Depletion spectrum with well resolved rotational structure

6.3.2 Laser mixing

There are multiple ways to create a superposition of wavefunctions. Fig. 6.5 presents the idea in a pictorial form. When mixing with a static field one can take advantage of the quasi-degeneracy of selected levels; since the characteristic parameter in eq. 6.5, $x \sim \frac{1}{\Delta E}$, a small splitting can greatly facilitate the wavefunc-

tion admixture process. On the other hand, using an AC field requires the direct overlap of the wavefunctions, the Franck-Condon principle, which is precisely not the case when the levels are nearly degenerate (and the two potentials are nearly identical). In fact the FCF for these levels is very small. A hand-waving expla-

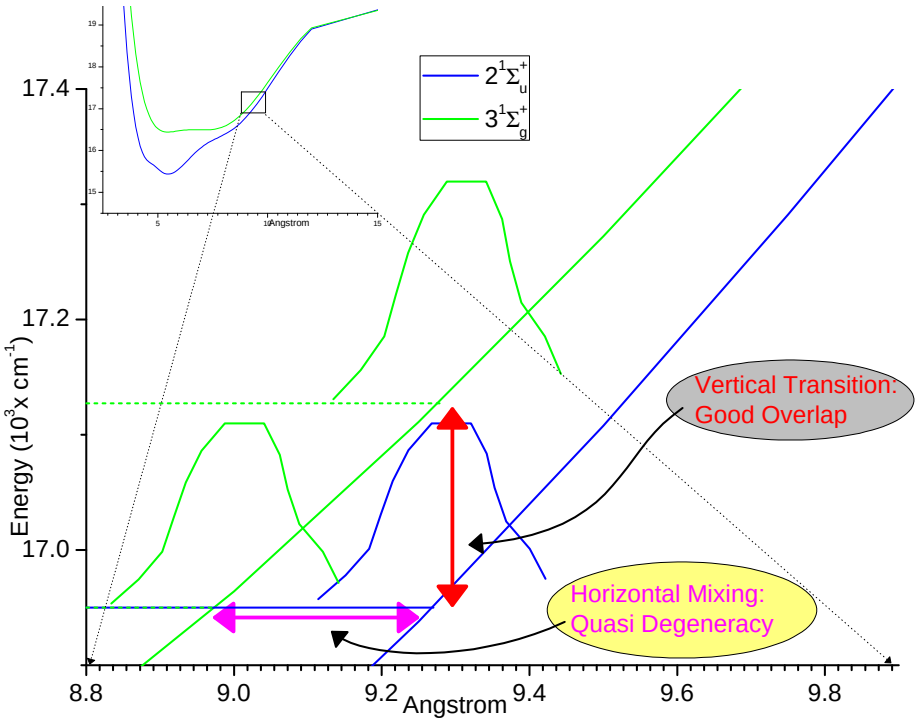

Fig. 6.5: The PEC for $2^1\Sigma_u^+$ and $3^1\Sigma_g^+$ are very similar in the ion pair branch, they run almost parallel to each other. Optimal Franck-Condon coupling happens when the turning points are vertically aligned.

nation can be made by thinking that the two wavefunctions belong to the same potential but with distinct vibrational quantum numbers. This would make the overlap integral rigorously zero. This is not exactly true because the states $2^1\Sigma_u^+$ and $3^1\Sigma_g^+$ are different, even very different far away from the ion-pair branch, but the difference is numerically very small for nearly degenerate states: all the FCFs

for pairs in the table 6.2 lie below 10^{-7}. Fig. 6.6 shows the FCFs for the transitions $2^1\Sigma_u^+ \leftrightarrow 3^1\Sigma_g^+$. In red are highlighted the FCFs for table 6.2. The range of frequencies necessary for optimal radiative coupling can be estimated quickly from Fig 6.6: vertical transitions need $\lambda \sim 55\ \mu m$. Vitiello *et al.* [84] have recently published a review of Quantum Cascade Lasers (QCLs), and Fig. 6.7 presents an overview of emission wavelength vs operating temperature.

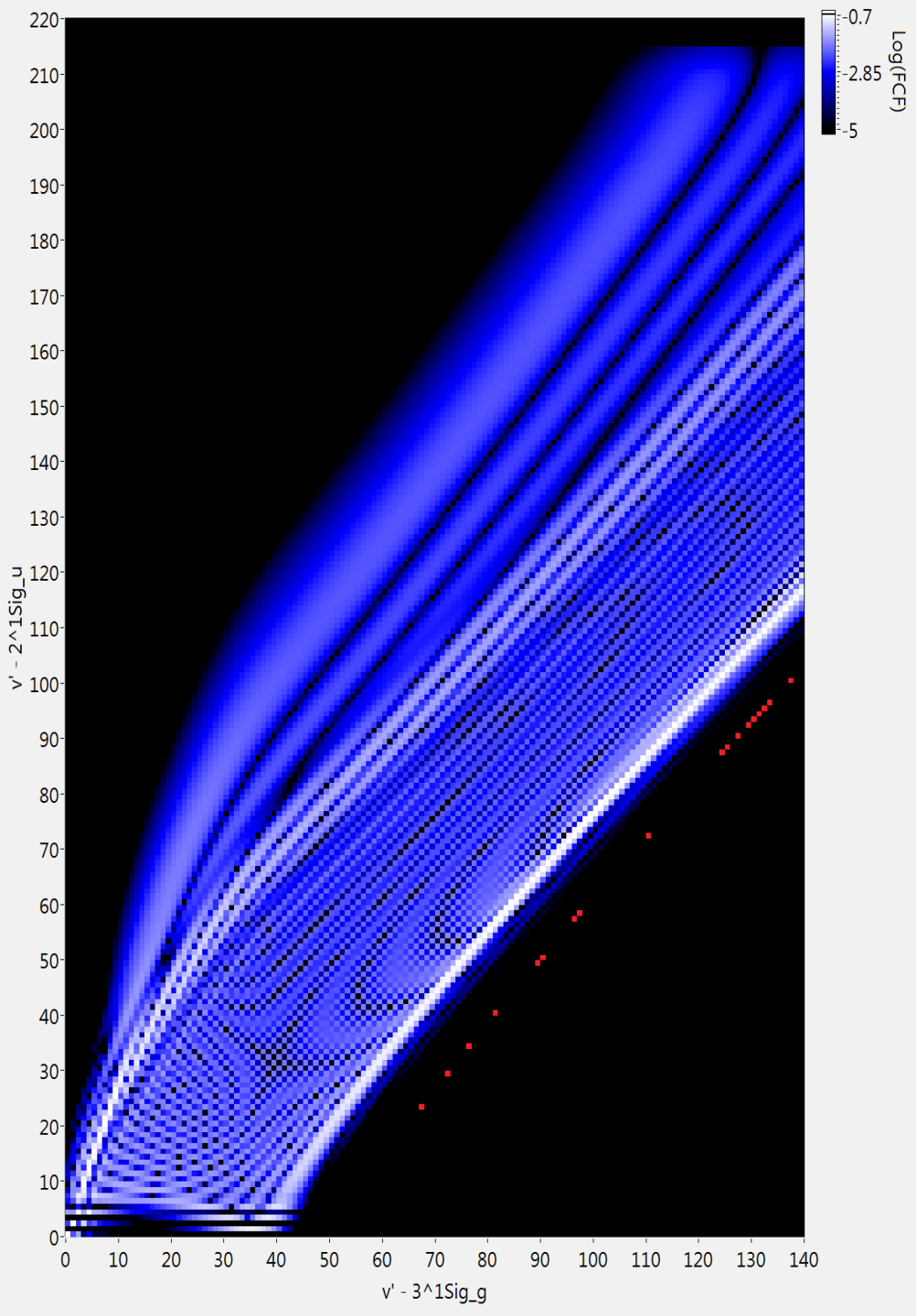

Fig. 6.6: FCF intensity graph for $2^1\Sigma_u^+ \leftrightarrow 3^1\Sigma_g^+$. The representation is logarithmic. In red are reported the 19 level pairs reported in Table 6.2. From the red dot curve to the white ridge there are $\Delta v' \sim 10 - 15$; for both states $\Delta G_{v'+\frac{1}{2}} \sim 15\ cm^{-1}$. Vertical transitions require about 150 to 225 cm^{-1} radiation or wavelength of 44 to 66 μm.

While the possibility of coupling states matching the Condon point is technically feasible this would be challenging since nearly all CW lasers at $\lambda \sim 50\ \mu m$ operate at liquid nitrogen temperature. Naturally diagonal coupling is also pos-

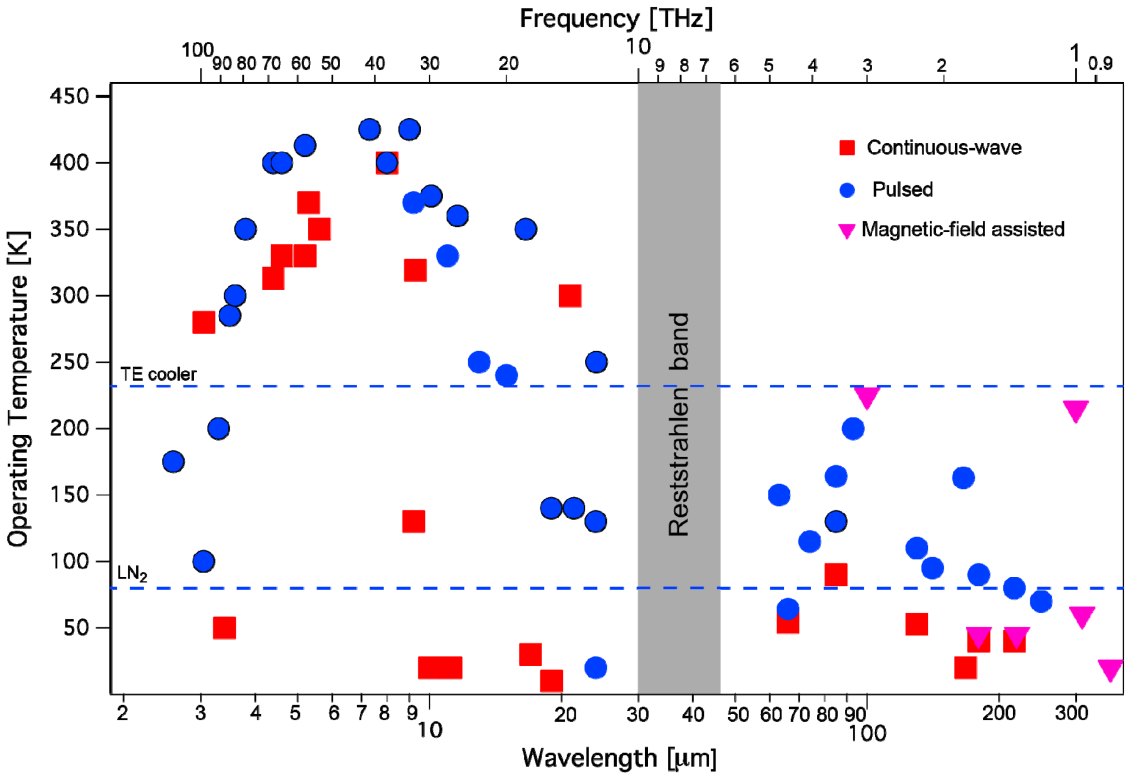

Fig. 6.7: Extracted from this year's review of Vitiello et al. an overview of Quantum Cascade Lasers operating temperature. [84]

sible as long as FCFs admit it. This is a matter of trade off between cost, FCF values and power. It turns out that there are more than 700 transitions belonging to the ion pair branch with $\lambda < 11\ \mu m$, FCFs>1%. It may be possible to use a CO_2 laser, and there are many lasers diodes (QCLs) near 10 μm available from major suppliers for less than the cost of three months of graduate student salary.

Appendix A

Notes on fitting methods

An iterative fitting method that is robust against outliers.

A.1 General Nonlinear fit

In the most general case, considering a set of data points (x_i, y_i) with associated error $(\delta x_i, \delta y_i)$ one cannot neglect neither the error on x nor the error on y.

Let $y = f(x, p)$ be the relationship between x and y, with $p = \{p_1, p_2, .., p_k\}$ being a set of parameters for which we want to determine the best values based on our experimental data. The first question that rises is: if the error δx_i cannot be neglected, then what value of x within the error range should be taken? To determine this one computes the values of $\bar{x}_i, \bar{y}_i$ by minimizing the functional:

$$\sum_{i=1}^{n} \left[\left(\frac{y_i - \bar{y}_i}{\delta y_i} \right)^2 + \left(\frac{x_i - \bar{x}_i}{\delta x_i} \right)^2 \right] \tag{A.1}$$

where $\bar{y}_i = f(\bar{x}_i, p)$. This is nothing more than the distance of the function f from the data points weighted by the associated errors. There is, in addition, the relationship $\bar{y}_i = f(\bar{x}_i, p)$ with $i = 1, 2, ..., N$, which constitutes a constraint. This

is a constrained minimum problem and can be solved by applying the Lagrange multipliers method. That brings about the following function to be minimized:

$$S = \sum_{i=1}^{n} \left[\left(\frac{y_i - \bar{y}_i}{\delta y_i} \right)^2 + \left(\frac{x_i - \bar{x}_i}{\delta x_i} \right)^2 + \lambda_i (\bar{y}_i - f(\bar{x}_i, p)) \right] \tag{A.2}$$

with respect to $\bar{x}_i, \bar{y}_i, \lambda_i, p$:

$$\begin{aligned} \frac{\partial S}{\partial \bar{x}_i} &= \frac{2(x_i - \bar{x}_i)}{\delta x_i^2} - \lambda_i \frac{\partial f(\bar{x}_i, p)}{\partial \bar{x}_i} = 0 \\ \frac{\partial S}{\partial \bar{y}_i} &= \frac{2(y_i - \bar{y}_i)}{\delta y_i^2} + \lambda_i = 0 \\ \frac{\partial S}{\partial \lambda_i} &= \bar{y}_i - f(\bar{x}_i, p) = 0 \\ \frac{\partial S}{\partial p_j} &= \sum_{i=1}^{n} -\lambda_i \frac{\partial f(\bar{x}_i, p)}{\partial p_j} = 0 \end{aligned} \tag{A.3}$$

where this last equation constitutes a system of k equations. Note that labeled p with the subscript j to emphasize the partial derivative for each of the k parameters. To actually proceed and perform this fit is quite laborious. We need:

- an initial guess of the parameters p.
- a 1^{st} order expansion of f.
- to partially solve the system of equations A.3.
- to iteratively utilize the partial solution to refine the parameters starting from the initial guess.

The outline of the partial solution includes:

- from system A.3, isolate $\bar{x}_i$ and $\bar{y}_i$ from the 1^{st} and 2^{nd} equations respectively.

- insert the solutions $\bar{x}_i$ and $\bar{y}_i$ into the 3^{rd} equation (which has a linearized approximation of f) in order to isolate λ_i.

- insert λ_i just found into the 4^{th} equation (which is a system of k equations) to find a formula of the type:

$$p' = \frac{\sum G1(x_i, y_i, \delta x_i, \delta y_i, p)}{\sum G2(x_i, \delta x_i, \delta y_i, p)} \tag{A.4}$$

  which allows iteration.

A simple overview of this method can be found in [62] and a deeper treatment of independent variables with error [63].

This is quite a labor intensive process that is normally avoided by the simple condition of being able to neglect the error in one axis: in eq A.2 the 2^{nd} and 3^{rd} term in the sum would disappear leading to the least square or least χ^2 method. It is easier to ask the question: what is the condition for which the functional

$$\chi^2 = \sum_{i=1}^{n} \left(\frac{y_i - f(x_i, p)}{\delta y_i} \right)^2 \tag{A.5}$$

is as good as A.1 in determining fit parameters? Evaluating the x-error propagation through a single term of equation A.5

$$\left| \frac{1}{\left(\frac{y_i - -f(x_i,p)}{\delta y_i} \right)^2} \frac{\partial \left(\frac{y_i - f(x_i,p)}{\delta y_i} \right)^2}{\partial x_i} \delta x_i \right| \ll 1 \tag{A.6}$$

we have:

$$\left| \frac{\delta x_i}{\left(\frac{y_i - f(x_i,p)}{\delta y_i}\right)^2}(-2)\left(\frac{y_i - f(x_i,p)}{\delta y_i}\right)\frac{1}{\delta y_i}\frac{\partial f(x_i,p)}{\partial x_i}\right| = \\ = \frac{2\delta x_i}{\delta y_i\left(\frac{y_i - f(x_i,p)}{\delta y_i}\right)}\frac{\partial f(x_i,p)}{\partial x_i} \ll 1 \tag{A.7}$$

Considering that $\left(\frac{y_i - f(x_i,p)}{\delta y_i}\right) \sim 1$ the answer becomes:

$$\frac{\delta x_i}{\delta y_i}\frac{\partial f(x_i,p)}{\partial x_i} \ll 1 \tag{A.8}$$

Fig. A.1 shows intuitively what is happening: when this condition is met the x-error has little influence on the distance from the data point to the fit (case (a)), while in case (b) the two errors give similar contributions.

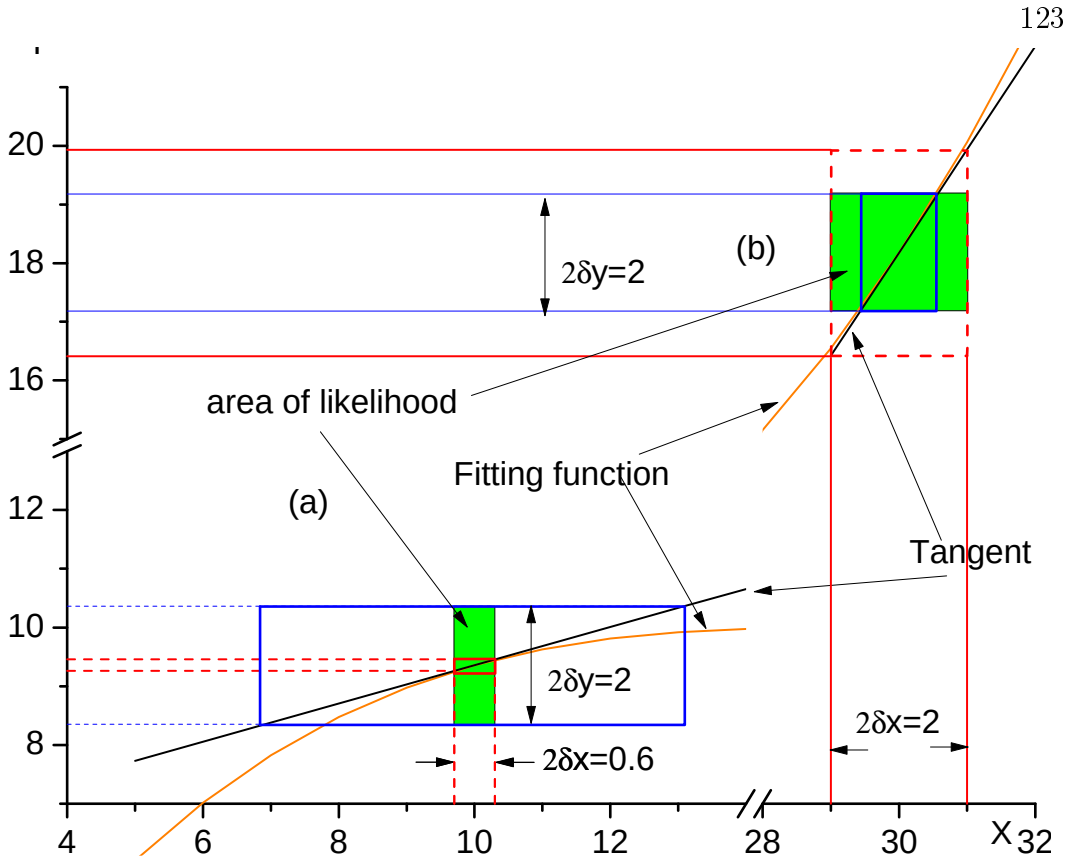

Fig. A.1: The rectangles show the the areas of uncertainty determined by the error of each vadiable, red for x blue for y. Shown in green is the area of likelihood determined by both uncertainties. In case (a) δx_i determines an area of uncertainty (innermost red rectangle) small compared to the area of likelihood, this translates into a small contribution to the maximum distance the experimental point can have from the fit and can be neglected, $\frac{dy}{dx} \sim 0.32 \ll \frac{\delta y_i}{\delta x_i} \sim 3.3$. In case (b) δx_i and δy_i contribute nearly equally and neither can be neglected, actually if δx_i is neglected an appropriate choice of $\bar{x}_i$ can completely compensate any error on y without any effect on the functional: the area of likelihood is completely contained in the red dashed rectangle. $\frac{dy}{dx} \sim 1.75 \sim \frac{\delta y_i}{\delta x_i} = 1$

A.2 Bi-square fitting

In this section is given an overview of the bi-square fitting method that has been employed widely in this analysis. More details may be found in [64] [65] [66].

A.2.1 Least square fitting

Least square (LS) fitting is a mathematical procedure for finding the best-fitting curve to a given set of points by minimizing the sum of the squares of the offsets ("the residuals") of the points from the curve. The sum of the **squares** of the offset has a substantial advantage over the absolute values because it allows the residuals to be treated as a continuous differentiable quantity. This advantage has the adverse effect that with a non-Gaussian distribution, or even Gaussian but bi or multi-modal distribution the outliers have a large weight in the functional which is minimized. For this specific reason alternative methods are often employed, Least Absolute Residuals (LAR), bi-square, and more. In particular bi-square is based on LS fitting but introducing weights w_i and iteration makes it possible to become insensitive to outliers.

$$\chi^2 = \sum_{i=1}^{n} w_i \left(\frac{y_i - f(x_i, p)}{\delta y_i} \right)^2 \tag{A.9}$$

A.2.2 Bi-Square iteration

In the first step LS is applied with all $w_i = 1$. From here the iteration starts:

1 - From the resulting residuals $\left(\frac{y_i - f(x_i,p)}{\delta y_i} \right) = r_i$, a new set of weights is evaluated:

$$w_i = \left(1 - (\frac{r_i}{6\,m})^2 \right)^2 \tag{A.10}$$

where m is the median absolute deviation of the residuals. This weighting is shown in Fig. A.2. Note that if $\frac{r_i}{6\,m} \geq 1$ then $w_i = 0$.

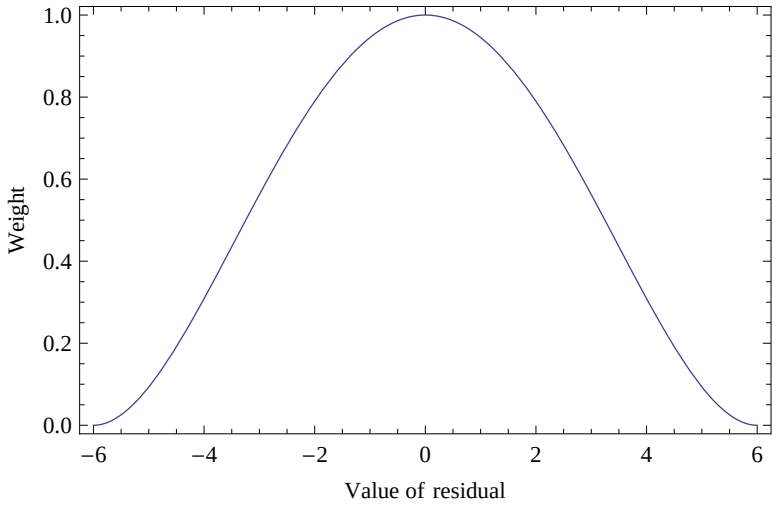

Fig. A.2: Bisquare weighting function with unitary median

2 - LS is applied, if the variation of parameters is less than the tolerance, $|\Delta p| \leq \delta p$, the process ends, otherwise return to item 1

Fig A.3 shows a flow diagram. This method provides an effective alternative to deleting specific points. Extreme outliers are deleted, but mild outliers are downweighted rather than deleted altogether. In the case of normally distributed data bi-square fitting has nearly the same behavior of LS fitting: for a Gaussian distribution the median absolute deviation relates to the standard deviation, $\sigma = 1.4826m \Rightarrow 6\,m \sim 4.04\,\sigma$ or a probability $P(|r| > 6\,m) \sim 6\,10^{-5}$.

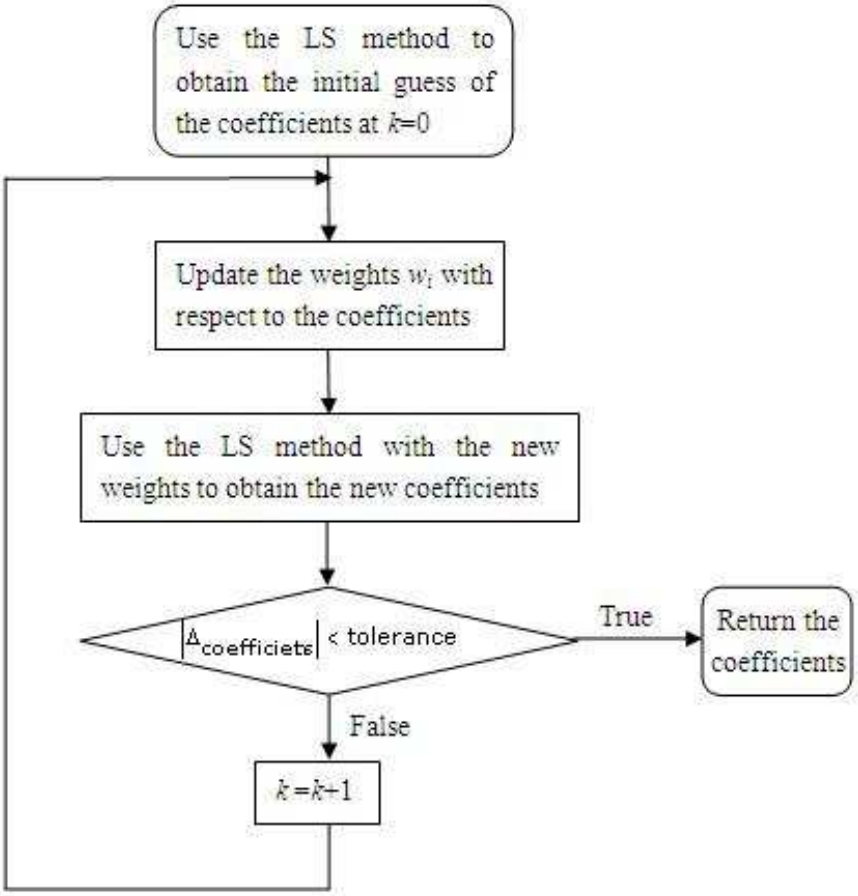

Fig. A.3: flow diagram of bi-square fitting

Appendix B

Table of assigned transitions of the $2^1\Sigma_u^+$ state from the $X^1\Sigma_g^+$

.

v'	Term Ev' (cm^{-1})	v"	Binding E	Line E (cm^{-1})	Amplitude	σ (cm^{-1})
15	16530.40	116	2.30	16532.70	0.24	0.33
15	16530.40	114	4.89	16535.29	0.51	0.32
15	16530.40	113	6.74	16537.14	0.43	0.32
18	16562.98	116	2.30	16565.28	0.46	0.27
18	16562.98	115	3.43	16566.41	0.45	0.27
18	16562.98	114	4.89	16567.87	0.85	0.23
21	16598.28	115	3.43	16601.71	1.66	0.24
21	16598.28	114	4.89	16603.17	3.00	0.28
21	16598.28	113	6.74	16605.02	1.37	0.30
21	16598.28	112	9.05	16607.33	2.50	0.33
21	16598.28	111	11.76	16610.04	0.25	0.33
21	16598.28	110	15.21	16613.49	0.54	0.22
22	16611.22	116	2.30	16613.52	0.44	0.20
22	16611.22	115	3.43	16614.65	1.30	0.29
22	16611.22	114	4.89	16616.11	1.81	0.26
22	16611.22	113	6.74	16617.96	0.90	0.26
22	16611.22	112	9.05	16620.27	2.30	0.31
23	16623.44	115	3.43	16626.87	1.27	0.39
23	16623.44	114	4.89	16628.33	1.09	0.38
23	16623.44	112	9.05	16632.49	0.87	0.27
24	16636.28	118	0.84	16637.12	0.21	0.19
24	16636.28	117	1.44	16637.72	0.18	0.38
24	16636.28	115	3.43	16639.71	3.37	0.26
24	16636.28	114	4.89	16641.17	3.99	0.33
24	16636.28	113	6.74	16643.02	1.10	0.31

v'	Term Ev' (cm^{-1})	v"	Binding E	Line E (cm^{-1})	Amplitude	σ (cm^{-1})
24	16636.28	112	9.05	16645.33	1.68	0.28
25	16649.33	116	2.30	16651.63	0.09	0.11
25	16649.33	115	3.43	16652.76	2.96	0.32
25	16649.33	114	4.89	16654.22	4.82	0.33
25	16649.33	113	6.74	16656.07	2.19	0.38
25	16649.33	112	9.05	16658.38	4.08	0.38
25	16649.33	111	11.76	16661.09	0.17	0.40
26	16662.43	114	4.89	16667.32	1.49	0.35
26	16662.43	113	6.74	16669.17	0.86	0.29
26	16662.43	112	9.05	16671.48	1.99	0.34
27	16675.68	118	0.84	16676.52	0.12	0.41
27	16675.68	115	3.43	16679.11	1.28	0.30
27	16675.68	114	4.89	16680.57	1.43	0.30
27	16675.68	113	6.74	16682.42	0.22	0.26
27	16675.68	112	9.05	16684.73	0.19	0.37
27	16675.68	111	11.76	16687.44	0.13	0.11
28	16689.03	116	2.30	16691.33	0.23	0.20
28	16689.03	115	3.43	16692.46	2.53	0.25
28	16689.03	114	4.89	16693.92	3.40	0.36
28	16689.03	113	6.74	16695.77	1.19	0.36
28	16689.03	112	9.05	16698.08	2.15	0.25
28	16689.03	110	15.21	16704.24	0.07	0.18
29	16702.58	118	0.84	16703.42	0.16	0.15
29	16702.58	115	3.43	16706.01	1.26	0.31
29	16702.58	114	4.89	16707.47	2.40	0.35
29	16702.58	113	6.74	16709.32	1.06	0.28
29	16702.58	112	9.05	16711.63	1.69	0.37
30	16716.37	115	3.43	16719.80	0.11	0.32
30	16716.37	114	4.89	16721.26	0.40	0.32
30	16716.37	113	6.74	16723.11	0.38	0.35
30	16716.37	112	9.05	16725.42	0.62	0.35
31	16730.22	118	0.84	16731.06	0.13	0.30
31	16730.22	114	4.89	16735.11	0.10	0.25
31	16730.22	113	6.74	16736.96	0.15	0.47
31	16730.22	112	9.05	16739.27	0.16	0.37
32	16743.93	116	2.30	16746.23	0.08	0.17
32	16743.93	115	3.43	16747.36	0.55	0.29
32	16743.93	114	4.89	16748.82	1.24	0.33
32	16743.93	113	6.74	16750.67	0.61	0.29
32	16743.93	112	9.05	16752.98	1.94	0.34
33	16757.98	115	3.43	16761.41	0.60	0.27

v'	Term Ev' (cm^{-1})	v"	Binding E	Line E (cm^{-1})	Amplitude	σ (cm^{-1})
33	16757.98	114	4.89	16762.87	1.40	0.38
33	16757.98	113	6.74	16764.72	1.21	0.33
33	16757.98	112	9.05	16767.03	2.15	0.29
34	16772.18	115	3.43	16775.61	0.99	0.38
34	16772.18	114	4.89	16777.07	1.20	0.30
34	16772.18	112	9.05	16781.23	0.64	0.21
35	16786.13	118	0.84	16786.97	0.29	0.24
35	16786.13	115	3.43	16789.56	3.00	0.34
35	16786.13	114	4.89	16791.02	4.69	0.36
35	16786.13	113	6.74	16792.87	1.22	0.29
35	16786.13	112	9.05	16795.18	1.19	0.18
35	16786.13	110	15.21	16801.34	0.10	0.24
36	16800.53	118	0.84	16801.37	0.14	0.34
36	16800.53	116	2.30	16802.83	0.14	0.19
36	16800.53	115	3.43	16803.96	1.28	0.33
36	16800.53	114	4.89	16805.42	2.70	0.37
36	16800.53	113	6.74	16807.27	0.77	0.33
36	16800.53	112	9.05	16809.58	1.56	0.30
37	16815.05	114	4.89	16819.94	0.49	0.46
37	16815.05	113	6.74	16821.79	0.36	0.43
37	16815.05	110	15.21	16830.26	0.10	0.47
38	16829.43	117	1.44	16830.87	0.24	0.26
38	16829.43	116	2.30	16831.73	0.10	0.43
38	16829.43	115	3.43	16832.86	0.74	0.29
38	16829.43	114	4.89	16834.32	1.80	0.28
38	16829.40	113	6.74	16836.14	0.47	0.25
38	16829.43	112	9.05	16838.48	0.79	0.39
39	16844.08	118	0.84	16844.92	0.10	0.13
39	16844.08	115	3.43	16847.51	2.18	0.29
39	16844.08	114	4.89	16848.97	3.10	0.33
39	16844.08	113	6.74	16850.82	1.75	0.32
39	16844.08	112	9.05	16853.13	3.47	0.33
40	16858.83	115	3.43	16862.26	0.39	0.24
40	16858.83	114	4.89	16863.72	1.96	0.26
40	16858.83	113	6.74	16865.57	1.45	0.32
40	16858.83	112	9.05	16867.88	2.87	0.36
40	16858.83	111	11.76	16870.59	0.43	0.21
40	16858.83	110	15.21	16874.04	0.37	0.20
41	16873.63	118	0.84	16874.47	0.22	0.36
41	16873.63	117	1.44	16875.07	0.19	0.20
41	16873.63	116	2.30	16875.93	0.22	0.30

v'	Term Ev' (cm^{-1})	v"	Binding E	Line E (cm^{-1})	Amplitude	σ (cm^{-1})
41	16873.63	115	3.43	16877.06	1.63	0.32
41	16873.63	114	4.89	16878.52	1.91	0.24
41	16873.63	113	6.74	16880.37	0.24	0.41
41	16873.63	112	9.05	16882.68	0.29	0.33
41	16873.63	111	11.76	16885.39	0.29	0.28
42	16888.33	115	3.43	16891.76	1.48	0.25
42	16888.33	114	4.89	16893.22	1.65	0.25
43	16903.45	115	3.43	16906.88	0.12	-0.33
43	16903.45	113	6.74	16910.19	0.25	0.22
43	16903.45	112	9.05	16912.50	1.87	0.31
43	16903.45	110	15.21	16918.66	0.15	0.44
44	16918.18	115	3.43	16921.61	1.52	0.29
44	16918.18	114	4.89	16923.07	1.88	0.30
44	16918.18	112	9.05	16927.23	0.33	0.33
45	16933.58	116	2.30	16935.88	0.42	0.41
45	16933.58	115	3.43	16937.01	3.19	0.30
45	16933.58	114	4.89	16938.47	4.70	0.38
45	16933.58	113	6.74	16940.32	1.53	0.33
45	16933.58	112	9.05	16942.63	2.70	0.31
46	16948.78	115	3.43	16952.21	1.89	0.30
46	16948.78	114	4.89	16953.67	3.17	0.39
46	16948.78	113	6.74	16955.52	1.74	0.32
46	16948.78	112	9.05	16957.83	2.45	0.22
47	16963.93	114	4.89	16968.82	0.25	0.18
47	16963.93	113	6.74	16970.67	0.13	0.22
47	16963.93	112	9.05	16972.98	0.22	0.18
48	16979.18	118	0.84	16980.02	0.11	0.33
48	16979.18	115	3.43	16982.61	0.82	0.28
48	16979.18	114	4.89	16984.07	1.56	0.34
48	16979.18	113	6.74	16985.92	0.63	0.36
48	16979.18	112	9.05	16988.23	1.47	0.26
49	16994.68	117	1.44	16996.12	0.09	0.13
49	16994.68	115	3.43	16998.11	0.83	0.44
49	16994.68	114	4.89	16999.57	3.01	0.40
49	16994.68	113	6.74	17001.42	1.49	0.39
49	16994.68	112	9.05	17003.73	2.74	0.28
50	17010.12	113	6.74	17016.86	0.20	0.34
50	17010.12	112	9.05	17019.17	0.26	0.43
50	17010.12	111	11.76	17021.88	0.08	0.16
51	17025.58	115	3.43	17029.01	0.40	0.24
51	17025.58	114	4.89	17030.47	0.41	0.32

v'	Term Ev' (cm^{-1})	v"	Binding E	Line E (cm^{-1})	Amplitude	σ (cm^{-1})
52	17041.03	118	0.84	17041.87	0.10	0.23
52	17041.03	113	6.74	17047.77	0.08	0.16
52	17041.03	112	9.05	17050.08	0.80	0.37
52	17041.03	111	11.76	17052.79	0.15	0.30
53	17056.71	115	3.43	17060.14	0.48	0.12
53	17056.71	112	9.05	17065.76	0.99	0.31
53	17056.71	111	11.76	17068.47	0.14	0.32
54	17072.18	118	0.84	17073.02	0.19	0.21
54	17072.18	115	3.43	17075.61	1.41	0.28
54	17072.18	114	4.89	17077.07	1.76	0.38
54	17072.18	113	6.74	17078.92	0.46	0.23
54	17072.18	111	11.76	17083.94	0.12	0.15
55	17087.93	116	2.30	17090.23	0.13	0.11
55	17087.93	115	3.43	17091.36	1.18	0.32
55	17087.93	114	4.89	17092.82	1.92	0.34
55	17087.93	113	6.74	17094.67	0.49	0.28
55	17087.93	112	9.05	17096.98	0.18	0.34
57	17119.83	115	3.43	17123.26	1.66	0.33
57	17119.83	114	4.89	17124.72	2.48	0.35
57	17119.83	113	6.74	17126.57	0.96	0.25
57	17119.83	112	9.05	17128.88	1.00	0.23
58	17135.43	117	1.44	17136.87	0.18	0.25
58	17135.43	116	2.30	17137.73	0.18	0.30
58	17135.43	115	3.43	17138.86	1.14	0.27
58	17135.43	114	4.89	17140.32	1.27	0.23
58	17135.43	113	6.74	17142.17	0.61	0.23
58	17135.43	112	9.05	17144.48	1.20	0.34
59	17151.43	112	9.05	17160.48	0.20	0.33
60	17167.23	114	4.89	17172.12	0.15	0.22
60	17167.23	113	6.74	17173.97	0.38	0.31
60	17167.23	112	9.05	17176.28	0.26	0.29
61	17183.05	115	3.43	17186.48	0.33	0.17
61	17183.05	114	4.89	17187.94	0.65	0.34
61	17183.05	113	6.74	17189.79	0.54	0.38
61	17183.05	112	9.05	17192.10	0.61	0.37
62	17199.40	115	3.43	17202.83	0.12	0.30
62	17199.40	113	6.74	17206.14	0.12	0.19
62	17199.40	112	9.05	17208.45	0.32	0.36
63	17215.65	118	0.84	17216.49	0.02	0.16
63	17215.65	117	1.44	17217.09	0.04	0.24
63	17215.65	116	2.30	17217.95	0.06	0.31

v'	Term Ev' (cm^{-1})	v"	Binding E	Line E (cm^{-1})	Amplitude	σ (cm^{-1})
63	17215.65	115	3.43	17219.08	0.22	0.26
63	17215.65	114	4.89	17220.54	0.12	0.24
63	17215.65	112	9.05	17224.70	0.12	0.24
63	17215.65	111	11.76	17227.41	0.03	0.24
64	17231.40	117	1.44	17232.84	0.11	0.22
64	17231.40	113	6.74	17238.14	0.34	0.24
65	17247.50	118	0.84	17248.34	0.08	0.25
65	17247.50	116	2.30	17249.80	0.10	0.22
65	17247.50	115	3.43	17250.93	0.36	0.29
65	17247.50	114	4.89	17252.39	0.21	0.27
66	17263.75	118	0.84	17264.59	0.12	0.11
66	17263.75	117	1.44	17265.19	0.21	0.17
66	17263.75	115	3.43	17267.18	0.62	0.31
66	17263.75	114	4.89	17268.64	0.86	0.33
66	17263.75	113	6.74	17270.49	0.40	0.42
67	17280.00	115	3.43	17283.43	0.18	0.46
67	17280.00	114	4.89	17284.89	0.17	0.35
68	17296.45	115	3.43	17299.88	0.46	0.40
68	17296.45	114	4.89	17301.34	0.58	0.21
69	17312.60	115	3.43	17316.03	0.53	0.29
69	17312.60	114	4.89	17317.49	0.99	0.39
69	17312.60	113	6.74	17319.34	0.54	0.41
70	17328.95	115	3.43	17332.38	0.23	0.29
70	17328.95	114	4.89	17333.84	0.53	0.39
70	17328.95	113	6.74	17335.69	0.28	0.31
70	17328.95	111	11.76	17340.71	0.14	0.31
71	17345.55	115	3.43	17348.98	0.21	0.20
71	17345.55	114	4.89	17350.44	0.44	0.32
71	17345.55	113	6.74	17352.29	0.18	0.30
72	17361.80	117	1.44	17363.24	0.08	0.23
72	17361.80	115	3.43	17365.23	0.48	0.37
72	17361.80	114	4.89	17366.69	0.99	0.31
72	17361.80	113	6.74	17368.54	0.78	0.50
73	17378.20	118	0.84	17379.04	0.18	0.17
73	17378.20	117	1.44	17379.64	0.18	0.23
73	17378.20	114	4.89	17383.09	0.23	0.24
73	17378.20	113	6.74	17384.94	0.43	0.33
74	17394.98	115	3.43	17398.41	0.20	0.23
74	17394.98	114	4.89	17399.87	0.10	0.17
74	17394.98	113	6.74	17401.72	0.30	0.29
75	17411.20	114	4.89	17416.09	0.58	0.35

v'	Term Ev' (cm^{-1})	v"	Binding E	Line E (cm^{-1})	Amplitude	σ (cm^{-1})
75	17411.20	113	6.74	17417.94	0.66	0.29
76	17427.63	115	3.43	17431.06	0.23	0.15
76	17427.63	113	6.74	17434.37	0.26	0.18
76	17427.63	112	9.05	17436.68	0.53	0.21
77	17444.01	115	3.43	17447.44	0.29	0.18
77	17444.01	114	4.89	17448.90	0.15	0.16
77	17444.01	112	9.05	17453.06	0.25	0.17
78	17460.86	116	2.30	17463.16	0.29	0.21
78	17460.86	115	3.43	17464.29	0.32	0.36
78	17460.86	113	6.74	17467.60	0.23	0.27
78	17460.86	112	9.05	17469.91	0.67	0.21
79	17477.53	115	3.43	17480.96	0.82	0.17
79	17477.53	114	4.89	17482.42	0.68	0.15
79	17477.53	112	9.05	17486.58	0.67	0.16
80	17493.93	115	3.43	17497.36	0.97	0.18
80	17493.93	114	4.89	17498.82	1.61	0.15
80	17493.93	113	6.74	17500.67	0.21	0.13
80	17493.93	112	9.05	17502.98	0.09	0.15
81	17511.01	118	0.84	17511.85	0.06	0.19
81	17511.01	116	2.30	17513.31	0.06	0.19
81	17511.01	115	3.43	17514.44	0.26	0.19
81	17511.01	114	4.89	17515.90	0.21	0.19
81	17511.01	113	6.74	17517.75	0.19	0.17
82	17527.78	115	3.43	17531.21	1.45	0.19
82	17527.78	114	4.89	17532.67	1.90	0.20
82	17527.78	113	6.74	17534.52	0.19	0.23
83	17544.78	115	3.43	17548.21	1.60	0.18
83	17544.78	114	4.89	17549.67	2.19	0.20
83	17544.78	113	6.74	17551.52	0.77	0.18
83	17544.78	112	9.05	17553.83	0.10	0.14
84	17561.98	116	2.30	17564.28	0.11	0.16
84	17561.98	115	3.43	17565.41	0.39	0.26
84	17561.98	114	4.89	17566.87	0.56	0.19
84	17561.98	112	9.05	17571.03	0.13	0.19
84	17561.98	111	11.76	17573.74	0.08	0.16
85	17578.18	115	3.43	17581.61	1.00	0.17
85	17578.18	114	4.89	17583.07	2.19	0.18
85	17578.18	113	6.74	17584.92	0.71	0.20
85	17578.18	112	9.05	17587.23	0.18	0.15
86	17595.13	115	3.43	17598.56	0.96	0.17
86	17595.13	114	4.89	17600.02	2.50	0.18

v'	Term Ev' (cm^{-1})	v"	Binding E	Line E (cm^{-1})	Amplitude	σ (cm^{-1})
86	17595.13	113	6.74	17601.87	0.97	0.22
86	17595.13	112	9.05	17604.18	0.60	0.19
87	17611.68	114	4.89	17616.57	0.59	0.17
87	17611.68	113	6.74	17618.42	0.32	0.25
88	17628.58	115	3.43	17632.01	0.64	0.18
88	17628.58	114	4.89	17633.47	1.43	0.18
88	17628.58	113	6.74	17635.32	1.10	0.18
88	17628.58	112	9.05	17637.63	0.66	0.21
89	17645.43	115	3.43	17648.86	0.18	0.19
89	17645.43	114	4.89	17650.32	1.69	0.17
89	17645.43	113	6.74	17652.17	0.88	0.18
89	17645.43	112	9.05	17654.48	1.27	0.19
90	17662.00	113	6.74	17668.74	0.34	0.19
90	17662.00	112	9.05	17671.05	0.28	0.20
91	17678.58	114	4.89	17683.47	0.65	0.20
91	17678.58	113	6.74	17685.32	0.61	0.20
91	17678.58	112	9.05	17687.63	0.76	0.22
92	17695.23	115	3.43	17698.66	0.13	0.20
92	17695.23	114	4.89	17700.12	0.13	0.19
92	17695.23	113	6.74	17701.97	0.53	0.19
92	17695.23	112	9.05	17704.28	0.80	0.18
92	17695.23	110	15.21	17710.44	0.37	0.19
93	17711.58	115	3.43	17715.01	0.37	0.15
93	17711.58	113	6.74	17718.32	0.17	0.19
93	17711.58	112	9.05	17720.63	0.62	0.19
94	17728.58	114	4.89	17733.47	0.14	0.19
94	17728.58	113	6.74	17735.32	0.55	0.19
94	17728.58	112	9.05	17737.63	1.26	0.22
95	17745.38	115	3.43	17748.81	0.58	0.22
95	17745.38	114	4.89	17750.27	0.30	0.17
95	17745.38	113	6.74	17752.12	0.08	0.19
95	17745.38	112	9.05	17754.43	0.83	0.19
96	17762.13	115	3.43	17765.56	0.60	0.14
96	17762.13	114	4.89	17767.02	0.48	0.17
96	17762.13	112	9.05	17771.18	0.82	0.18
97	17779.03	115	3.43	17782.46	0.33	0.17
97	17779.03	114	4.89	17783.92	0.10	0.19
97	17779.03	113	6.74	17785.77	0.30	0.15
97	17779.03	112	9.05	17788.08	1.66	0.21
98	17795.88	115	3.43	17799.31	1.42	0.19
98	17795.88	114	4.89	17800.77	1.88	0.19

v'	Term Ev' (cm^{-1})	v"	Binding E	Line E (cm^{-1})	Amplitude	σ (cm^{-1})
98	17795.88	113	6.74	17802.62	0.10	0.17
98	17795.88	112	9.05	17804.93	0.28	0.23
99	17812.81	115	3.43	17816.24	0.65	0.18
99	17812.81	114	4.89	17817.70	0.98	0.17
99	17812.81	112	9.05	17821.86	0.49	0.21
100	17829.83	115	3.43	17833.26	0.57	0.17
100	17829.83	114	4.89	17834.72	0.60	0.20
100	17829.83	112	9.05	17838.88	0.84	0.17
101	17846.78	115	3.43	17850.21	1.21	0.19
101	17846.78	114	4.89	17851.67	2.06	0.18
101	17846.78	113	6.74	17853.52	0.59	0.17
102	17863.63	115	3.43	17867.06	0.31	0.20
102	17863.63	114	4.89	17868.52	0.78	0.20
102	17863.63	113	6.74	17870.37	0.09	0.17
102	17863.63	112	9.05	17872.68	0.33	0.18
103	17880.33	115	3.43	17883.76	0.69	0.18
103	17880.33	114	4.89	17885.22	1.45	0.17
103	17880.33	113	6.74	17887.07	0.31	0.17
103	17880.33	112	9.05	17889.38	0.11	0.26
104	17897.13	115	3.43	17900.56	0.64	0.16
104	17897.13	114	4.89	17902.02	2.36	0.16
104	17897.13	113	6.74	17903.87	0.66	0.20
104	17897.13	112	9.05	17906.18	0.17	0.22
105	17914.03	114	4.89	17918.92	0.51	0.14
105	17914.03	113	6.74	17920.77	0.21	0.21
106	17930.73	115	3.43	17934.16	0.45	0.17
106	17930.73	114	4.89	17935.62	1.82	0.16
106	17930.73	113	6.74	17937.47	0.84	0.15
106	17930.73	112	9.05	17939.78	0.15	0.14
107	17947.58	115	3.43	17951.01	0.22	0.13
107	17947.58	114	4.89	17952.47	1.14	0.16
107	17947.58	113	6.74	17954.32	0.68	0.18
107	17947.58	112	9.05	17956.63	0.40	0.15
108	17964.53	114	4.89	17969.42	0.50	0.20
108	17964.53	113	6.74	17971.27	0.48	0.19
108	17964.53	112	9.05	17973.58	0.10	0.14
109	17981.28	115	3.43	17984.71	0.28	0.15
109	17981.28	114	4.89	17986.17	1.42	0.17
109	17981.28	113	6.74	17988.02	1.05	0.18
109	17981.28	112	9.05	17990.33	0.64	0.17
110	17998.13	115	3.43	18001.56	0.09	0.18

v'	Term Ev' (cm^{-1})	v"	Binding E	Line E (cm^{-1})	Amplitude	σ (cm^{-1})
110	17998.13	114	4.89	18003.02	0.43	0.16
110	17998.13	113	6.74	18004.87	0.56	0.21
110	17998.13	112	9.05	18007.18	0.36	0.19
110	17998.13	111	11.76	18009.89	0.09	0.23
111	18014.98	115	3.43	18018.41	0.10	0.12
111	18014.98	114	4.89	18019.87	0.23	0.18
111	18014.98	113	6.74	18021.72	0.73	0.18
111	18014.98	112	9.05	18024.03	0.78	0.24
112	18031.88	114	4.89	18036.77	0.74	0.18
112	18031.88	113	6.74	18038.62	0.88	0.18
112	18031.88	112	9.05	18040.93	1.31	0.21
113	18048.68	118	0.84	18049.52	0.11	0.27
113	18048.68	115	3.43	18052.11	0.71	0.17
113	18048.68	114	4.89	18053.57	0.09	0.12
113	18048.68	113	6.74	18055.42	0.29	0.19
113	18048.68	112	9.05	18057.73	0.61	0.19
114	18065.38	115	3.43	18068.81	0.18	0.15
114	18065.38	113	6.74	18072.12	0.58	0.18
114	18065.38	112	9.05	18074.43	1.12	0.22
115	18082.30	115	3.43	18085.73	0.59	0.18
115	18082.30	113	6.74	18089.04	0.39	0.16
115	18082.30	112	9.05	18091.35	1.11	0.18
116	18098.98	115	3.43	18102.41	1.01	0.20
116	18098.98	114	4.89	18103.87	0.69	0.17
116	18098.98	112	9.05	18108.03	0.77	0.16
117	18115.73	115	3.43	18119.16	0.29	0.17
117	18115.73	113	6.74	18122.47	0.37	0.20
117	18115.73	112	9.05	18124.78	1.27	0.20
118	18132.58	115	3.43	18136.01	0.85	0.23
118	18132.58	114	4.89	18137.47	0.94	0.21
118	18132.58	112	9.05	18141.63	0.96	0.18
119	18149.23	115	3.43	18152.66	0.73	0.16
119	18149.23	114	4.89	18154.12	0.82	0.16
119	18149.23	112	9.05	18158.28	1.08	0.19
120	18165.98	115	3.43	18169.41	0.47	0.15
120	18165.98	114	4.89	18170.87	0.52	0.17
120	18165.98	112	9.05	18175.03	1.06	0.19
121	18182.63	115	3.43	18186.06	0.92	0.18
121	18182.63	114	4.89	18187.52	1.26	0.20
121	18182.63	113	6.74	18189.37	0.12	0.17
121	18182.63	112	9.05	18191.68	0.38	0.21

v'	Term Ev' (cm^{-1})	v"	Binding E	Line E (cm^{-1})	Amplitude	σ (cm^{-1})
122	18199.58	116	2.30	18201.88	0.23	0.15
122	18199.58	115	3.43	18203.01	0.34	0.10
122	18199.58	114	4.89	18204.47	0.56	0.19

Appendix C

Table of assigned transitions of the $3^1\Sigma_g$ state from the $a^3\Sigma_u^+$ state

v'	Term Ev' (cm^{-1})	v''	Binding E	Line E (cm^{-1})	Amplitude	σ (cm^{-1})
52	16377.02	32	3.242	16380.3	0.617	0.136
52	16377.02	33	2.186	16379.2	0.851	0.367
52	16377.02	34	1.385	16378.4	0.452	0.379
52	16377.02	35	0.806	16377.8	0.259	0.071
56	16440.87	31	4.580	16445.4	3.400	0.155
56	16440.87	32	3.242	16444.1	3.600	0.205
58	16472.99	32	3.242	16476.2	0.186	0.193
58	16472.99	33	2.186	16475.2	3.407	0.188
58	16472.99	34	1.385	16474.4	2.688	0.205
58	16472.99	35	0.806	16473.8	0.477	0.229
60	16507.23	31	4.580	16511.8	0.276	0.328
60	16507.23	32	3.242	16510.5	4.742	0.499
60	16507.23	33	2.186	16509.4	2.833	0.262
60	16507.23	34	1.385	16508.6	0.407	0.290
61	16523.18	32	3.242	16526.4	0.203	0.188
61	16523.18	33	2.186	16525.4	0.969	0.178
61	16523.18	34	1.385	16524.6	0.994	0.161
61	16523.18	35	0.806	16524.0	0.101	0.204
61	16523.18	36	0.416	16523.6	0.100	0.200
63	16556.41	32	3.242	16559.7	0.349	0.179
63	16556.41	33	2.186	16558.6	2.891	0.182
63	16556.41	34	1.385	16557.8	5.973	0.196
63	16556.41	35	0.806	16557.2	0.805	0.179
65	16589.70	31	4.580	16594.3	0.919	0.180
65	16589.70	32	3.242	16592.9	5.505	0.174
65	16589.70	33	2.186	16591.9	14.457	0.223
65	16589.70	34	1.385	16591.1	1.100	0.279
66	16606.47	32	3.242	16609.7	0.169	0.298
66	16606.47	33	2.186	16608.7	1.008	0.379

v'	Term Ev' (cm^{-1})	v"	Binding E	Line E (cm^{-1})	Amplitude	σ (cm^{-1})
66	16606.47	34	1.385	16607.9	2.244	0.217
66	16606.47	35	0.806	16607.3	2.636	0.352
67	16623.19	32	3.242	16626.4	0.626	0.113
67	16623.19	33	2.186	16625.4	1.236	0.129
67	16623.19	34	1.385	16624.6	5.569	0.109
67	16623.19	35	0.806	16624.0	1.965	0.179
68	16639.03	32	3.242	16642.3	0.402	0.167
68	16639.03	33	2.186	16641.2	1.343	0.111
68	16639.03	34	1.385	16640.4	4.065	0.147
68	16639.03	35	0.806	16639.8	2.109	0.136
69	16654.11	34	1.385	16655.5	2.889	0.204
69	16654.11	35	0.806	16654.9	3.185	0.204
70	16670.98	32	3.242	16674.2	0.079	0.129
70	16670.98	33	2.186	16673.2	0.732	0.219
70	16670.98	34	1.385	16672.4	1.412	0.196
70	16670.98	35	0.806	16671.8	0.929	0.152
70	16670.98	36	0.416	16671.4	0.582	0.134
71	16686.31	32	3.242	16689.6	0.580	0.230
71	16686.31	33	2.186	16688.5	3.682	0.295
71	16686.31	34	1.385	16687.7	4.495	0.258
71	16686.31	35	0.806	16687.1	0.559	0.546
72	16702.39	32	3.242	16705.6	1.057	0.262
72	16702.39	33	2.186	16704.6	2.527	0.397
72	16702.39	34	1.385	16703.8	2.558	0.377
73	16719.09	32	3.242	16722.3	0.320	0.210
73	16719.09	33	2.186	16721.3	3.957	0.256
73	16719.09	34	1.385	16720.5	5.397	0.316
73	16719.09	35	0.806	16719.9	0.489	0.465
74	16737.61	32	3.242	16740.9	0.002	0.134
74	16737.61	33	2.186	16739.8	0.464	0.164
74	16737.61	34	1.385	16739.0	0.374	0.235
75	16754.67	33	2.186	16756.9	0.211	0.089
75	16754.67	34	1.385	16756.1	0.581	0.083
76	16772.04	32	3.242	16775.3	0.099	0.116
76	16772.04	33	2.186	16774.2	1.393	0.210
76	16772.04	34	1.385	16773.4	3.333	0.226
76	16772.04	35	0.806	16772.8	0.717	0.244
77	16790.02	32	3.242	16793.3	0.068	0.138
77	16790.02	33	2.186	16792.2	0.695	0.217
77	16790.02	34	1.385	16791.4	0.804	0.195
77	16790.02	35	0.806	16790.8	0.158	0.193

v'	Term Ev' (cm^{-1})	v"	Binding E	Line E (cm^{-1})	Amplitude	σ (cm^{-1})
79	16822.98	32	3.242	16826.2	0.240	0.133
79	16822.98	33	2.186	16825.2	0.868	0.146
79	16822.98	34	1.385	16824.4	1.583	0.132
79	16822.98	35	0.806	16823.8	0.277	0.133
81	16858.02	33	2.186	16860.2	1.113	0.219
81	16858.02	34	1.385	16859.4	0.612	0.281
82	16875.49	32	3.242	16878.7	0.120	0.387
82	16875.49	33	2.186	16877.7	1.388	0.281
82	16875.49	34	1.385	16876.9	2.225	0.171
82	16875.49	35	0.806	16876.3	0.357	0.965
83	16893.17	32	3.242	16896.4	0.313	0.102
83	16893.17	34	1.385	16894.6	0.608	0.170
83	16893.17	35	0.806	16894.0	0.840	0.118
83	16893.17	36	0.416	16893.6	0.500	0.100
84	16908.98	32	3.242	16912.2	0.395	0.091
84	16908.98	33	2.186	16911.2	2.986	0.265
84	16908.98	34	1.385	16910.4	3.260	0.203
84	16908.98	35	0.806	16909.8	0.274	0.290
85	16925.24	32	3.242	16928.5	3.600	0.284
85	16925.24	33	2.186	16927.4	3.376	0.284
85	16925.24	34	1.385	16926.6	0.593	0.284
86	16940.95	33	2.186	16943.1	1.246	0.205
86	16940.95	34	1.385	16942.3	0.644	0.157
88	16977.73	32	3.242	16981.0	0.299	0.128
88	16977.73	33	2.186	16979.9	0.861	0.126
89	16994.48	33	2.186	16996.7	1.051	0.150
89	16994.48	34	1.385	16995.9	0.610	0.108
90	17010.17	32	3.242	17013.4	0.322	0.058
90	17010.17	33	2.186	17012.4	0.125	0.142
90	17010.17	34	1.385	17011.6	1.043	0.092
90	17010.17	35	0.806	17011.0	0.801	0.152
92	17047.65	32	3.242	17050.9	0.323	0.113
92	17047.65	33	2.186	17049.8	0.797	0.095
92	17047.65	34	1.385	17049.0	4.841	0.127
92	17047.65	35	0.806	17048.5	0.250	0.097
93	17065.35	32	3.242	17068.6	0.606	0.171
93	17065.35	34	1.385	17066.7	0.915	0.144
95	17101.25	32	3.242	17104.5	1.030	0.124
95	17101.25	33	2.186	17103.4	2.257	0.168
96	17118.60	32	3.242	17121.8	0.500	0.095
96	17118.60	33	2.186	17120.8	0.389	0.115

v'	Term Ev' (cm^{-1})	v"	Binding E	Line E (cm^{-1})	Amplitude	σ (cm^{-1})
96	17118.60	34	1.385	17120.0	0.300	0.081
96	17118.60	35	0.806	17119.4	0.200	0.081
96	17118.60	36	0.416	17119.0	0.200	0.081
97	17135.47	33	2.186	17137.7	1.293	0.111
97	17135.47	34	1.385	17136.9	0.563	0.134
97	17135.47	35	0.806	17136.3	0.451	0.107
98	17152.58	35	0.806	17153.4	0.367	0.170
98	17152.58	36	0.416	17153.0	0.824	0.071
98	17152.58	37	0.178	17152.8	1.545	0.109
98	17152.58	38	0.054	17152.6	0.155	0.123
99	17169.72	32	3.242	17173.0	0.525	0.077
99	17169.72	33	2.186	17171.9	1.119	0.104
99	17169.72	34	1.385	17171.1	0.949	0.108
99	17169.72	35	0.806	17170.5	0.223	0.138
100	17187.18	32	3.242	17190.4	1.041	0.132
100	17187.18	33	2.186	17189.4	0.353	0.277
102	17221.48	33	2.186	17223.7	0.760	0.182
102	17221.48	34	1.385	17222.9	0.613	0.230
102	17221.48	35	0.806	17222.3	0.282	0.291
105	17274.04	32	3.242	17277.3	0.496	0.081
105	17274.04	33	2.186	17276.2	1.258	0.134
105	17274.04	34	1.385	17275.4	0.708	0.331
105	17274.04	35	0.806	17274.8	0.182	0.144
107	17308.80	32	3.242	17312.0	0.282	0.324
107	17308.80	33	2.186	17311.0	3.090	0.212
107	17308.80	34	1.385	17310.2	2.925	0.212
109	17344.13	32	3.242	17347.4	0.360	0.129
109	17344.13	33	2.186	17346.3	1.651	0.151
109	17344.13	34	1.385	17345.5	1.551	0.190
109	17344.13	35	0.806	17344.9	0.158	0.188
110	17362.13	32	3.242	17365.4	0.080	0.079
110	17362.13	33	2.186	17364.3	0.891	0.238
110	17362.13	34	1.385	17363.5	1.218	0.147
110	17362.13	35	0.806	17362.9	0.271	0.333
112	17399.04	32	3.242	17402.3	0.556	0.273
112	17399.04	33	2.186	17401.2	3.579	0.196
112	17399.04	34	1.385	17400.4	4.018	0.206
112	17399.04	35	0.806	17399.8	0.640	0.104
113	17416.81	34	1.385	17418.2	0.601	0.306
113	17416.81	35	0.806	17417.6	0.628	0.253
113	17416.81	36	0.416	17417.2	0.182	0.105

v'	Term Ev' (cm^{-1})	v"	Binding E	Line E (cm^{-1})	Amplitude	σ (cm^{-1})
113	17416.81	37	0.178	17417.0	0.626	0.277
113	17416.81	38	0.054	17416.9	0.331	0.872
114	17434.75	33	2.186	17436.9	0.306	0.169
114	17434.75	34	1.385	17436.1	0.931	0.170
114	17434.75	35	0.806	17435.6	0.621	0.179
114	17434.75	36	0.416	17435.2	1.250	0.163
114	17434.75	37	0.178	17434.9	0.301	0.160
114	17434.75	38	0.054	17434.8	0.305	0.160
114	17434.75	39	0.007	17434.8	0.405	0.160
115	17452.86	32	3.242	17456.1	0.203	0.530
115	17452.86	33	2.186	17455.0	0.644	0.487
115	17452.86	34	1.385	17454.2	0.102	0.118
116	17471.26	32	3.242	17474.5	0.087	0.296
116	17471.26	33	2.186	17473.4	0.260	0.298
116	17471.26	35	0.806	17472.1	0.144	0.188
117	17488.47	33	2.186	17490.7	0.197	0.168
117	17488.47	34	1.385	17489.9	0.097	0.108
117	17488.47	35	0.806	17489.3	0.105	0.423
117	17488.47	36	0.416	17488.9	0.197	0.161
117	17488.47	38	0.054	17488.5	0.073	0.120
120	17541.58	32	3.242	17544.8	0.285	0.207
120	17541.58	33	2.186	17543.8	0.894	0.367
120	17541.58	34	1.385	17543.0	0.872	0.224
120	17541.58	35	0.806	17542.4	0.293	0.149
120	17541.58	36	0.416	17542.0	0.200	0.200
122	17575.84	34	1.385	17577.2	2.543	0.255
122	17575.84	35	0.806	17576.6	2.663	0.353
122	17575.84	36	0.416	17576.3	1.671	0.193
122	17575.84	37	0.178	17576.0	0.065	0.157
126	17642.66	35	0.806	17643.5	1.808	0.139
126	17642.66	36	0.416	17643.1	2.592	0.102
126	17642.66	37	0.178	17642.8	1.147	0.065
126	17642.66	38	0.054	17642.7	0.702	0.135
126	17642.66	39	0.007	17642.7	0.150	0.250
127	17661.74	32	3.242	17665.0	0.840	0.170
127	17661.74	33	2.186	17663.9	5.193	0.184
127	17661.74	34	1.385	17663.1	3.252	0.168
129	17695.80	32	3.242	17699.0	1.995	0.184
129	17695.80	33	2.186	17698.0	3.845	0.233
129	17695.80	34	1.385	17697.2	2.043	0.173
129	17695.80	35	0.806	17696.6	1.664	0.158

v'	Term Ev' (cm^{-1})	v"	Binding E	Line E (cm^{-1})	Amplitude	σ (cm^{-1})
130	17712.37	32	3.242	17715.6	2.044	0.329
130	17712.37	33	2.186	17714.6	4.632	0.313
130	17712.37	34	1.385	17713.8	1.218	0.204
131	17729.44	32	3.242	17732.7	0.624	0.267
131	17729.44	33	2.186	17731.6	2.086	0.250
131	17729.44	34	1.385	17730.8	-0.000	0.089
131	17729.44	35	0.806	17730.2	0.396	0.289
132	17746.29	32	3.242	17749.5	1.129	0.391
132	17746.29	33	2.186	17748.5	4.041	0.402
132	17746.29	34	1.385	17747.7	0.037	0.269
132	17746.29	35	0.806	17747.1	0.282	0.208
133	17763.24	32	3.242	17766.5	1.006	0.153
133	17763.24	33	2.186	17765.4	4.374	0.155
133	17763.24	34	1.385	17764.6	1.302	0.141
133	17763.24	35	0.806	17764.0	0.715	0.101
133	17763.24	36	0.416	17763.7	0.301	0.101
134	17780.31	32	3.242	17783.5	3.635	0.203
134	17780.31	33	2.186	17782.5	2.427	0.387
134	17780.31	34	1.385	17781.7	0.553	0.302
134	17780.31	35	0.806	17781.1	0.100	0.149
135	17797.72	32	3.242	17801.0	0.414	0.189
135	17797.72	33	2.186	17799.9	2.373	0.388
135	17797.72	34	1.385	17799.1	5.065	0.314
135	17797.72	35	0.806	17798.5	0.888	0.360
136	17814.41	32	3.242	17817.7	0.366	0.280
136	17814.41	33	2.186	17816.6	2.736	0.360
136	17814.41	34	1.385	17815.8	3.125	0.257
136	17814.41	35	0.806	17815.2	0.759	0.159
137	17830.63	33	2.186	17832.8	1.508	0.251
137	17830.63	34	1.385	17832.0	1.093	0.223
137	17830.63	35	0.806	17831.4	0.527	0.101
138	17848.46	32	3.242	17851.7	0.181	0.278
138	17848.46	33	2.186	17850.6	2.879	0.255
138	17848.46	34	1.385	17849.8	1.849	0.248
138	17848.46	35	0.806	17849.3	0.199	0.211
139	17865.30	32	3.242	17868.5	0.256	0.186
139	17865.30	33	2.186	17867.5	1.103	0.305
139	17865.30	34	1.385	17866.7	0.923	0.328
139	17865.30	35	0.806	17866.1	0.642	0.197
140	17882.20	33	2.186	17884.4	1.183	0.422
140	17882.20	34	1.385	17883.6	0.697	0.207

v'	Term Ev' (cm^{-1})	v"	Binding E	Line E (cm^{-1})	Amplitude	σ (cm^{-1})
141	17898.92	32	3.242	17902.2	0.059	0.418
141	17898.92	33	2.186	17901.1	2.194	0.302
141	17898.92	34	1.385	17900.3	1.097	0.185
142	17915.28	32	3.242	17918.5	0.264	0.302
142	17915.28	33	2.186	17917.5	1.363	0.321
142	17915.28	34	1.385	17916.7	0.524	0.163
142	17915.28	35	0.806	17916.1	0.000	0.297
143	17932.00	32	3.242	17935.2	0.529	0.460
144	17949.91	33	2.186	17952.1	0.034	0.277
144	17949.91	34	1.385	17951.3	0.525	0.175
144	17949.91	35	0.806	17950.7	0.322	0.331
145	17965.90	32	3.242	17969.1	1.020	0.320
145	17965.90	33	2.186	17968.1	1.787	0.262
145	17965.90	34	1.385	17967.3	0.149	0.108
145	17965.90	35	0.806	17966.7	0.087	0.093
146	17983.45	34	1.385	17984.8	1.004	0.167
146	17983.45	35	0.806	17984.3	0.134	0.052
147	18000.34	33	2.186	18002.5	1.667	0.322
147	18000.34	34	1.385	18001.7	4.839	0.227
147	18000.34	35	0.806	18001.1	0.675	0.375
148	18017.36	32	3.242	18020.6	0.216	0.151
148	18017.36	33	2.186	18019.5	1.143	0.147
148	18017.36	34	1.385	18018.7	4.841	0.208
148	18017.36	35	0.806	18018.2	0.501	0.145
148	18017.36	36	0.416	18017.8	0.701	0.151
148	18017.36	37	0.178	18017.5	0.181	0.101
148	18017.36	38	0.054	18017.4	0.181	0.101
149	18034.02	32	3.242	18037.3	0.436	0.195
149	18034.02	33	2.186	18036.2	0.803	0.247
149	18034.02	34	1.385	18035.4	3.205	0.190
149	18034.02	35	0.806	18034.8	0.282	0.137
150	18051.11	32	3.242	18054.3	0.180	0.629
150	18051.11	33	2.186	18053.3	2.676	0.214
150	18051.11	34	1.385	18052.5	5.488	0.224
150	18051.11	35	0.806	18051.9	1.645	0.187
150	18051.11	36	0.416	18051.5	1.100	0.200
151	18067.15	32	3.242	18070.4	0.505	0.412
151	18067.15	33	2.186	18069.3	3.648	0.281
151	18067.15	34	1.385	18068.5	0.433	0.198
151	18067.15	35	0.806	18068.0	0.181	0.071
152	18084.69	32	3.242	18087.9	0.138	0.206

v'	Term Ev' (cm^{-1})	v"	Binding E	Line E (cm^{-1})	Amplitude	σ (cm^{-1})
152	18084.69	33	2.186	18086.9	1.673	0.288
152	18084.69	34	1.385	18086.1	1.984	0.205
152	18084.69	35	0.806	18085.5	0.714	0.276
152	18084.69	36	0.416	18085.1	0.353	0.120
152	18084.69	37	0.178	18084.9	0.305	0.120
152	18084.69	38	0.054	18084.7	0.155	0.120
153	18102.21	33	2.186	18104.4	2.519	0.188
153	18102.21	34	1.385	18103.6	1.201	0.207
153	18102.21	35	0.806	18103.0	2.669	0.229
153	18102.21	36	0.416	18102.6	2.012	0.132
153	18102.21	37	0.178	18102.4	0.000	0.038
154	18118.35	32	3.242	18121.6	0.179	0.053
154	18118.35	33	2.186	18120.5	1.193	0.230
154	18118.35	34	1.385	18119.7	2.465	0.151
154	18118.35	35	0.806	18119.2	0.441	0.469
155	18135.26	32	3.242	18138.5	0.446	0.094
155	18135.26	33	2.186	18137.4	0.767	0.208
155	18135.26	34	1.385	18136.6	1.693	0.228
155	18135.26	35	0.806	18136.1	0.758	0.194
156	18152.02	33	2.186	18154.2	0.478	0.196
156	18152.02	34	1.385	18153.4	0.737	0.224
156	18152.02	35	0.806	18152.8	0.264	0.169
157	18168.75	33	2.186	18170.9	1.059	0.282
157	18168.75	34	1.385	18170.1	1.478	0.195
157	18168.75	35	0.806	18169.6	0.422	0.157
158	18185.57	32	3.242	18188.8	0.345	0.196
158	18185.57	33	2.186	18187.8	1.523	0.233
158	18185.57	34	1.385	18187.0	1.877	0.223
158	18185.57	35	0.806	18186.4	0.903	0.109
158	18185.57	36	0.416	18186.0	0.900	0.109

Appendix D

Table of assigned transitions of the A series of the $2^3\Pi_g$ state from the $a^3\Sigma_u^+$ state

v'	Term Ev' (cm^{-1})	v''	Binding E	Line E (cm^{-1})	Amplitude	σ (cm^{-1})
5	16434.05	34	1.385	16435.4	0.898	0.125
5	16434.05	35	0.806	16434.9	0.535	0.237
5	16434.05	36	0.416	16434.5	0.328	0.094
5	16434.05	37	0.178	16434.2	0.000	0.059
5	16434.05	38	0.054	16434.1	0.287	0.128
5	16434.05	39	0.007	16434.1	0.073	0.186
6	16468.94	32	3.240	16472.2	1.224	0.243
6	16468.94	33	2.186	16471.1	10.773	0.270
6	16468.94	34	1.385	16470.3	11.400	0.281
6	16468.94	36	0.416	16469.4	0.639	0.231
6	16468.94	38	0.054	16469.0	0.000	0.434
7	16499.29	33	2.186	16501.5	6.482	0.255
7	16499.29	34	1.385	16500.7	6.601	0.308
7	16499.29	36	0.416	16499.7	0.888	0.088
7	16499.29	37	0.007	16499.3	0.404	0.400
8	16532.60	33	2.186	16534.8	1.171	0.376
8	16532.60	34	1.385	16534.0	7.023	0.333
8	16532.60	35	0.806	16533.4	9.186	0.289
8	16532.60	36	0.416	16533.0	5.088	0.128
8	16532.60	37	0.178	16532.8	0.947	0.076
8	16532.60	38	0.054	16532.7	1.436	0.089
8	16532.60	39	0.007	16532.6	0.897	0.636
9	16564.54	32	3.240	16567.8	1.178	0.169
9	16564.54	33	2.186	16566.7	8.751	0.317
9	16564.54	34	1.385	16565.9	11.111	0.289
9	16564.54	35	0.806	16565.4	1.474	0.337
9	16564.54	36	0.416	16565.0	0.323	0.222
9	16564.54	37	0.178	16564.7	0.000	0.307
9	16564.54	38	0.054	16564.6	0.379	0.060

v'	Term Ev' (cm^{-1})	v"	Binding E	Line E (cm^{-1})	Amplitude	σ (cm^{-1})
10	16597.22	32	3.240	16600.5	1.334	0.142
10	16597.22	33	2.186	16599.4	4.104	0.261
10	16597.22	34	1.385	16598.6	2.039	0.174
10	16597.22	35	0.806	16598.0	0.162	0.328
11	16629.75	32	3.240	16633.0	0.949	0.231
11	16629.75	33	2.186	16631.9	5.765	0.338
11	16629.75	34	1.385	16631.1	6.822	0.270
11	16629.75	35	0.806	16630.6	0.418	0.087
11	16629.75	36	0.416	16630.2	0.308	0.227
11	16629.75	38	0.054	16629.8	0.678	0.089
12	16661.79	32	3.240	16665.0	0.715	0.321
12	16661.79	33	2.186	16664.0	5.314	0.276
12	16661.79	34	1.385	16663.2	5.541	0.267
12	16661.79	35	0.806	16662.6	0.914	0.136
12	16661.79	36	0.416	16662.2	0.490	0.179
12	16661.79	39	0.007	16661.8	0.199	0.079
13	16695.09	32	3.240	16698.3	0.080	0.260
13	16695.09	34	1.385	16696.5	0.024	0.134
13	16695.09	35	0.806	16695.9	0.176	0.231
13	16695.09	36	0.416	16695.5	0.187	0.102
13	16695.09	38	0.054	16695.1	0.000	0.150
13	16695.09	39	0.007	16695.1	0.001	0.144
14	16727.25	34	1.385	16728.6	1.896	0.233
14	16727.25	35	0.806	16728.1	1.295	0.375
14	16727.25	36	0.416	16727.7	2.926	0.224
14	16727.25	37	0.178	16727.4	0.000	0.606
14	16727.25	39	0.007	16727.3	0.581	0.111
15	16758.20	33	2.186	16760.4	2.910	0.327
15	16758.20	34	1.385	16759.6	3.729	0.243
15	16758.20	35	0.806	16759.0	0.336	0.147
16	16790.02	32	3.240	16793.3	0.070	0.153
16	16790.02	33	2.186	16792.2	0.699	0.217
16	16790.02	34	1.385	16791.4	0.807	0.199
16	16790.02	35	0.806	16790.8	0.165	0.159
16	16790.02	36	0.416	16790.4	0.034	0.142
16	16790.02	37	0.178	16790.2	0.017	0.065
17	16822.63	32	3.240	16825.9	0.174	0.121
17	16822.63	33	2.186	16824.8	0.765	0.151
17	16822.63	34	1.385	16824.0	1.581	0.144
17	16822.63	35	0.806	16823.4	0.506	0.183
17	16822.63	36	0.416	16823.0	0.200	0.069

v'	Term Ev' (cm^{-1})	v"	Binding E	Line E (cm^{-1})	Amplitude	σ (cm^{-1})
17	16822.63	37	0.178	16822.8	0.200	0.065
18	16853.79	32	3.240	16857.0	0.179	0.141
18	16853.79	33	2.186	16856.0	1.134	0.334
18	16853.79	34	1.385	16855.2	2.010	0.290
18	16853.79	35	0.806	16854.6	1.575	0.273
18	16853.79	36	0.416	16854.2	1.049	0.252
19	16885.75	34	1.385	16887.1	0.816	0.210
19	16885.75	35	0.806	16886.6	0.507	0.310
19	16885.75	36	0.416	16886.2	0.736	0.225
19	16885.75	37	0.178	16885.9	0.215	0.054
19	16885.75	38	0.054	16885.8	0.025	0.616
19	16885.75	39	0.007	16885.8	0.405	0.552
20	16917.40	32	3.240	16920.6	0.111	0.141
20	16917.40	33	2.186	16919.6	3.415	0.130
20	16917.40	34	1.385	16918.8	1.112	0.092
20	16917.40	35	0.806	16918.2	0.242	0.117
21	16948.60	31	4.570	16953.2	0.306	0.250
21	16948.60	32	3.240	16951.8	0.280	0.117
21	16948.60	33	2.186	16950.8	2.008	0.106
21	16948.60	34	1.385	16950.0	2.897	0.229
21	16948.60	35	0.806	16949.4	0.544	0.192
21	16948.60	36	0.416	16949.0	0.364	0.106
21	16948.60	37	0.178	16948.8	0.000	0.171
21	16948.60	39	0.007	16948.6	0.280	0.297
22	16978.90	33	2.186	16981.1	0.318	0.092
22	16978.90	34	1.385	16980.3	0.872	0.131
22	16978.90	35	0.806	16979.7	1.623	0.119
22	16978.90	37	0.178	16979.1	0.000	0.133
22	16978.90	38	0.054	16978.9	0.000	0.117
22	16978.90	39	0.007	16978.9	1.112	0.087
23	17010.23	33	2.186	17012.4	0.190	0.172
23	17010.23	34	1.385	17011.6	0.827	0.125
23	17010.23	35	0.806	17011.0	0.890	0.178
23	17010.23	36	0.416	17010.6	1.194	0.090
23	17010.23	37	0.178	17010.4	0.727	0.104
23	17010.23	38	0.054	17010.3	0.135	0.083
23	17010.23	39	0.007	17010.2	0.241	0.175
24	17041.62	35	0.806	17042.4	0.408	0.141
24	17041.62	36	0.416	17042.0	0.550	0.091
24	17041.62	37	0.178	17041.8	0.838	0.071
25	17072.07	32	3.242	17075.3	0.000	0.189

v'	Term Ev' (cm^{-1})	v"	Binding E	Line E (cm^{-1})	Amplitude	σ (cm^{-1})
25	17072.07	33	2.186	17074.3	1.588	0.154
25	17072.07	34	1.385	17073.5	2.855	0.177
25	17072.07	35	0.806	17072.9	4.030	0.183
25	17072.07	36	0.416	17072.5	0.468	0.111
25	17072.07	37	0.178	17072.3	0.568	0.076
26	17103.17	33	2.186	17105.4	0.480	0.138
26	17103.17	34	1.385	17104.6	0.801	0.071
26	17103.17	35	0.806	17104.0	3.601	0.155
26	17103.17	36	0.416	17103.6	1.272	0.087
26	17103.17	37	0.178	17103.4	2.052	0.139
26	17103.17	38	0.054	17103.2	0.302	0.167
26	17103.17	39	0.007	17103.2	0.000	0.057
27	17132.97	33	2.186	17135.2	4.502	0.170
27	17132.97	34	1.385	17134.4	4.574	0.122
29	17194.72	34	1.385	17196.1	0.456	0.253
29	17194.72	35	0.806	17195.5	1.152	0.127
29	17194.72	36	0.416	17195.1	0.779	0.079
29	17194.72	37	0.178	17194.9	0.439	0.053
29	17194.72	39	0.007	17194.7	0.000	0.052
30	17225.04	33	2.186	17227.2	2.651	0.343
30	17225.04	34	1.385	17226.4	2.260	0.241
31	17255.31	33	2.186	17257.5	0.762	0.235
31	17255.31	34	1.385	17256.7	0.652	0.514
31	17255.31	35	0.806	17256.1	5.338	0.176
31	17255.31	36	0.416	17255.7	0.000	0.163
31	17255.31	37	0.178	17255.5	2.786	0.157
31	17255.31	38	0.054	17255.4	2.451	0.073
31	17255.31	39	0.007	17255.3	1.534	0.292
32	17284.12	32	3.242	17287.4	0.409	0.187
32	17284.12	33	2.186	17286.3	2.441	0.239
32	17284.12	34	1.385	17285.5	1.697	0.217
32	17284.12	35	0.806	17284.9	0.298	0.153
32	17284.12	36	0.416	17284.5	0.526	0.222
32	17284.12	37	0.178	17284.3	0.000	0.259
32	17284.12	38	0.054	17284.2	0.000	0.174
32	17284.12	39	0.007	17284.1	0.300	0.146
33	17313.89	33	2.186	17316.1	1.342	0.139
33	17313.89	34	1.385	17315.3	3.042	0.169
33	17313.89	35	0.806	17314.7	0.816	0.171
33	17313.89	36	0.416	17314.3	3.471	0.155
33	17313.89	38	0.054	17313.9	0.000	0.207

v'	Term Ev' (cm^{-1})	v"	Binding E	Line E (cm^{-1})	Amplitude	σ (cm^{-1})
33	17313.89	39	0.007	17313.9	0.000	0.107
34	17344.12	33	2.186	17346.3	1.655	0.157
34	17344.12	34	1.385	17345.5	1.551	0.191
34	17344.12	35	0.806	17344.9	0.478	0.090
34	17344.12	36	0.416	17344.5	0.385	0.164
34	17344.12	37	0.178	17344.3	0.000	0.070
35	17373.49	32	3.242	17376.7	0.498	0.290
35	17373.49	33	2.186	17375.7	5.154	0.198
35	17373.49	34	1.385	17374.9	4.899	0.154
35	17373.49	35	0.806	17374.3	0.481	0.126
35	17373.49	36	0.416	17373.9	0.536	0.124
35	17373.49	37	0.178	17373.7	0.068	0.125
36	17402.96	35	0.806	17403.8	0.633	0.173
36	17402.96	36	0.416	17403.4	0.932	0.081
36	17402.96	37	0.178	17403.1	0.050	0.056
36	17402.96	38	0.054	17403.0	0.000	0.248
36	17402.96	39	0.007	17403.0	0.247	0.387
37	17432.41	32	3.242	17435.7	0.762	0.171
37	17432.41	33	2.186	17434.6	0.648	0.174
38	17461.76	33	2.186	17463.9	0.599	0.275
38	17461.76	34	1.385	17463.1	1.221	0.253
38	17461.76	35	0.806	17462.6	0.372	0.207
38	17461.76	36	0.416	17462.2	0.385	0.175
38	17461.76	37	0.178	17461.9	0.129	0.151
38	17461.76	38	0.054	17461.8	0.072	0.164
38	17461.76	39	0.007	17461.8	0.054	0.187
39	17490.89	33	2.186	17493.1	0.398	0.384
39	17490.89	34	1.385	17492.3	0.799	0.326
39	17490.89	35	0.806	17491.7	0.398	0.195
39	17490.89	36	0.416	17491.3	0.588	0.239
39	17490.89	38	0.054	17490.9	0.085	0.083
39	17490.89	39	0.007	17490.9	0.059	0.089
40	17520.25	32	3.242	17523.5	3.164	0.284
40	17520.25	33	2.186	17522.4	3.151	0.293
40	17520.25	34	1.385	17521.6	0.568	0.216
41	17548.66	30	6.226	17554.9	0.557	0.406
41	17548.66	31	4.580	17553.2	1.096	0.402
41	17548.66	32	3.242	17551.9	3.478	0.446
41	17548.66	33	2.186	17550.8	0.673	0.460
42	17577.88	31	4.580	17582.5	0.084	0.150
42	17577.88	32	3.242	17581.1	2.697	0.524

v'	Term Ev' (cm^{-1})	v"	Binding E	Line E (cm^{-1})	Amplitude	σ (cm^{-1})
42	17577.88	33	2.186	17580.1	1.598	0.356
42	17577.88	35	0.806	17578.7	0.053	0.092
42	17577.88	36	0.416	17578.3	0.585	0.185
43	17606.17	33	2.186	17608.4	0.265	0.304
43	17606.17	34	1.385	17607.6	0.429	0.183
43	17606.17	35	0.806	17607.0	0.632	0.147
43	17606.17	36	0.416	17606.6	2.189	0.198
43	17606.17	37	0.178	17606.3	0.301	0.154
43	17606.17	38	0.054	17606.2	0.458	0.154
43	17606.17	39	0.007	17606.2	0.750	0.153
44	17635.41	32	3.242	17638.7	2.810	0.211
44	17635.41	33	2.186	17637.6	1.911	0.265
44	17635.41	34	1.385	17636.8	0.145	0.233
44	17635.41	35	0.806	17636.2	0.162	0.252
45	17664.19	31	4.580	17668.8	1.612	0.263
45	17664.19	32	3.242	17667.4	4.735	0.297
45	17664.19	33	2.186	17666.4	7.602	0.217
45	17664.19	34	1.385	17665.6	1.037	0.133
45	17664.19	35	0.806	17665.0	0.854	0.115
45	17664.19	36	0.416	17664.6	0.335	0.103
45	17664.19	37	0.178	17664.4	1.287	0.082
45	17664.19	38	0.054	17664.2	0.351	0.189
46	17691.95	36	0.416	17692.4	4.849	0.114
46	17691.95	37	0.178	17692.1	3.550	0.070
46	17691.95	38	0.054	17692.0	0.308	0.056
46	17691.95	39	0.007	17692.0	3.579	0.095
47	17719.31	33	2.186	17721.5	1.159	0.204
47	17719.31	34	1.385	17720.7	4.409	0.203
47	17719.31	35	0.806	17720.1	3.596	0.223
47	17719.31	36	0.416	17719.7	4.705	0.166
47	17719.31	37	0.178	17719.5	0.933	0.227
48	17748.18	33	2.186	17750.4	0.283	0.246
48	17748.18	34	1.385	17749.6	1.450	0.193
48	17748.18	35	0.806	17749.0	2.768	0.197
48	17748.18	36	0.416	17748.6	3.129	0.148
48	17748.18	39	0.007	17748.2	3.622	0.202
49	17775.69	34	1.385	17777.1	0.351	0.269
49	17775.69	35	0.806	17776.5	0.692	0.406
49	17775.69	36	0.416	17776.1	0.509	0.182
50	17804.12	35	0.806	17804.9	0.390	0.165
50	17804.12	37	0.178	17804.3	0.000	0.376

v'	Term Ev' (cm^{-1})	v"	Binding E	Line E (cm^{-1})	Amplitude	σ (cm^{-1})
50	17804.12	38	0.054	17804.2	0.597	0.281
51	17831.51	34	1.385	17832.9	2.816	0.231
51	17831.51	35	0.806	17832.3	2.588	0.241
51	17831.51	36	0.416	17831.9	1.451	0.177
51	17831.51	37	0.178	17831.7	0.957	0.142
51	17831.51	38	0.054	17831.6	0.226	0.159
52	17859.11	34	1.385	17860.5	3.203	0.236
52	17859.11	35	0.806	17859.9	3.800	0.359
52	17859.11	36	0.416	17859.5	2.837	0.247
52	17859.11	37	0.178	17859.3	0.000	0.542
52	17859.11	38	0.054	17859.2	0.445	0.553
53	17886.74	34	1.385	17888.1	3.805	0.221
53	17886.74	35	0.806	17887.5	3.895	0.313
53	17886.74	36	0.416	17887.2	2.369	0.207
53	17886.74	39	0.007	17886.8	1.079	0.147
54	17914.04	34	1.385	17915.4	2.746	0.242
54	17914.04	35	0.806	17914.8	1.699	0.198
54	17914.04	36	0.416	17914.5	1.616	0.222
54	17914.04	39	0.007	17914.0	0.087	0.190
56	17967.78	33	2.186	17970.0	1.001	0.311
56	17967.78	34	1.385	17969.2	0.866	0.170
56	17967.78	35	0.806	17968.6	0.654	0.411
56	17967.78	36	0.416	17968.2	1.010	0.093
56	17967.78	37	0.178	17968.0	1.174	0.121
56	17967.78	38	0.054	17967.8	0.279	0.437
57	17994.69	33	2.186	17996.9	4.092	0.239
57	17994.69	34	1.385	17996.1	5.083	0.233
57	17994.69	35	0.806	17995.5	0.751	0.127
57	17994.69	36	0.416	17995.1	0.567	0.129
57	17994.69	38	0.054	17994.7	0.000	0.486
58	18021.51	32	3.242	18024.8	0.556	0.181
58	18021.51	33	2.186	18023.7	4.483	0.218
58	18021.51	34	1.385	18022.9	4.887	0.244
58	18021.51	35	0.806	18022.3	0.322	0.322
59	18048.31	34	1.385	18049.7	4.974	0.264
59	18048.31	35	0.806	18049.1	0.079	0.083
60	18074.84	33	2.186	18077.0	1.948	0.241
60	18074.84	34	1.385	18076.2	1.854	0.314
60	18074.84	35	0.806	18075.6	0.333	0.113
60	18074.84	36	0.416	18075.3	0.112	0.206
61	18101.51	33	2.186	18103.7	1.200	0.265

v'	Term Ev' (cm^{-1})	v"	Binding E	Line E (cm^{-1})	Amplitude	σ (cm^{-1})
61	18101.51	34	1.385	18102.9	1.426	0.235
61	18101.51	35	0.806	18102.3	0.857	0.188
61	18101.51	36	0.416	18101.9	0.000	0.054
61	18101.51	39	0.007	18101.5	0.023	0.053
62	18127.32	33	2.186	18129.5	1.617	0.286
62	18127.32	34	1.385	18128.7	2.586	0.183
62	18127.32	36	0.416	18127.7	0.024	0.394
62	18127.32	37	0.178	18127.5	0.249	0.182
62	18127.32	38	0.054	18127.4	0.000	0.090
63	18153.44	32	3.242	18156.7	4.424	0.199
63	18153.44	33	2.186	18155.6	3.496	0.188
63	18153.44	34	1.385	18154.8	3.031	0.201
63	18153.44	35	0.806	18154.2	0.884	0.136
63	18153.44	38	0.054	18153.5	0.755	0.127
63	18153.44	39	0.007	18153.4	1.738	0.132
64	18179.44	33	2.186	18181.6	3.315	0.238
64	18179.44	34	1.385	18180.8	2.499	0.241
64	18179.44	35	0.806	18180.3	1.329	0.085

Appendix E

Table of assigned transitions of the B series of the $2^3\Pi_g$ state from the $a^3\Sigma_u^+$ state

v'	Term Ev' (cm^{-1})	v''	Binding E	Line E (cm^{-1})	Amplitude	σ (cm^{-1})
5	16442.60	32	3.242	16445.8	3.170	0.284
5	16442.60	33	2.186	16444.8	9.692	0.181
5	16442.60	34	1.385	16444.0	3.795	0.216
5	16442.60	35	0.806	16443.4	1.032	0.138
5	16442.60	36	0.416	16443.0	0.631	0.230
6	16476.06	32	3.240	16479.3	3.594	0.436
6	16476.06	33	2.186	16478.2	12.847	0.463
6	16476.06	34	1.385	16477.4	3.967	0.173
6	16476.06	35	0.806	16476.9	1.124	0.365
6	16476.06	36	0.416	16476.5	0.000	0.547
6	16476.06	37	0.178	16476.2	0.000	0.173
6	16476.06	38	0.054	16476.1	0.724	0.109
7	16509.03	33	2.186	16511.2	1.563	0.255
7	16509.03	34	1.385	16510.4	4.455	0.388
7	16509.03	36	0.416	16509.4	2.802	0.227
7	16509.03	37	0.178	16509.2	0.084	0.395
8	16541.45	32	3.242	16544.7	0.699	0.308
8	16541.45	33	2.186	16543.6	6.212	0.288
8	16541.45	34	1.385	16542.8	8.320	0.326
8	16541.45	36	0.416	16541.9	1.880	0.143
8	16541.45	37	0.178	16541.6	1.890	0.164
9	16573.49	33	2.186	16575.7	0.327	0.458
9	16573.49	34	1.385	16574.9	1.060	0.206
9	16573.49	36	0.416	16573.9	0.643	0.221
9	16573.49	37	0.178	16573.7	0.059	0.128
9	16573.49	38	0.054	16573.5	0.000	0.434
10	16606.39	33	2.186	16608.6	0.902	0.216
10	16606.39	34	1.385	16607.8	2.850	0.278
10	16606.39	35	0.806	16607.2	2.303	0.184

v'	Term Ev' (cm^{-1})	v"	Binding E	Line E (cm^{-1})	Amplitude	σ (cm^{-1})
10	16606.39	36	0.416	16606.8	0.650	0.159
11	16638.66	32	3.240	16641.9	0.465	0.141
11	16638.66	33	2.186	16640.8	2.265	0.094
11	16638.66	34	1.385	16640.0	2.143	0.158
11	16638.66	35	0.806	16639.5	0.801	0.180
11	16638.66	36	0.416	16639.1	0.580	0.162
11	16638.66	37	0.178	16638.8	0.404	0.128
11	16638.66	39	0.007	16638.7	2.377	0.186
12	16670.99	32	3.240	16674.2	0.080	0.168
12	16670.99	33	2.186	16673.2	0.652	0.287
12	16670.99	34	1.385	16672.4	1.406	0.199
12	16670.99	35	0.806	16671.8	0.902	0.132
12	16670.99	36	0.416	16671.4	0.651	0.127
12	16670.99	37	0.178	16671.2	0.254	0.145
12	16670.99	38	0.054	16671.0	0.250	0.199
12	16670.99	39	0.007	16671.0	0.092	0.107
13	16703.36	33	2.186	16705.5	1.059	0.281
13	16703.36	34	1.385	16704.7	2.253	0.238
13	16703.36	35	0.806	16704.2	2.629	0.293
13	16703.36	36	0.416	16703.8	1.103	0.191
13	16703.36	37	0.178	16703.5	0.588	0.204
13	16703.36	38	0.054	16703.4	0.607	0.162
13	16703.36	39	0.007	16703.4	0.500	0.491
14	16735.18	34	1.385	16736.6	3.103	0.166
14	16735.18	35	0.806	16736.0	2.202	0.193
14	16735.18	36	0.416	16735.6	1.447	0.235
14	16735.18	37	0.178	16735.4	0.000	0.091
15	16767.04	34	1.385	16768.4	0.167	0.232
15	16767.04	35	0.806	16767.8	0.227	0.114
15	16767.04	36	0.416	16767.5	0.180	0.363
15	16767.04	37	0.178	16767.2	0.048	0.116
15	16767.04	38	0.054	16767.1	0.060	0.057
16	16798.58	33	2.186	16800.8	1.791	0.409
16	16798.58	34	1.385	16800.0	4.967	0.206
16	16798.58	35	0.806	16799.4	2.852	0.214
16	16798.58	36	0.416	16799.0	1.179	0.274
16	16798.58	37	0.178	16798.8	0.000	0.126
17	16830.87	33	2.186	16833.1	1.195	0.539
17	16830.87	34	1.385	16832.3	4.568	0.453
17	16830.87	35	0.806	16831.7	1.162	0.218
17	16830.87	36	0.416	16831.3	3.384	0.261

v'	Term Ev' (cm^{-1})	v"	Binding E	Line E (cm^{-1})	Amplitude	σ (cm^{-1})
17	16830.87	38	0.054	16830.9	0.910	0.096
18	16862.07	33	2.186	16864.3	0.094	0.274
18	16862.07	34	1.385	16863.5	0.770	0.424
18	16862.07	35	0.806	16862.9	1.217	0.277
18	16862.07	36	0.416	16862.5	0.358	0.093
18	16862.07	37	0.178	16862.2	0.320	0.171
18	16862.07	38	0.054	16862.1	1.204	0.259
19	16892.98	35	0.806	16893.8	1.286	0.096
19	16892.98	36	0.416	16893.4	0.510	0.107
19	16892.98	37	0.178	16893.2	0.310	0.101
19	16892.98	38	0.054	16893.0	0.200	0.103
19	16892.98	39	0.007	16893.0	0.440	0.102
20	16924.69	35	0.806	16925.5	3.421	0.235
20	16924.69	36	0.416	16925.1	0.000	0.186
20	16924.69	37	0.178	16924.9	2.451	0.151
21	16955.52	33	2.186	16957.7	0.584	0.554
21	16955.52	34	1.385	16956.9	5.095	0.231
21	16955.52	35	0.806	16956.3	4.602	0.174
21	16955.52	36	0.416	16955.9	4.040	0.233
22	16987.15	33	2.186	16989.3	0.161	0.137
22	16987.15	34	1.385	16988.5	0.797	0.290
22	16987.15	35	0.806	16988.0	0.829	0.344
22	16987.15	36	0.416	16987.6	0.833	0.107
22	16987.15	37	0.178	16987.3	0.625	0.061
22	16987.15	38	0.054	16987.2	0.000	0.054
22	16987.15	39	0.007	16987.2	0.000	0.054
23	17017.72	35	0.806	17018.5	1.212	0.278
23	17017.72	37	0.178	17017.9	0.865	0.095
23	17017.72	38	0.054	17017.8	0.548	0.232
23	17017.72	39	0.007	17017.7	1.377	0.062
24	17049.34	35	0.806	17050.2	0.898	0.099
24	17049.34	36	0.416	17049.8	3.340	0.082
24	17049.34	37	0.178	17049.5	3.885	0.113
24	17049.34	39	0.007	17049.4	1.000	0.091
25	17079.75	33	2.186	17081.9	0.413	0.167
25	17079.75	34	1.385	17081.1	2.167	0.105
25	17079.75	35	0.806	17080.6	4.060	0.174
25	17079.75	36	0.416	17080.2	3.918	0.085
25	17079.75	37	0.178	17079.9	4.506	0.141
25	17079.75	38	0.054	17079.8	0.000	0.172
25	17079.75	39	0.007	17079.8	0.000	0.270

v'	Term Ev' (cm^{-1})	v"	Binding E	Line E (cm^{-1})	Amplitude	σ (cm^{-1})
26	17110.14	37	0.178	17110.3	0.309	0.107
26	17110.14	39	0.007	17110.1	1.283	0.191
27	17140.51	36	0.416	17140.9	0.175	0.090
27	17140.51	38	0.054	17140.6	0.000	0.077
27	17140.51	39	0.007	17140.5	0.231	0.057
28	17170.67	34	1.385	17172.1	1.063	0.137
28	17170.67	35	0.806	17171.5	1.363	0.133
28	17170.67	36	0.416	17171.1	0.815	0.132
28	17170.67	38	0.054	17170.7	0.369	0.117
28	17170.67	39	0.007	17170.7	0.152	0.121
29	17200.62	34	1.385	17202.0	1.010	0.119
29	17200.62	35	0.806	17201.4	5.812	0.117
29	17200.62	36	0.416	17201.0	0.501	0.103
29	17200.62	37	0.178	17200.8	2.875	0.091
29	17200.62	38	0.054	17200.7	0.865	0.091
29	17200.62	39	0.007	17200.6	2.795	0.095
30	17231.08	36	0.416	17231.5	1.747	0.116
30	17231.08	37	0.178	17231.3	1.266	0.053
30	17231.08	38	0.054	17231.1	0.422	0.123
30	17231.08	39	0.007	17231.1	0.563	0.078
31	17261.54	35	0.806	17262.3	0.677	0.186
31	17261.54	36	0.416	17262.0	0.101	0.082
31	17261.54	37	0.178	17261.7	0.608	0.063
31	17261.54	38	0.054	17261.6	0.614	0.084
32	17291.11	33	2.186	17293.3	0.496	0.111
32	17291.11	34	1.385	17292.5	0.153	0.114
32	17291.11	35	0.806	17291.9	0.620	0.091
32	17291.11	36	0.416	17291.5	0.510	0.069
32	17291.11	38	0.054	17291.2	0.213	0.074
32	17291.11	39	0.007	17291.1	0.608	0.115
33	17321.42	35	0.806	17322.2	2.340	0.118
33	17321.42	36	0.416	17321.8	1.488	0.131
33	17321.42	37	0.178	17321.6	0.645	0.147
33	17321.42	39	0.007	17321.4	1.039	0.143
34	17351.40	35	0.806	17352.2	2.813	0.159
34	17351.40	36	0.416	17351.8	0.833	0.063
34	17351.40	37	0.178	17351.6	2.166	0.095
34	17351.40	38	0.054	17351.5	0.000	0.095
34	17351.40	39	0.007	17351.4	0.647	0.100
35	17380.85	35	0.806	17381.7	0.000	0.134
35	17380.85	36	0.416	17381.3	0.982	0.165

v'	Term Ev' (cm^{-1})	v"	Binding E	Line E (cm^{-1})	Amplitude	σ (cm^{-1})
35	17380.85	37	0.178	17381.0	0.204	0.118
35	17380.85	38	0.054	17380.9	0.060	0.155
35	17380.85	39	0.007	17380.9	0.268	0.079
36	17410.70	35	0.806	17411.5	0.098	0.316
36	17410.70	36	0.416	17411.1	0.236	0.179
36	17410.70	39	0.007	17410.7	0.312	0.132
37	17440.04	34	1.385	17441.4	0.093	0.196
37	17440.04	35	0.806	17440.8	0.070	0.172
37	17440.04	36	0.416	17440.5	0.191	0.296
37	17440.04	37	0.178	17440.2	0.014	0.100
37	17440.04	38	0.054	17440.1	0.174	0.228
37	17440.04	39	0.007	17440.0	0.295	0.278
38	17469.72	33	2.186	17471.9	0.036	0.307
38	17469.72	34	1.385	17471.1	0.285	0.202
38	17469.72	35	0.806	17470.5	1.421	0.167
38	17469.72	36	0.416	17470.1	1.375	0.171
38	17469.72	37	0.178	17469.9	0.450	0.151
38	17469.72	39	0.007	17469.7	1.433	0.185
39	17498.34	33	2.186	17500.5	0.148	0.150
39	17498.34	34	1.385	17499.7	1.167	0.246
39	17498.34	35	0.806	17499.1	2.259	0.247
39	17498.34	36	0.416	17498.8	1.193	0.133
39	17498.34	37	0.178	17498.5	1.363	0.135
39	17498.34	38	0.054	17498.4	0.386	0.133
39	17498.34	39	0.007	17498.3	0.829	0.215
40	17528.08	32	3.242	17531.3	0.789	0.182
40	17528.08	33	2.186	17530.3	1.413	0.187
41	17556.29	33	2.186	17558.5	0.547	0.317
41	17556.29	34	1.385	17557.7	1.505	0.336
41	17556.29	35	0.806	17557.1	1.040	0.179
41	17556.29	36	0.416	17556.7	0.627	0.132
41	17556.29	37	0.178	17556.5	0.042	0.136
41	17556.29	38	0.054	17556.3	0.112	0.246
41	17556.29	39	0.007	17556.3	0.393	0.311
42	17585.25	33	2.186	17587.4	0.168	0.241
42	17585.25	36	0.416	17585.7	0.405	0.166
43	17613.81	34	1.385	17615.2	0.482	0.210
43	17613.81	35	0.806	17614.6	0.173	0.391
43	17613.81	36	0.416	17614.2	0.187	0.236
43	17613.81	37	0.178	17614.0	0.746	0.579
43	17613.81	38	0.054	17613.9	0.350	0.211

v'	Term Ev' (cm^{-1})	v"	Binding E	Line E (cm^{-1})	Amplitude	σ (cm^{-1})
44	17642.50	34	1.385	17643.9	2.904	0.169
44	17642.50	35	0.806	17643.3	1.005	0.167
44	17642.50	36	0.416	17642.9	0.984	0.150
44	17642.50	37	0.178	17642.7	0.378	0.125
44	17642.50	38	0.054	17642.6	0.316	0.120
45	17671.21	34	1.385	17672.6	1.205	0.187
45	17671.21	35	0.806	17672.0	1.101	0.147
45	17671.21	36	0.416	17671.6	1.931	0.119
45	17671.21	37	0.178	17671.4	1.333	0.113
45	17671.21	38	0.054	17671.3	2.633	0.124
46	17699.60	36	0.416	17700.0	2.134	0.103
46	17699.60	39	0.007	17699.6	1.993	0.172
47	17727.56	34	1.385	17728.9	0.117	0.411
47	17727.56	35	0.806	17728.4	1.091	0.339
47	17727.56	36	0.416	17728.0	0.085	0.055
47	17727.56	37	0.178	17727.7	0.000	0.301
47	17727.56	38	0.054	17727.6	0.893	0.265
49	17784.17	34	1.385	17785.6	0.354	0.293
49	17784.17	36	0.416	17784.6	1.131	0.177
49	17784.17	38	0.054	17784.2	2.553	0.239
50	17811.69	34	1.385	17813.1	0.786	0.208
50	17811.69	35	0.806	17812.5	1.407	0.209
50	17811.69	36	0.416	17812.1	3.369	0.219
50	17811.69	39	0.007	17811.7	2.734	0.196
51	17839.05	33	2.186	17841.2	0.400	0.494
51	17839.05	34	1.385	17840.4	2.457	0.302
51	17839.05	35	0.806	17839.9	2.670	0.311
51	17839.05	36	0.416	17839.5	1.552	0.290
51	17839.05	37	0.178	17839.2	0.000	0.676
51	17839.05	38	0.054	17839.1	1.908	0.152
52	17866.59	35	0.806	17867.4	1.164	0.355
52	17866.59	36	0.416	17867.0	0.060	0.091
52	17866.59	37	0.178	17866.8	0.152	0.177
52	17866.59	38	0.054	17866.6	0.658	0.229
53	17894.14	34	1.385	17895.5	0.205	0.284
53	17894.14	35	0.806	17894.9	0.096	0.120
53	17894.14	36	0.416	17894.6	0.000	0.237
53	17894.14	38	0.054	17894.2	0.276	0.355
53	17894.14	39	0.007	17894.1	0.195	0.104
54	17921.51	36	0.416	17921.9	0.678	0.155
54	17921.51	37	0.178	17921.7	0.000	0.148

v'	Term Ev' (cm^{-1})	v"	Binding E	Line E (cm^{-1})	Amplitude	σ (cm^{-1})
54	17921.51	38	0.054	17921.6	0.000	0.145
54	17921.51	39	0.007	17921.5	0.586	0.139
55	17948.80	33	2.186	17951.0	0.404	0.529
55	17948.80	35	0.806	17949.6	0.116	0.159
55	17948.80	38	0.054	17948.8	2.344	0.419
56	17975.82	34	1.385	17977.2	0.328	0.056
56	17975.82	36	0.416	17976.2	2.276	0.275
56	17975.82	37	0.178	17976.0	1.028	0.131
57	18002.37	35	0.806	18003.2	3.351	0.179
57	18002.37	36	0.416	18002.8	1.007	0.102
57	18002.37	38	0.054	18002.4	3.249	0.254
58	18029.19	35	0.806	18030.0	1.452	0.199
58	18029.19	36	0.416	18029.6	1.199	0.118
58	18029.19	37	0.178	18029.4	1.592	0.118
58	18029.19	38	0.054	18029.2	0.000	0.512
60	18082.82	32	3.242	18086.1	2.227	0.229
61	18108.65	34	1.385	18110.0	0.505	0.105
61	18108.65	35	0.806	18109.5	1.362	0.169
61	18108.65	36	0.416	18109.1	1.369	0.163
61	18108.65	38	0.054	18108.7	1.690	0.077
62	18135.25	33	2.186	18137.4	1.617	0.245
62	18135.25	34	1.385	18136.6	2.661	0.232
62	18135.25	35	0.806	18136.1	0.625	0.213
62	18135.25	36	0.416	18135.7	1.356	0.099
62	18135.25	37	0.178	18135.4	1.216	0.157
62	18135.25	38	0.054	18135.3	0.666	0.068
63	18160.93	35	0.806	18161.7	1.326	0.151
63	18160.93	38	0.054	18161.0	1.290	0.168
63	18160.93	39	0.007	18160.9	1.511	0.540
64	18186.92	35	0.806	18187.7	1.514	0.228
64	18186.92	39	0.007	18186.9	2.011	0.239

Appendix F

Table of assigned transitions of the C series of the $2^3\Pi_g$ state from the $a^3\Sigma_u^+$ state

v'	Term Ev' (cm^{-1})	v''	Binding E	Line E (cm^{-1})	Amplitude	σ (cm^{-1})
2	16492.11	34	1.385	16493.5	0.159	0.127
2	16492.11	37	0.178	16492.3	0.572	0.105
2	16492.11	38	0.054	16492.2	0.274	0.207
2	16492.11	39	0.007	16492.1	0.327	0.225
3	16525.24	37	0.178	16525.4	0.691	0.249
3	16525.24	38	0.054	16525.3	0.404	0.052
3	16525.24	39	0.007	16525.3	0.372	0.097
4	16558.40	36	0.416	16558.8	0.711	0.213
4	16558.40	37	0.178	16558.6	1.727	0.125
4	16558.40	38	0.054	16558.5	1.112	0.272
4	16558.40	39	0.007	16558.4	0.306	0.082
5	16591.65	33	2.186	16593.8	1.279	0.259
5	16591.65	34	1.385	16593.0	4.683	0.280
5	16591.65	35	0.806	16592.5	11.872	0.226
5	16591.65	36	0.416	16592.1	0.657	0.156
5	16591.65	37	0.178	16591.8	0.617	0.098
5	16591.65	39	0.007	16591.7	1.672	0.179
6	16624.81	33	2.186	16627.0	0.589	0.154
6	16624.81	34	1.385	16626.2	0.502	0.137
6	16624.81	35	0.806	16625.6	2.054	0.198
6	16624.81	36	0.416	16625.2	2.792	0.187
6	16624.81	37	0.178	16625.0	3.980	0.162
6	16624.81	39	0.007	16624.8	3.369	0.151
7	16658.13	33	2.186	16660.3	0.151	0.124
7	16658.13	34	1.385	16659.5	0.243	0.141
7	16658.13	35	0.806	16658.9	0.281	0.089
7	16658.13	37	0.178	16658.3	0.502	0.185
7	16658.13	39	0.007	16658.1	0.034	0.054
8	16690.50	33	2.186	16692.7	0.000	0.394

v'	Term Ev' (cm^{-1})	v"	Binding E	Line E (cm^{-1})	Amplitude	σ (cm^{-1})
8	16690.50	34	1.385	16691.9	0.026	0.561
8	16690.50	35	0.806	16691.3	2.236	0.295
8	16690.50	37	0.178	16690.7	0.645	0.249
8	16690.50	39	0.007	16690.5	4.562	0.243
9	16723.16	34	1.385	16724.5	0.156	0.114
9	16723.16	35	0.806	16724.0	0.164	0.153
9	16723.16	36	0.416	16723.6	0.167	0.194
10	16755.85	34	1.385	16757.2	0.211	0.091
10	16755.85	35	0.806	16756.7	0.212	0.089
10	16755.85	36	0.416	16756.3	0.503	0.085
10	16755.85	37	0.178	16756.0	0.000	0.074
10	16755.85	39	0.007	16755.9	0.150	0.103
11	16787.58	34	1.385	16789.0	0.258	0.364
11	16787.58	35	0.806	16788.4	1.779	0.230
11	16787.58	36	0.416	16788.0	0.002	0.064
11	16787.58	37	0.178	16787.8	0.000	0.304
11	16787.58	38	0.054	16787.6	1.433	0.265
11	16787.58	39	0.007	16787.6	2.873	0.262
12	16820.08	33	2.186	16822.3	0.014	0.051
12	16820.08	34	1.385	16821.5	0.722	0.606
12	16820.08	35	0.806	16820.9	0.588	0.244
12	16820.08	36	0.416	16820.5	0.000	0.159
12	16820.08	39	0.007	16820.1	1.053	0.207
13	16851.63	36	0.416	16852.0	0.040	0.058
13	16851.63	37	0.178	16851.8	0.082	0.081
13	16851.63	38	0.054	16851.7	0.000	0.179
13	16851.63	39	0.007	16851.6	0.178	0.186
14	16883.71	36	0.416	16884.1	0.484	0.101
14	16883.71	37	0.178	16883.9	0.120	0.054
14	16883.71	38	0.054	16883.8	0.000	0.064
14	16883.71	39	0.007	16883.7	0.000	0.063
15	16915.98	31	4.580	16920.6	1.121	0.114
15	16915.98	32	3.242	16919.2	2.435	0.151
16	16947.32	32	3.242	16950.6	1.427	0.099
17	16979.04	37	0.178	16979.2	1.052	0.135
17	16979.04	39	0.007	16979.0	0.493	0.056
18	17010.66	35	0.806	17011.5	2.037	0.155
18	17010.66	36	0.416	17011.1	1.799	0.154
18	17010.66	37	0.178	17010.8	0.012	0.069
18	17010.66	38	0.054	17010.7	0.885	0.177
18	17010.66	39	0.007	17010.7	1.302	0.090

v'	Term Ev' (cm^{-1})	v"	Binding E	Line E (cm^{-1})	Amplitude	σ (cm^{-1})
19	17042.03	36	0.416	17042.4	0.388	0.108
19	17042.03	37	0.178	17042.2	0.185	0.076
19	17042.03	38	0.054	17042.1	0.110	0.109
19	17042.03	39	0.007	17042.0	0.562	0.058
20	17073.41	34	1.385	17074.8	0.250	0.153
20	17073.41	35	0.806	17074.2	1.044	0.189
20	17073.41	36	0.416	17073.8	0.161	0.113
20	17073.41	37	0.178	17073.6	0.664	0.081
20	17073.41	38	0.054	17073.5	0.981	0.144
20	17073.41	39	0.007	17073.4	2.693	0.240
21	17104.49	39	0.007	17104.5	1.509	0.100
22	17135.54	33	2.186	17137.7	0.690	0.131
22	17135.54	34	1.385	17136.9	0.959	0.096
22	17135.54	35	0.806	17136.3	0.308	0.144
23	17166.58	31	4.580	17171.2	0.666	0.159
23	17166.58	36	0.416	17167.0	0.189	0.121
23	17166.58	37	0.178	17166.8	0.462	0.105
23	17166.58	35	0.806	17167.4	0.203	0.120
24	17197.75	31	4.580	17202.3	1.901	0.119
24	17197.75	32	3.242	17201.0	3.792	0.091
25	17228.18	32	3.242	17231.4	0.368	0.087
25	17228.18	34	1.385	17229.6	0.329	0.159
26	17259.08	31	4.580	17263.7	1.038	0.267
26	17259.08	32	3.242	17262.3	0.761	0.189
26	17259.08	34	1.385	17260.5	0.604	0.167
27	17289.75	34	1.385	17291.1	0.365	0.157
27	17289.75	35	0.806	17290.6	0.241	0.153
27	17289.75	36	0.416	17290.2	0.283	0.163
27	17289.75	39	0.007	17289.8	0.241	0.064
28	17320.04	32	3.242	17323.3	0.694	0.104
28	17320.04	33	2.186	17322.2	1.581	0.104
28	17320.04	34	1.385	17321.4	1.856	0.144
28	17320.04	35	0.806	17320.8	0.611	0.124
29	17350.38	32	3.242	17353.6	0.375	0.144
29	17350.38	33	2.186	17352.6	0.619	0.144
29	17350.38	34	1.385	17351.8	1.054	0.144
30	17380.45	34	1.385	17381.8	0.245	0.188
30	17380.45	35	0.806	17381.3	1.371	0.169
30	17380.45	36	0.416	17380.9	0.552	0.100
31	17410.70	35	0.806	17411.5	0.257	0.283
31	17410.70	36	0.416	17411.1	0.349	0.163

v'	Term Ev' (cm^{-1})	v"	Binding E	Line E (cm^{-1})	Amplitude	σ (cm^{-1})
31	17410.70	37	0.178	17410.9	0.209	0.088
31	17410.70	39	0.007	17410.7	0.442	0.088
32	17440.73	35	0.806	17441.5	0.055	0.147
32	17440.73	37	0.178	17440.9	0.061	0.142
32	17440.73	38	0.054	17440.8	0.054	0.154
32	17440.73	39	0.007	17440.7	0.052	0.182
33	17470.62	34	1.385	17472.0	0.051	0.187
33	17470.62	35	0.806	17471.4	0.084	0.161
33	17470.62	36	0.416	17471.0	0.465	0.183
33	17470.62	37	0.178	17470.8	0.253	0.090
33	17470.62	38	0.054	17470.7	0.000	0.104
33	17470.62	39	0.007	17470.6	0.107	0.081
34	17500.39	35	0.806	17501.2	0.124	0.105
34	17500.39	36	0.416	17500.8	0.283	0.169
35	17530.01	33	2.186	17532.2	0.392	0.195
35	17530.01	34	1.385	17531.4	0.985	0.194
35	17530.01	35	0.806	17530.8	2.019	0.191
35	17530.01	36	0.416	17530.4	0.911	0.184
35	17530.01	37	0.178	17530.2	0.097	0.184
35	17530.01	38	0.054	17530.1	0.271	0.188
35	17530.01	39	0.007	17530.0	0.674	0.185
36	17559.91	33	2.186	17562.1	0.331	0.224
36	17559.91	34	1.385	17561.3	0.351	0.305
36	17559.91	35	0.806	17560.7	0.309	0.152
36	17559.91	36	0.416	17560.3	0.209	0.135
36	17559.91	37	0.178	17560.1	0.055	0.085
36	17559.91	38	0.054	17560.0	0.065	0.086
36	17559.91	39	0.007	17559.9	0.184	0.290
37	17589.48	31	4.580	17594.1	0.150	0.219
37	17589.48	34	1.385	17590.9	0.264	0.300
37	17589.48	35	0.806	17590.3	0.127	0.142
37	17589.48	36	0.416	17589.9	0.079	0.264
37	17589.48	38	0.054	17589.5	0.000	0.123
37	17589.48	39	0.007	17589.5	0.027	0.136
39	17647.37	31	4.580	17651.9	0.215	0.166
39	17647.37	32	3.242	17650.6	0.465	0.120
39	17647.37	33	2.186	17649.6	0.699	0.102
39	17647.37	34	1.385	17648.8	0.354	0.080
39	17647.37	35	0.806	17648.2	0.252	0.082
39	17647.37	36	0.416	17647.8	0.000	0.113
39	17647.37	37	0.178	17647.5	0.719	0.109

v'	Term Ev' (cm^{-1})	v"	Binding E	Line E (cm^{-1})	Amplitude	σ (cm^{-1})
39	17647.37	38	0.054	17647.4	0.353	0.195
40	17676.51	31	4.580	17681.1	1.180	0.165
40	17676.51	32	3.242	17679.8	0.326	0.148
40	17676.51	33	2.186	17678.7	1.680	0.135
40	17676.51	34	1.385	17677.9	0.923	0.091
40	17676.51	35	0.806	17677.3	0.702	0.182
40	17676.51	36	0.416	17676.9	0.773	0.095
40	17676.51	39	0.007	17676.5	0.472	0.126
41	17705.51	35	0.806	17706.3	0.849	0.120
43	17762.92	31	4.580	17767.5	0.501	0.104
43	17762.92	32	3.242	17766.2	1.501	0.104
43	17762.92	33	2.186	17765.1	3.001	0.104
43	17762.92	34	1.385	17764.3	0.701	0.114
43	17762.92	35	0.806	17763.7	1.192	0.124
43	17762.92	37	0.178	17763.1	0.900	0.104
45	17819.86	35	0.806	17820.7	0.192	0.139
45	17819.86	36	0.416	17820.3	0.444	0.178
45	17819.86	37	0.178	17820.0	0.054	0.081
45	17819.86	38	0.054	17819.9	0.245	0.169
45	17819.86	39	0.007	17819.9	0.000	0.237
46	17848.50	32	3.242	17851.7	0.148	0.289
46	17848.50	34	1.385	17849.9	2.432	0.283
46	17848.50	35	0.806	17849.3	0.733	0.221
46	17848.50	36	0.416	17848.9	0.092	0.199
46	17848.50	37	0.178	17848.7	0.067	0.212
46	17848.50	39	0.007	17848.5	0.092	0.307
46	17848.50	33	2.186	17850.7	0.083	0.251
49	17932.89	31	4.580	17937.5	0.224	0.125
49	17932.89	32	3.242	17936.1	0.169	0.109
49	17932.89	36	0.416	17933.3	0.040	0.058
50	17960.66	33	2.186	17962.8	0.047	0.158
50	17960.66	34	1.385	17962.0	0.059	0.148
50	17960.66	36	0.416	17961.1	0.127	0.127
52	18016.14	32	3.242	18019.4	1.406	0.144
52	18016.14	33	2.186	18018.3	1.285	0.134
52	18016.14	36	0.416	18016.6	0.331	0.154
52	18016.14	37	0.178	18016.3	0.110	0.154
52	18016.14	38	0.054	18016.2	0.097	0.154
52	18016.14	39	0.007	18016.1	0.221	0.154
55	18098.33	31	4.580	18102.9	1.019	0.150
55	18098.33	34	1.385	18099.7	0.174	0.122

v'	Term Ev' (cm^{-1})	v"	Binding E	Line E (cm^{-1})	Amplitude	σ (cm^{-1})
56	18124.74	34	1.385	18126.1	2.731	0.150
56	18124.74	35	0.806	18125.5	2.026	0.180
56	18124.74	36	0.416	18125.2	0.762	0.260
56	18124.74	37	0.178	18124.9	0.000	0.154
56	18124.74	38	0.054	18124.8	0.000	0.604
56	18124.74	39	0.007	18124.7	0.346	0.089
57	18151.79	31	4.580	18156.4	1.809	0.114
57	18151.79	32	3.242	18155.0	2.330	0.114
57	18151.79	33	2.186	18154.0	0.844	0.144
57	18151.79	34	1.385	18153.2	1.503	0.144
58	18178.67	31	4.580	18183.2	1.434	0.174
58	18178.67	33	2.186	18180.9	1.650	0.174
58	18178.67	34	1.385	18180.1	1.003	0.084

Appendix G

The $X^1\Sigma_g^+ \rightarrow 2^1\Sigma_u^+$ spectrum plots and assignments.

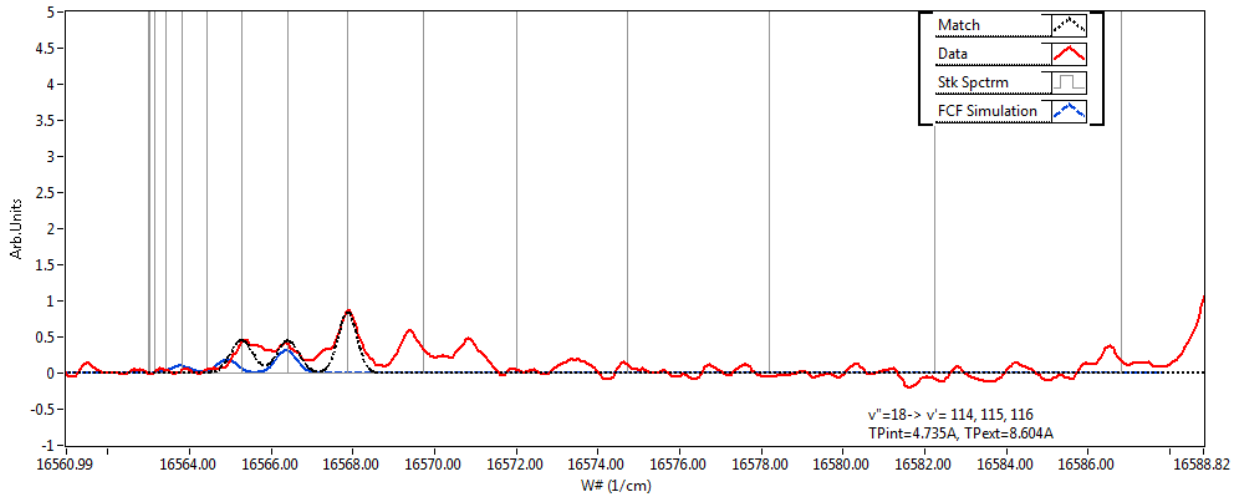
Match
Data
Stk Spctrm
FCF Simulation
Arb.Units
v"=18-> v'= 114, 115, 116
TPint=4.735A, TPext=8.604A
W# (1/cm)

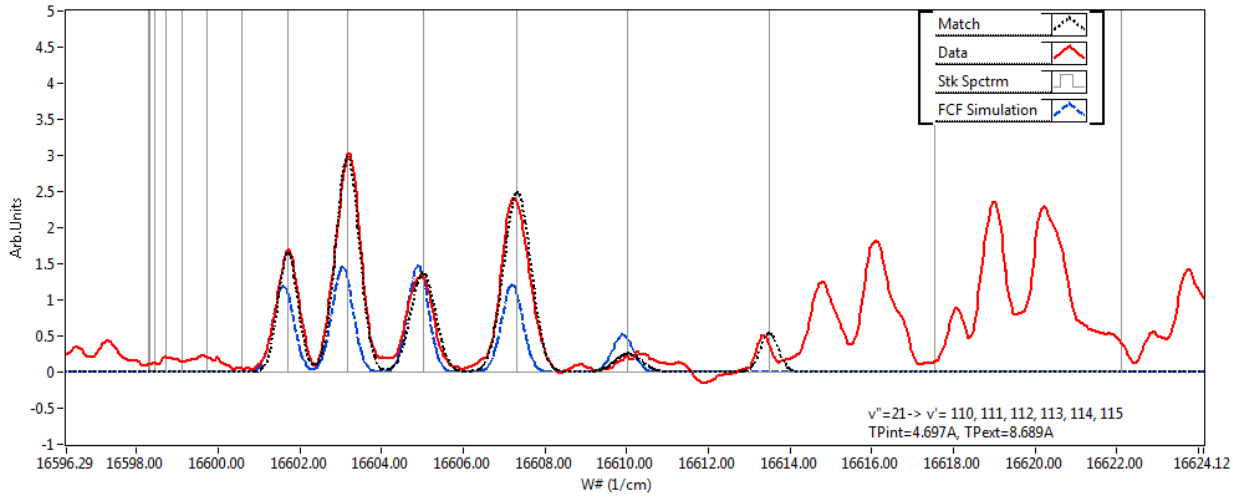
Match
Data
Stk Spctrm
FCF Simulation
Arb.Units
v"=21-> v'= 110, 111, 112, 113, 114, 115
TPint=4.697A, TPext=8.689A
W# (1/cm)

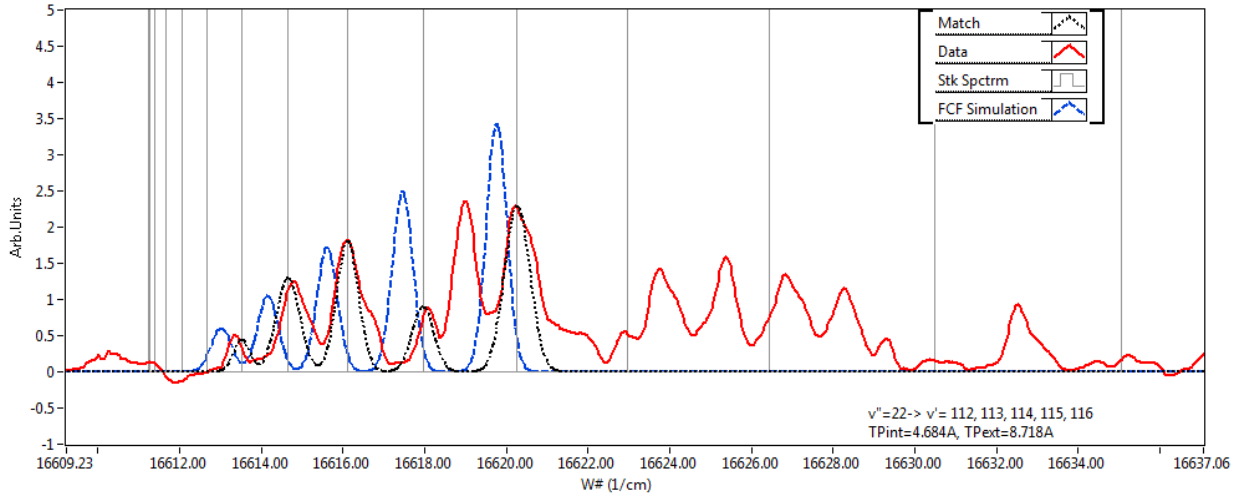
Match
Data
Stk Spctrm
FCF Simulation
Arb.Units
v"=22-> v'= 112, 113, 114, 115, 116
TPint=4.684A, TPext=8.718A
W# (1/cm)

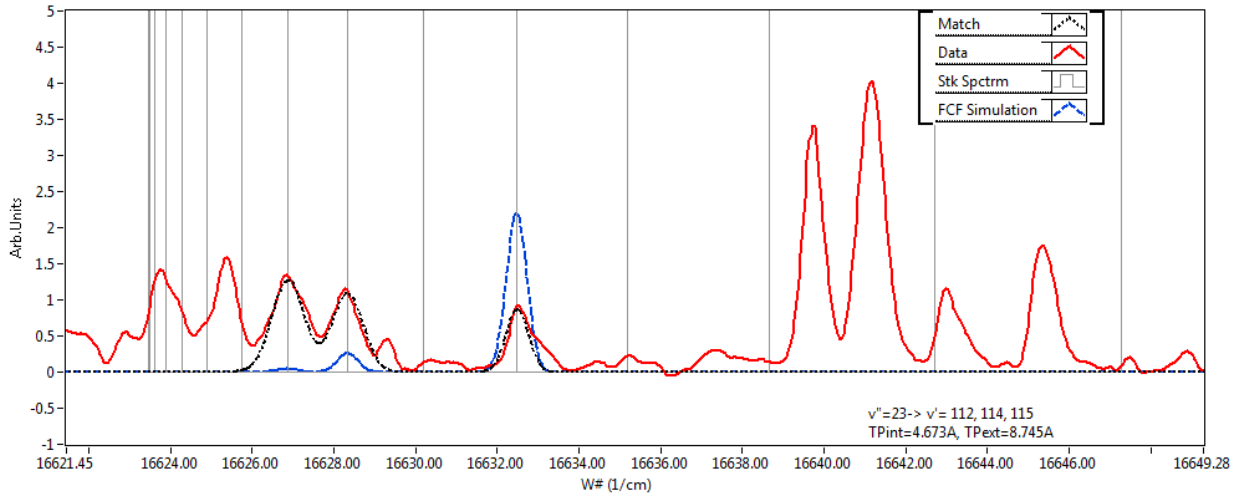
Match
Data
Stk Spctrm
FCF Simulation
v"=23-> v'= 112, 114, 115
TPint=4.673A, TPext=8.745A
Arb.Units
W# (1/cm)
5
4.5
4
3.5
3
2.5
2
1.5
1
0.5
0
-0.5
-1
16621.45
16624.00
16626.00
16628.00
16630.00
16632.00
16634.00
16636.00
16638.00
16640.00
16642.00
16644.00
16646.00
16649.28

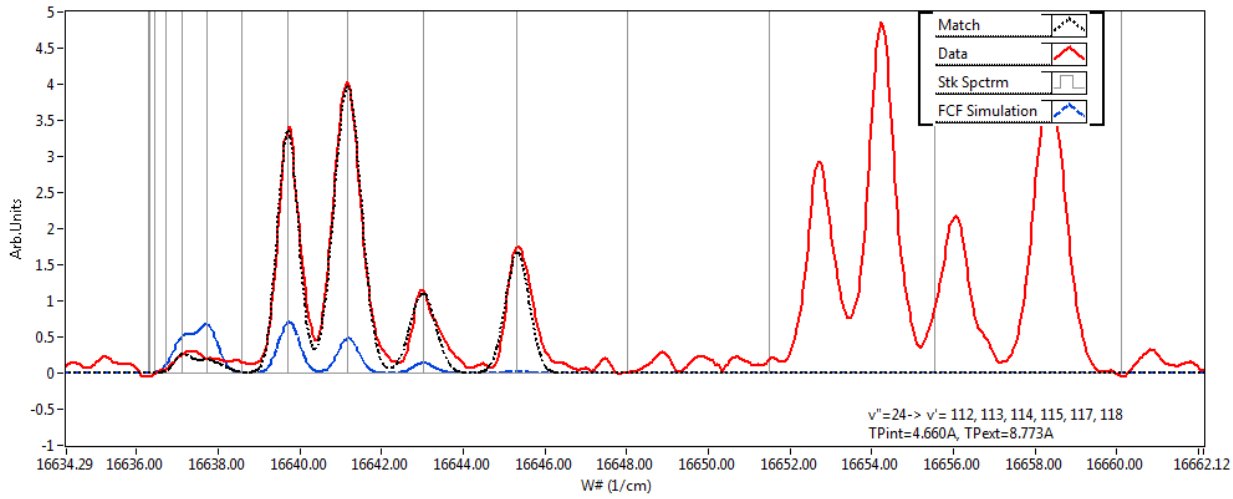
Match
Data
Stk Spctrm
FCF Simulation
Arb.Units
W# (1/cm)
v"=24-> v'= 112, 113, 114, 115, 117, 118
TPint=4.660A, TPext=8.773A

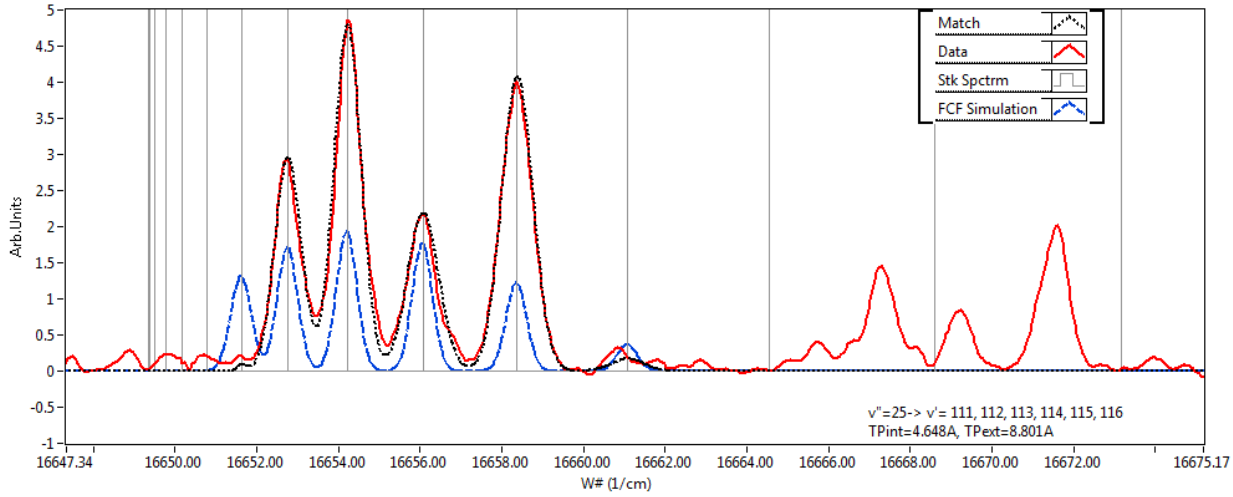
Match
Data
Stk Spctrm
FCF Simulation
Arb.Units
W# (1/cm)
v"=25-> v'= 111, 112, 113, 114, 115, 116
TPint=4.648A, TPext=8.801A

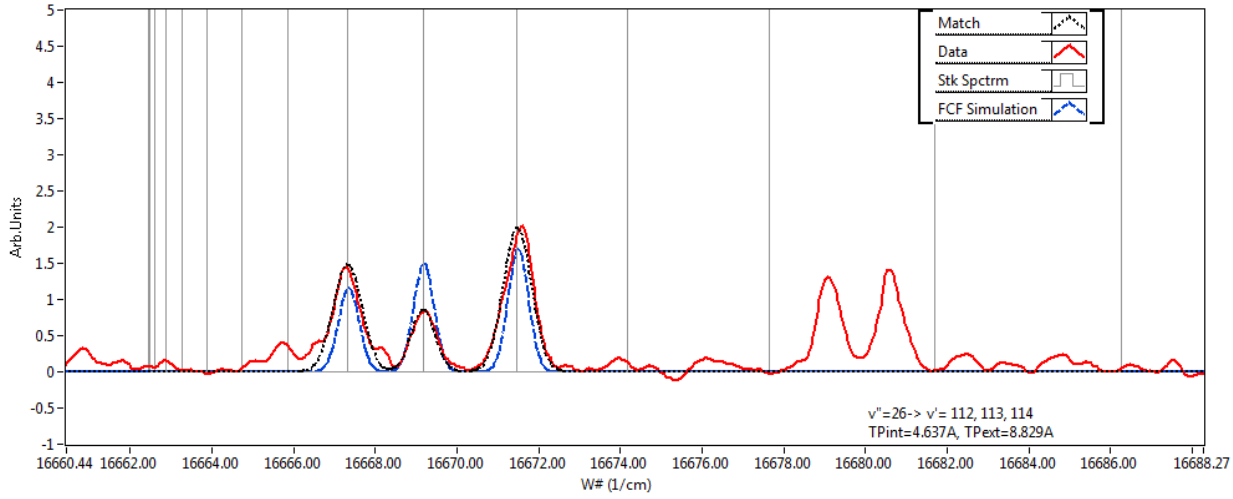
Match
Data
Stk Spctrm
FCF Simulation
Arb.Units
W# (1/cm)
v"=26-> v'= 112, 113, 114
TPint=4.637A, TPext=8.829A

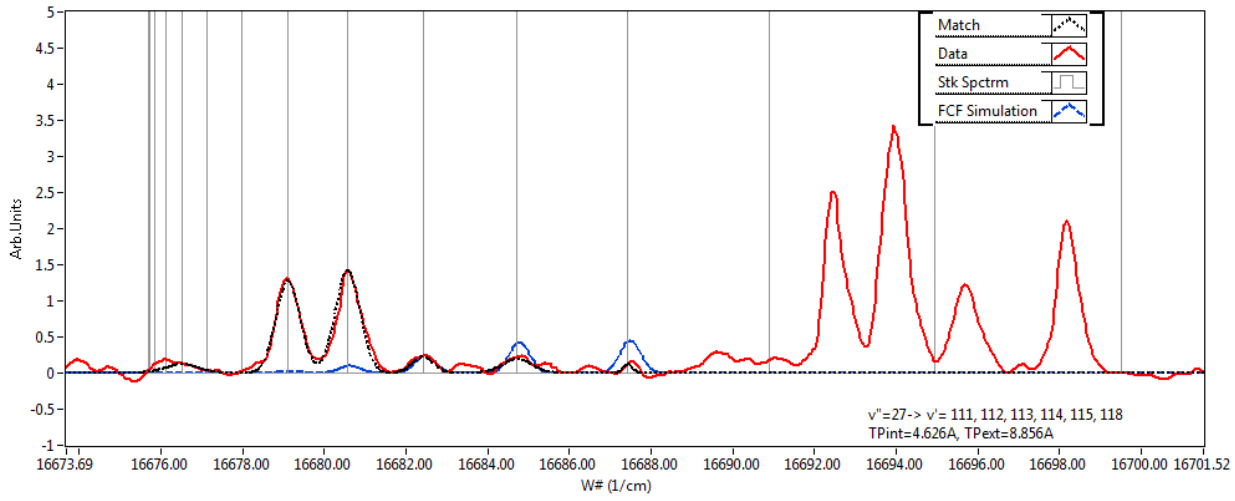
Match
Data
Stk Spctrm
FCF Simulation
Arb.Units
W# (1/cm)
v"=27-> v'= 111, 112, 113, 114, 115, 118
TPint=4.626A, TPext=8.856A

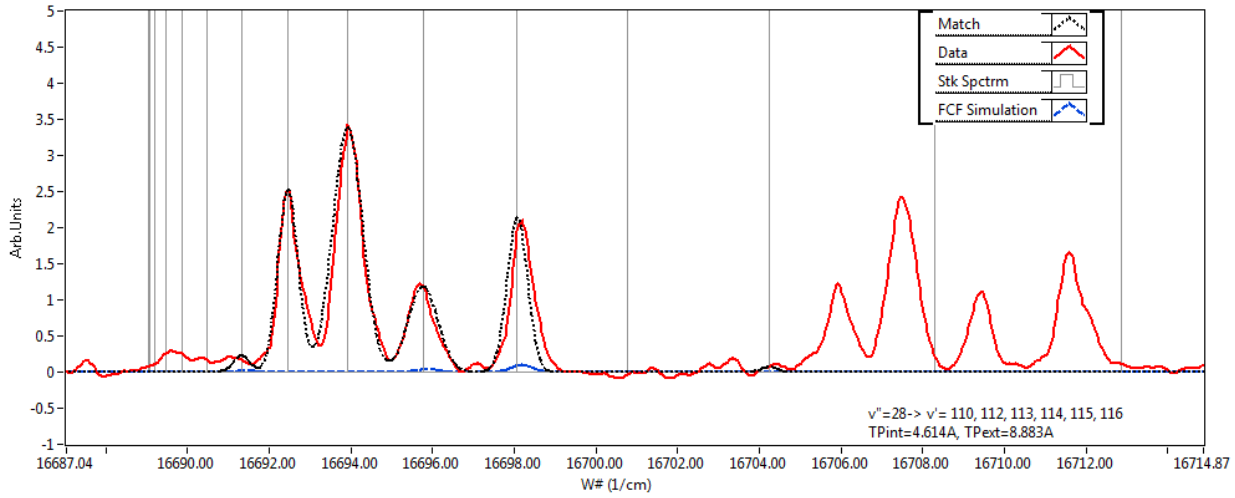
Match
Data
Stk Spctrm
FCF Simulation
Arb.Units
W# (1/cm)
v"=28-> v'= 110, 112, 113, 114, 115, 116
TPint=4.614A, TPext=8.883A

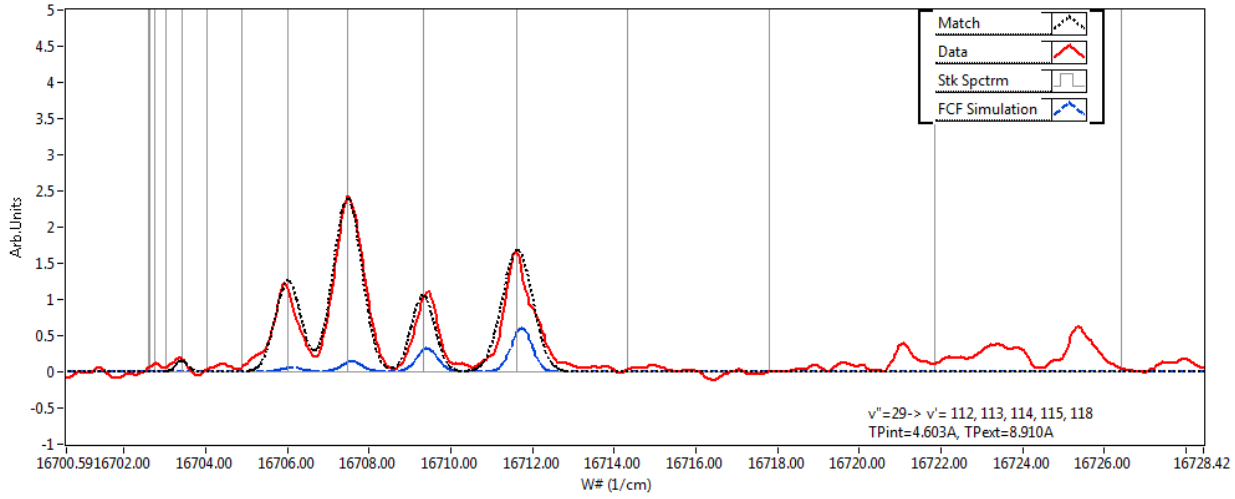
Match
Data
Stk Spctrm
FCF Simulation
Arb.Units
W# (1/cm)
v"=29-> v'= 112, 113, 114, 115, 118
TPint=4.603A, TPext=8.910A

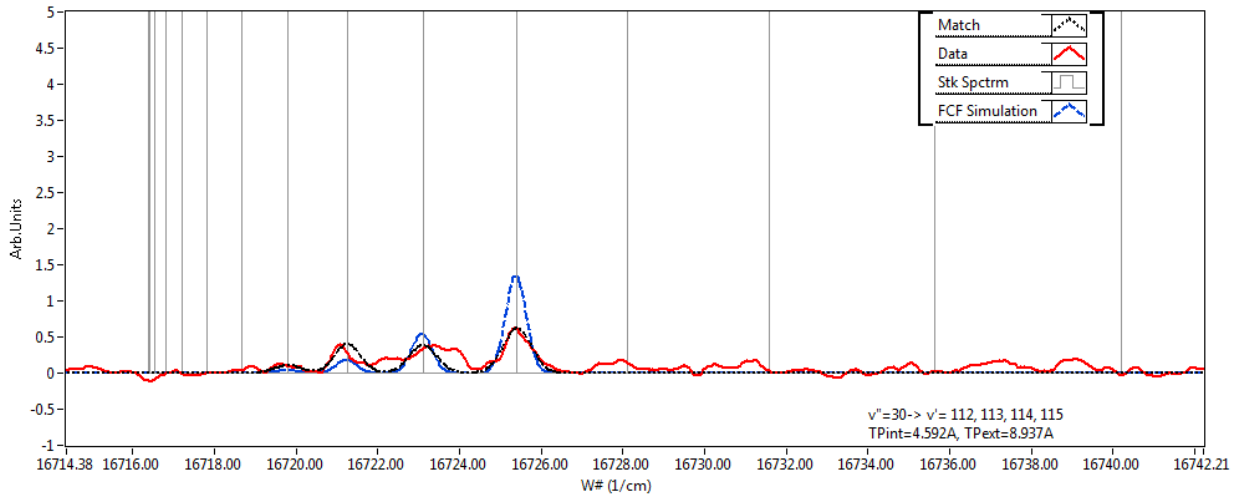
Match
Data
Stk Spctrm
FCF Simulation
Arb.Units
W# (1/cm)
v"=30-> v'= 112, 113, 114, 115
TPint=4.592A, TPext=8.937A

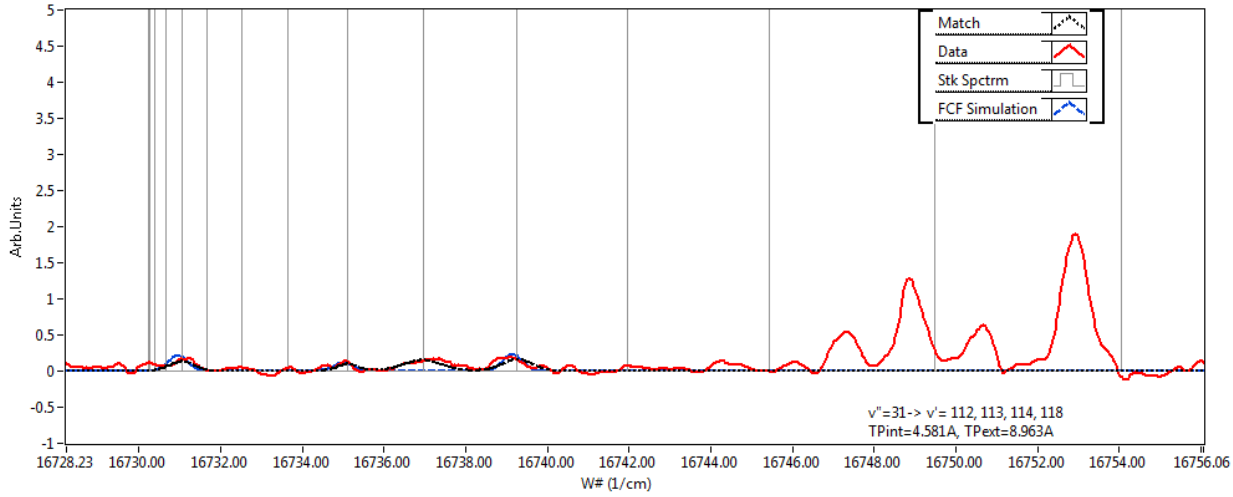
Match
Data
Stk Spctrm
FCF Simulation
Arb.Units
W# (1/cm)
v"=31-> v'= 112, 113, 114, 118
TPint=4.581A, TPext=8.963A

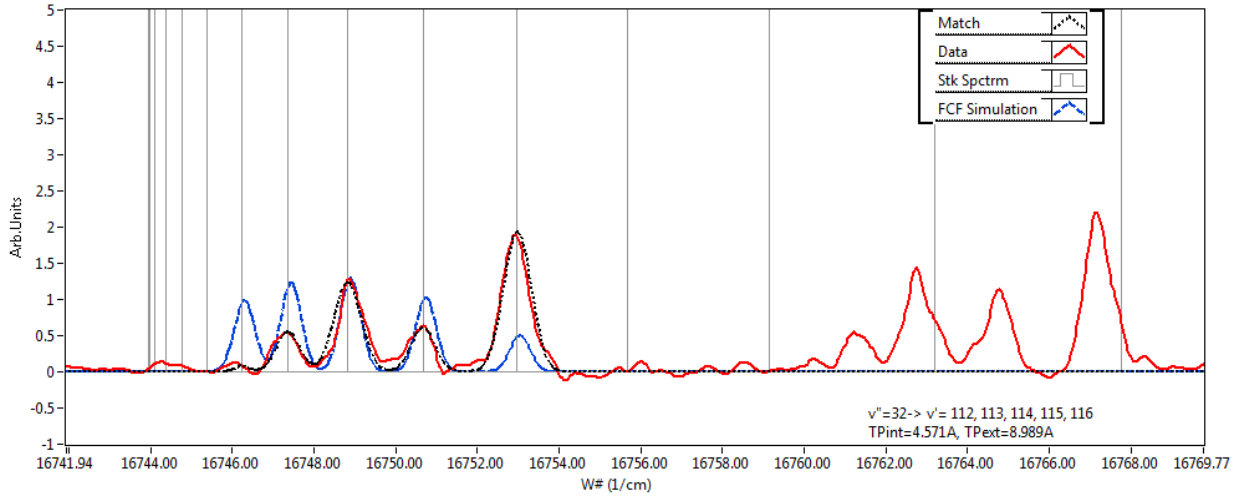
Match
Data
Stk Spctrm
FCF Simulation
Arb.Units
W# (1/cm)
v"=32-> v'= 112, 113, 114, 115, 116
TPint=4.571A, TPext=8.989A

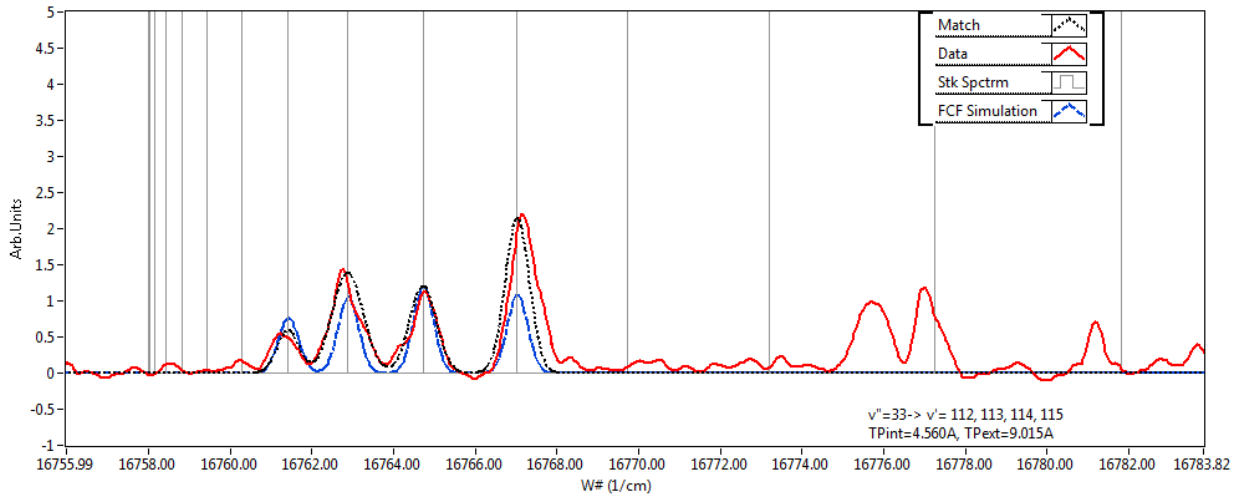
Match
Data
Stk Spctrm
FCF Simulation
Arb.Units
W# (1/cm)
v"=33-> v'= 112, 113, 114, 115
TPint=4.560A, TPext=9.015A

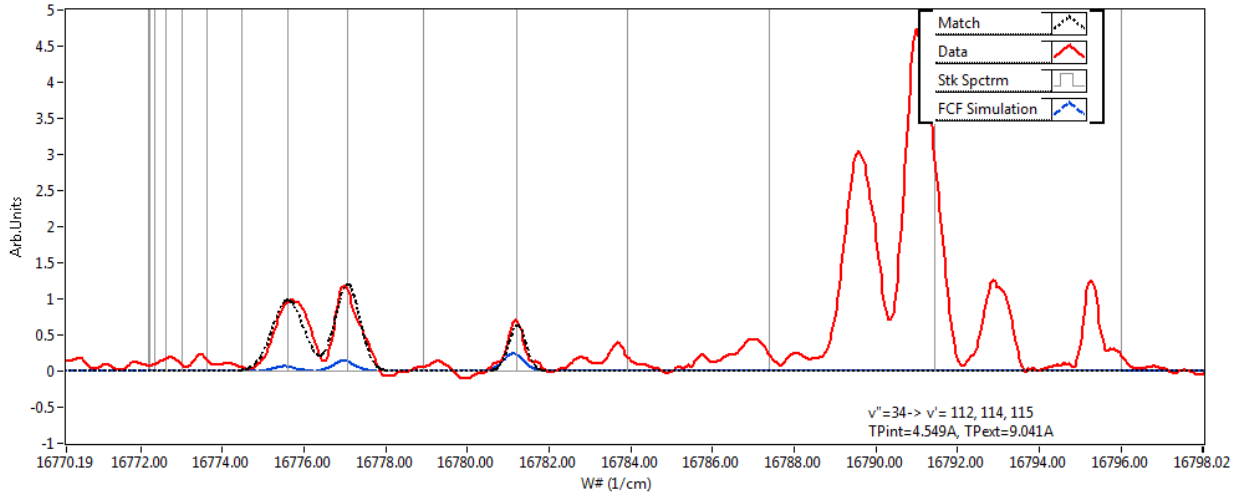
Match
Data
Stk Spctrm
FCF Simulation
Arb.Units
W# (1/cm)
v"=34-> v'= 112, 114, 115
TPint=4.549A, TPext=9.041A

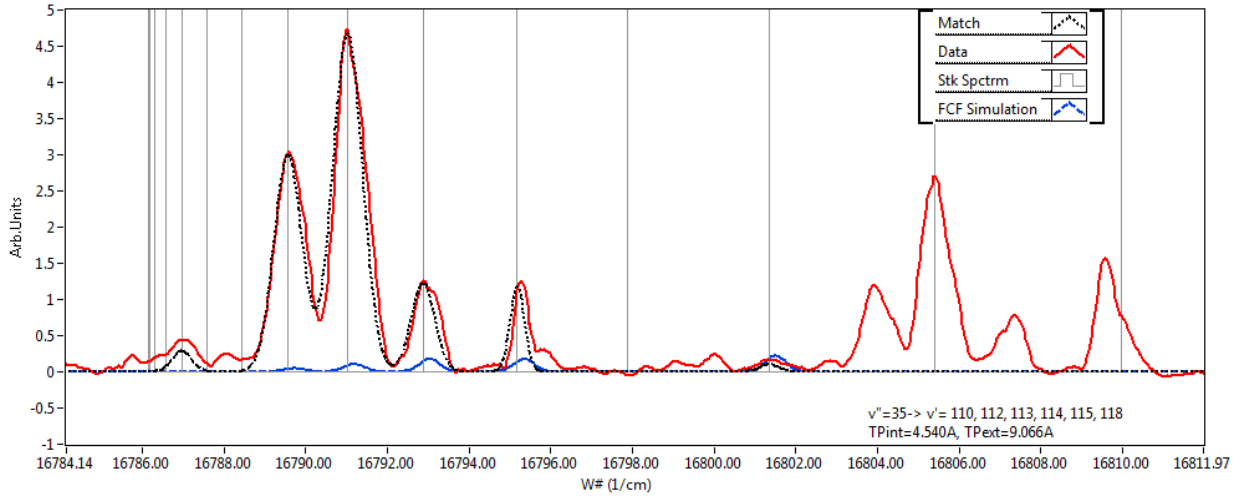
Match
Data
Stk Spctrm
FCF Simulation
Arb.Units
W# (1/cm)
v"=35-> v'= 110, 112, 113, 114, 115, 118
TPint=4.540A, TPext=9.066A

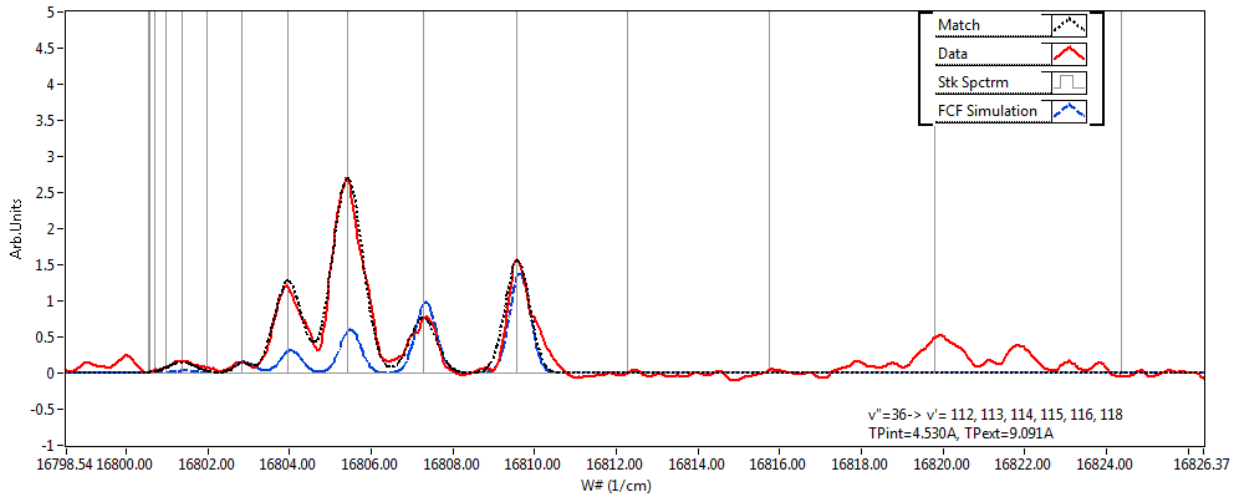
Match
Data
Stk Spctrm
FCF Simulation
Arb.Units
W# (1/cm)
v"=36-> v'= 112, 113, 114, 115, 116, 118
TPint=4.530A, TPext=9.091A

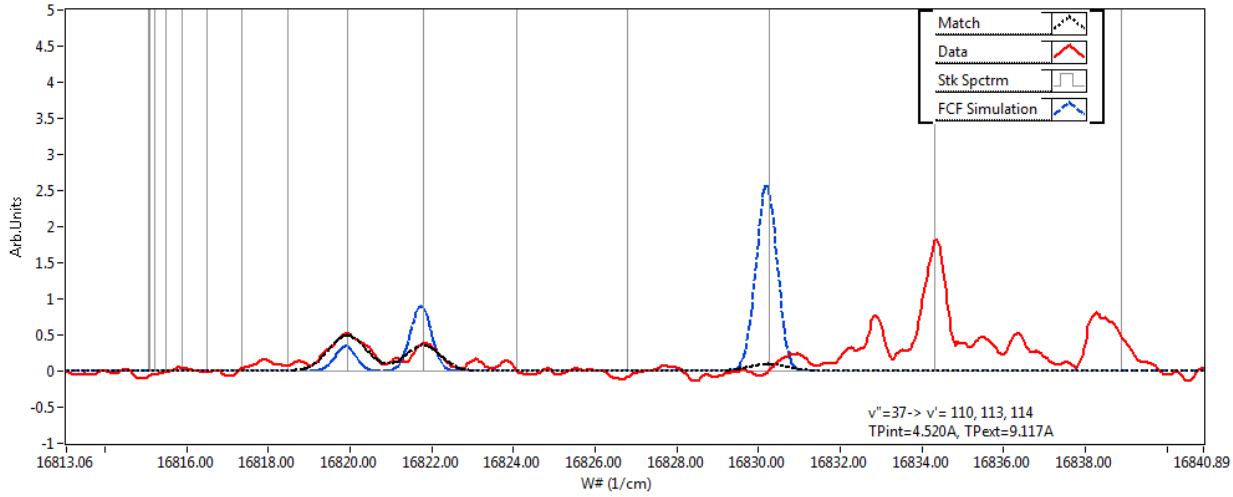
Match
Data
Stk Spctrm
FCF Simulation
Arb.Units
W# (1/cm)
v"=37-> v'= 110, 113, 114
TPint=4.520A, TPext=9.117A

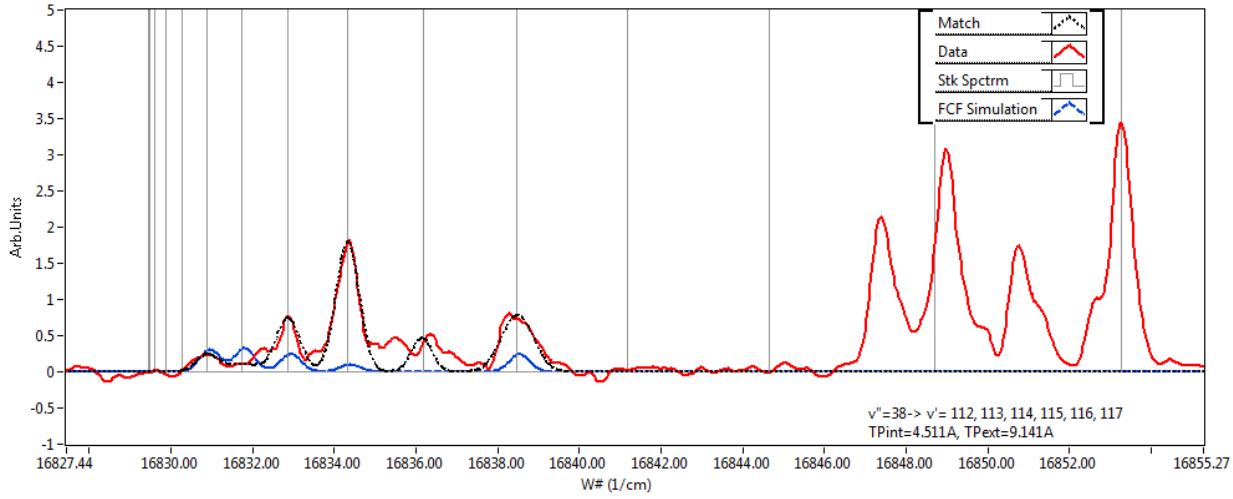
Match
Data
Stk Spctrm
FCF Simulation
Arb.Units
W# (1/cm)
v"=38-> v'= 112, 113, 114, 115, 116, 117
TPint=4.511A, TPext=9.141A

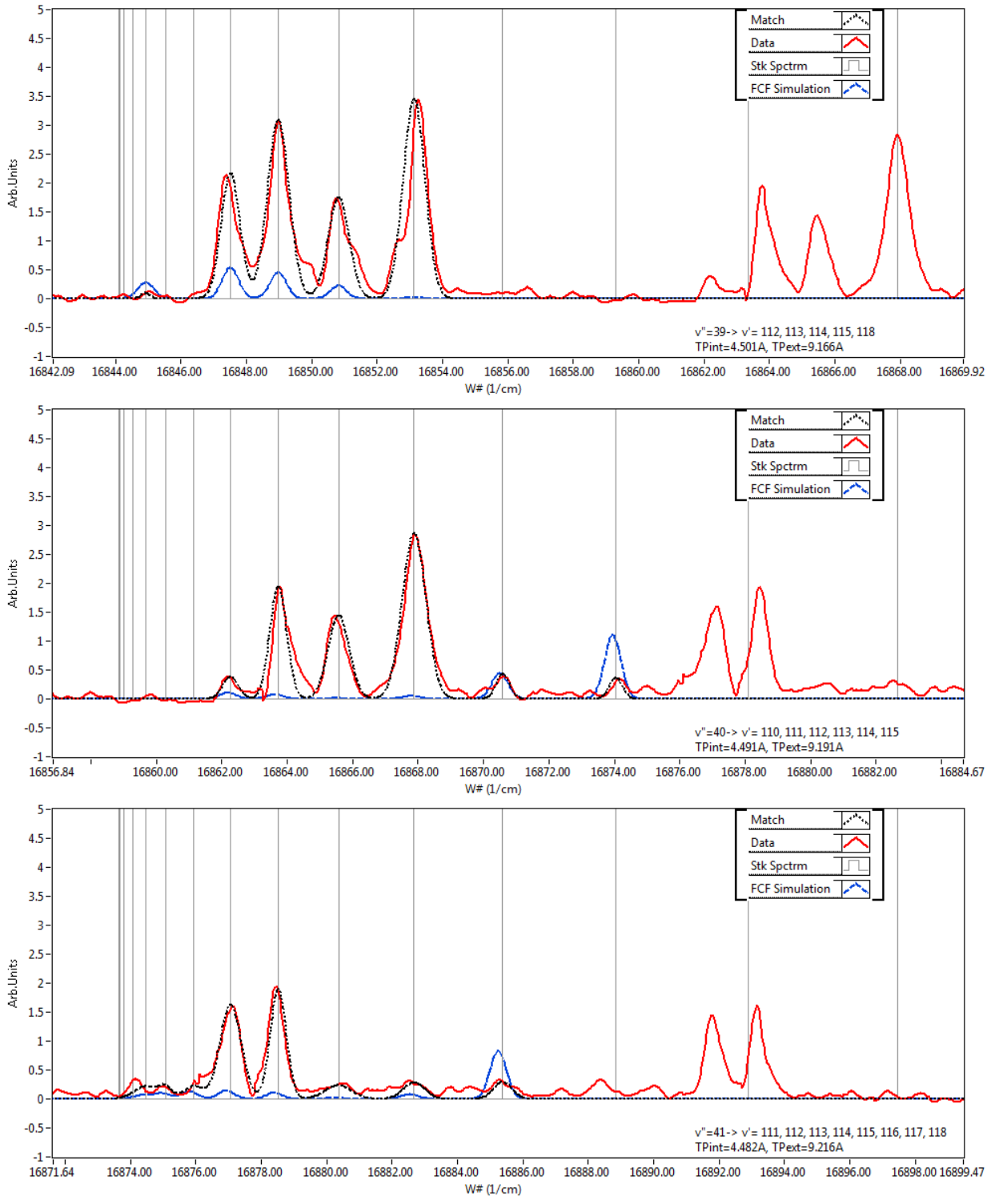
Match
Data
Stk Spctrm
FCF Simulation
Arb.Units
W# (1/cm)
v"=39-> v'= 112, 113, 114, 115, 118
TPint=4.501A, TPext=9.166A
v"=40-> v'= 110, 111, 112, 113, 114, 115
TPint=4.491A, TPext=9.191A
v"=41-> v'= 111, 112, 113, 114, 115, 116, 117, 118
TPint=4.482A, TPext=9.216A

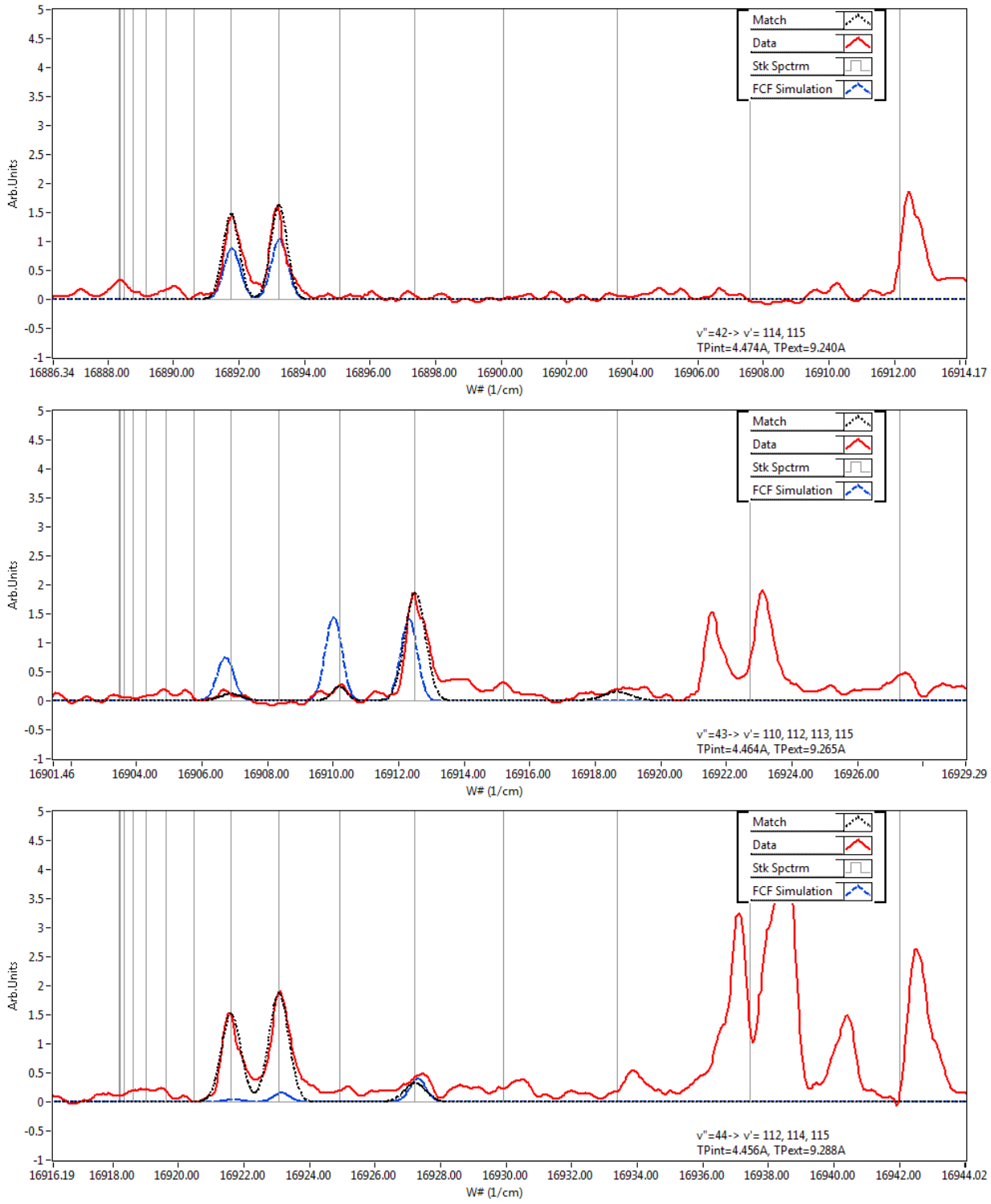
Match
Data
Stk Spctrm
FCF Simulation
Arb.Units
W# (1/cm)
v"=42-> v'= 114, 115
TPint=4.474A, TPext=9.240A
v"=43-> v'= 110, 112, 113, 115
TPint=4.464A, TPext=9.265A
v"=44-> v'= 112, 114, 115
TPint=4.456A, TPext=9.288A

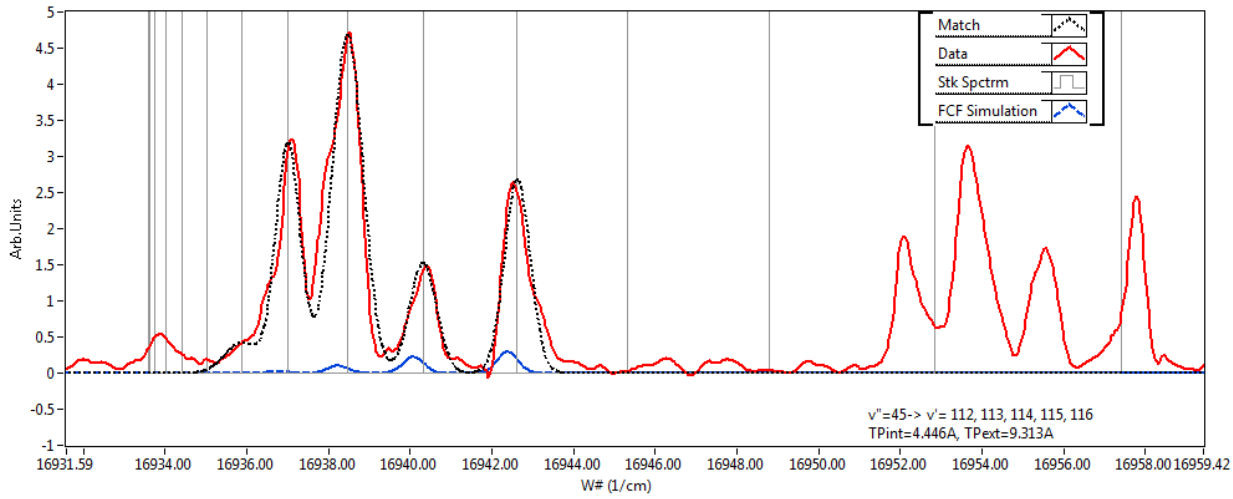
Match
Data
Stk Spctrm
FCF Simulation
Arb.Units
W# (1/cm)
v"=45-> v'= 112, 113, 114, 115, 116
TPint=4.446A, TPext=9.313A

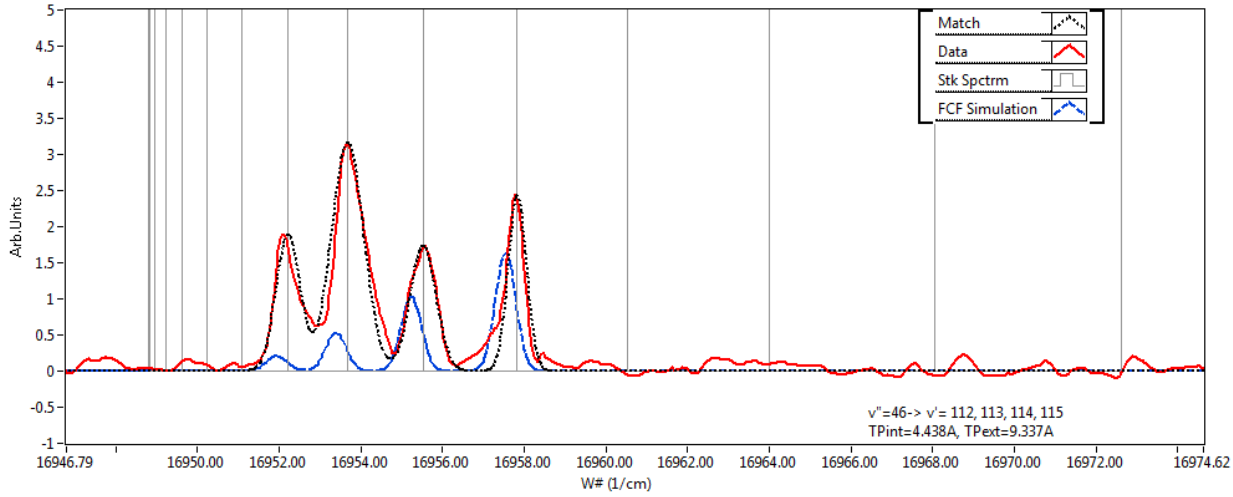
Match
Data
Stk Spctrm
FCF Simulation
Arb.Units
W# (1/cm)
v"=46-> v'= 112, 113, 114, 115
TPint=4.438A, TPext=9.337A

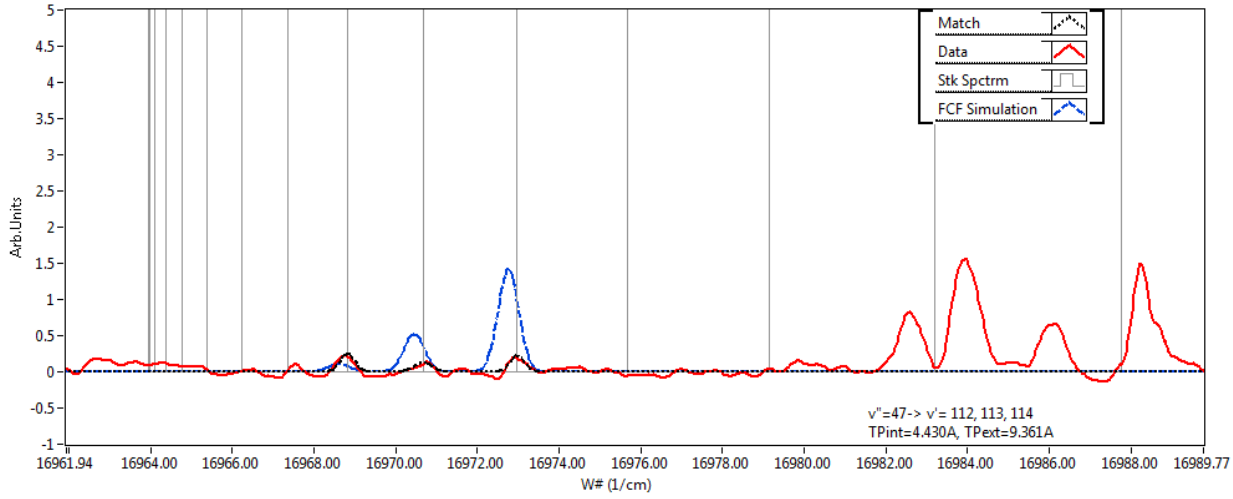
Match
Data
Stk Spctrm
FCF Simulation
Arb.Units
W# (1/cm)
v"=47-> v'= 112, 113, 114
TPint=4.430A, TPext=9.361A

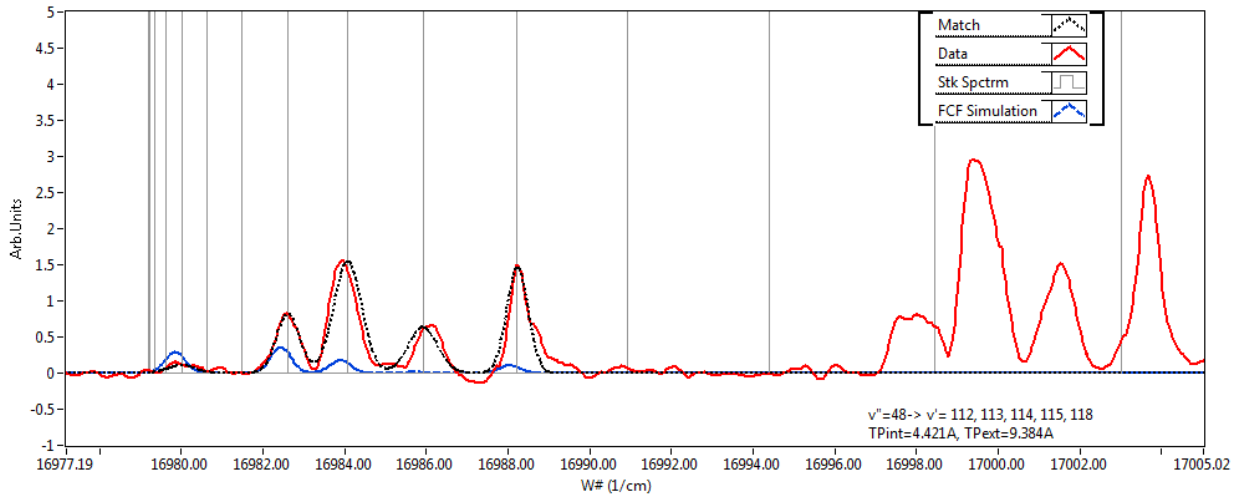
Match
Data
Stk Spctrm
FCF Simulation
Arb.Units
W# (1/cm)
v"=48-> v'= 112, 113, 114, 115, 118
TPint=4.421A, TPext=9.384A

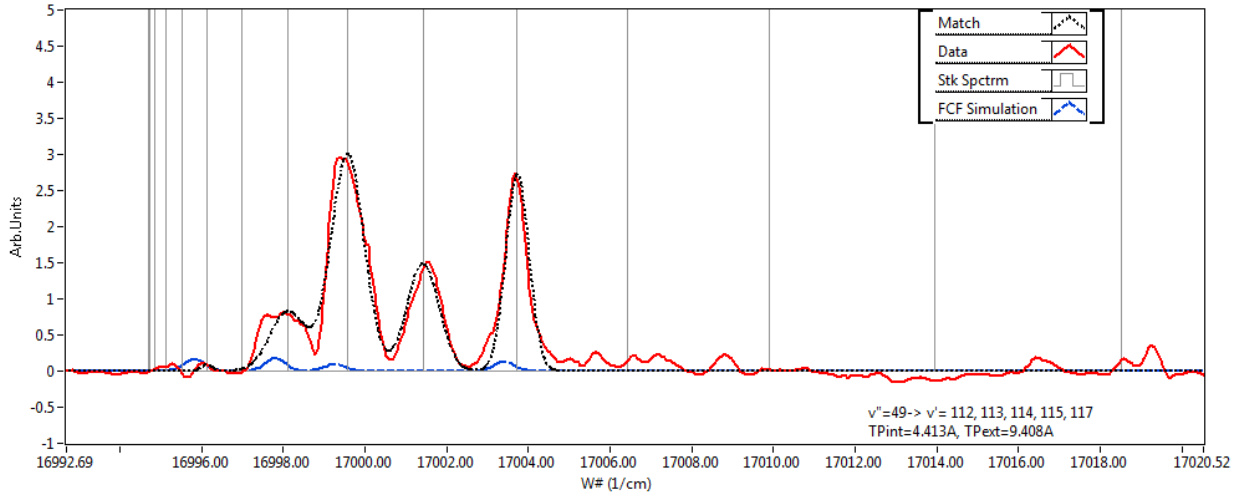
Match
Data
Stk Spctrm
FCF Simulation
Arb.Units
W# (1/cm)
v"=49-> v'= 112, 113, 114, 115, 117
TPint=4.413A, TPext=9.408A

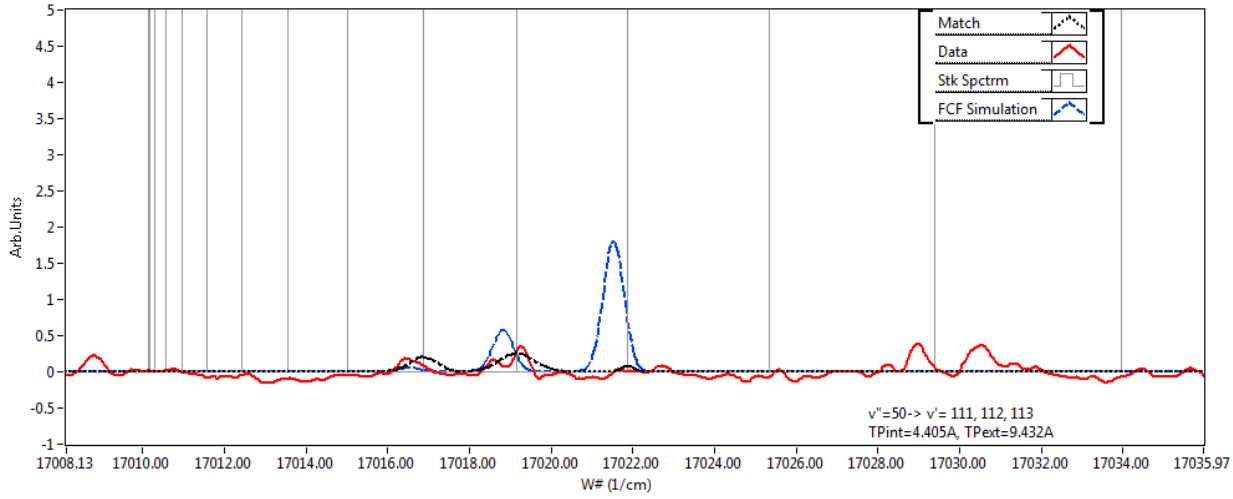
Match
Data
Stk Spctrm
FCF Simulation
Arb.Units
W# (1/cm)
v"=50-> v'= 111, 112, 113
TPint=4.405A, TPext=9.432A

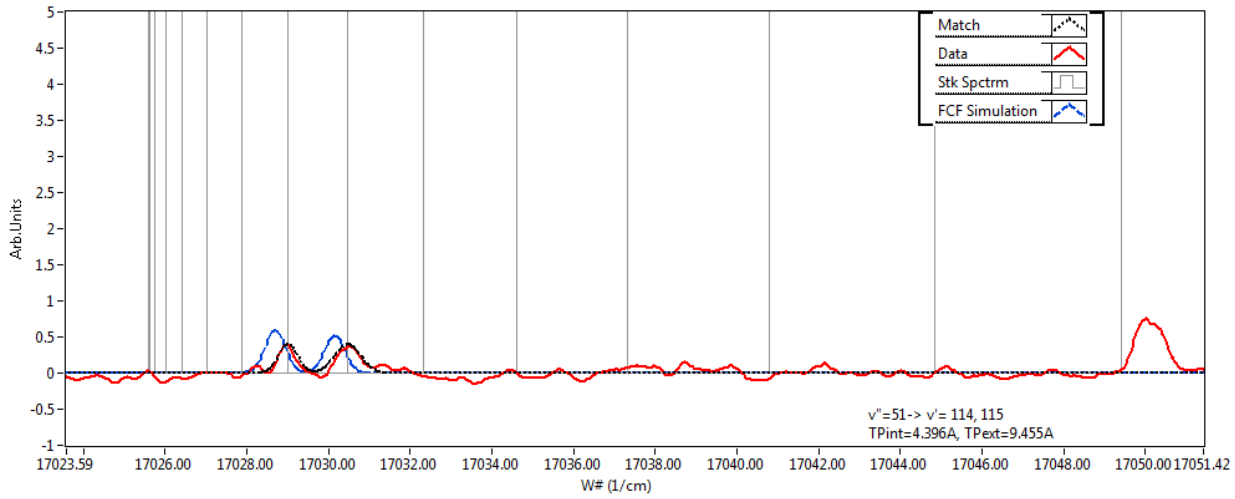
Match
Data
Stk Spctrm
FCF Simulation
Arb.Units
v"=51-> v'= 114, 115
TPint=4.396A, TPext=9.455A
W# (1/cm)

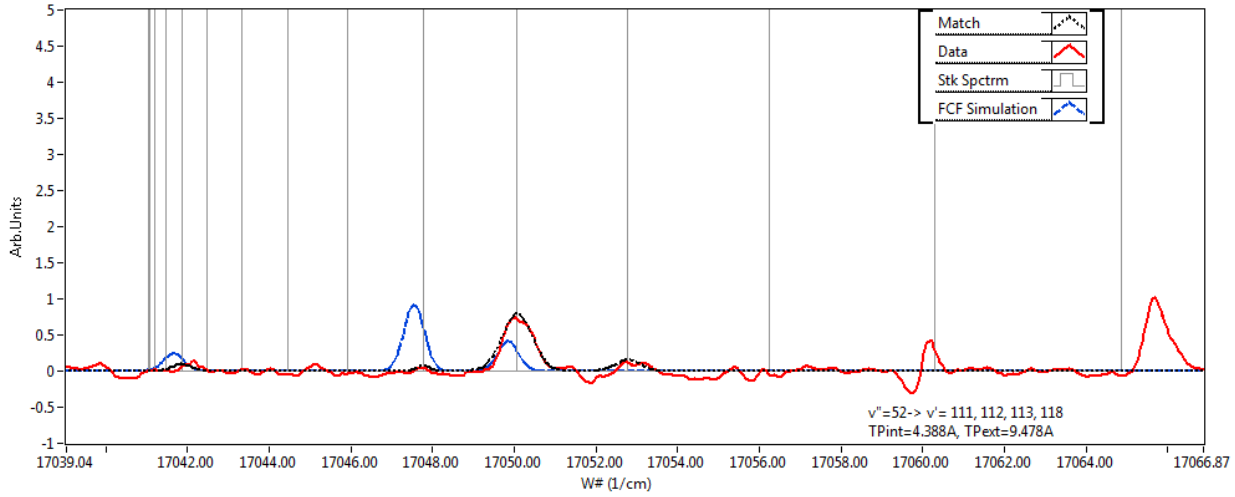
Match
Data
Stk Spctrm
FCF Simulation
Arb.Units
v"=52-> v'= 111, 112, 113, 118
TPint=4.388A, TPext=9.478A
W# (1/cm)

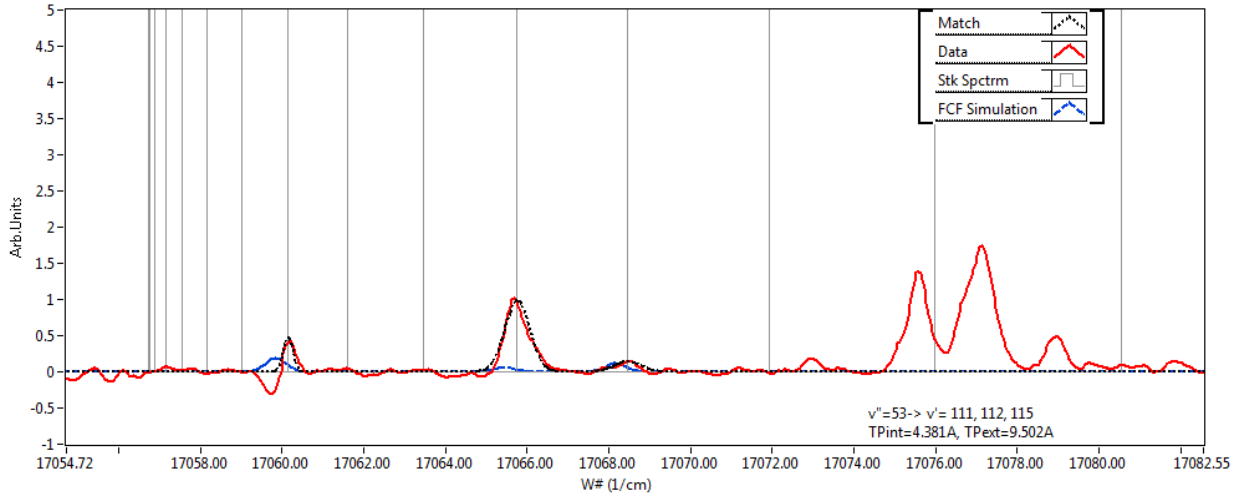
Match
Data
Stk Spctrm
FCF Simulation
Arb.Units
v"=53-> v'= 111, 112, 115
TPint=4.381A, TPext=9.502A
W# (1/cm)

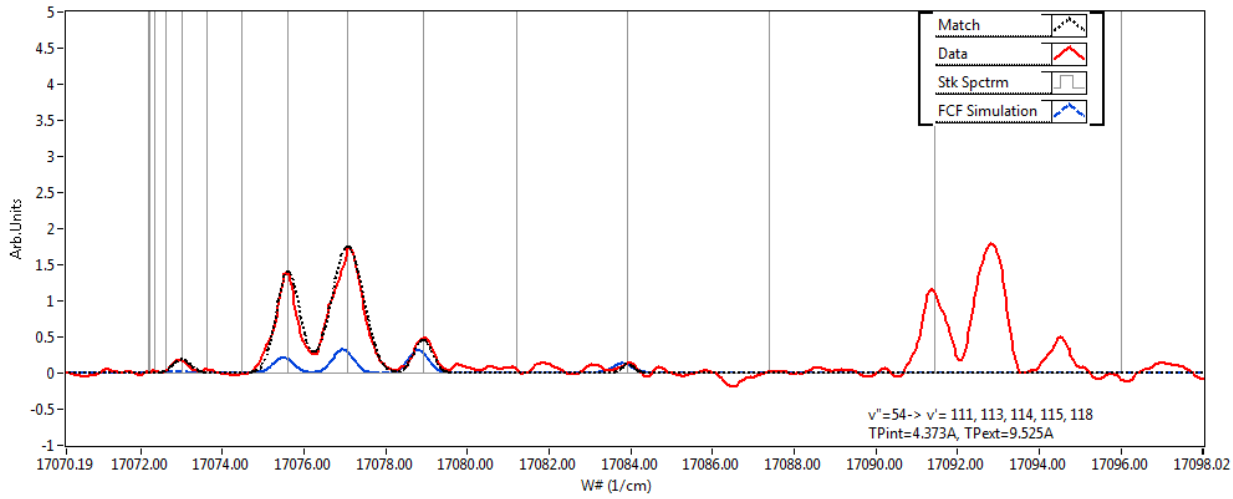
Match
Data
Stk Spctrm
FCF Simulation
Arb.Units
W# (1/cm)
v"=54-> v'= 111, 113, 114, 115, 118
TPint=4.373A, TPext=9.525A

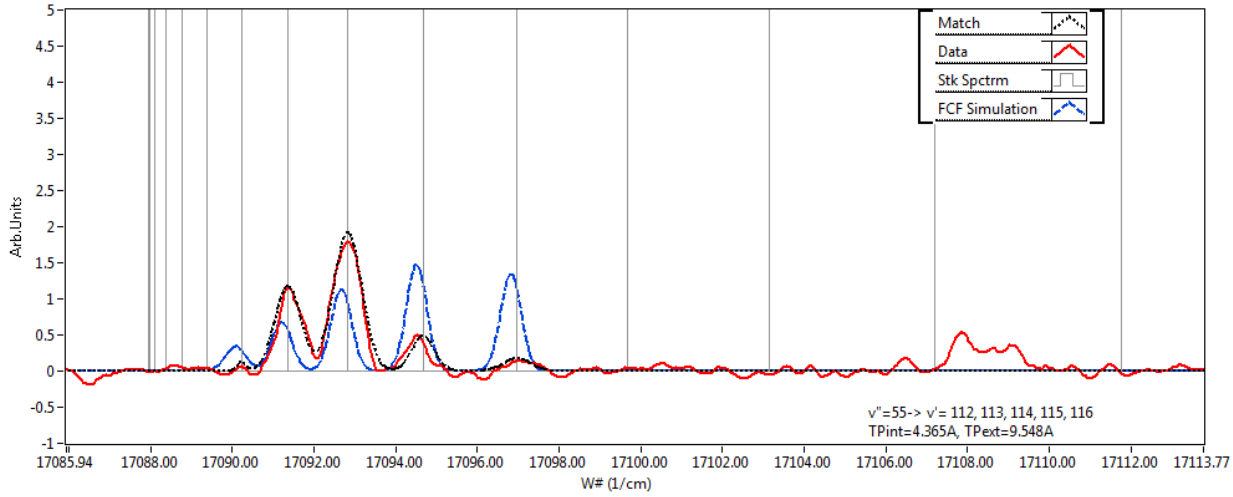
Match
Data
Stk Spctrm
FCF Simulation
Arb.Units
W# (1/cm)
v"=55-> v'= 112, 113, 114, 115, 116
TPint=4.365A, TPext=9.548A

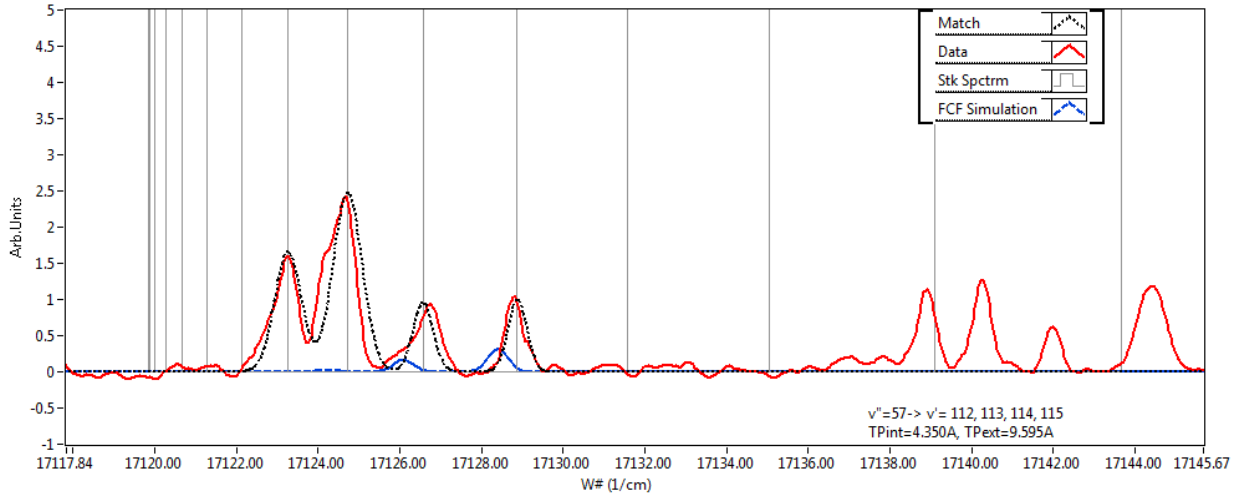
Match
Data
Stk Spctrm
FCF Simulation
Arb.Units
W# (1/cm)
v"=57-> v'= 112, 113, 114, 115
TPint=4.350A, TPext=9.595A

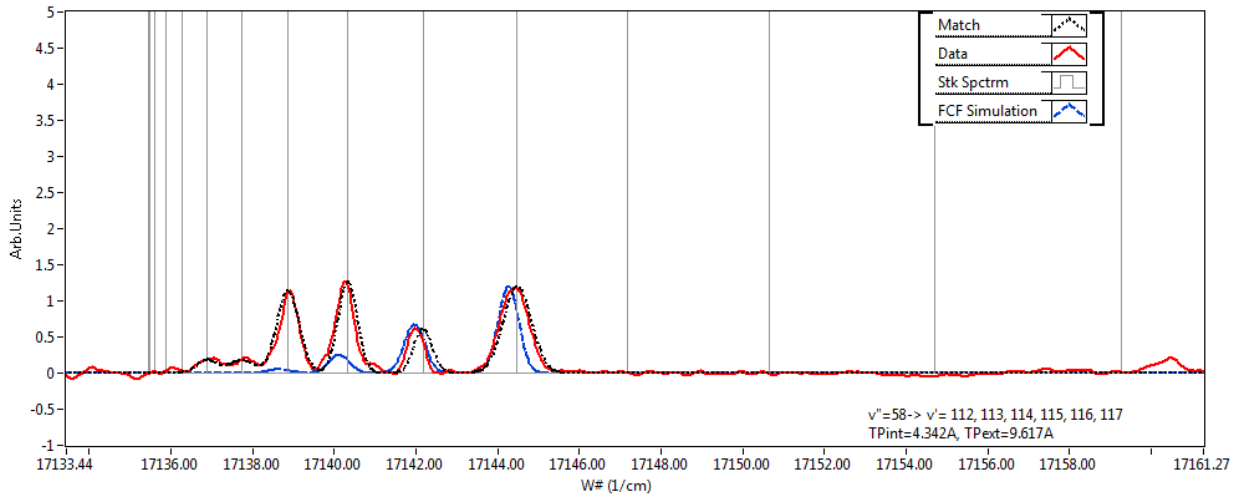
Match
Data
Stk Spctrm
FCF Simulation
Arb.Units
W# (1/cm)
v"=58-> v'= 112, 113, 114, 115, 116, 117
TPint=4.342A, TPext=9.617A

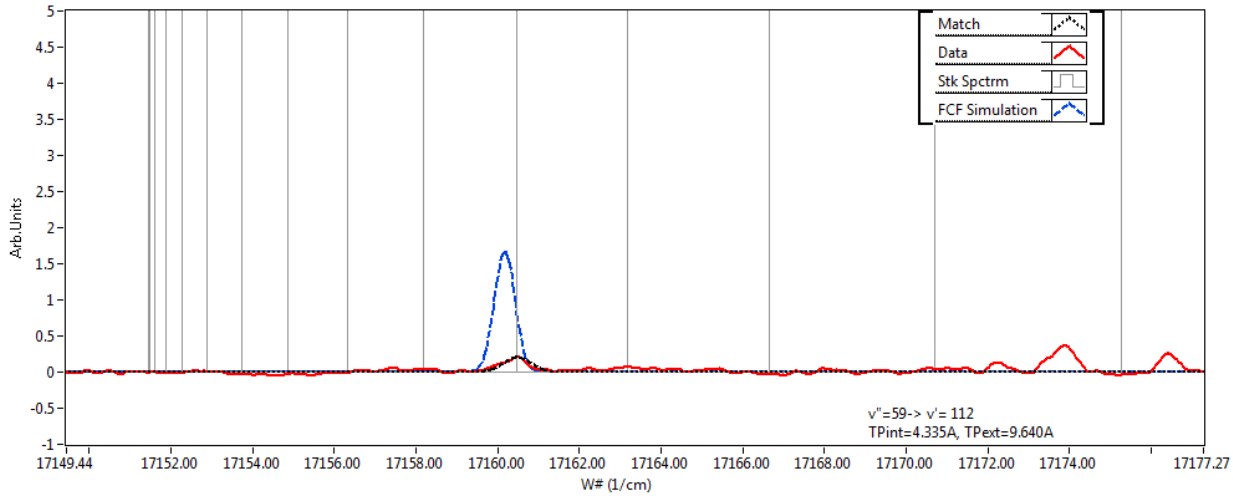
Match
Data
Stk Spctrm
FCF Simulation
Arb.Units
W# (1/cm)
v"=59-> v'= 112
TPint=4.335A, TPext=9.640A

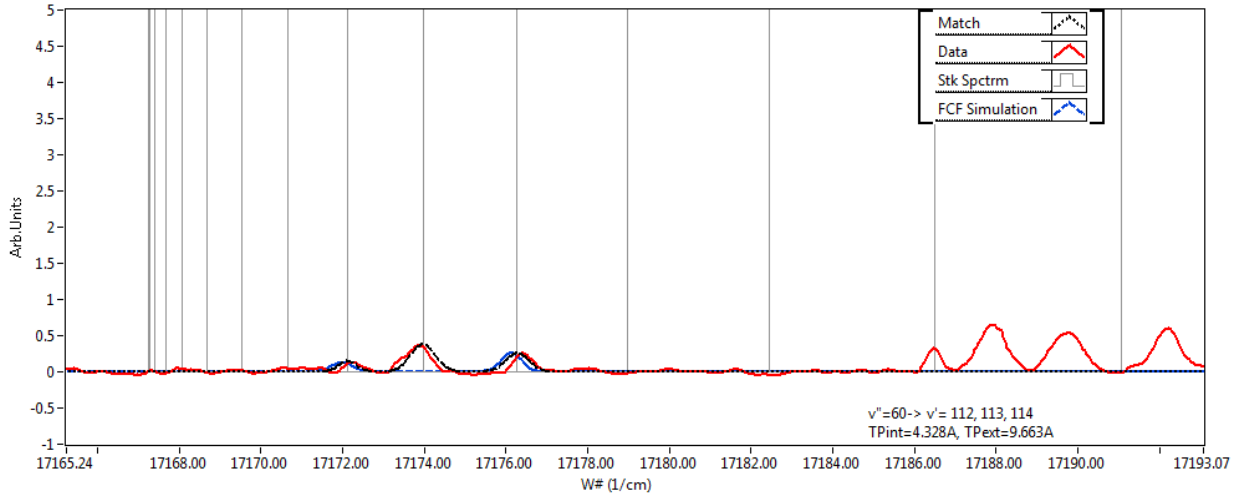
Match
Data
Stk Spctrm
FCF Simulation
Arb.Units
W# (1/cm)
v"=60-> v'= 112, 113, 114
TPint=4.328A, TPext=9.663A

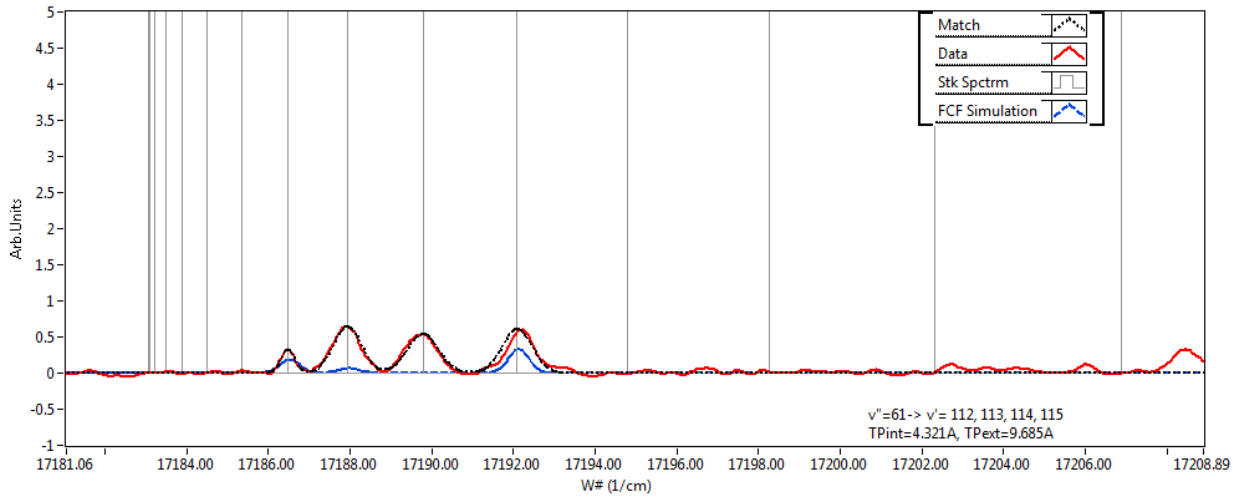
Match
Data
Stk Spctrm
FCF Simulation
Arb.Units
v"=61-> v'= 112, 113, 114, 115
TPint=4.321A, TPext=9.685A
W# (1/cm)

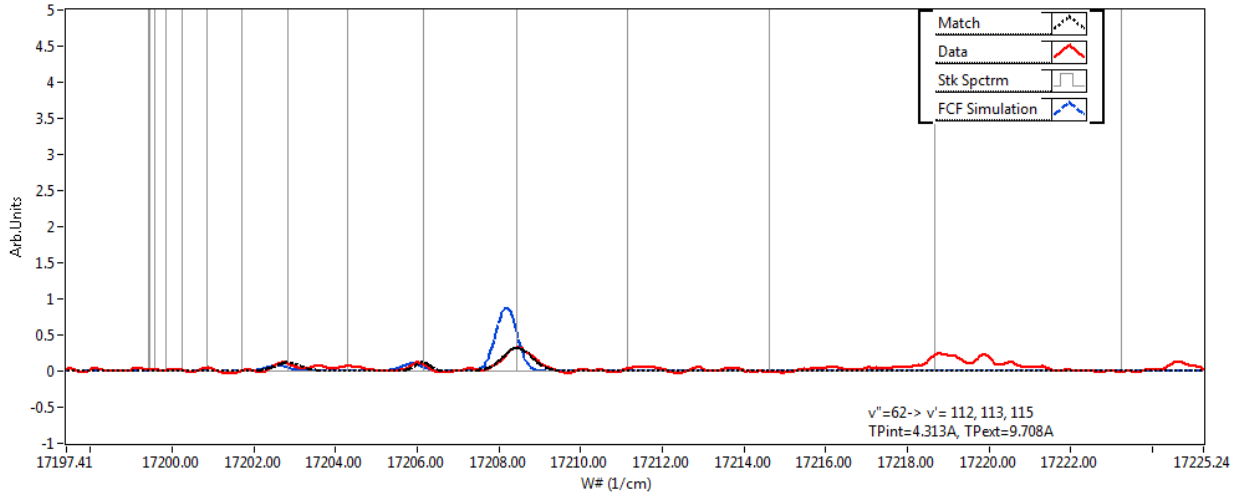
Match
Data
Stk Spctrm
FCF Simulation
Arb.Units
v"=62-> v'= 112, 113, 115
TPint=4.313A, TPext=9.708A
W# (1/cm)

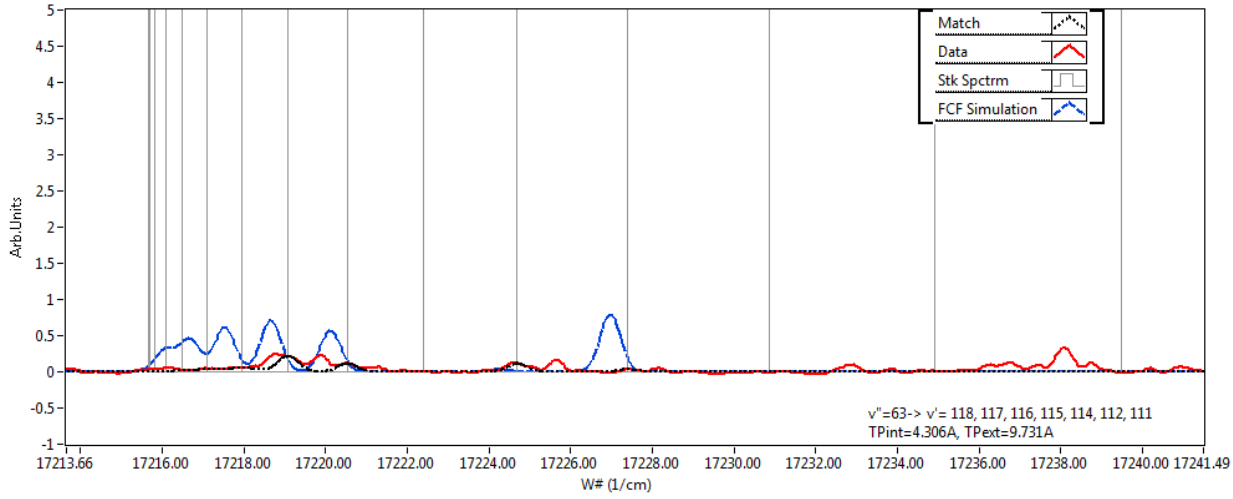
Match
Data
Stk Spctrm
FCF Simulation
Arb.Units
v"=63-> v'= 118, 117, 116, 115, 114, 112, 111
TPint=4.306A, TPext=9.731A
W# (1/cm)

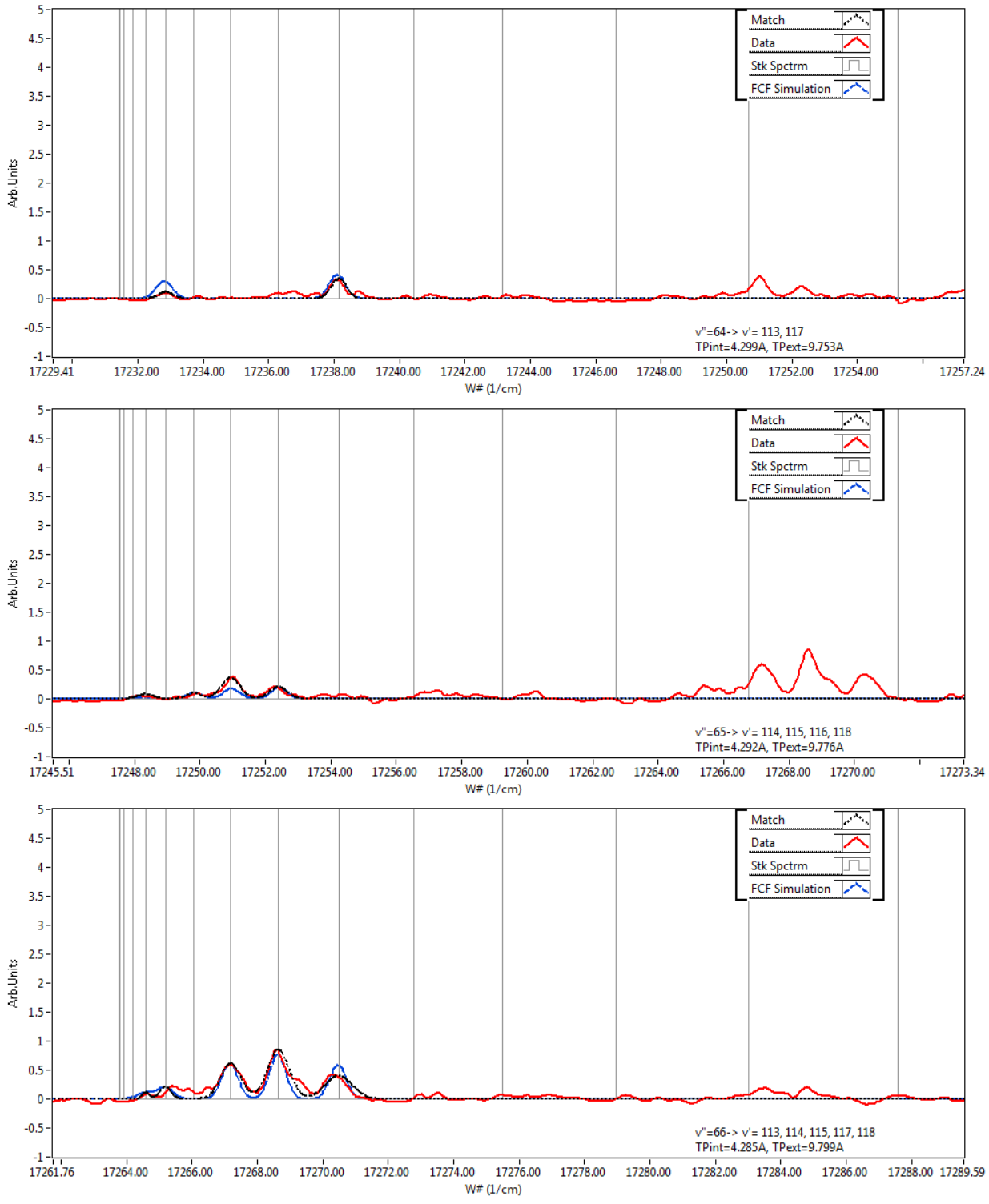
Match
Data
Stk Spctrm
FCF Simulation
Arb.Units
W# (1/cm)
v"=64-> v'= 113, 117
TPint=4.299A, TPext=9.753A
v"=65-> v'= 114, 115, 116, 118
TPint=4.292A, TPext=9.776A
v"=66-> v'= 113, 114, 115, 117, 118
TPint=4.285A, TPext=9.799A

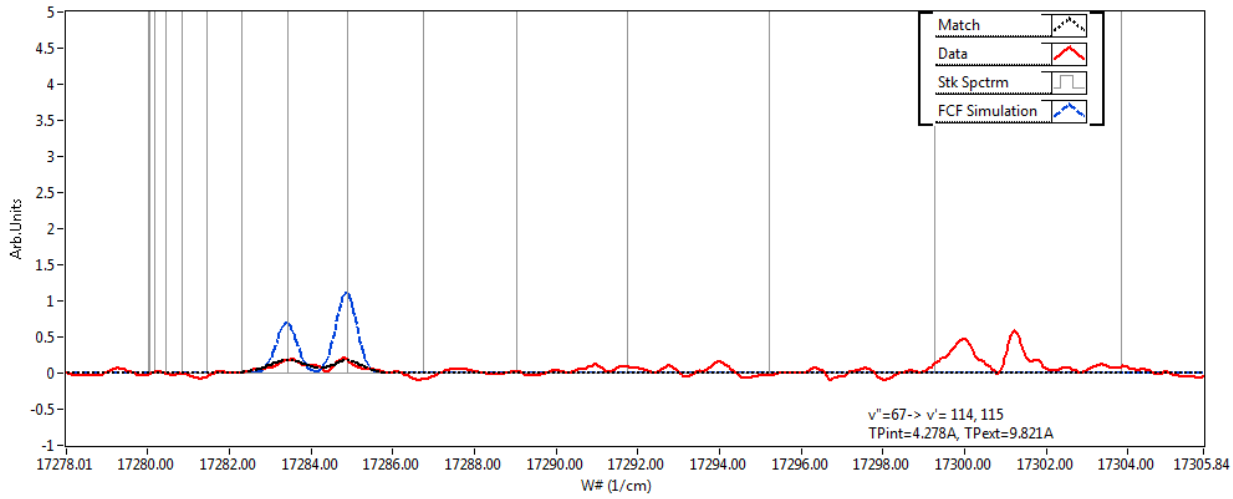
Match
Data
Stk Spctrm
FCF Simulation
Arb.Units
W# (1/cm)
v"=67-> v'= 114, 115
TPint=4.278A, TPext=9.821A

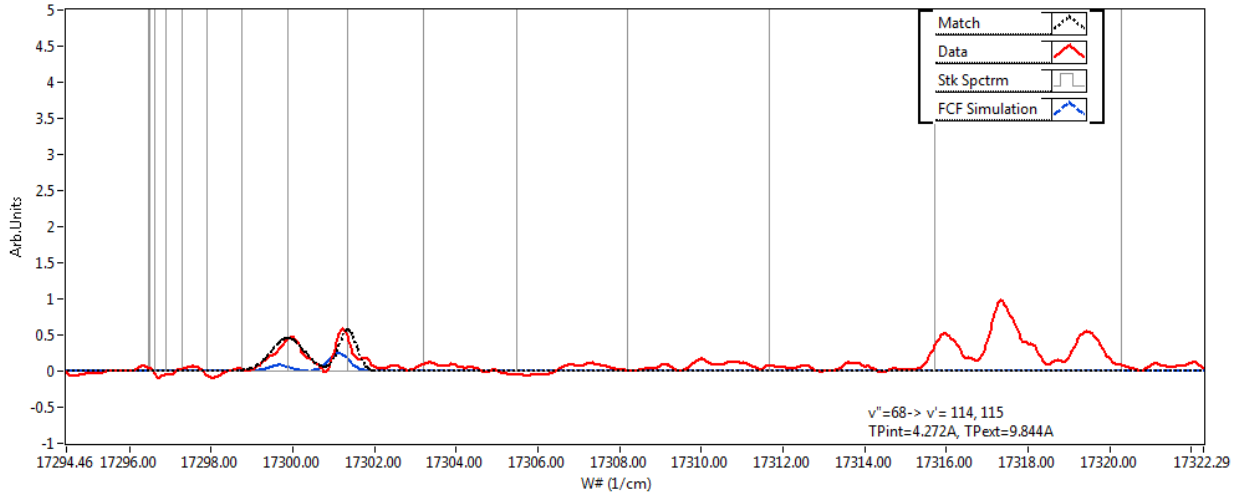
Match
Data
Stk Spctrm
FCF Simulation
Arb.Units
W# (1/cm)
v"=68-> v'= 114, 115
TPint=4.272A, TPext=9.844A

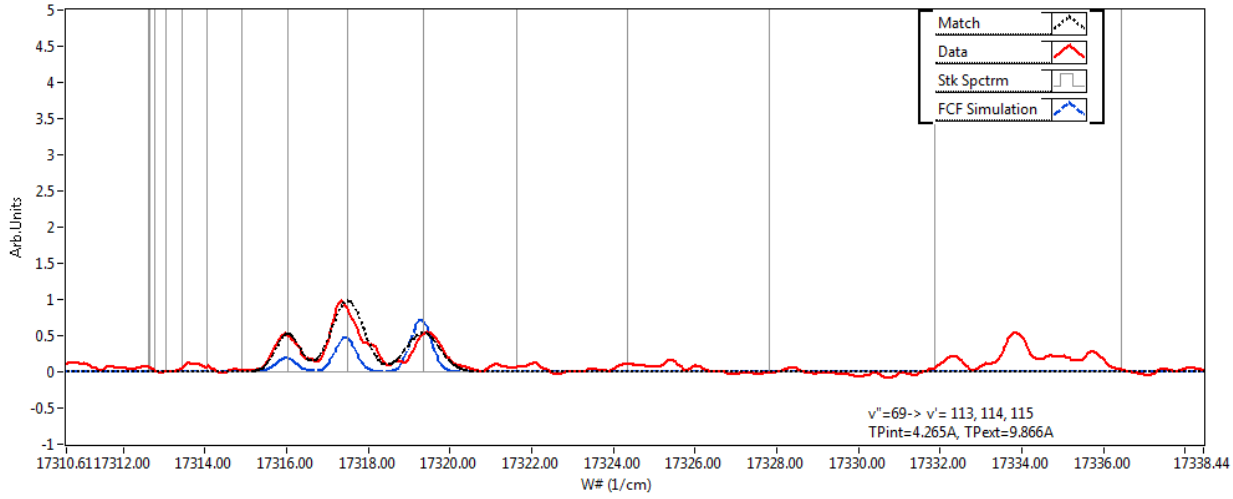
Match
Data
Stk Spctrm
FCF Simulation
Arb.Units
W# (1/cm)
v"=69-> v'= 113, 114, 115
TPint=4.265A, TPext=9.866A

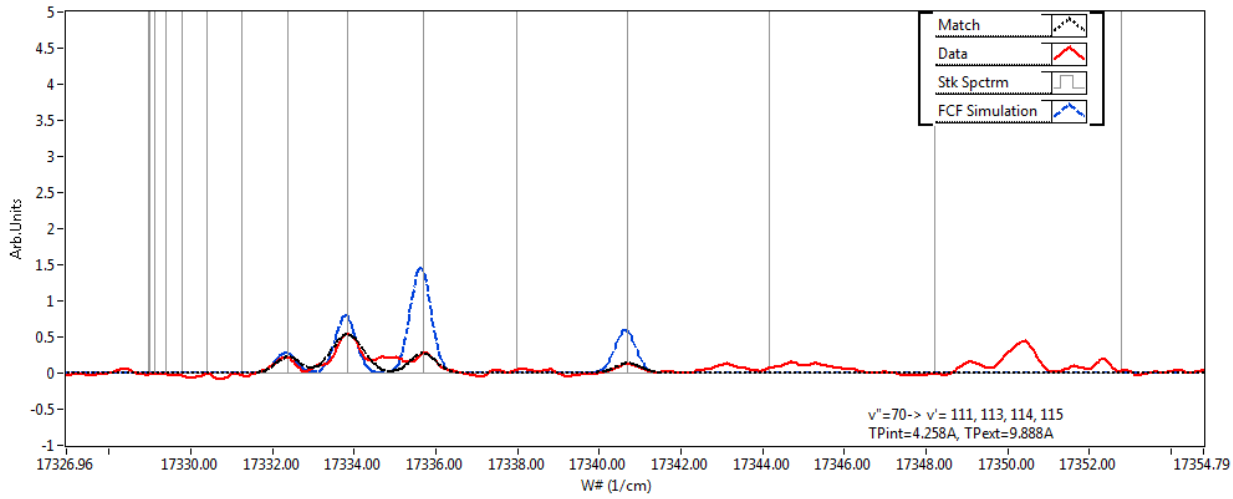
Match
Data
Stk Spctrm
FCF Simulation
Arb.Units
W# (1/cm)
v"=70-> v'= 111, 113, 114, 115
TPint=4.258A, TPext=9.888A

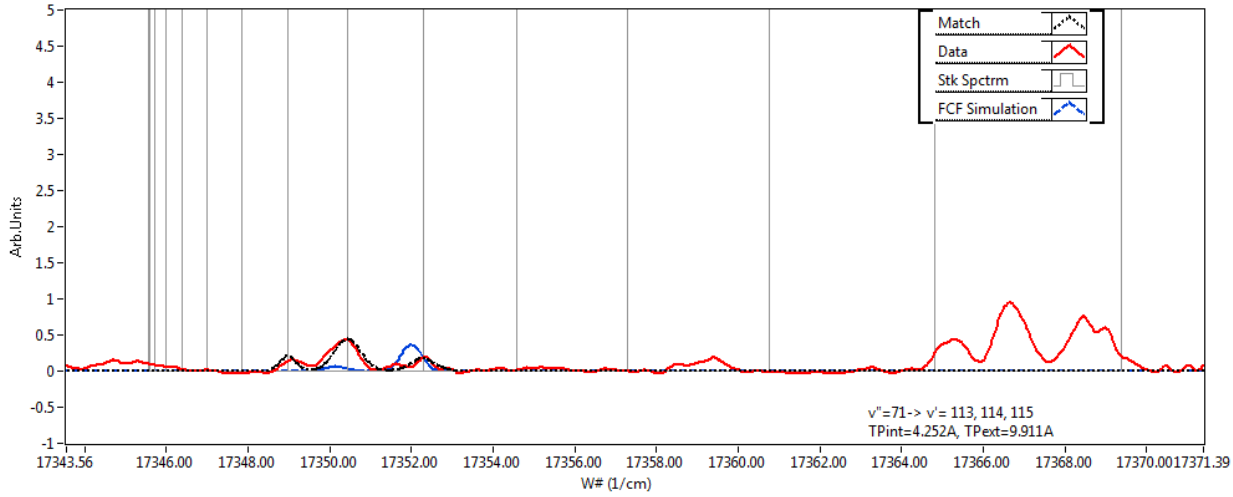
Match
Data
Stk Spctrm
FCF Simulation
Arb.Units
W# (1/cm)
v"=71-> v'= 113, 114, 115
TPint=4.252A, TPext=9.911A

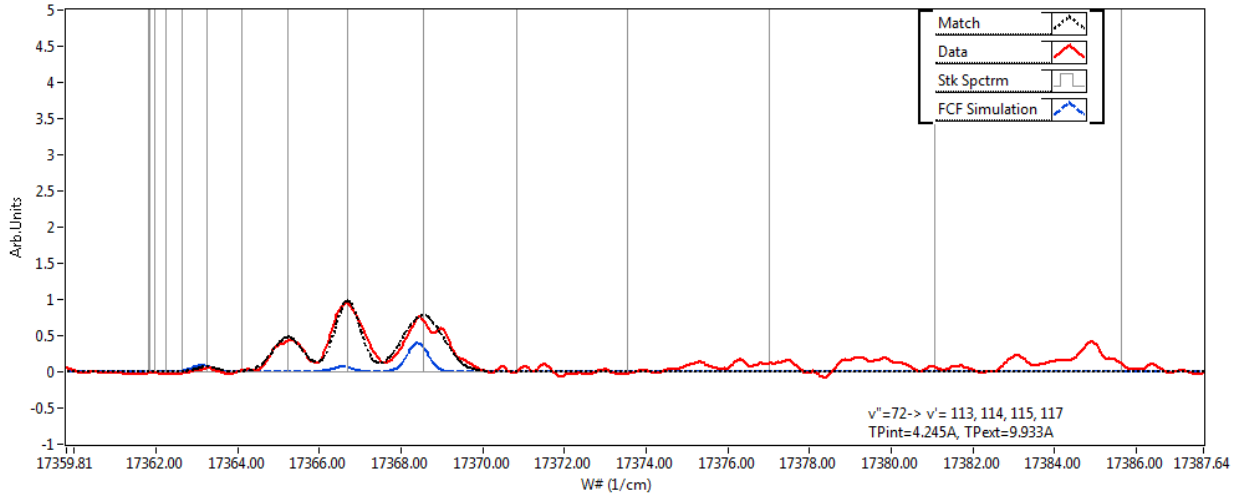
Match
Data
Stk Spctrm
FCF Simulation
Arb.Units
W# (1/cm)
v"=72-> v'= 113, 114, 115, 117
TPint=4.245A, TPext=9.933A

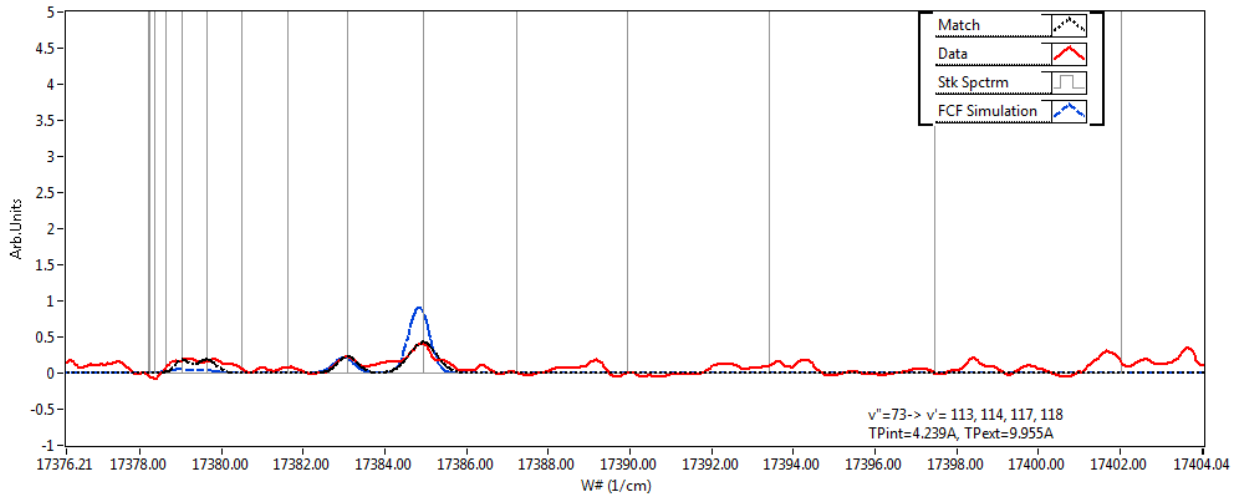
Match
Data
Stk Spctrm
FCF Simulation
Arb.Units
W# (1/cm)
v"=73-> v'= 113, 114, 117, 118
TPint=4.239A, TPext=9.955A

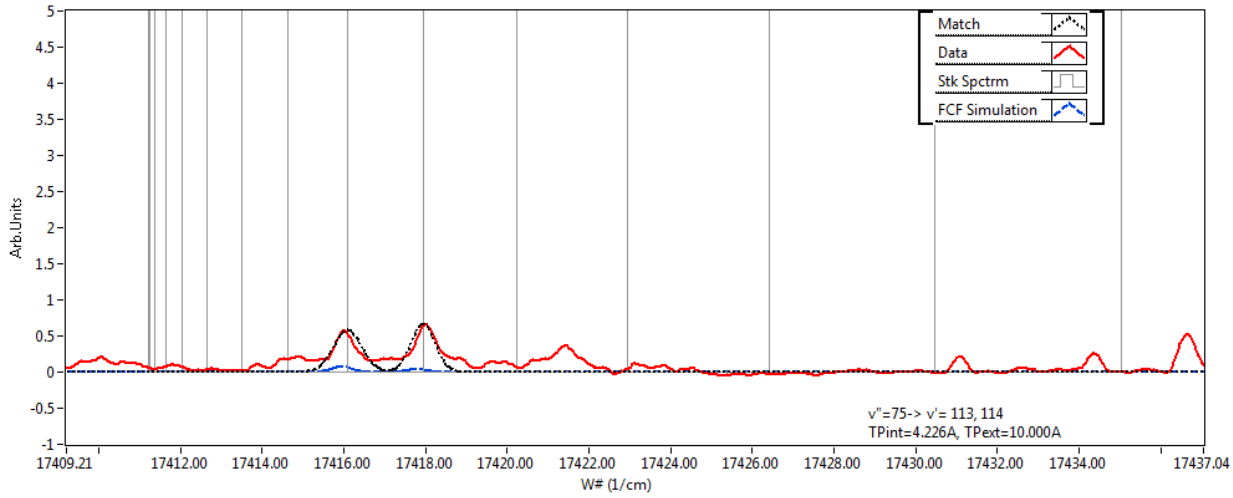
Match
Data
Stk Spctrm
FCF Simulation
Arb.Units
W# (1/cm)
v"=75-> v'= 113, 114
TPint=4.226A, TPext=10.000A

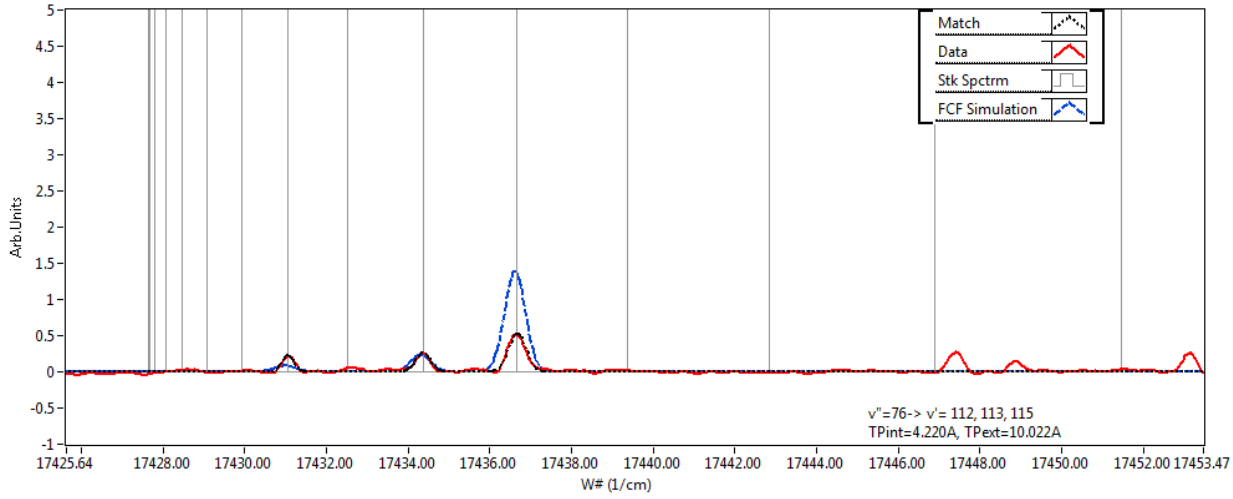
Match
Data
Stk Spctrm
FCF Simulation
Arb.Units
W# (1/cm)
v"=76-> v'= 112, 113, 115
TPint=4.220A, TPext=10.022A

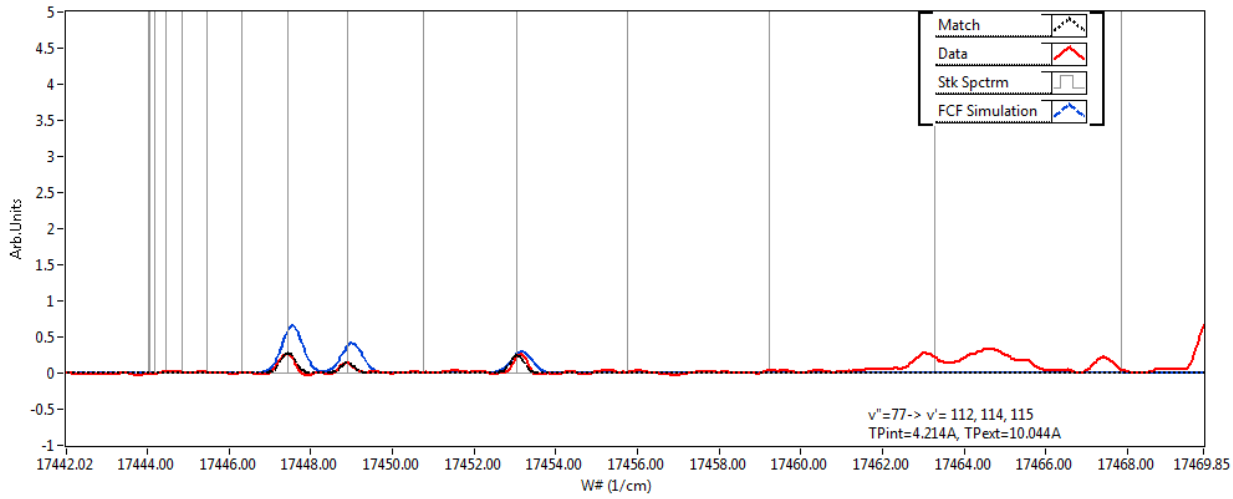
Match
Data
Stk Spctrm
FCF Simulation
Arb.Units
W# (1/cm)
v"=77-> v'= 112, 114, 115
TPint=4.214A, TPext=10.044A

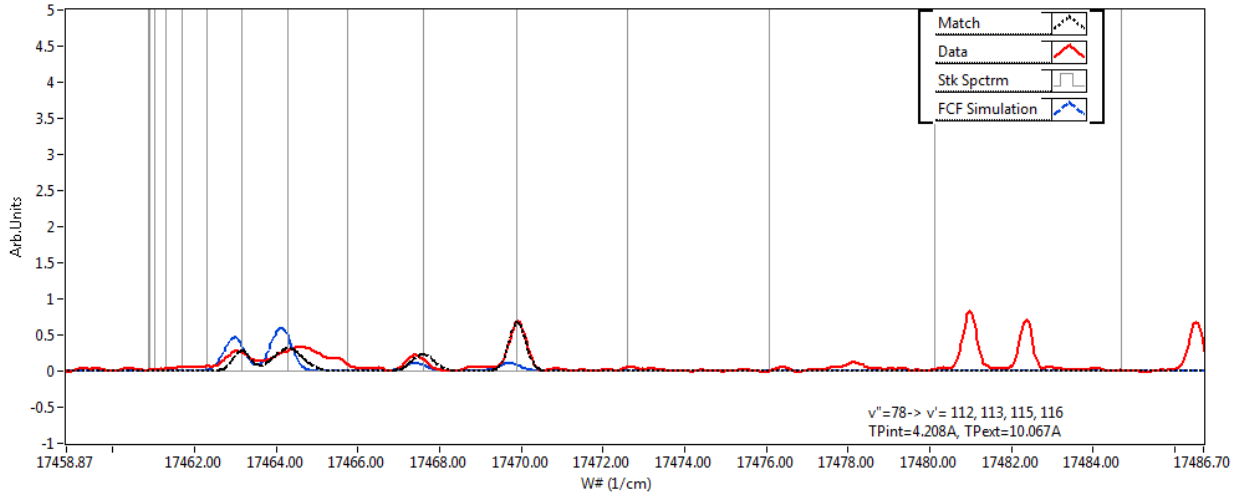
Match
Data
Stk Spctrm
FCF Simulation
Arb.Units
W# (1/cm)
v"=78-> v'= 112, 113, 115, 116
TPint=4.208A, TPext=10.067A

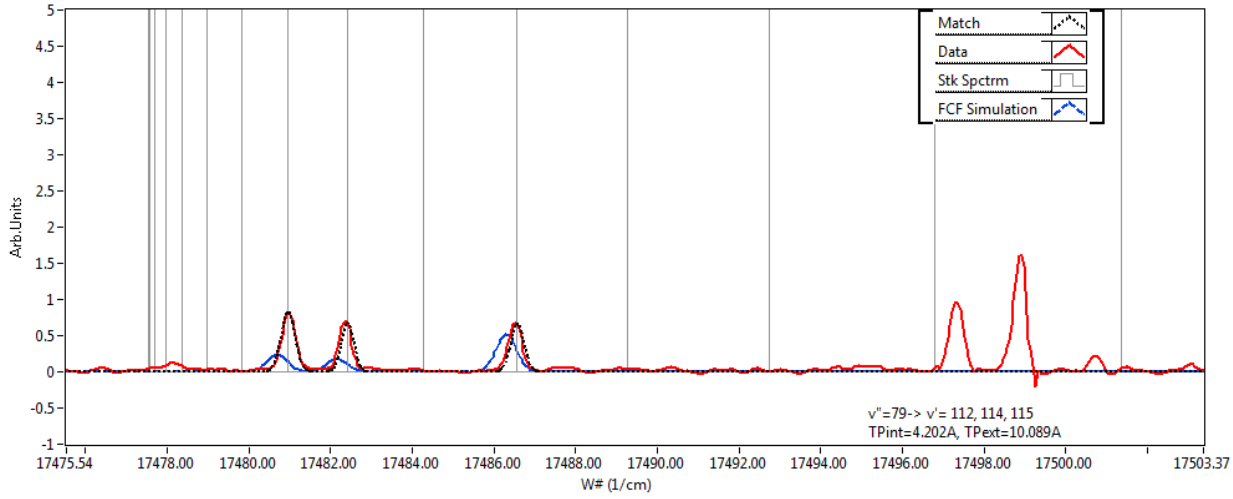
Match
Data
Stk Spctrm
FCF Simulation
Arb.Units
W# (1/cm)
v"=79-> v'= 112, 114, 115
TPint=4.202A, TPext=10.089A

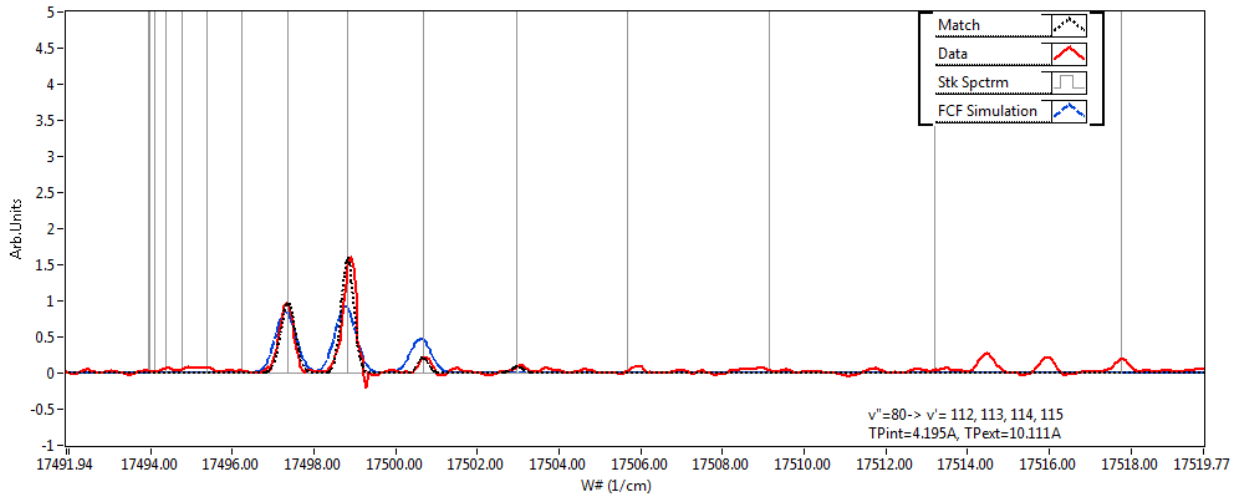
Match
Data
Stk Spctrm
FCF Simulation
Arb.Units
W# (1/cm)
v"=80-> v'= 112, 113, 114, 115
TPint=4.195A, TPext=10.111A

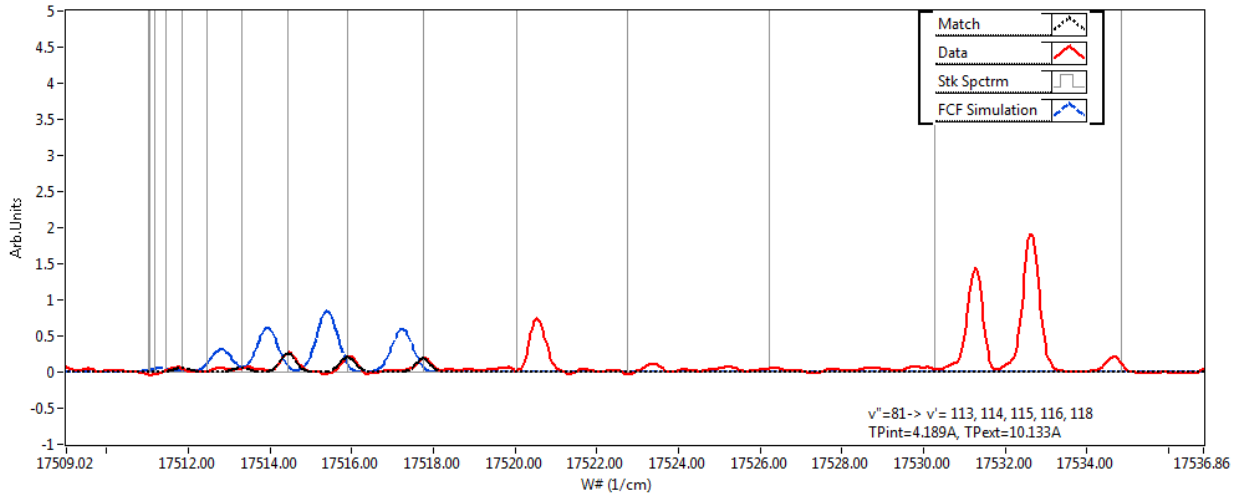
Match
Data
Stk Spctrm
FCF Simulation
Arb.Units
W# (1/cm)
v"=81-> v'= 113, 114, 115, 116, 118
TPint=4.189A, TPext=10.133A

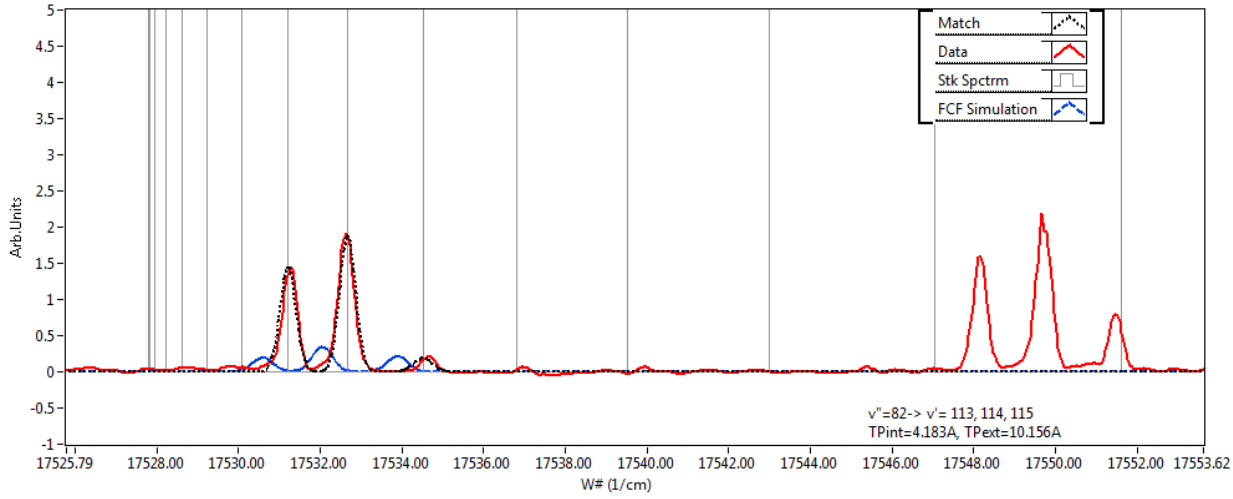
Match
Data
Stk Spctrm
FCF Simulation
Arb.Units
W# (1/cm)
v"=82-> v'= 113, 114, 115
TPint=4.183A, TPext=10.156A

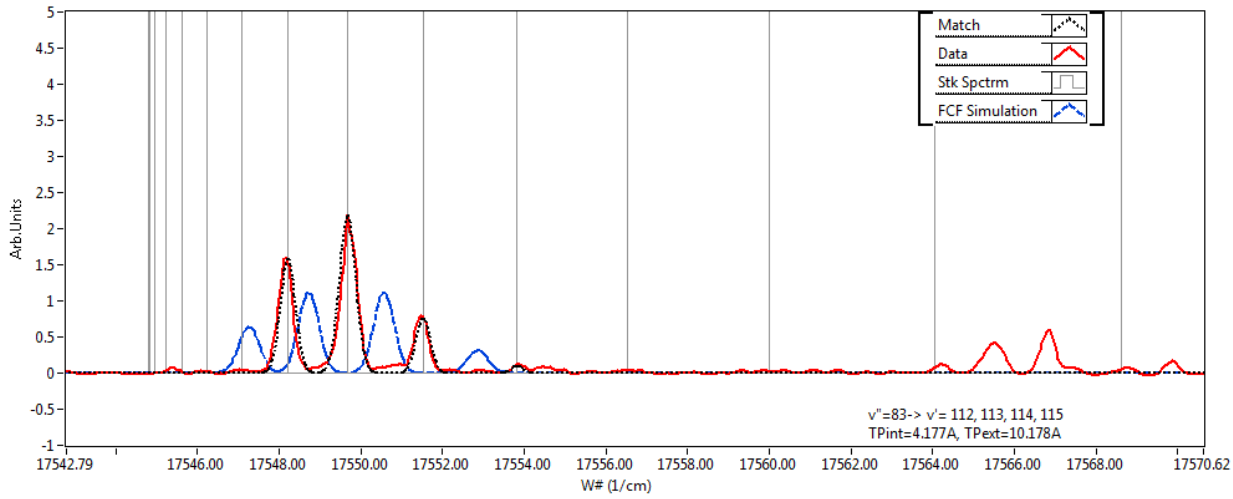
Match
Data
Stk Spctrm
FCF Simulation
Arb.Units
W# (1/cm)
v"=83-> v'= 112, 113, 114, 115
TPint=4.177A, TPext=10.178A

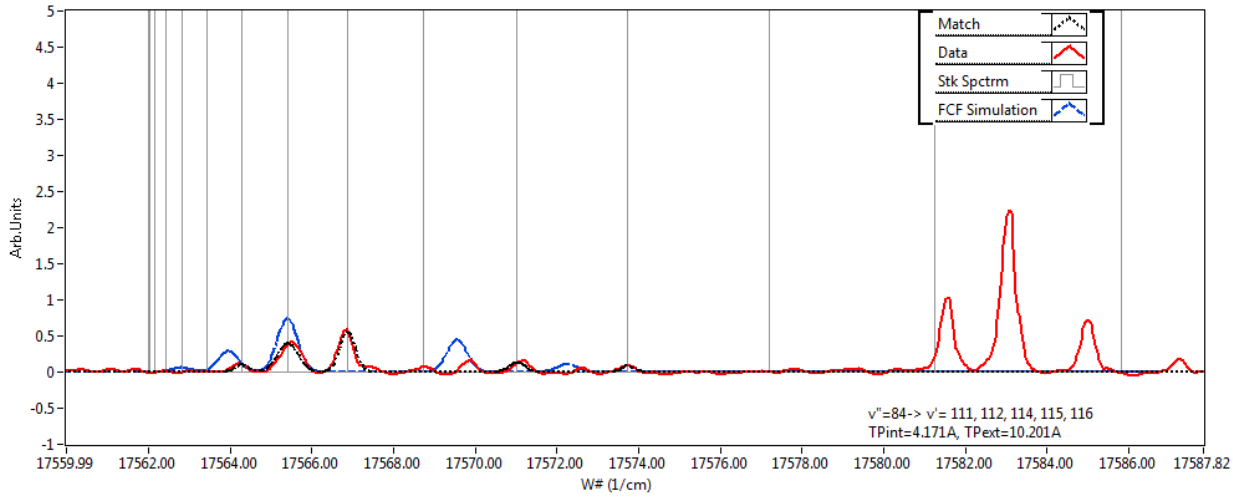
Match
Data
Stk Spctrm
FCF Simulation
Arb.Units
W# (1/cm)
v"=84-> v'= 111, 112, 114, 115, 116
TPint=4.171A, TPext=10.201A

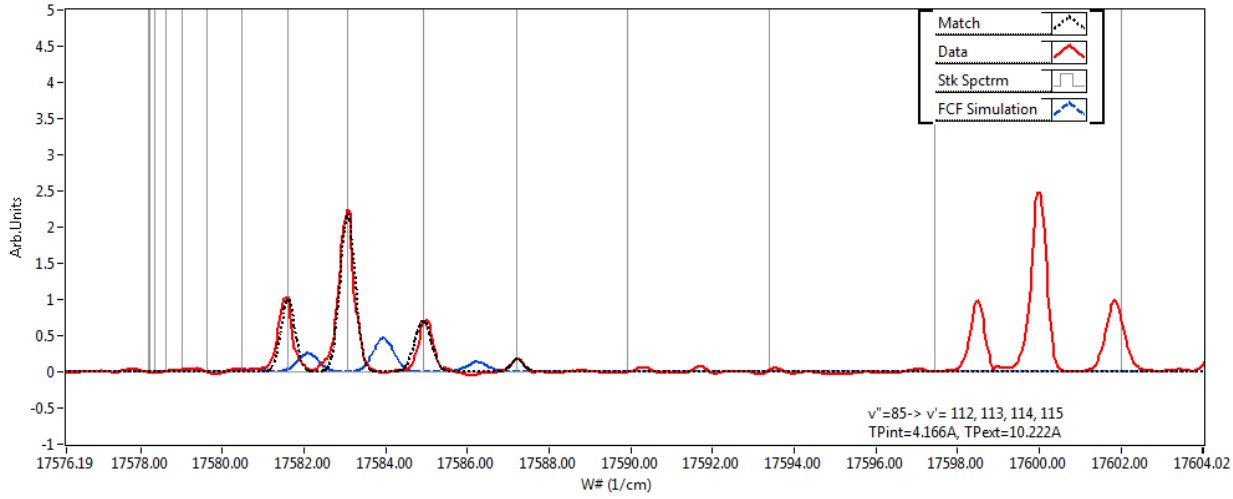
Match
Data
Stk Spctrm
FCF Simulation
Arb.Units
W# (1/cm)
v"=85-> v'= 112, 113, 114, 115
TPint=4.166A, TPext=10.222A

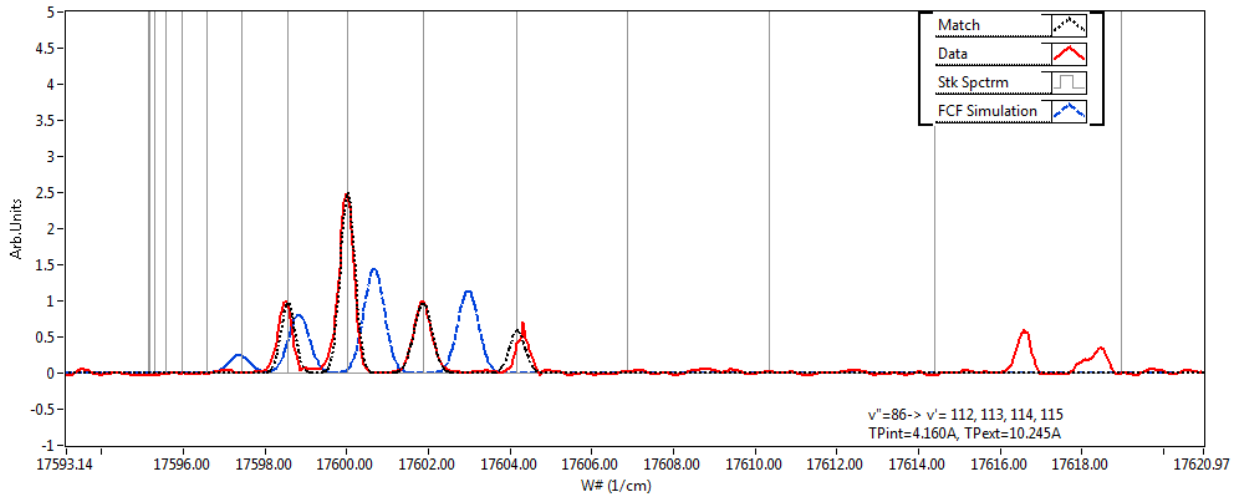
Match
Data
Stk Spctrm
FCF Simulation
Arb.Units
W# (1/cm)
v"=86-> v'= 112, 113, 114, 115
TPint=4.160A, TPext=10.245A

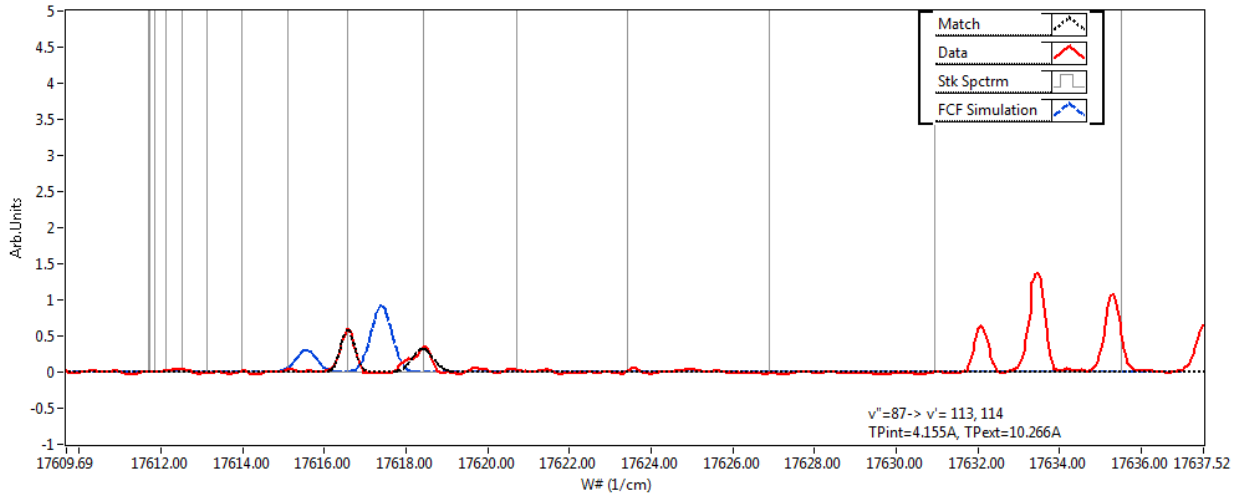
Match
Data
Stk Spctrm
FCF Simulation
Arb.Units
W# (1/cm)
v"=87-> v'= 113, 114
TPint=4.155A, TPext=10.266A

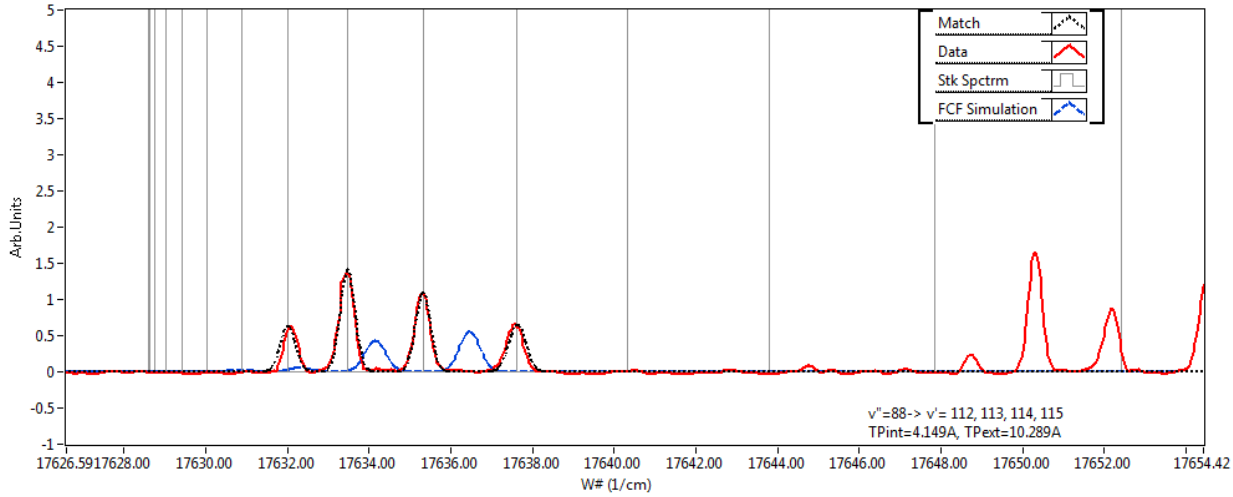
Match
Data
Stk Spctrm
FCF Simulation
Arb.Units
W# (1/cm)
v"=88-> v'= 112, 113, 114, 115
TPint=4.149A, TPext=10.289A

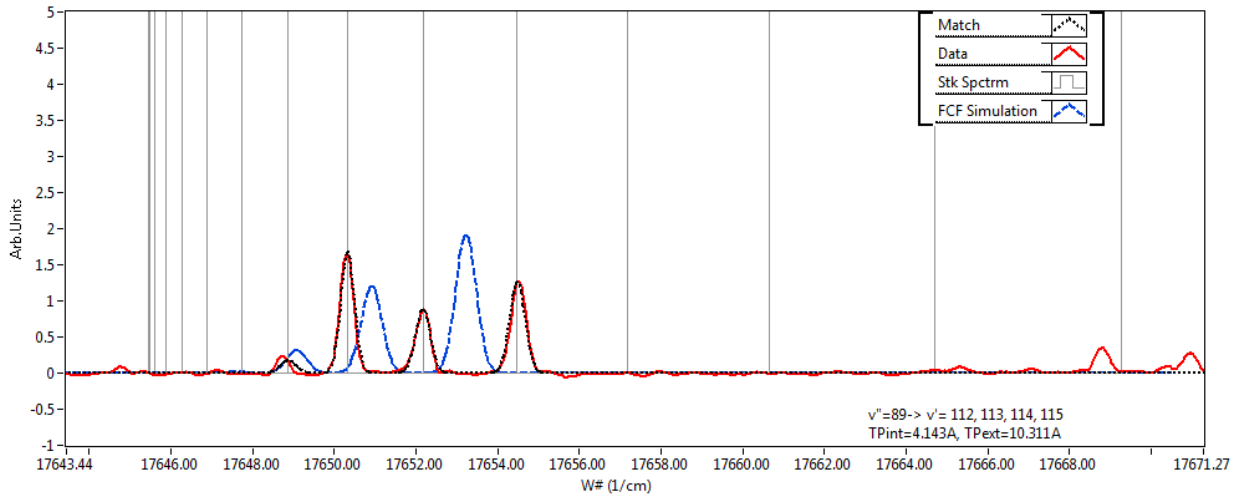
Match
Data
Stk Spctrm
FCF Simulation
Arb.Units
W# (1/cm)
v"=89-> v'= 112, 113, 114, 115
TPint=4.143A, TPext=10.311A

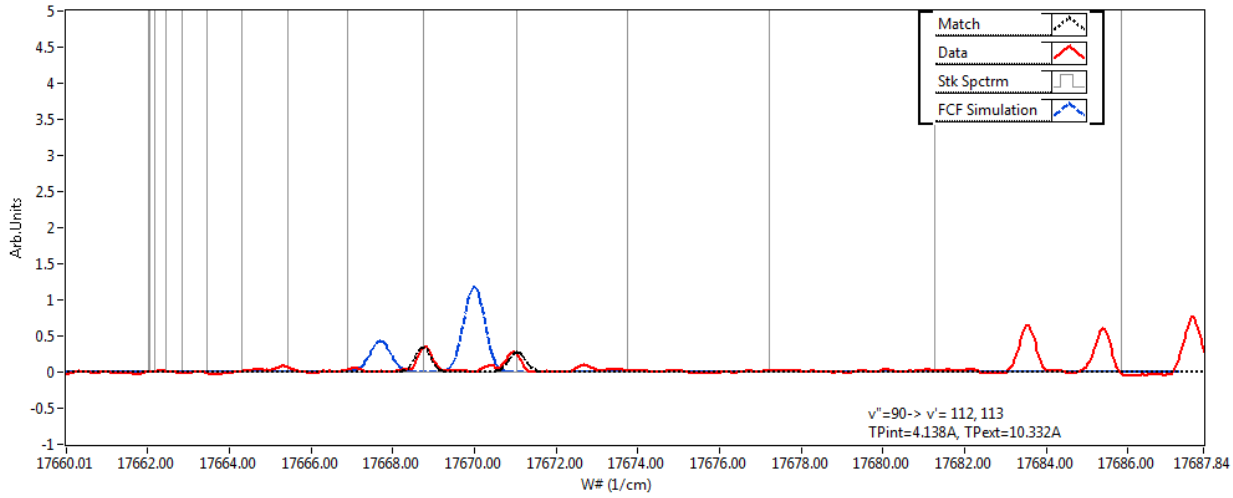
Match
Data
Stk Spctrm
FCF Simulation
Arb.Units
W# (1/cm)
v"=90-> v'= 112, 113
TPint=4.138A, TPext=10.332A

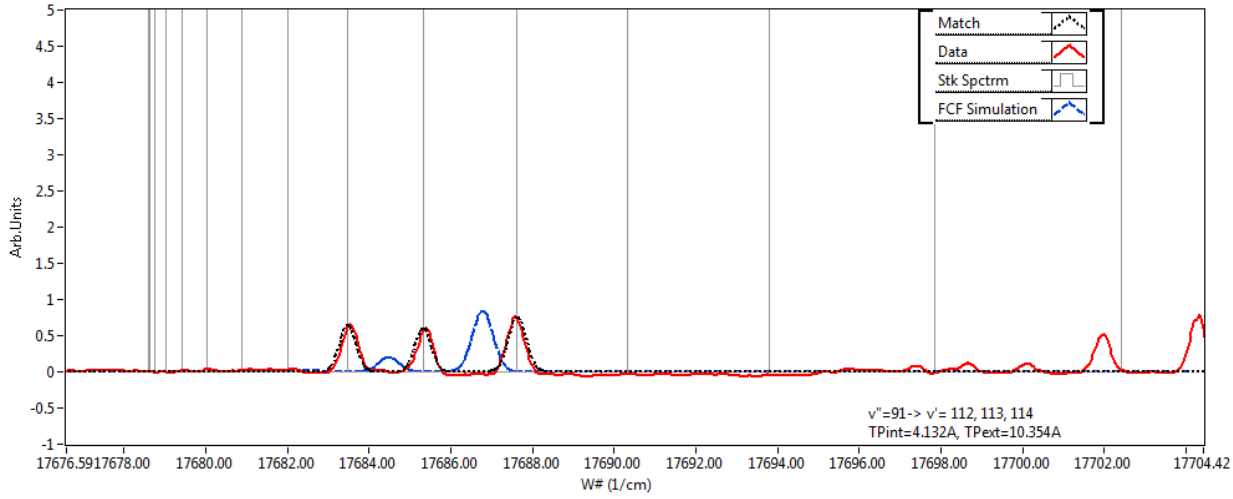
Match
Data
Stk Spctrm
FCF Simulation
Arb.Units
W# (1/cm)
v"=91-> v'= 112, 113, 114
TPint=4.132A, TPext=10.354A

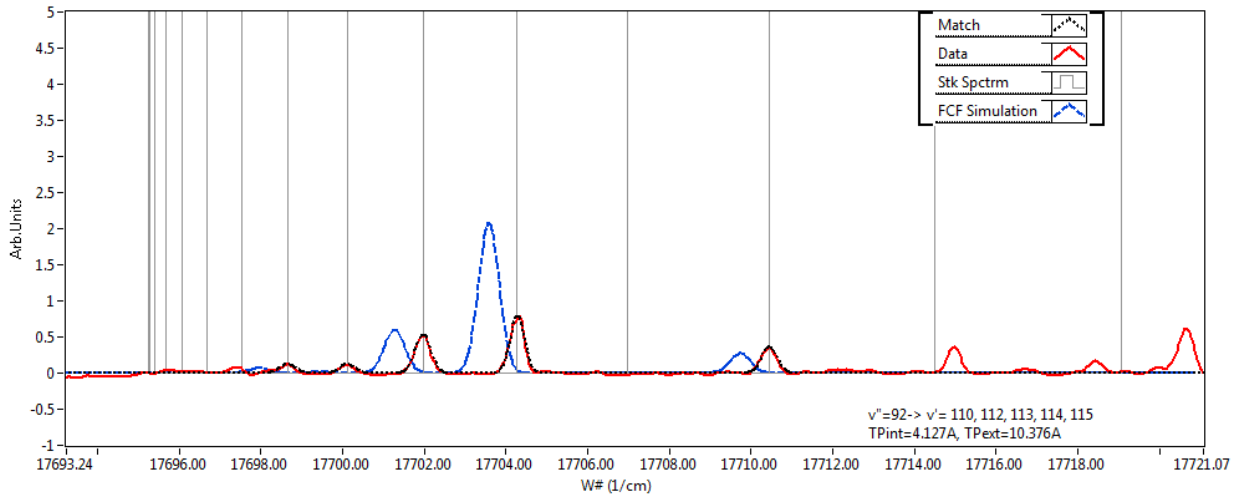
Match
Data
Stk Spctrm
FCF Simulation
Arb.Units
W# (1/cm)
v"=92-> v'= 110, 112, 113, 114, 115
TPint=4.127A, TPext=10.376A

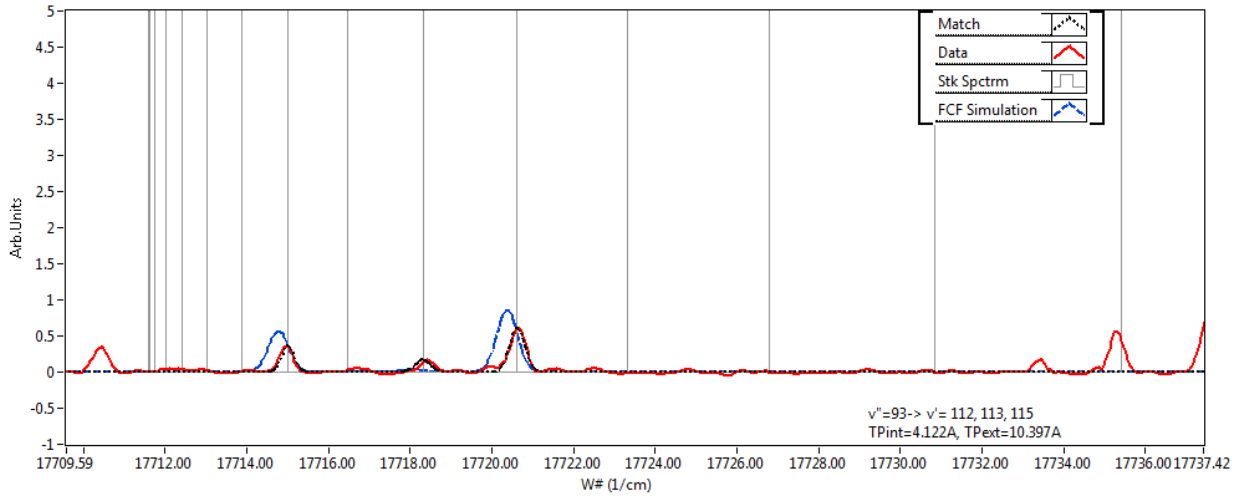
Match
Data
Stk Spctrm
FCF Simulation
Arb.Units
W# (1/cm)
v"=93-> v'= 112, 113, 115
TPint=4.122A, TPext=10.397A

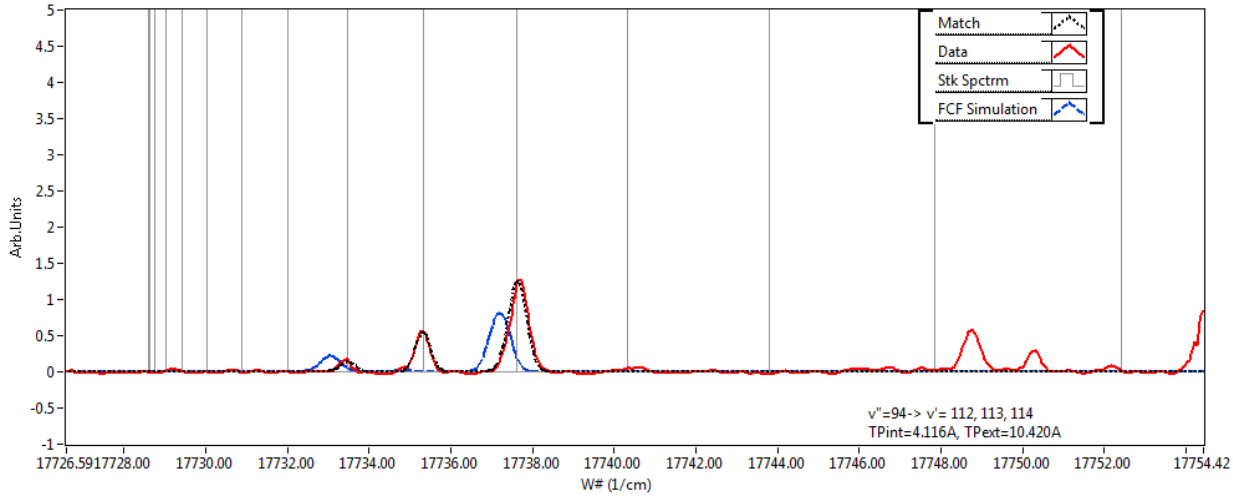
Match
Data
Stk Spctrm
FCF Simulation
Arb.Units
W# (1/cm)
v"=94-> v'= 112, 113, 114
TPint=4.116A, TPext=10.420A

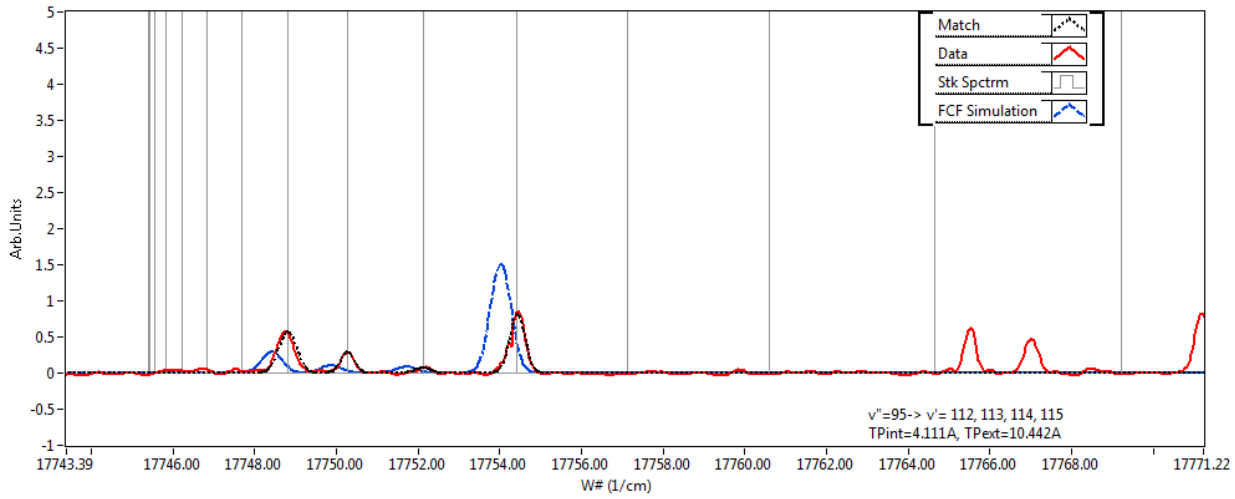
Match
Data
Stk Spctrm
FCF Simulation
Arb.Units
v"=95-> v'= 112, 113, 114, 115
TPint=4.111A, TPext=10.442A
W# (1/cm)

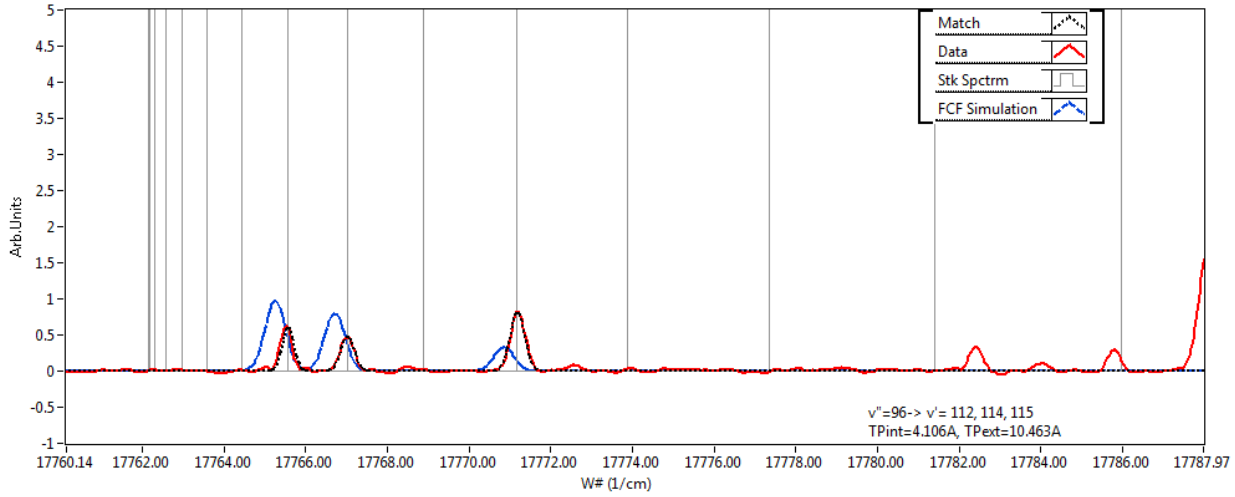
Match
Data
Stk Spctrm
FCF Simulation
Arb.Units
v"=96-> v'= 112, 114, 115
TPint=4.106A, TPext=10.463A
W# (1/cm)

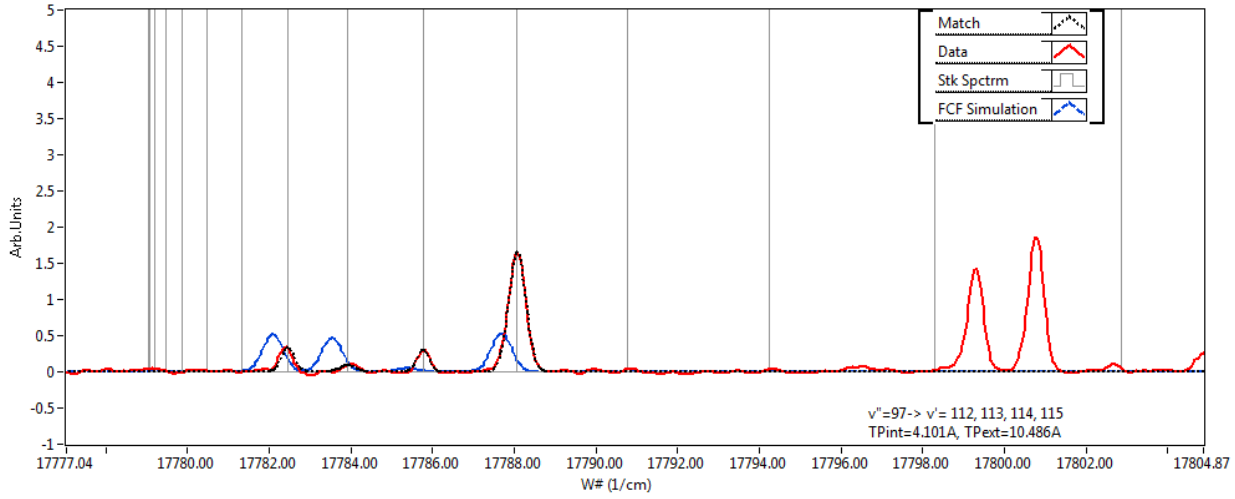
Match
Data
Stk Spctrm
FCF Simulation
Arb.Units
v"=97-> v'= 112, 113, 114, 115
TPint=4.101A, TPext=10.486A
W# (1/cm)

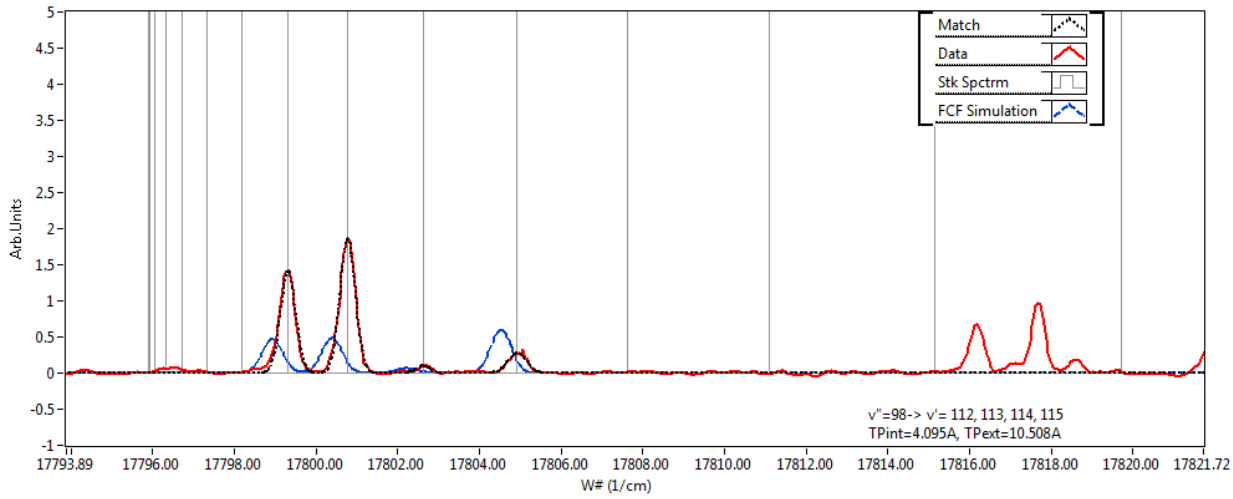
Match
Data
Stk Spctrm
FCF Simulation
Arb.Units
W# (1/cm)
v"=98-> v'= 112, 113, 114, 115
TPint=4.095A, TPext=10.508A

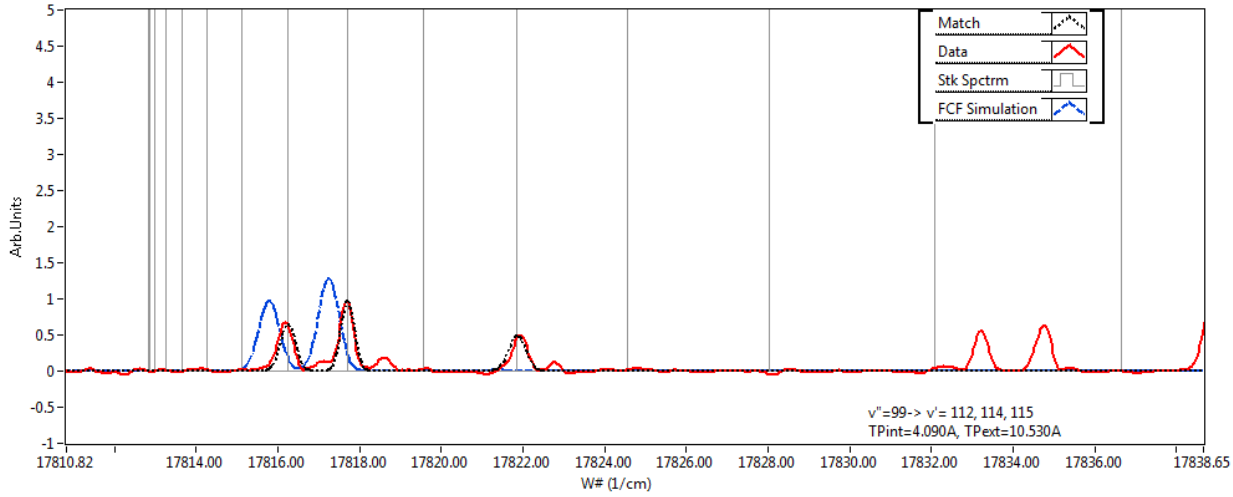
Match
Data
Stk Spctrm
FCF Simulation
Arb.Units
W# (1/cm)
v"=99-> v'= 112, 114, 115
TPint=4.090A, TPext=10.530A

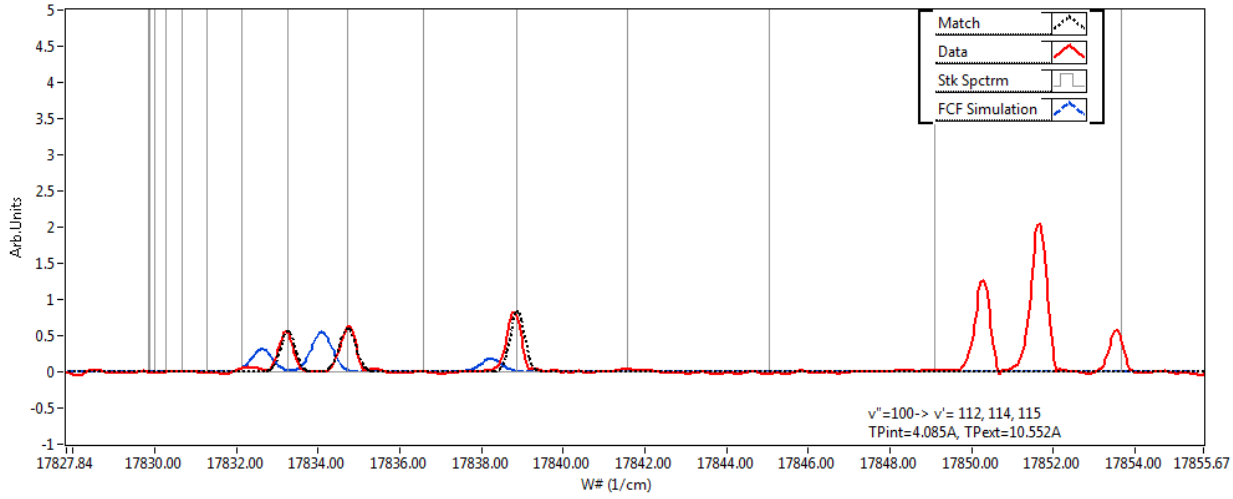
Match
Data
Stk Spctrm
FCF Simulation
Arb.Units
W# (1/cm)
v"=100-> v'= 112, 114, 115
TPint=4.085A, TPext=10.552A

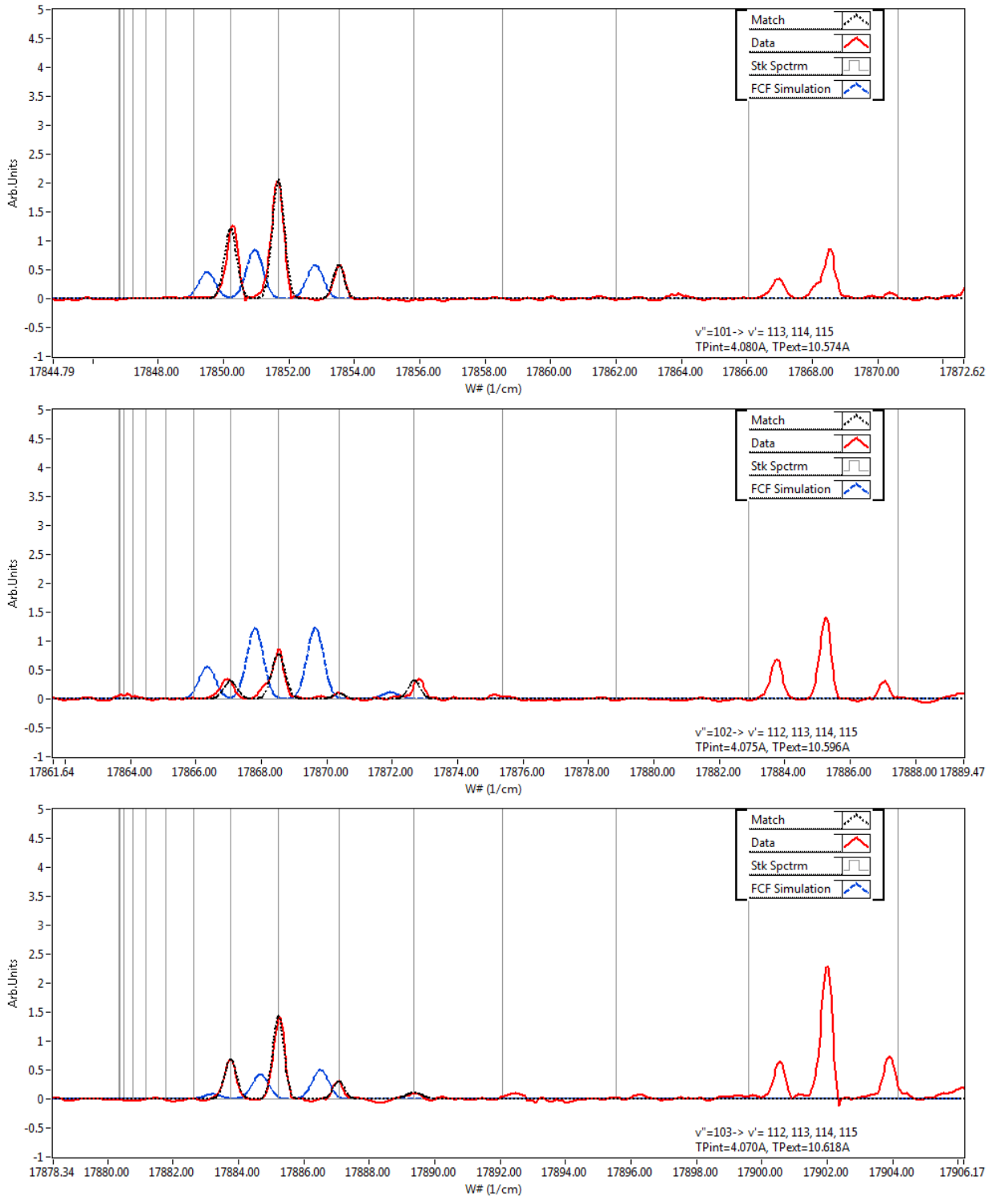
Match
Data
Stk Spctrm
FCF Simulation
Arb.Units
W# (1/cm)
v"=101-> v'= 113, 114, 115
TPint=4.080A, TPext=10.574A
v"=102-> v'= 112, 113, 114, 115
TPint=4.075A, TPext=10.596A
v"=103-> v'= 112, 113, 114, 115
TPint=4.070A, TPext=10.618A

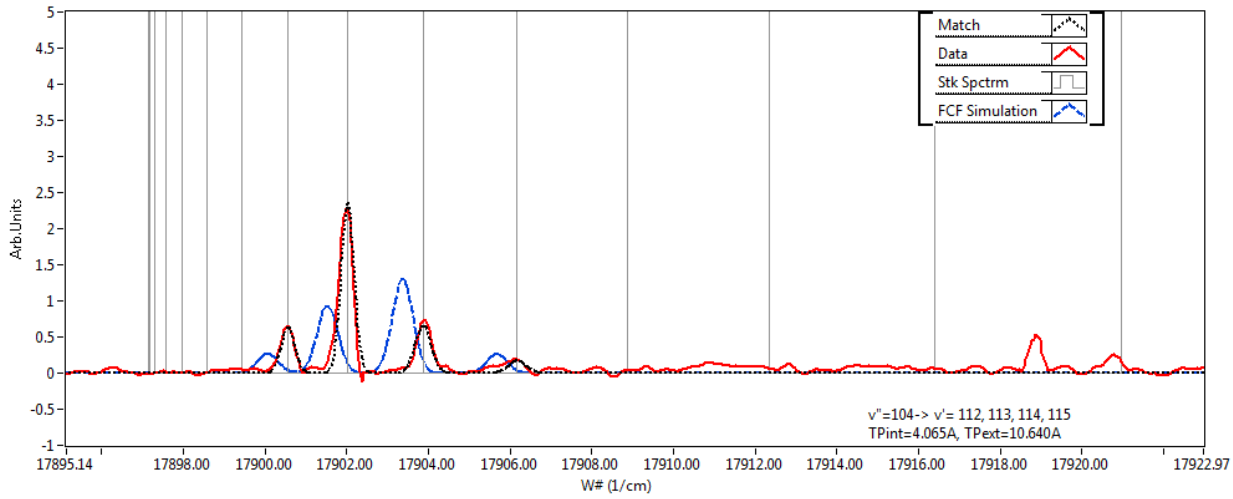
Match
Data
Stk Spctrm
FCF Simulation
Arb.Units
v"=104-> v'= 112, 113, 114, 115
TPint=4.065A, TPext=10.640A
W# (1/cm)

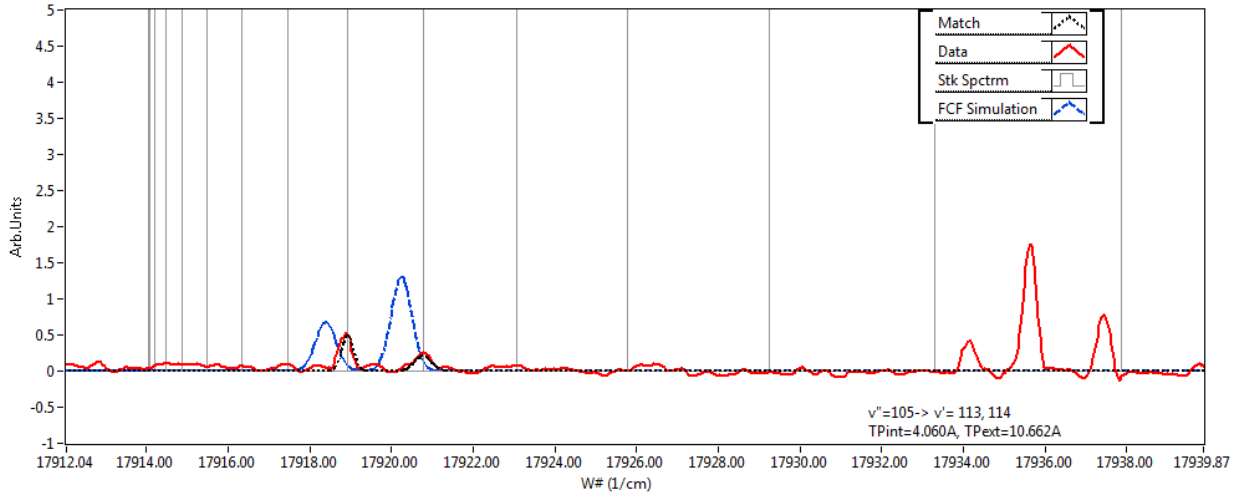
Match
Data
Stk Spctrm
FCF Simulation
Arb.Units
v"=105-> v'= 113, 114
TPint=4.060A, TPext=10.662A
W# (1/cm)

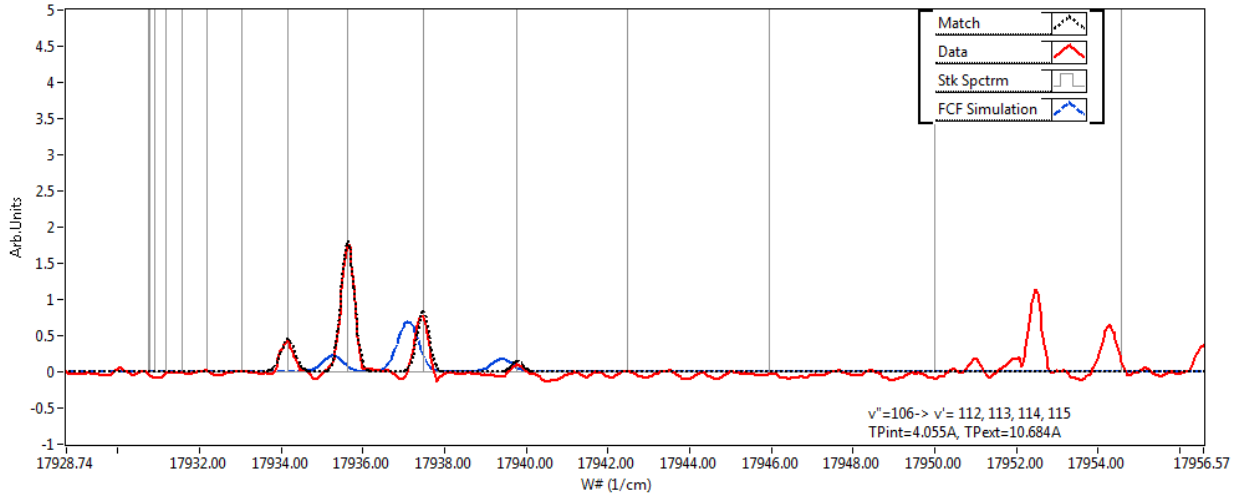
Match
Data
Stk Spctrm
FCF Simulation
Arb.Units
v"=106-> v'= 112, 113, 114, 115
TPint=4.055A, TPext=10.684A
W# (1/cm)

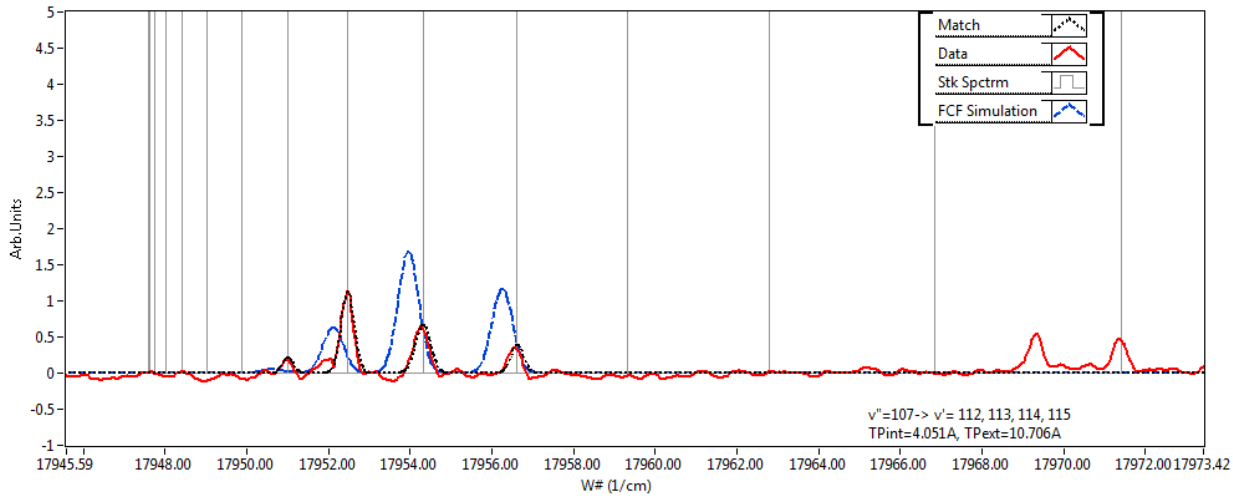
Match
Data
Stk Spctrm
FCF Simulation
Arb.Units
W# (1/cm)
v"=107-> v'= 112, 113, 114, 115
TPint=4.051A, TPext=10.706A

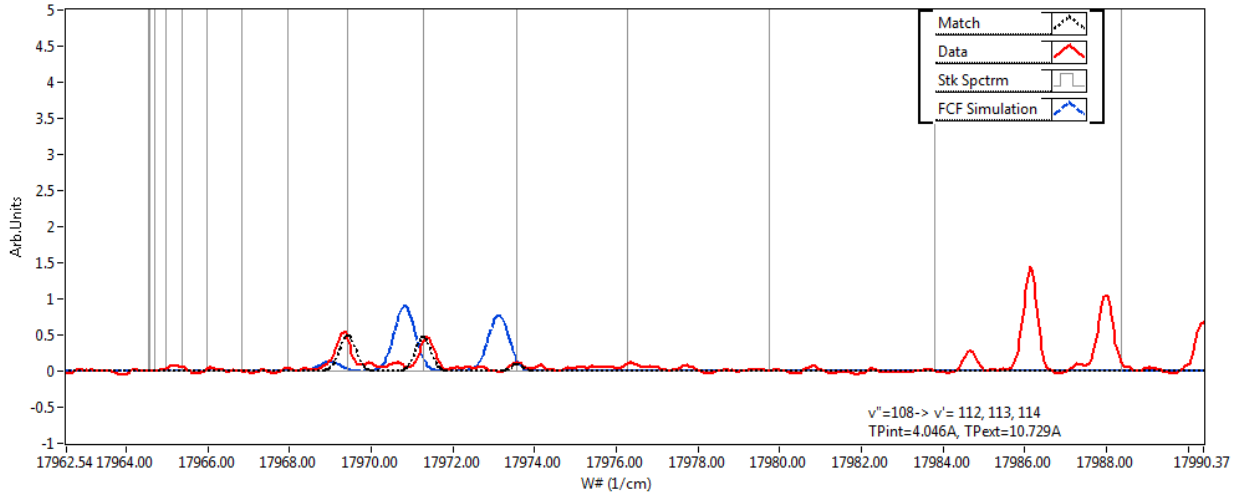
Match
Data
Stk Spctrm
FCF Simulation
Arb.Units
W# (1/cm)
v"=108-> v'= 112, 113, 114
TPint=4.046A, TPext=10.729A

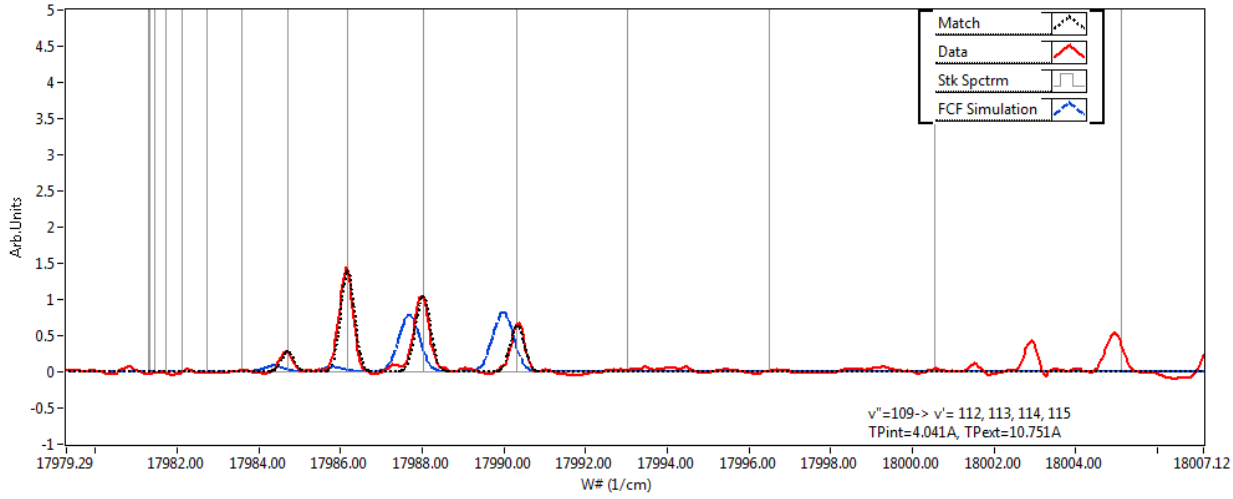
Match
Data
Stk Spctrm
FCF Simulation
Arb.Units
W# (1/cm)
v"=109-> v'= 112, 113, 114, 115
TPint=4.041A, TPext=10.751A

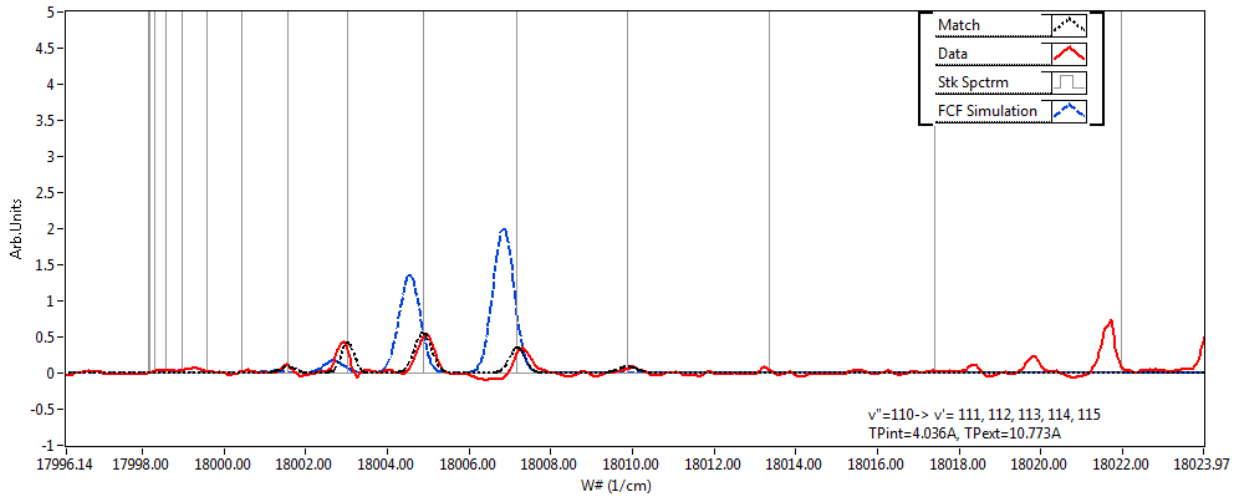
Match
Data
Stk Spctrm
FCF Simulation
Arb.Units
W# (1/cm)
v"=110-> v'= 111, 112, 113, 114, 115
TPint=4.036A, TPext=10.773A

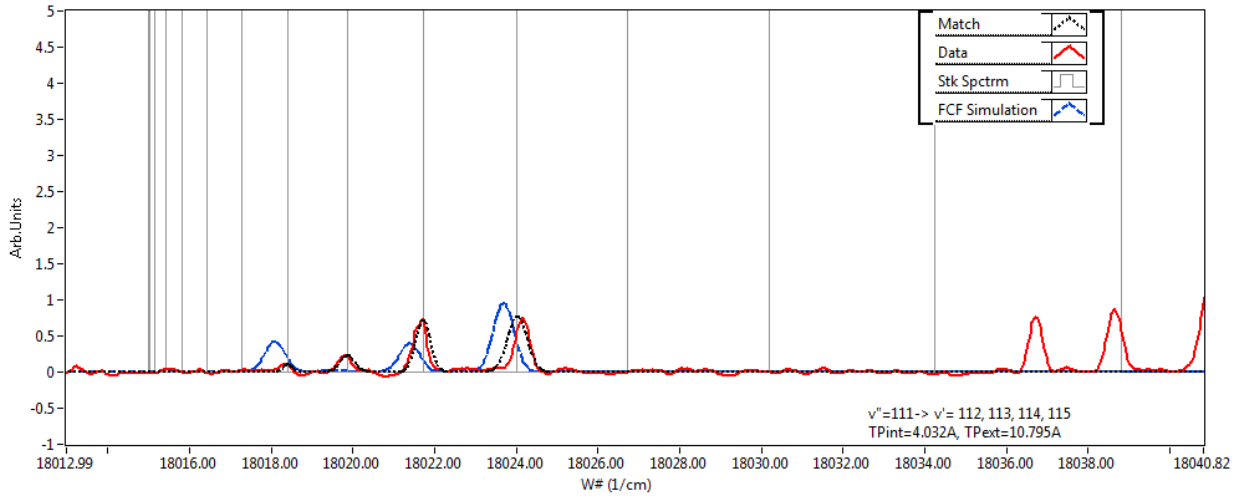
Match
Data
Stk Spctrm
FCF Simulation
Arb.Units
W# (1/cm)
v"=111-> v'= 112, 113, 114, 115
TPint=4.032A, TPext=10.795A

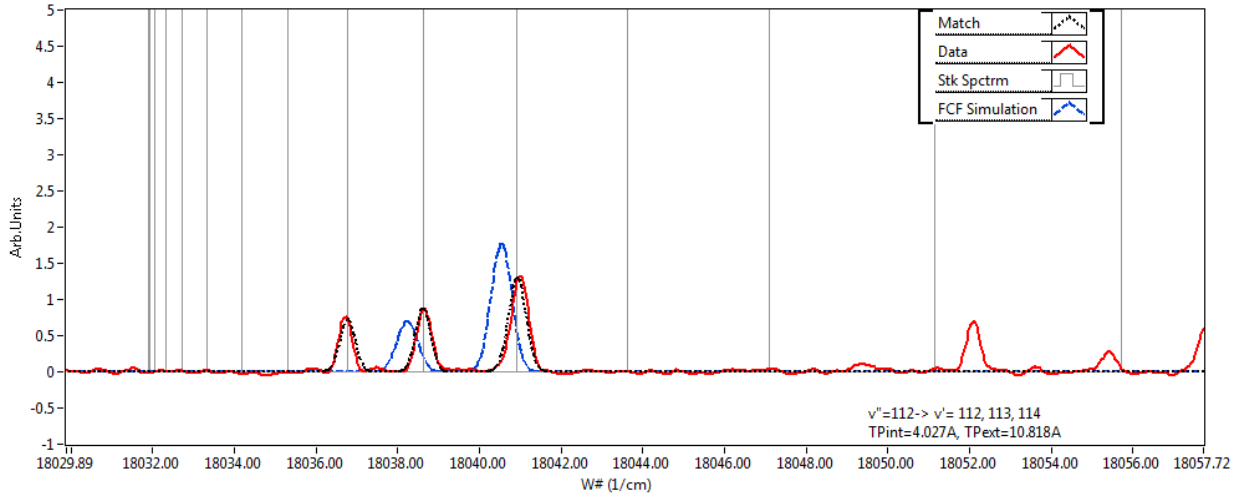
Match
Data
Stk Spctrm
FCF Simulation
Arb.Units
W# (1/cm)
v"=112-> v'= 112, 113, 114
TPint=4.027A, TPext=10.818A

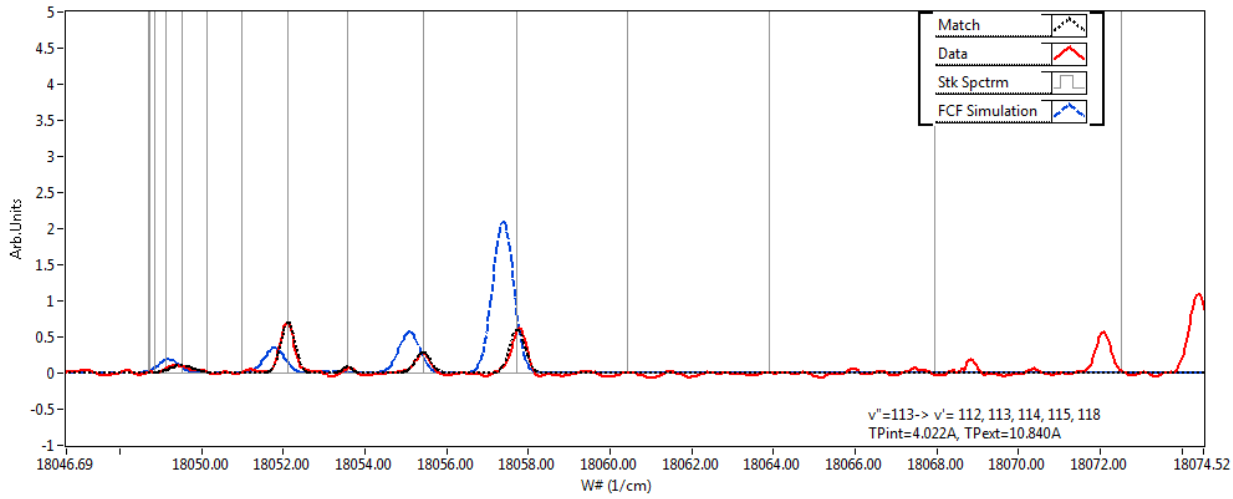
Match
Data
Stk Spctrm
FCF Simulation
Arb.Units
v"=113-> v'= 112, 113, 114, 115, 118
TPint=4.022A, TPext=10.840A
W# (1/cm)

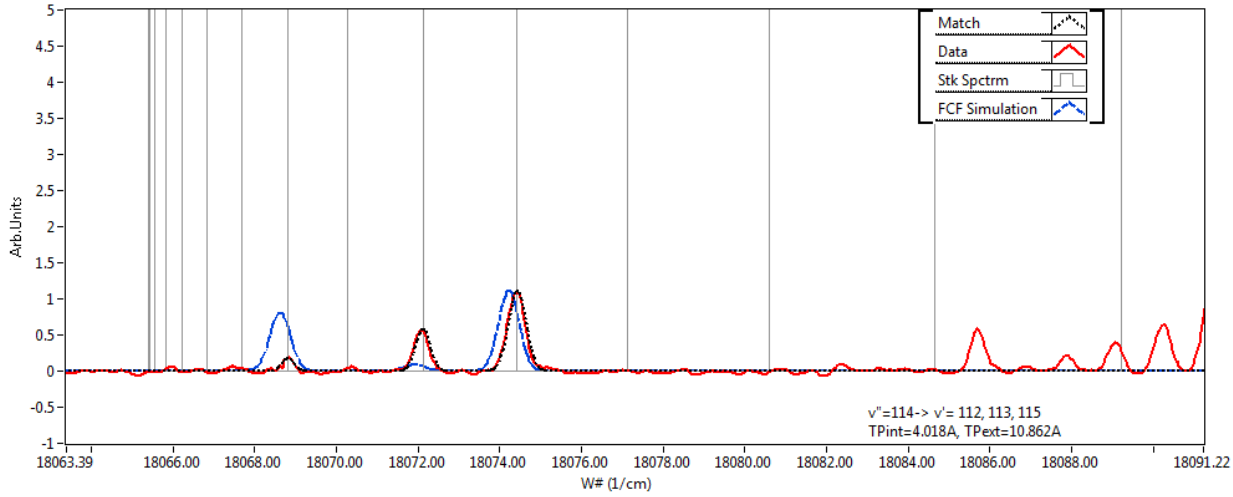
Match
Data
Stk Spctrm
FCF Simulation
Arb.Units
v"=114-> v'= 112, 113, 115
TPint=4.018A, TPext=10.862A
W# (1/cm)

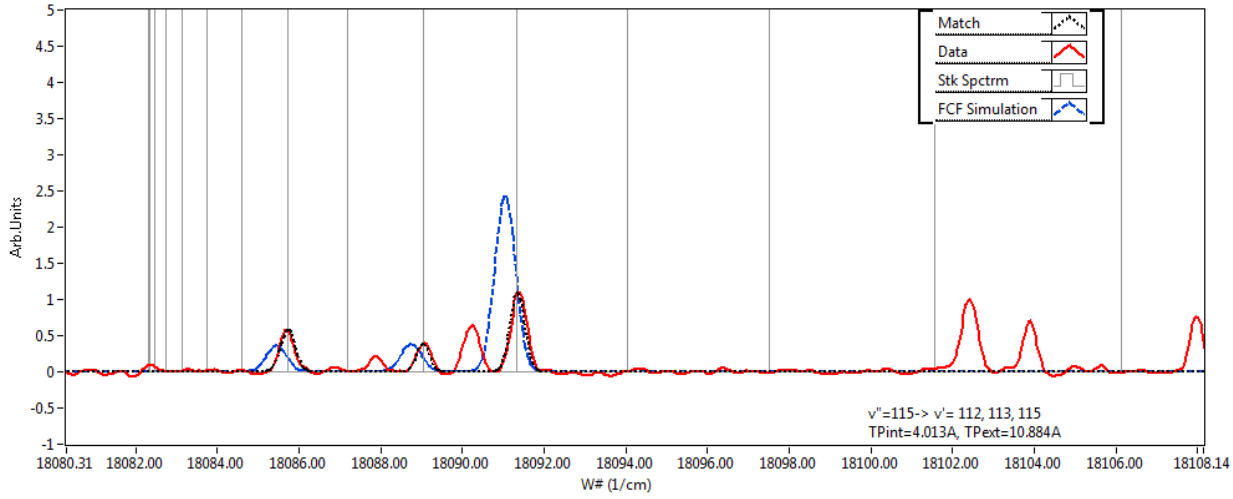
Match
Data
Stk Spctrm
FCF Simulation
Arb.Units
v"=115-> v'= 112, 113, 115
TPint=4.013A, TPext=10.884A
W# (1/cm)

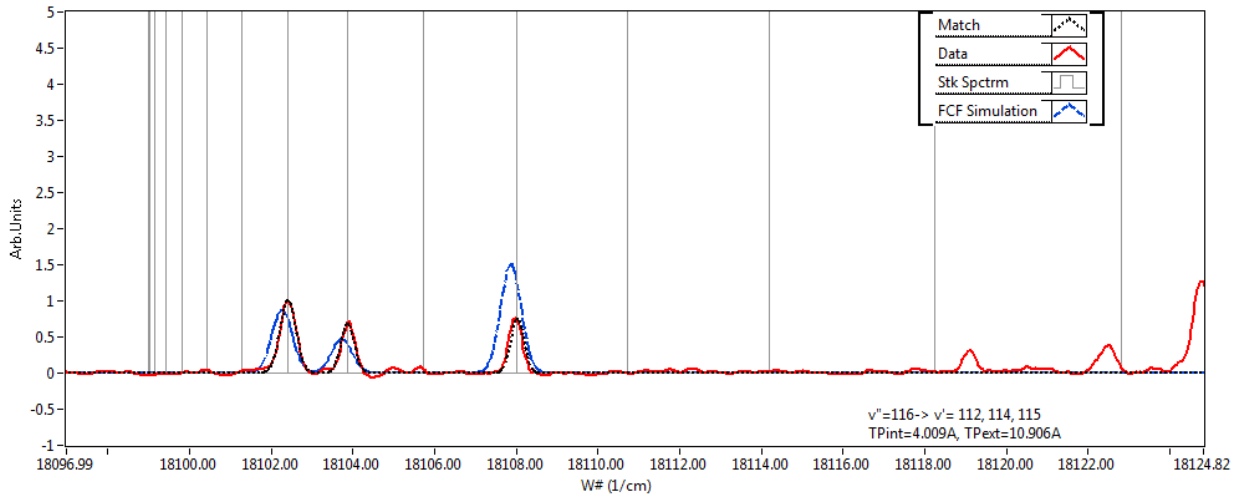
Match
Data
Stk Spctrm
FCF Simulation
Arb.Units
v"=116-> v'= 112, 114, 115
TPint=4.009A, TPext=10.906A
W# (1/cm)

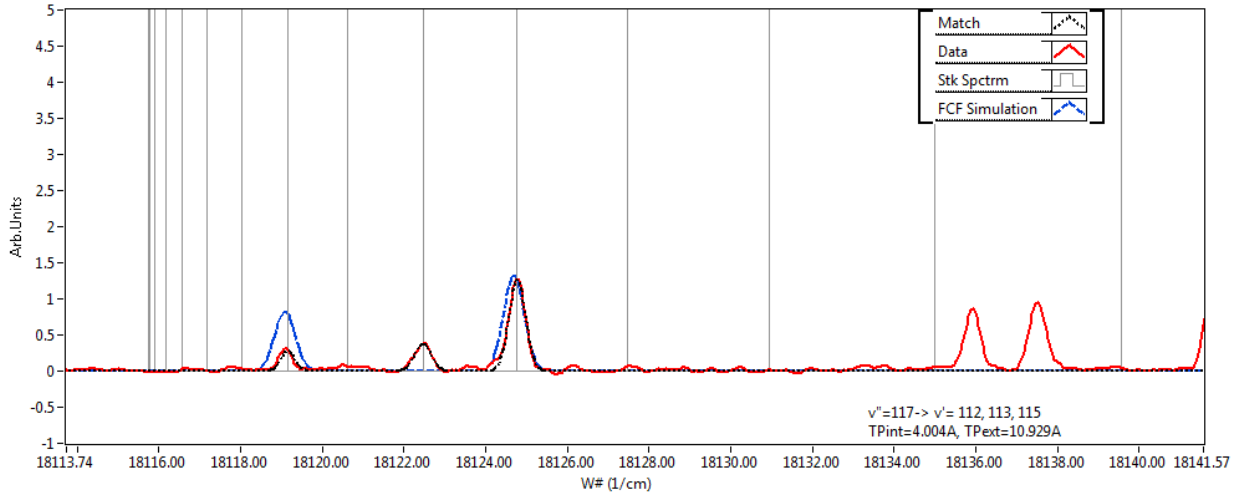
Match
Data
Stk Spctrm
FCF Simulation
Arb.Units
v"=117-> v'= 112, 113, 115
TPint=4.004A, TPext=10.929A
W# (1/cm)

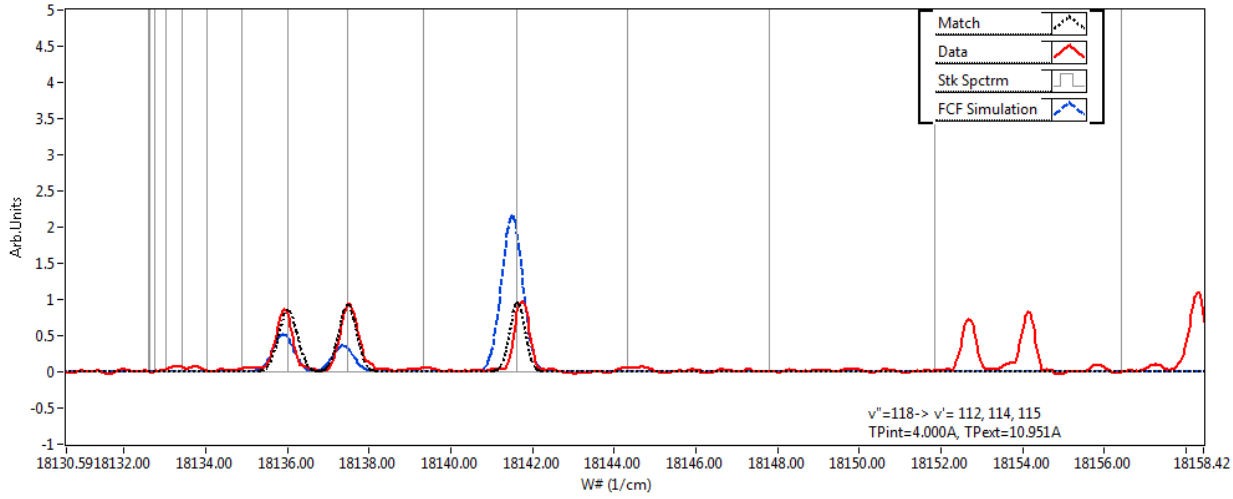
Match
Data
Stk Spctrm
FCF Simulation
Arb.Units
v"=118-> v'= 112, 114, 115
TPint=4.000A, TPext=10.951A
W# (1/cm)

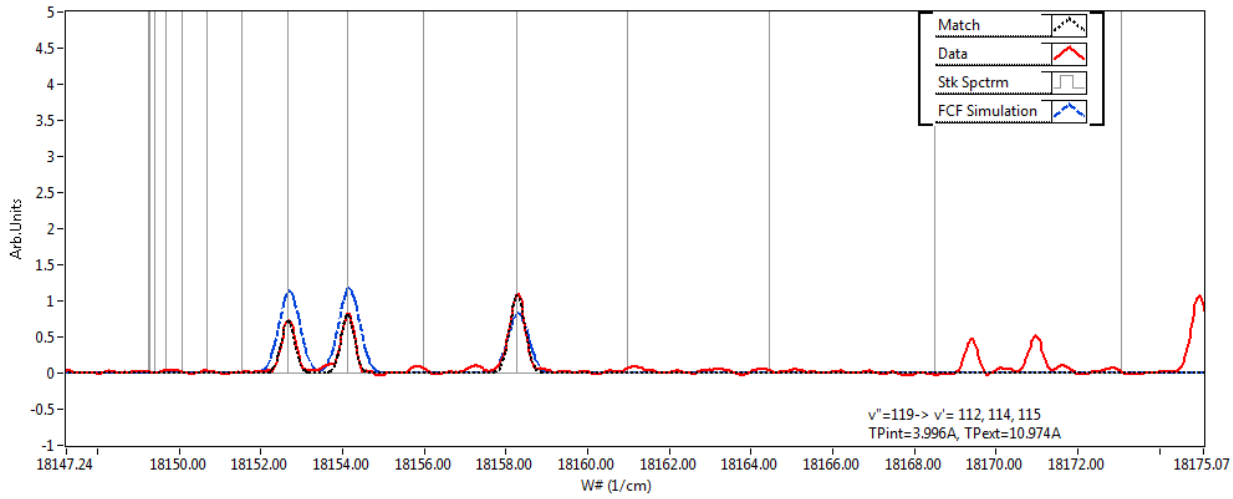
Match
Data
Stk Spctrm
FCF Simulation
Arb.Units
W# (1/cm)
v"=119-> v'= 112, 114, 115
TPint=3.996A, TPext=10.974A

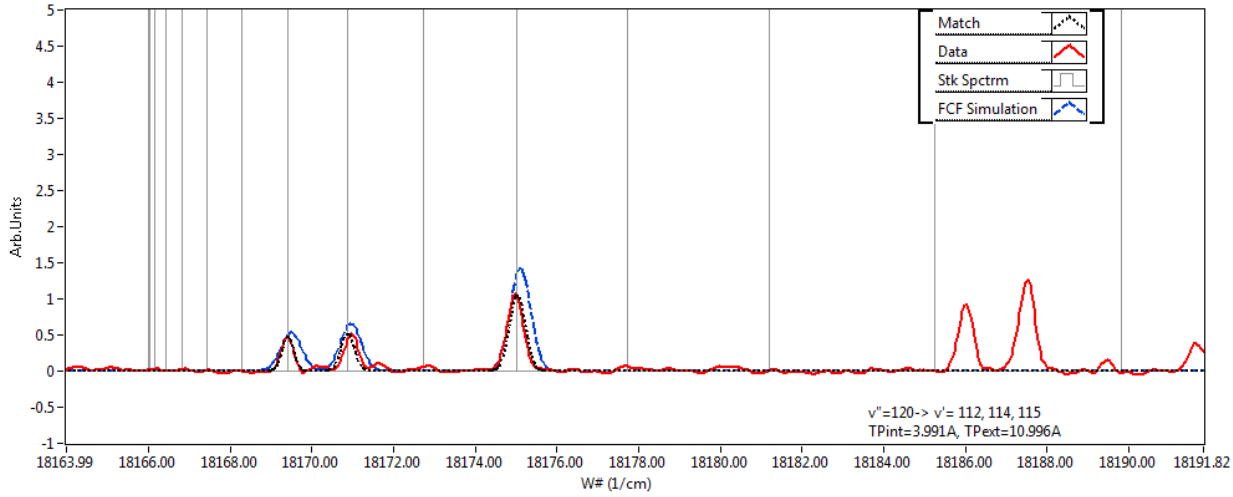
Match
Data
Stk Spctrm
FCF Simulation
Arb.Units
W# (1/cm)
v"=120-> v'= 112, 114, 115
TPint=3.991A, TPext=10.996A

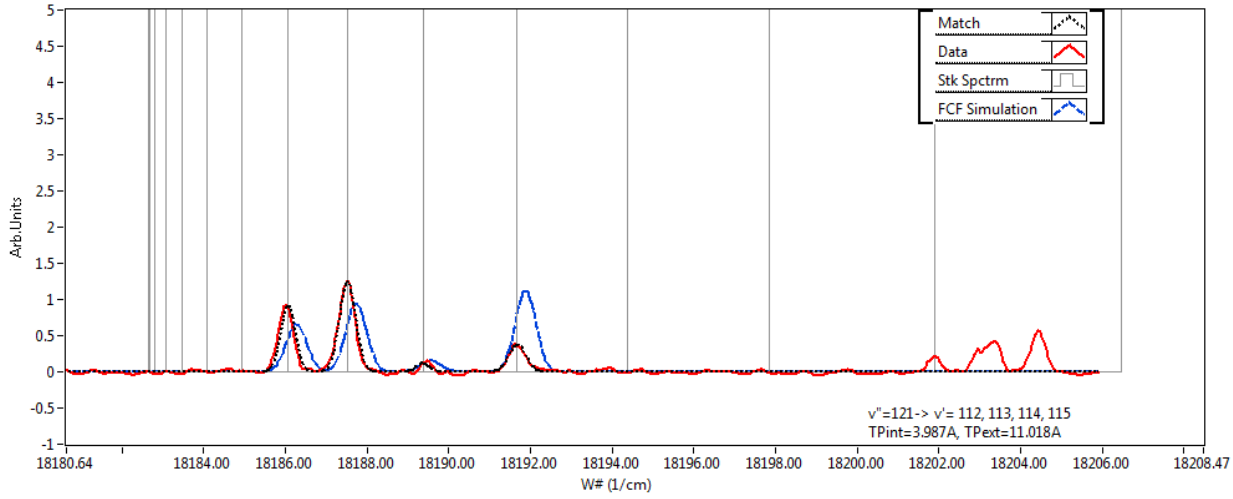
Match
Data
Stk Spctrm
FCF Simulation
Arb.Units
W# (1/cm)
v"=121-> v'= 112, 113, 114, 115
TPint=3.987A, TPext=11.018A

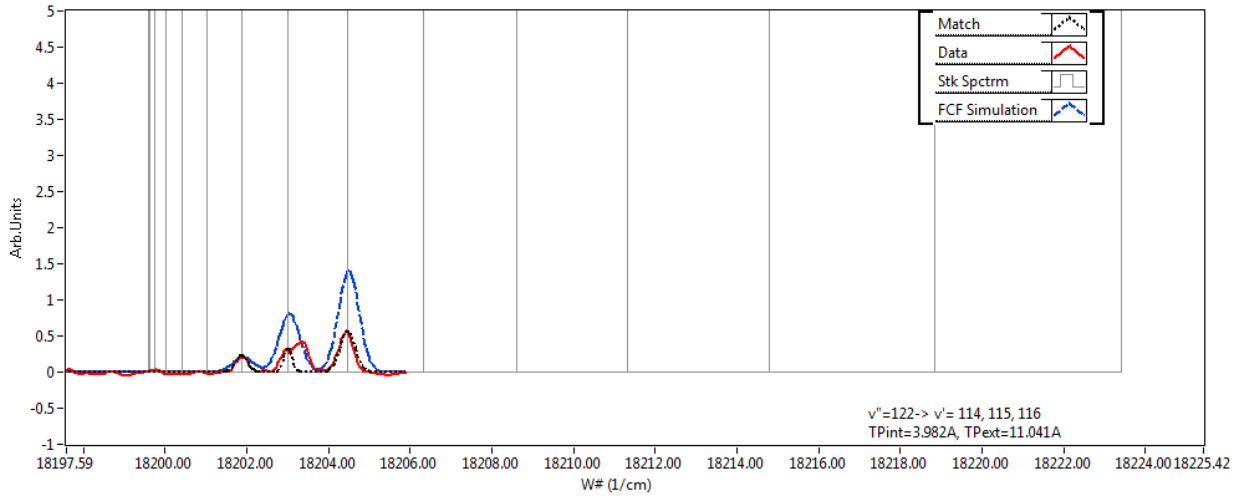
Match
Data
Stk Spctrm
FCF Simulation
v"=122-> v'= 114, 115, 116
TPint=3.982A, TPext=11.041A
Arb.Units
W# (1/cm)
5
4.5
4
3.5
3
2.5
2
1.5
1
0.5
0
-0.5
-1
18197.59
18200.00
18202.00
18204.00
18206.00
18208.00
18210.00
18212.00
18214.00
18216.00
18218.00
18220.00
18222.00
18224.00
18225.42

Appendix H

The $a^3\Sigma_u^+ \rightarrow 2^3\Pi_g$ and $3^1\Sigma_g^+$ spectrum plots and assignments.

This appendix shows an overview and a detailed view of the excitation spectrum from the $a^1\Sigma_u^+$*state*. All the fits are represented in red throughout.
The detailed spectrum, with individual state fit results, shows:

- the data spectrum along with the sum of all the individual state fits
- individual state fits along with their corresponding Franck-Condon simulation.

In the simulation, only assigned levels are shown and they are given the same linewidth as the corresponding transition in the fit.

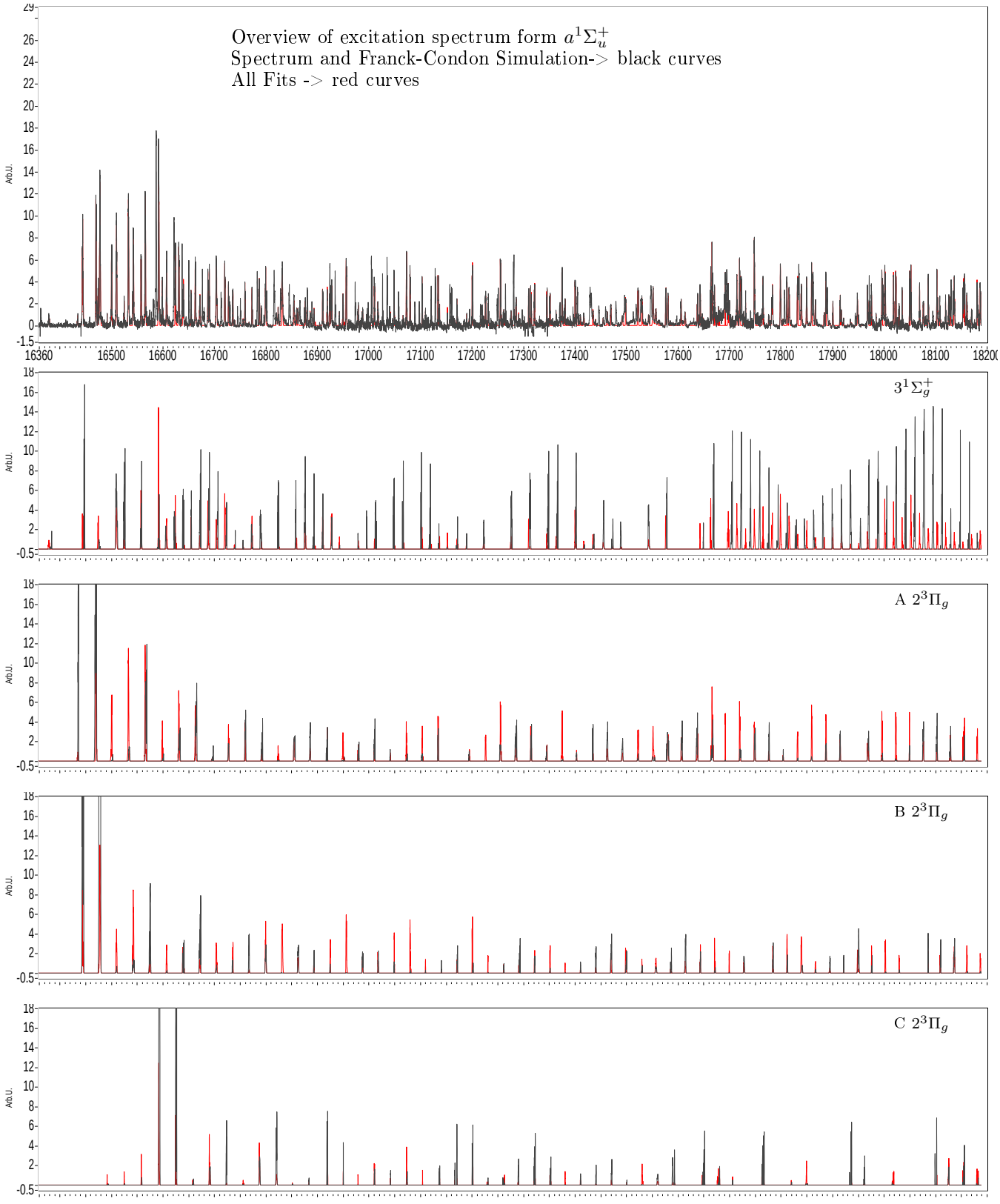
Overview of excitation spectrum form $a^1\Sigma_u^+$
Spectrum and Franck-Condon Simulation-> black curves
All Fits -> red curves
Arb.U.
$3^1\Sigma_g^+$
A $2^3\Pi_g$
B $2^3\Pi_g$
C $2^3\Pi_g$

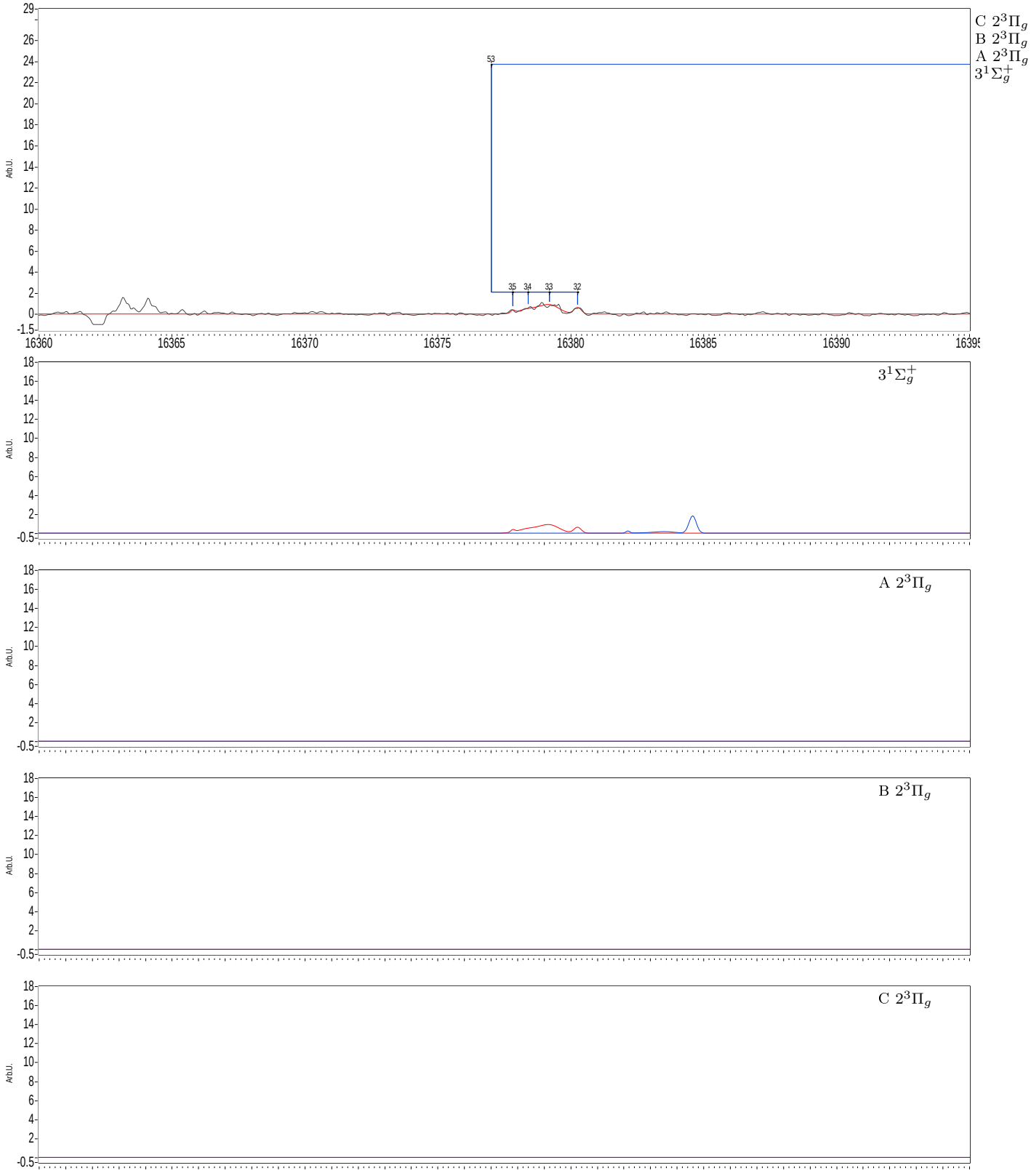
C $2^3\Pi_g$
B $2^3\Pi_g$
A $2^3\Pi_g$
$3^1\Sigma_g^+$
Arb.U.
53
35
34
33
32
16360
16365
16370
16375
16380
16385
16390
16395
$3^1\Sigma_g^+$
A $2^3\Pi_g$
B $2^3\Pi_g$
C $2^3\Pi_g$

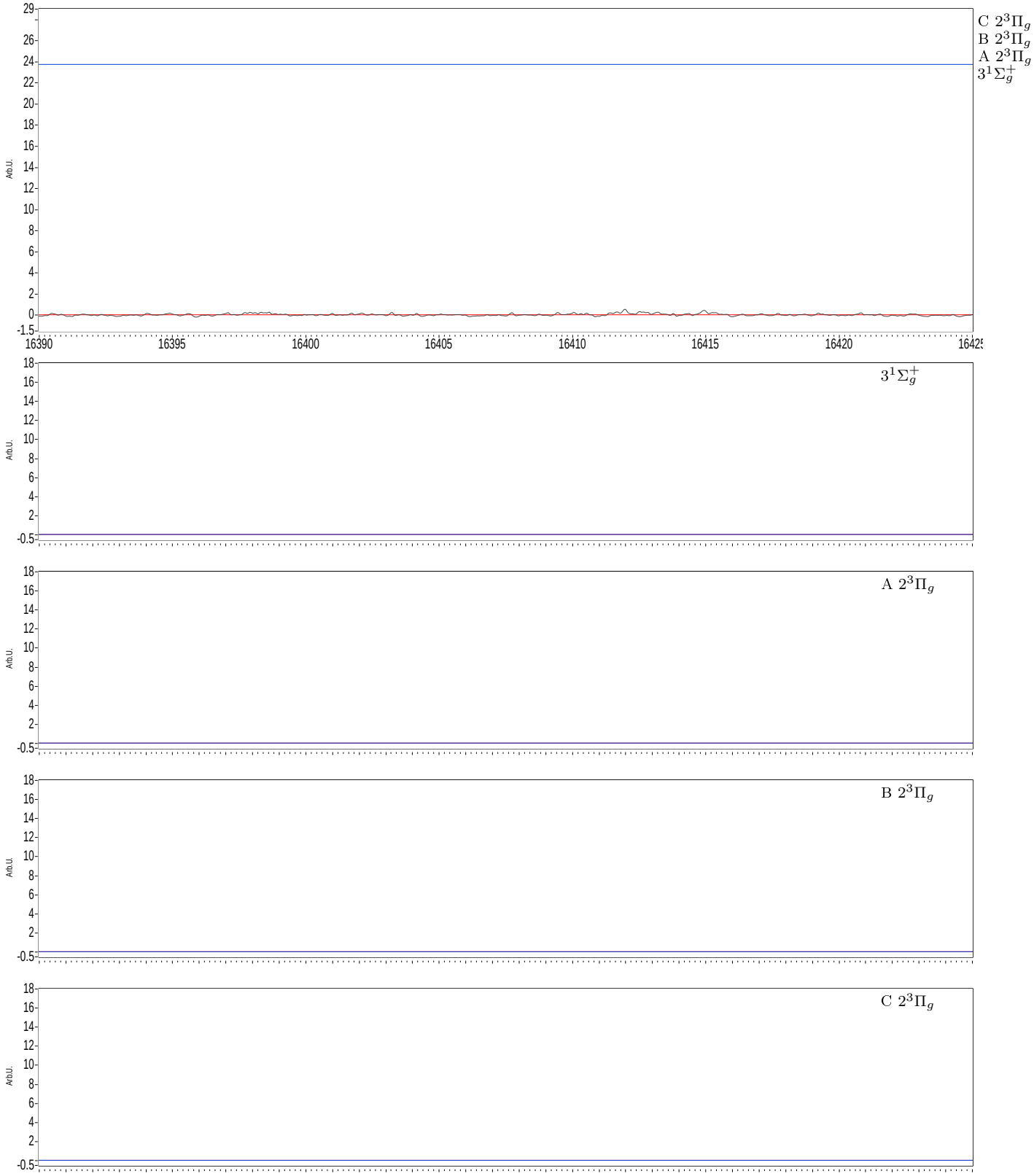
C $2^3\Pi_g$
B $2^3\Pi_g$
A $2^3\Pi_g$
$3^1\Sigma_g^+$
Arb.U.
16390
16395
16400
16405
16410
16415
16420
$3^1\Sigma_g^+$
A $2^3\Pi_g$
B $2^3\Pi_g$
C $2^3\Pi_g$

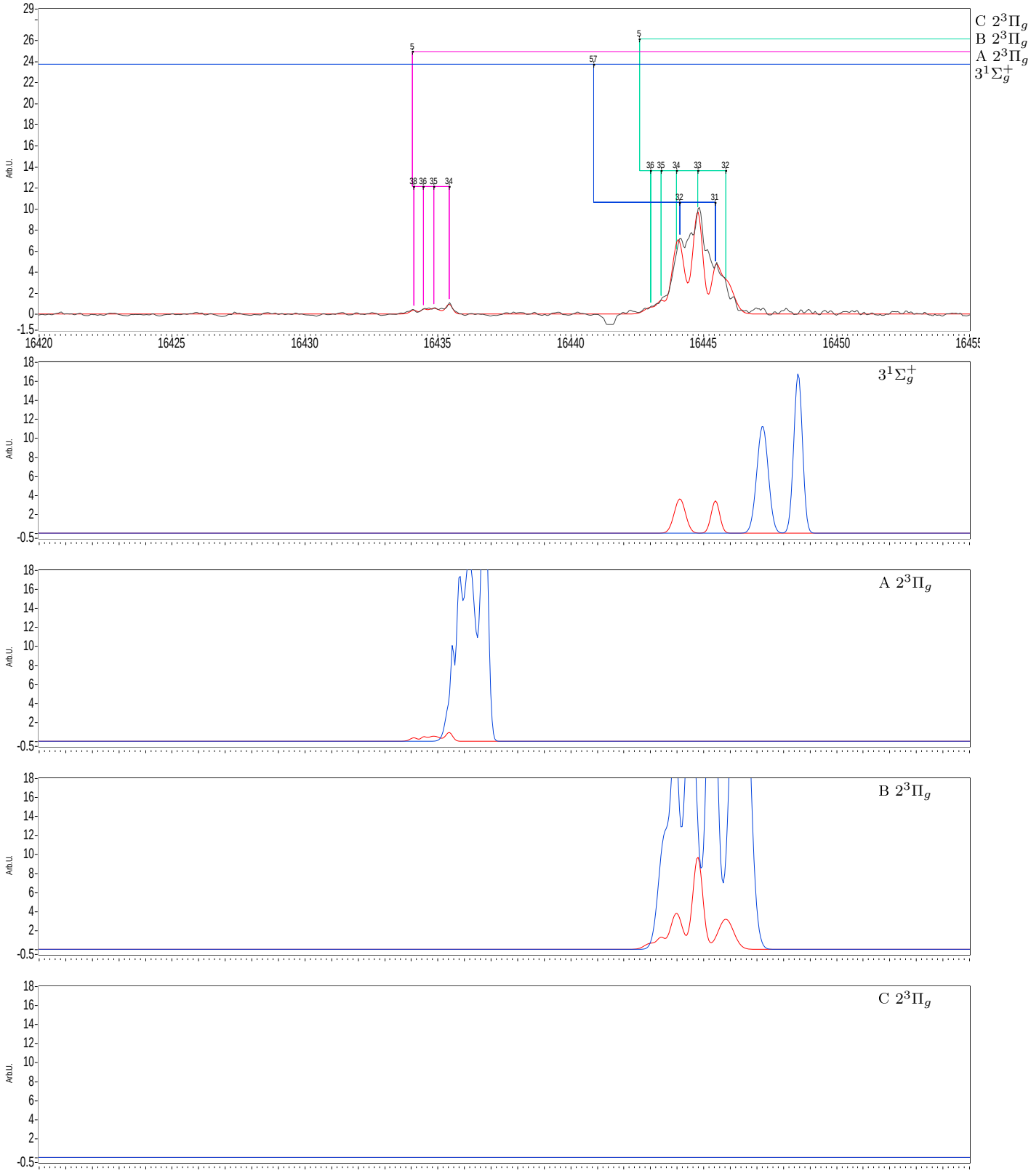
C $2^3\Pi_g$
B $2^3\Pi_g$
A $2^3\Pi_g$
$3^1\Sigma_g^+$
Arb.U.
16420
16425
16430
16435
16440
16445
16450
$3^1\Sigma_g^+$
A $2^3\Pi_g$
B $2^3\Pi_g$
C $2^3\Pi_g$

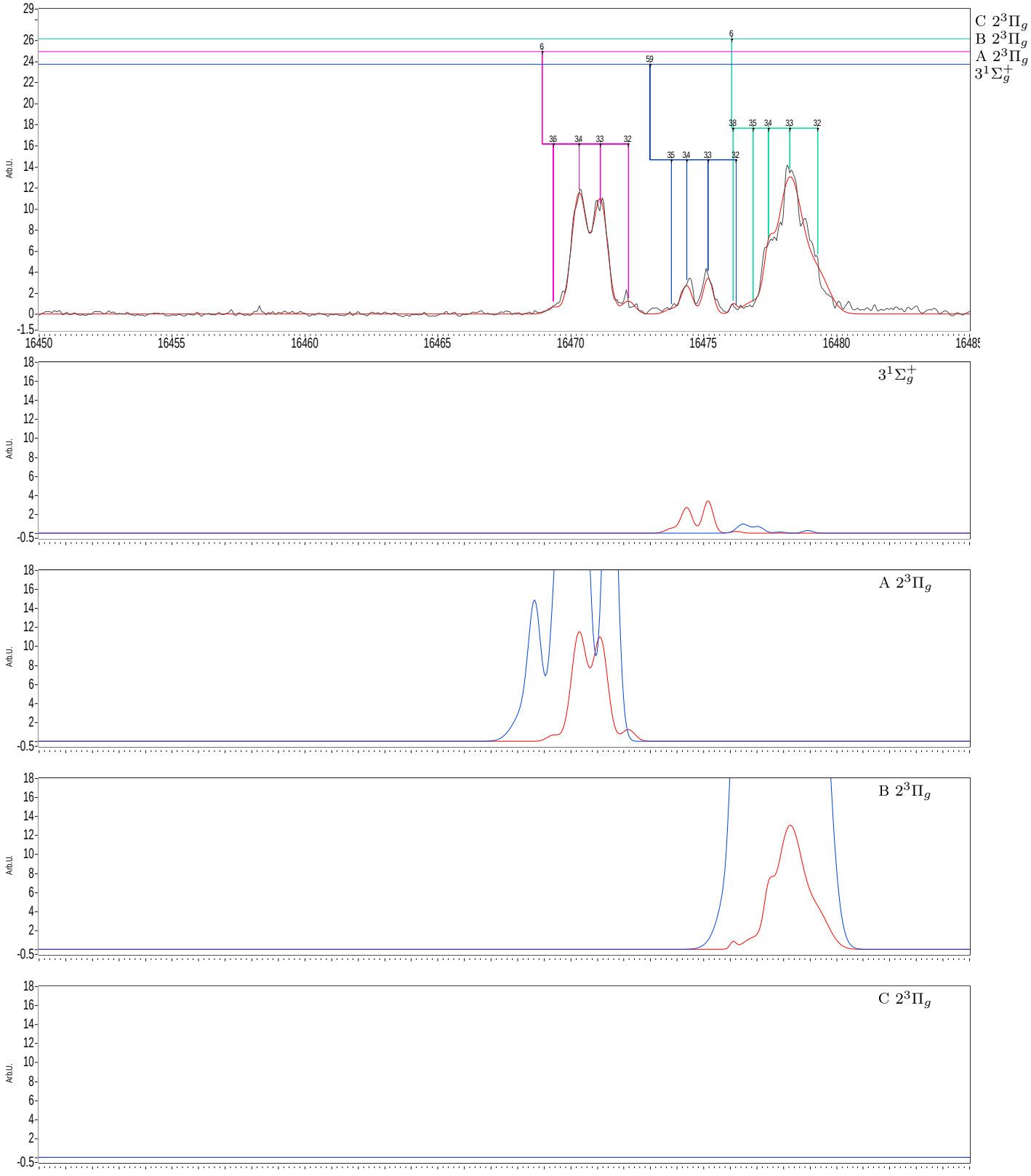
C $2^3\Pi_g$
B $2^3\Pi_g$
A $2^3\Pi_g$
$3^1\Sigma_g^+$
Arb.U.
16450
16455
16460
16465
16470
16475
16480
6
59
6
36
34
33
32
35
34
33
32
38
35
34
33
32
$3^1\Sigma_g^+$
A $2^3\Pi_g$
B $2^3\Pi_g$
C $2^3\Pi_g$

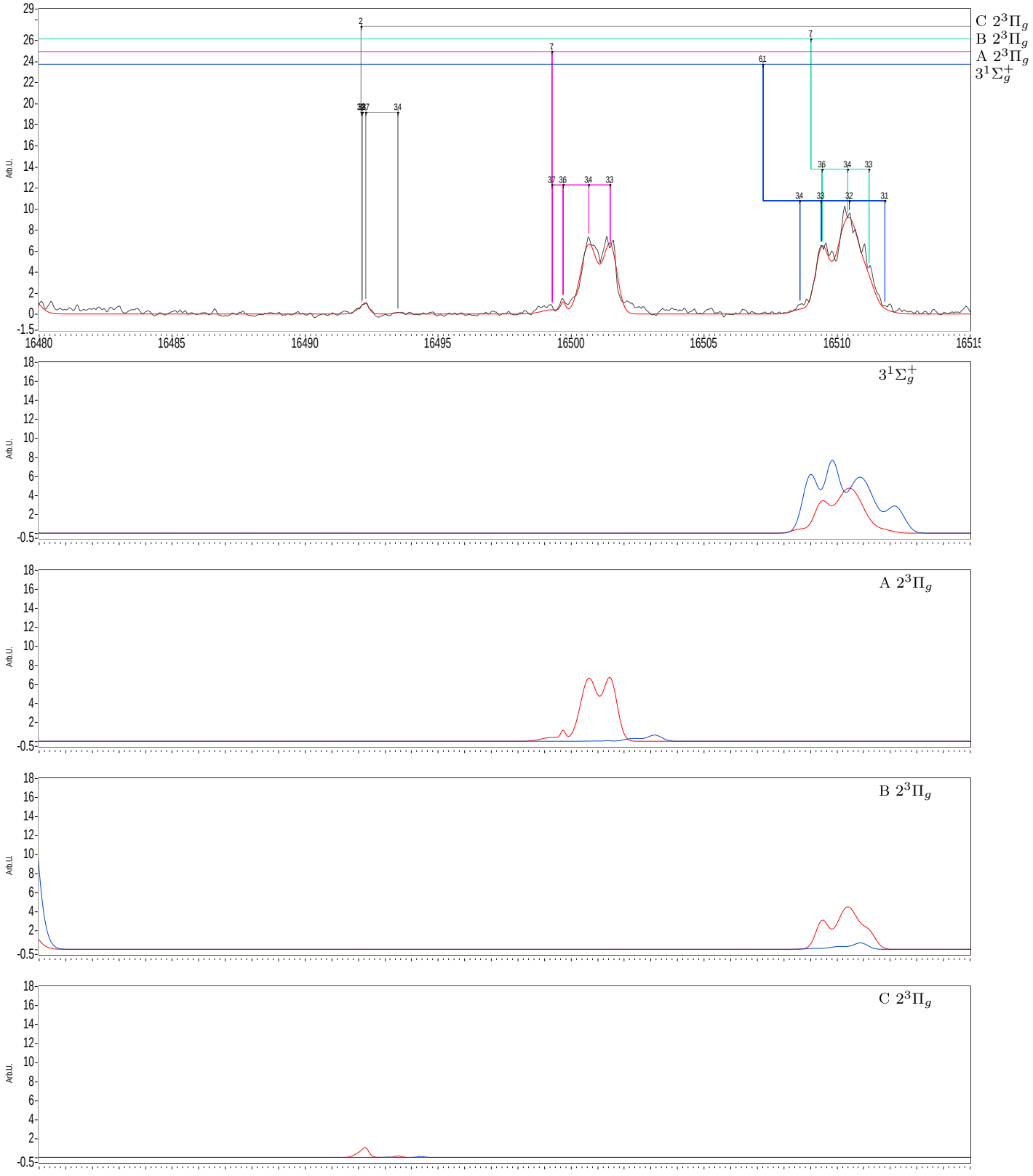
C $2^3\Pi_g$
B $2^3\Pi_g$
A $2^3\Pi_g$
$3^1\Sigma_g^+$
Arb.U.
16480
16485
16490
16495
16500
16505
16510
$3^1\Sigma_g^+$
A $2^3\Pi_g$
B $2^3\Pi_g$
C $2^3\Pi_g$

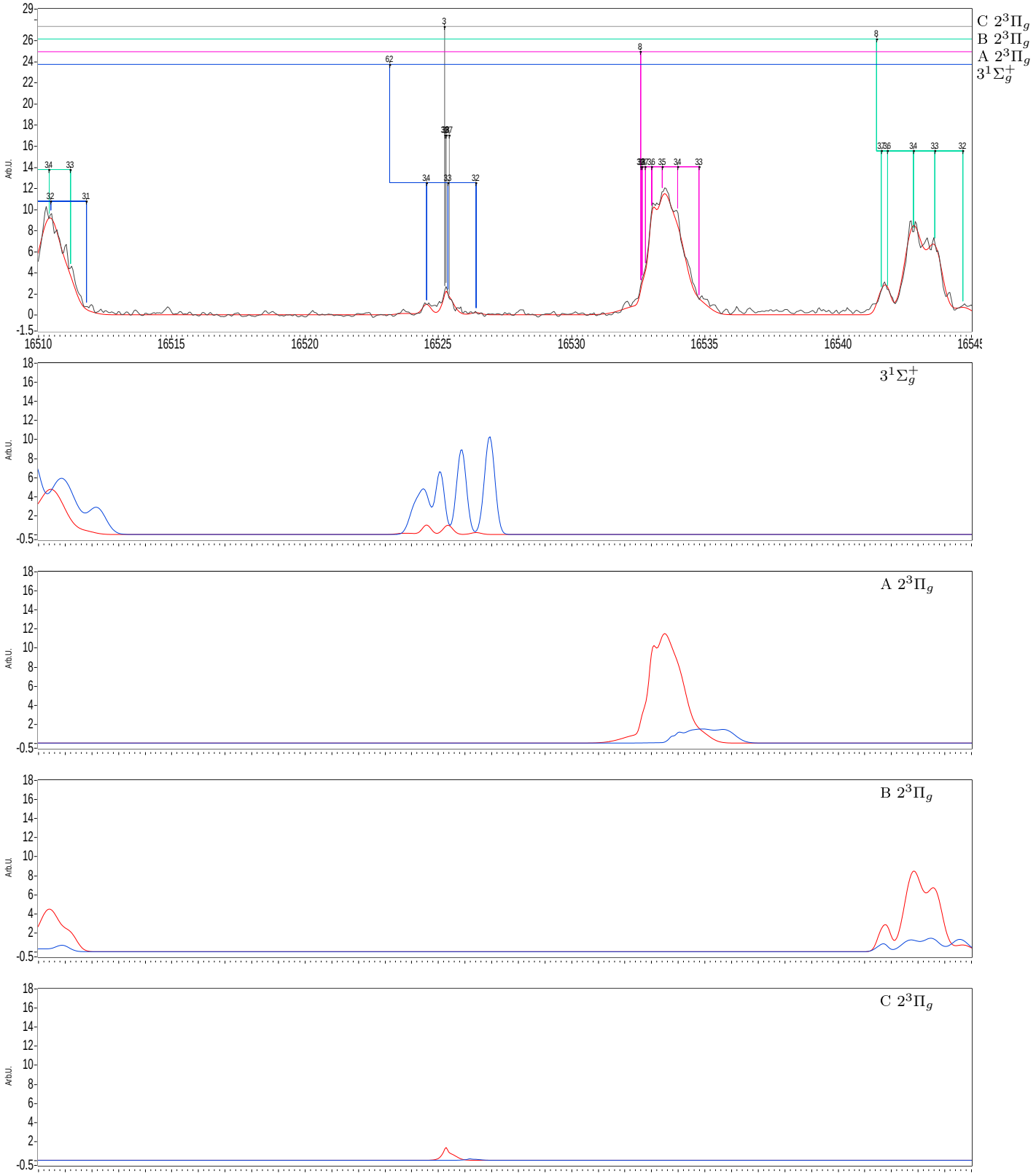
C $2^3\Pi_g$
B $2^3\Pi_g$
A $2^3\Pi_g$
$3^1\Sigma_g^+$
Arb.U.
16510
16515
16520
16525
16530
16535
16540
$3^1\Sigma_g^+$
A $2^3\Pi_g$
B $2^3\Pi_g$
C $2^3\Pi_g$

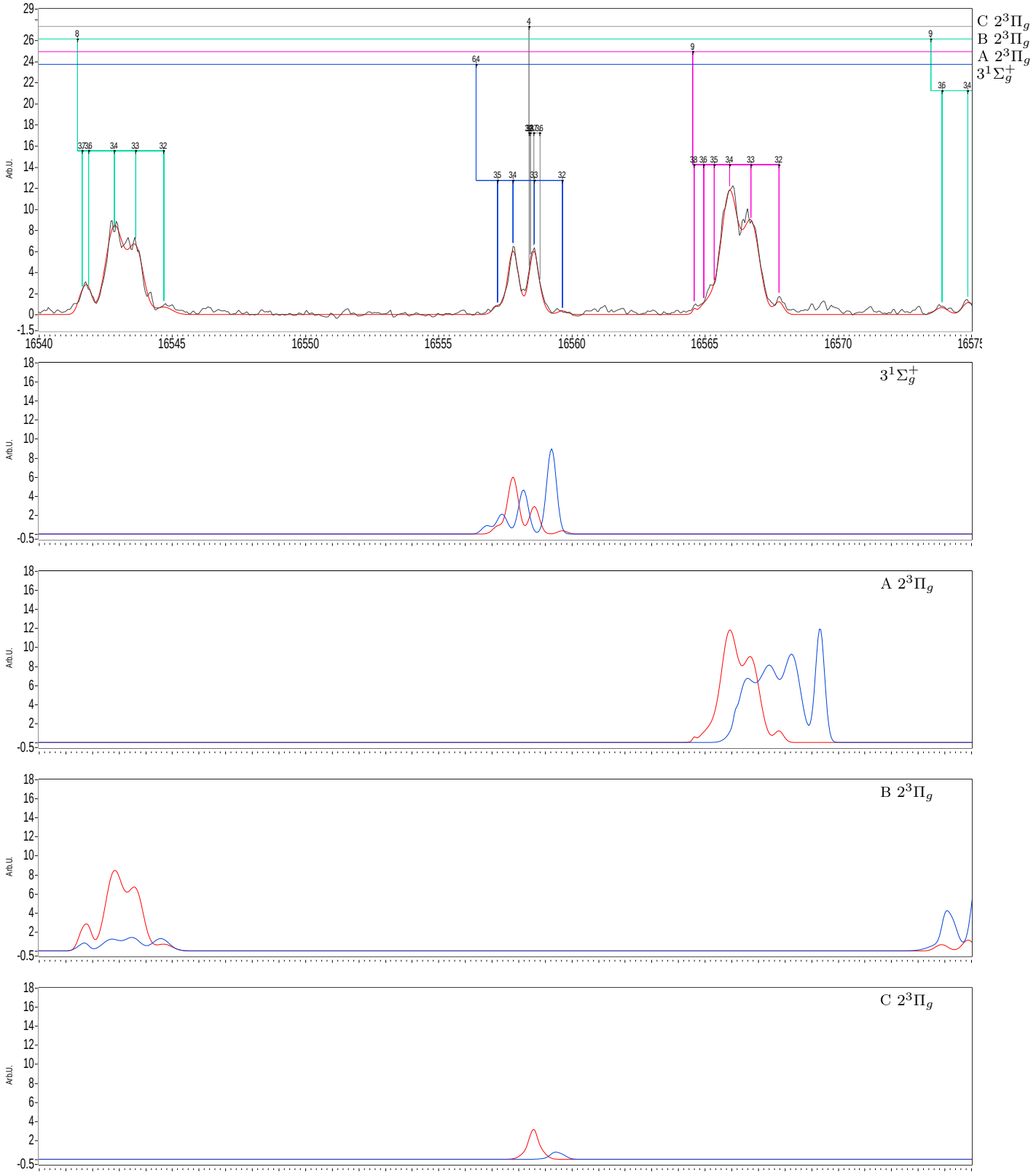
C $2^3\Pi_g$
B $2^3\Pi_g$
A $2^3\Pi_g$
$3^1\Sigma_g^+$
Arb.U.
16540
16545
16550
16555
16560
16565
16570
$3^1\Sigma_g^+$
A $2^3\Pi_g$
B $2^3\Pi_g$
C $2^3\Pi_g$

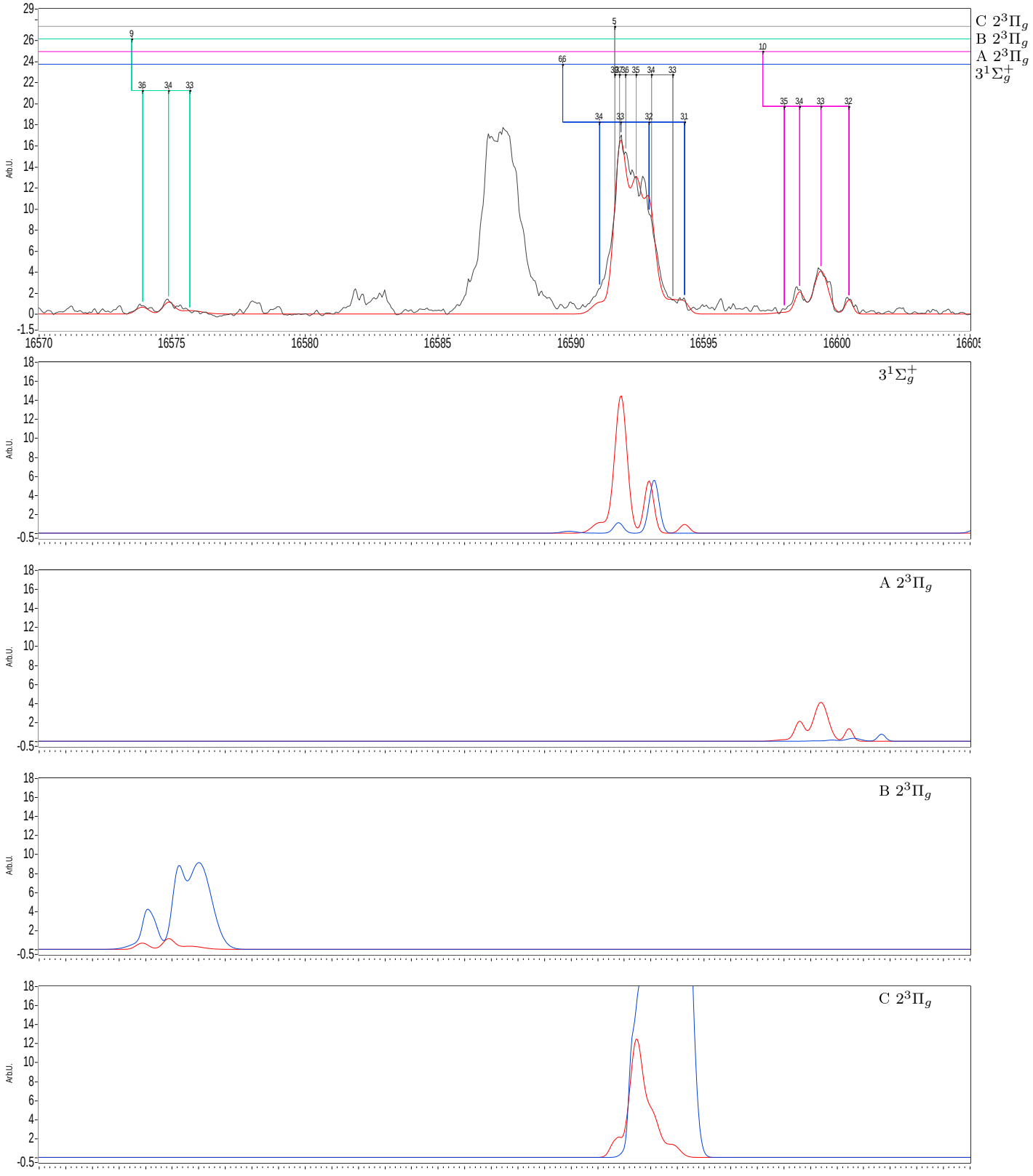
C $2^3\Pi_g$
B $2^3\Pi_g$
A $2^3\Pi_g$
$3^1\Sigma_g^+$
Arb.U.
16570
16575
16580
16585
16590
16595
16600
$3^1\Sigma_g^+$
A $2^3\Pi_g$
B $2^3\Pi_g$
C $2^3\Pi_g$

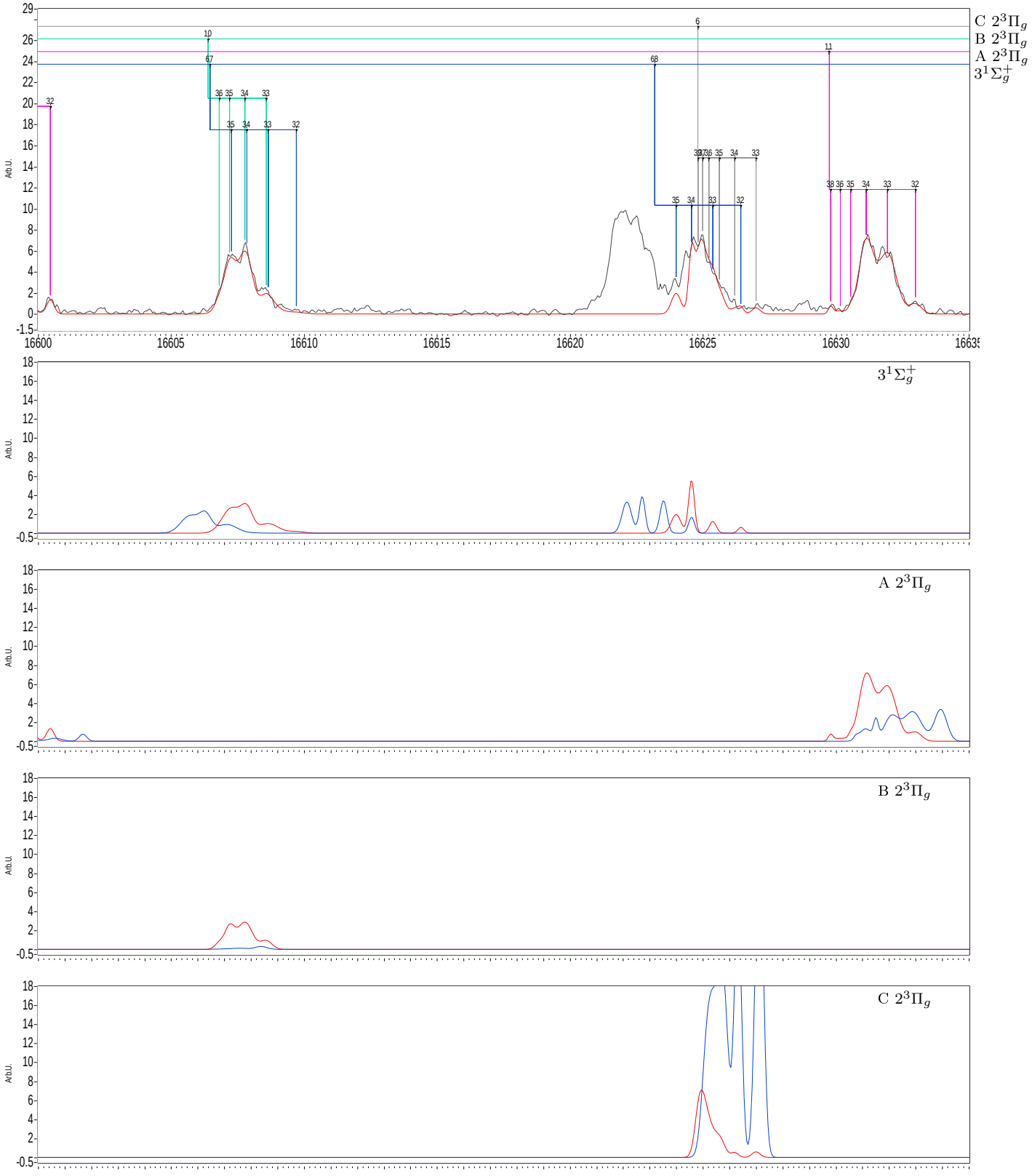
C $2^3\Pi_g$
B $2^3\Pi_g$
A $2^3\Pi_g$
$3^1\Sigma_g^+$
Arb.U.
16600
16605
16610
16615
16620
16625
16630
$3^1\Sigma_g^+$
A $2^3\Pi_g$
B $2^3\Pi_g$
C $2^3\Pi_g$

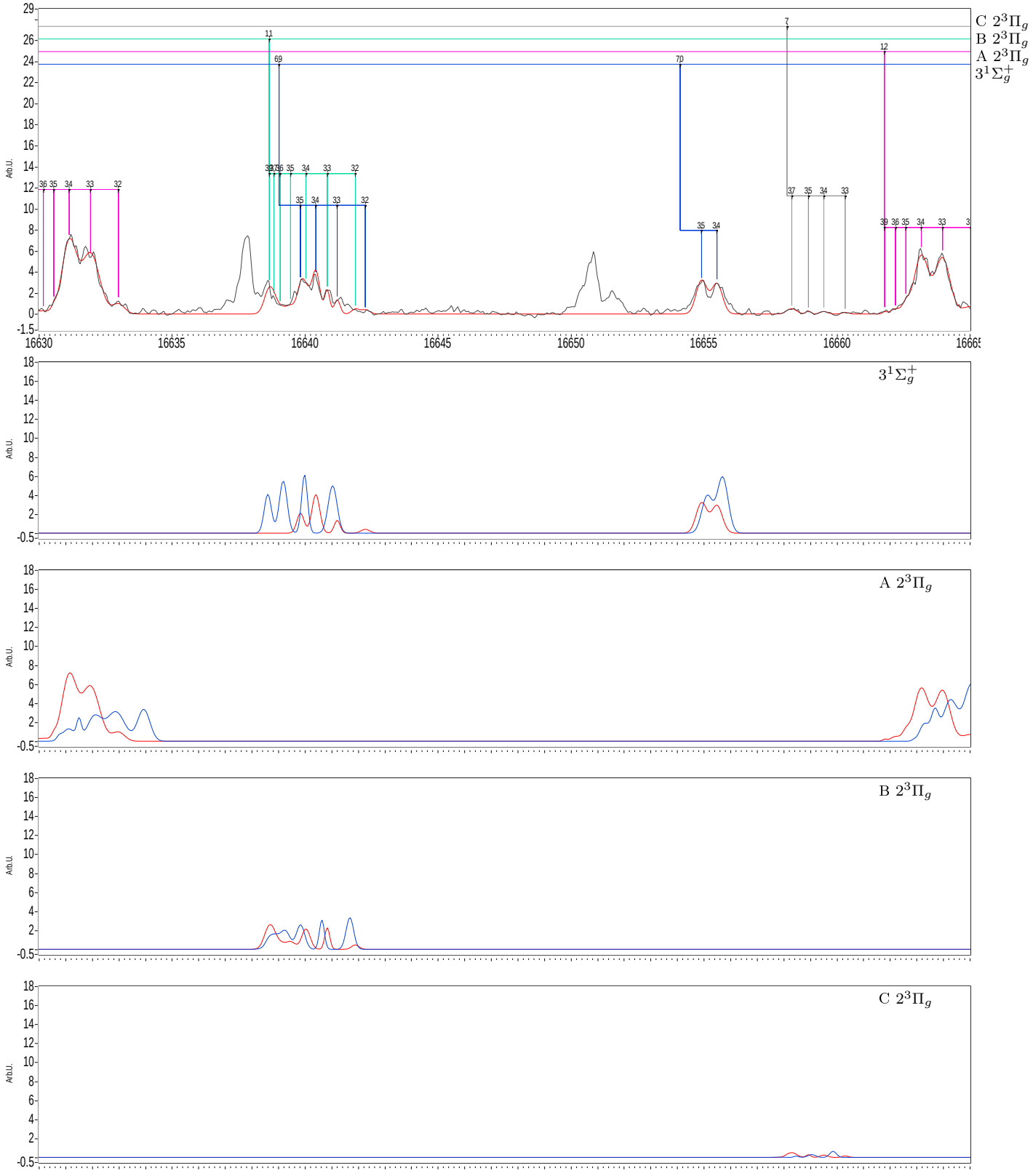
C $2^3\Pi_g$
B $2^3\Pi_g$
A $2^3\Pi_g$
$3^1\Sigma_g^+$
Arb.U.
16630
16635
16640
16645
16650
16655
16660
$3^1\Sigma_g^+$
A $2^3\Pi_g$
B $2^3\Pi_g$
C $2^3\Pi_g$

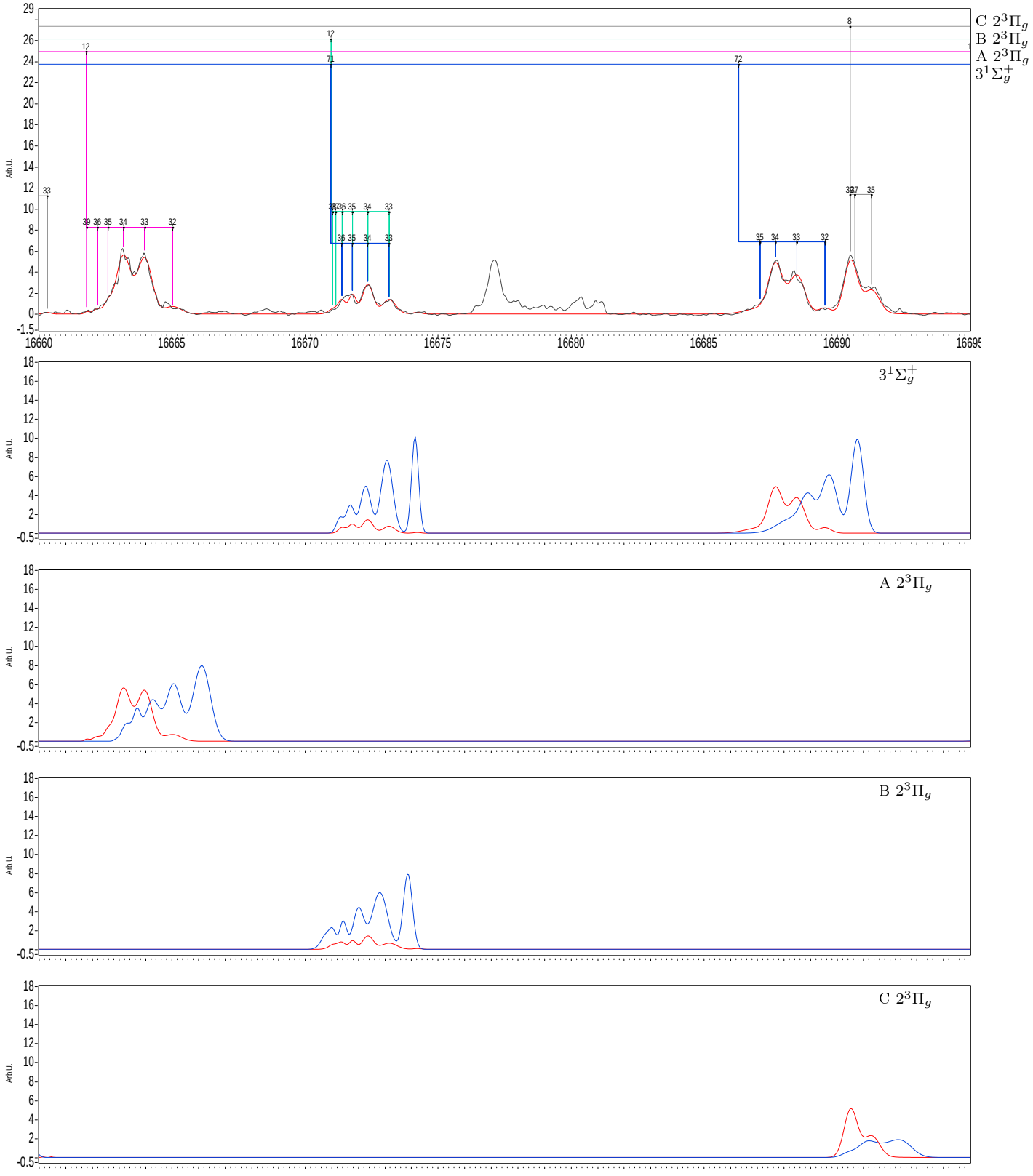
C $2^3\Pi_g$
B $2^3\Pi_g$
A $2^3\Pi_g$
$3^1\Sigma_g^+$
Arb.U.
16660
16665
16670
16675
16680
16685
16690
$3^1\Sigma_g^+$
A $2^3\Pi_g$
B $2^3\Pi_g$
C $2^3\Pi_g$

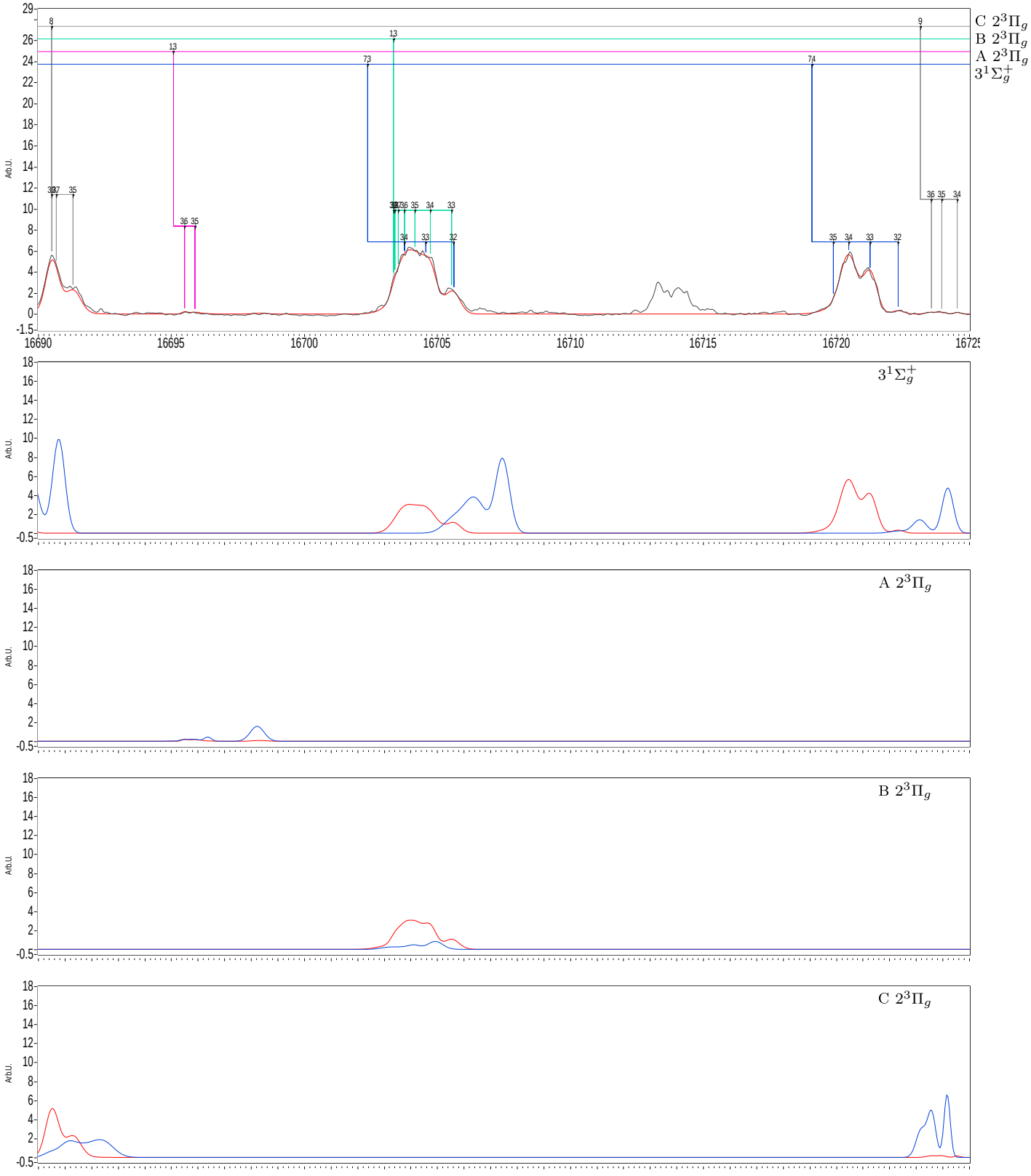
C $2^3\Pi_g$
B $2^3\Pi_g$
A $2^3\Pi_g$
$3^1\Sigma_g^+$
Arb.U.
16690
16695
16700
16705
16710
16715
16720
$3^1\Sigma_g^+$
A $2^3\Pi_g$
B $2^3\Pi_g$
C $2^3\Pi_g$

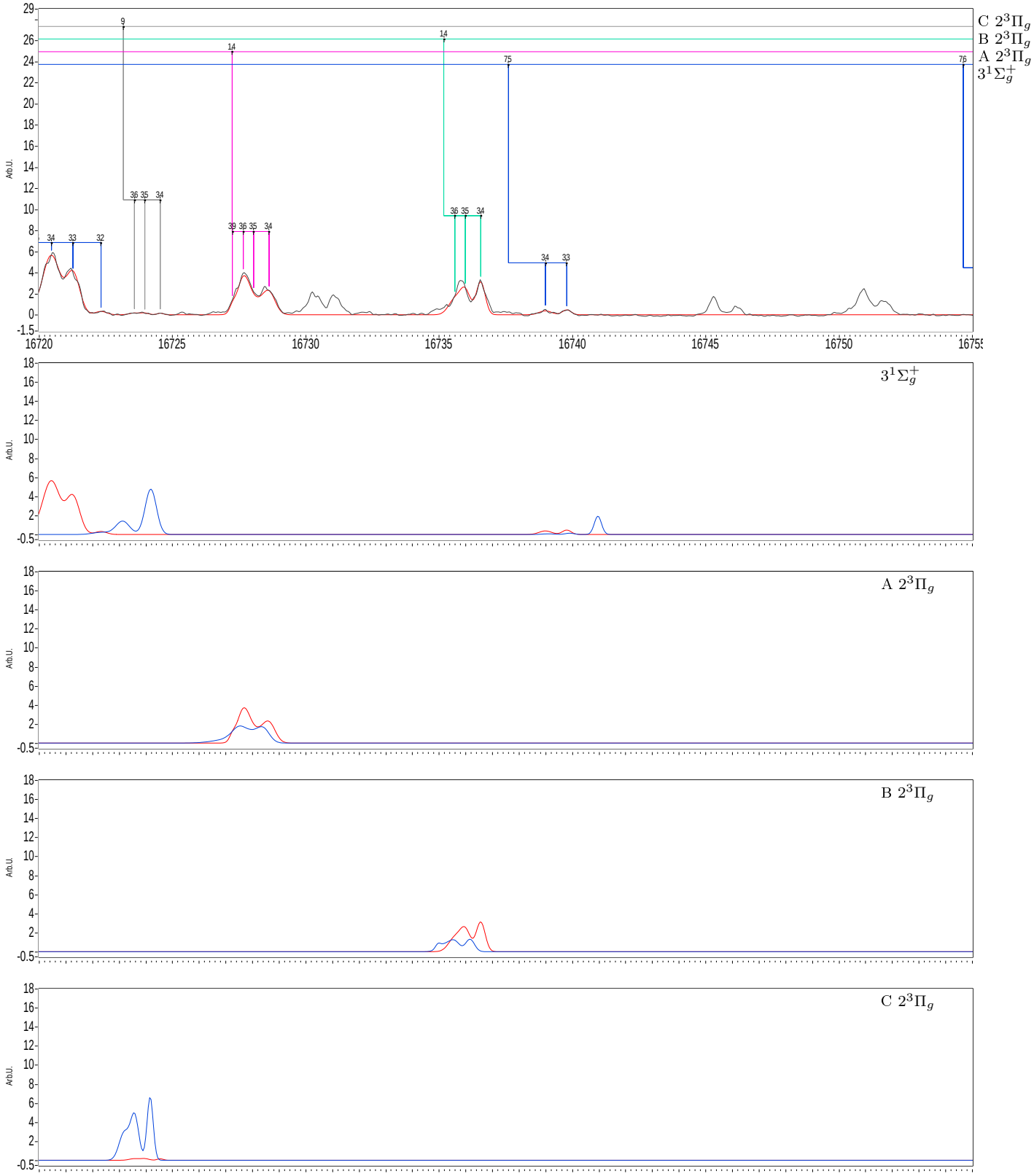
C $2^3\Pi_g$
B $2^3\Pi_g$
A $2^3\Pi_g$
$3^1\Sigma_g^+$
Arb.U.
16720
16725
16730
16735
16740
16745
16750
$3^1\Sigma_g^+$
A $2^3\Pi_g$
B $2^3\Pi_g$
C $2^3\Pi_g$

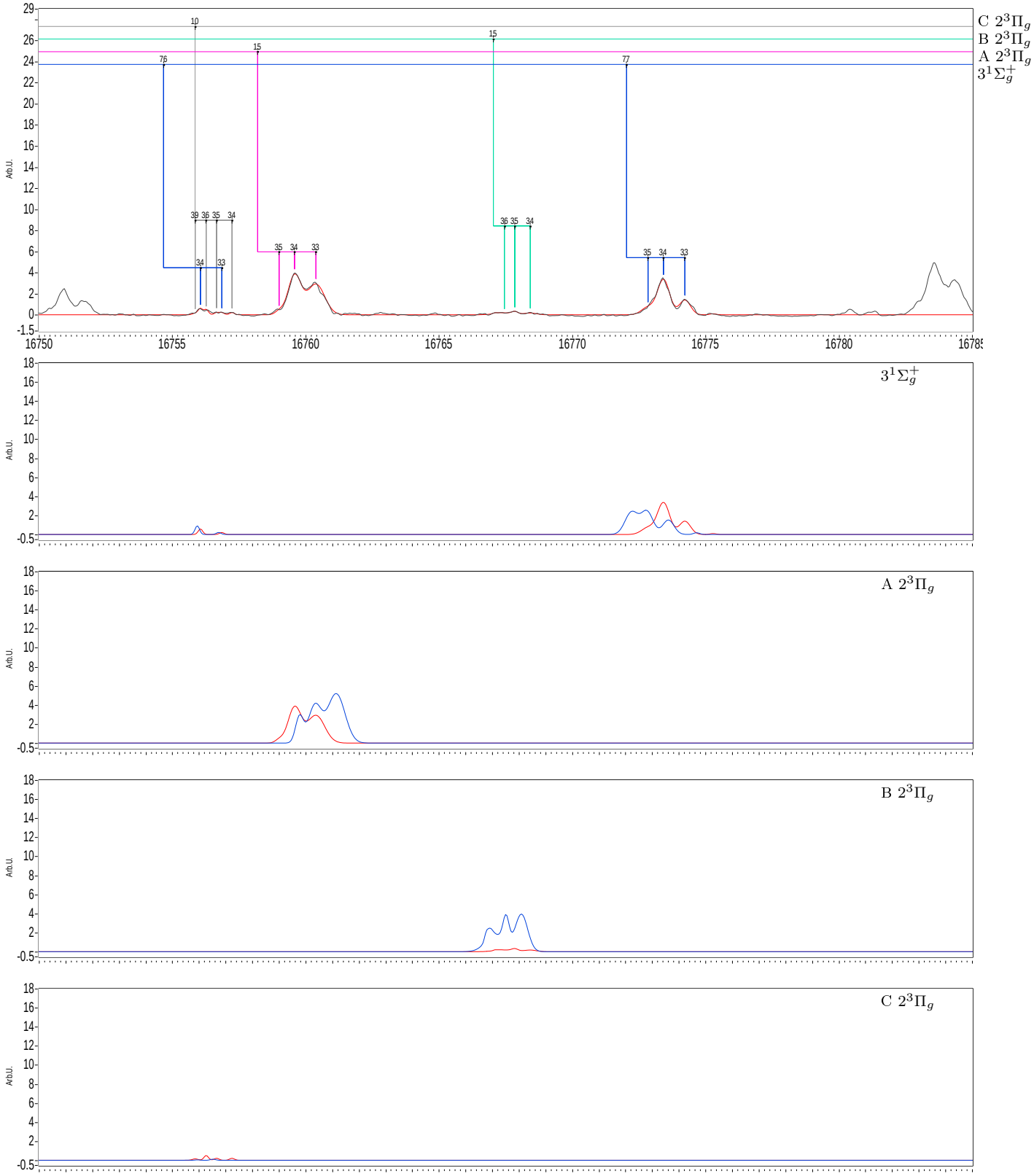
C $2^3\Pi_g$
B $2^3\Pi_g$
A $2^3\Pi_g$
$3^1\Sigma_g^+$
Arb.U.
16750
16755
16760
16765
16770
16775
16780
$3^1\Sigma_g^+$
A $2^3\Pi_g$
B $2^3\Pi_g$
C $2^3\Pi_g$

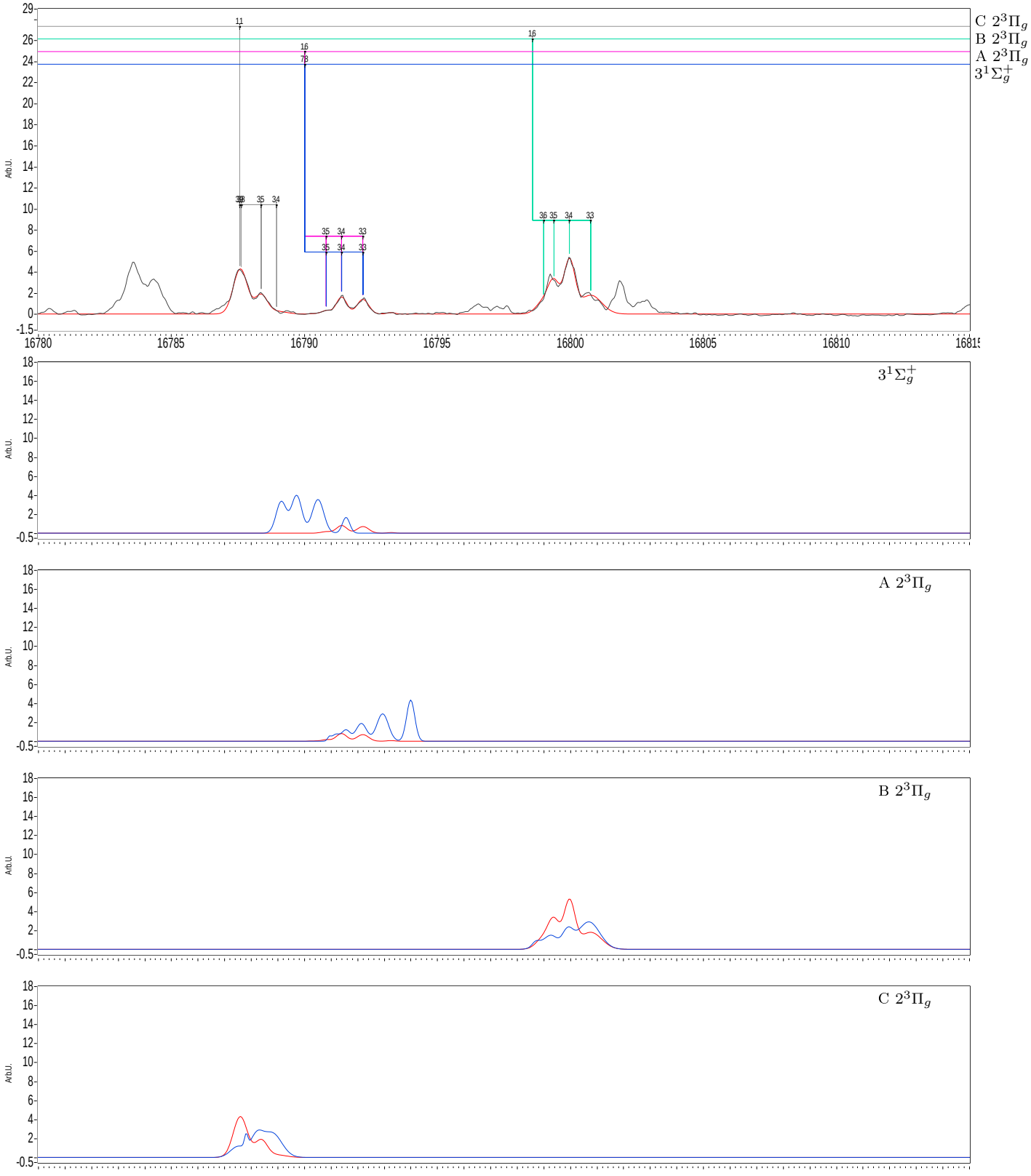
C $2^3\Pi_g$
B $2^3\Pi_g$
A $2^3\Pi_g$
$3^1\Sigma_g^+$
Arb.U.
16780
16785
16790
16795
16800
16805
16810
16815
$3^1\Sigma_g^+$
A $2^3\Pi_g$
B $2^3\Pi_g$
C $2^3\Pi_g$

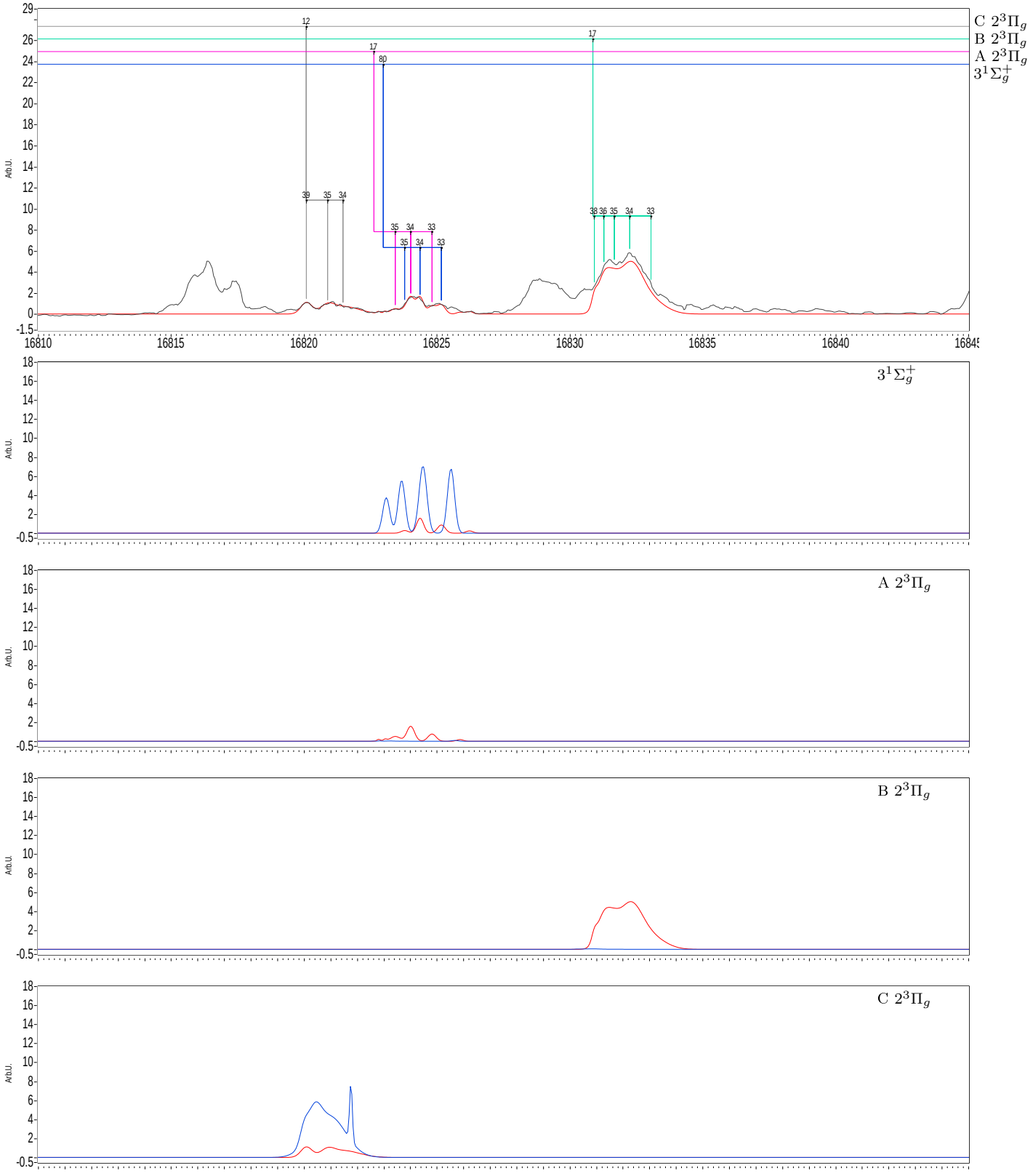
C $2^3\Pi_g$
B $2^3\Pi_g$
A $2^3\Pi_g$
$3^1\Sigma_g^+$
Arb.U.
16810
16815
16820
16825
16830
16835
16840
16845
12
17
80
39
35
34
33
38
36

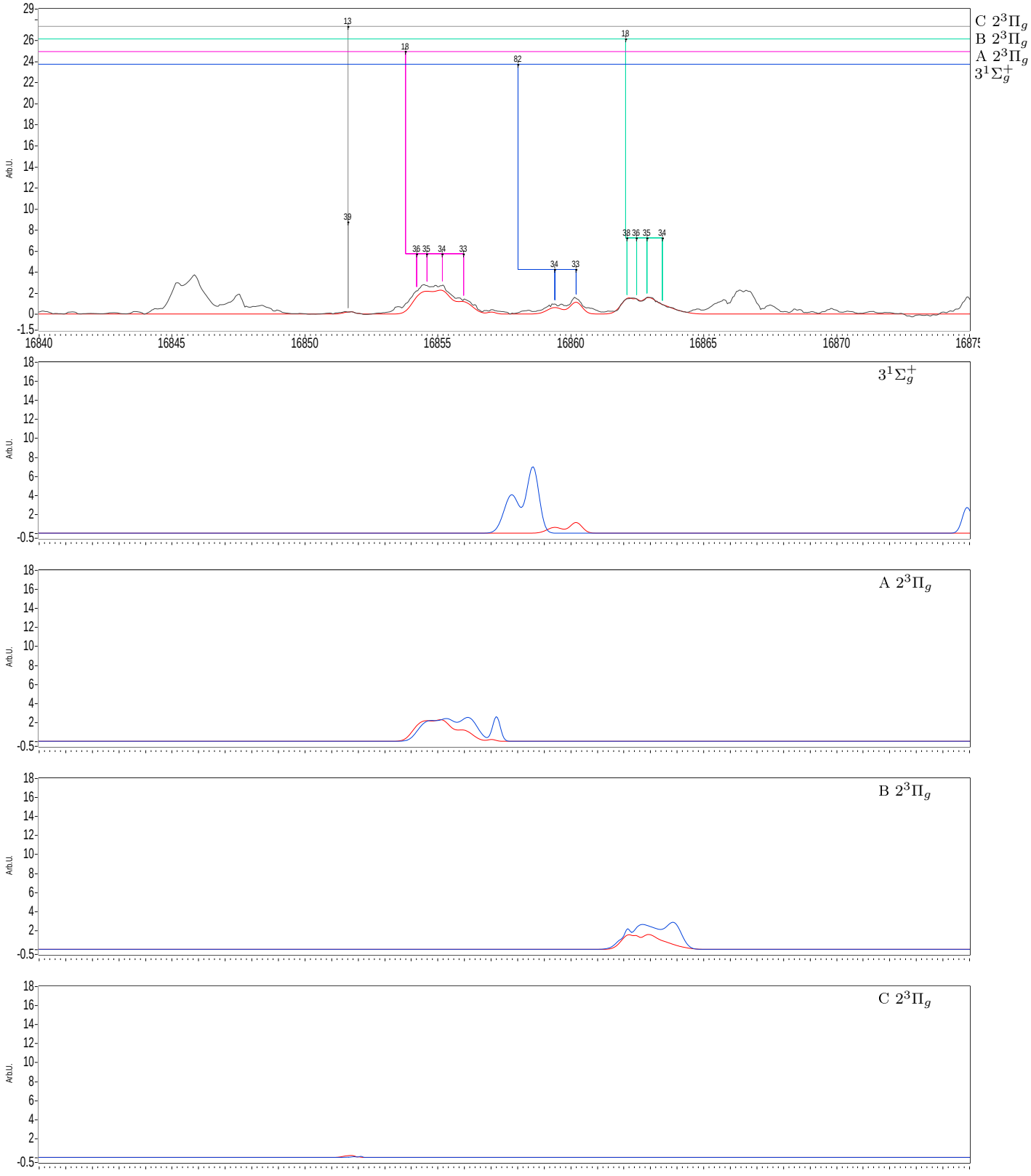
C $2^3\Pi_g$
B $2^3\Pi_g$
A $2^3\Pi_g$
$3^1\Sigma_g^+$
Arb.U.
16840
16845
16850
16855
16860
16865
16870
$3^1\Sigma_g^+$
A $2^3\Pi_g$
B $2^3\Pi_g$
C $2^3\Pi_g$

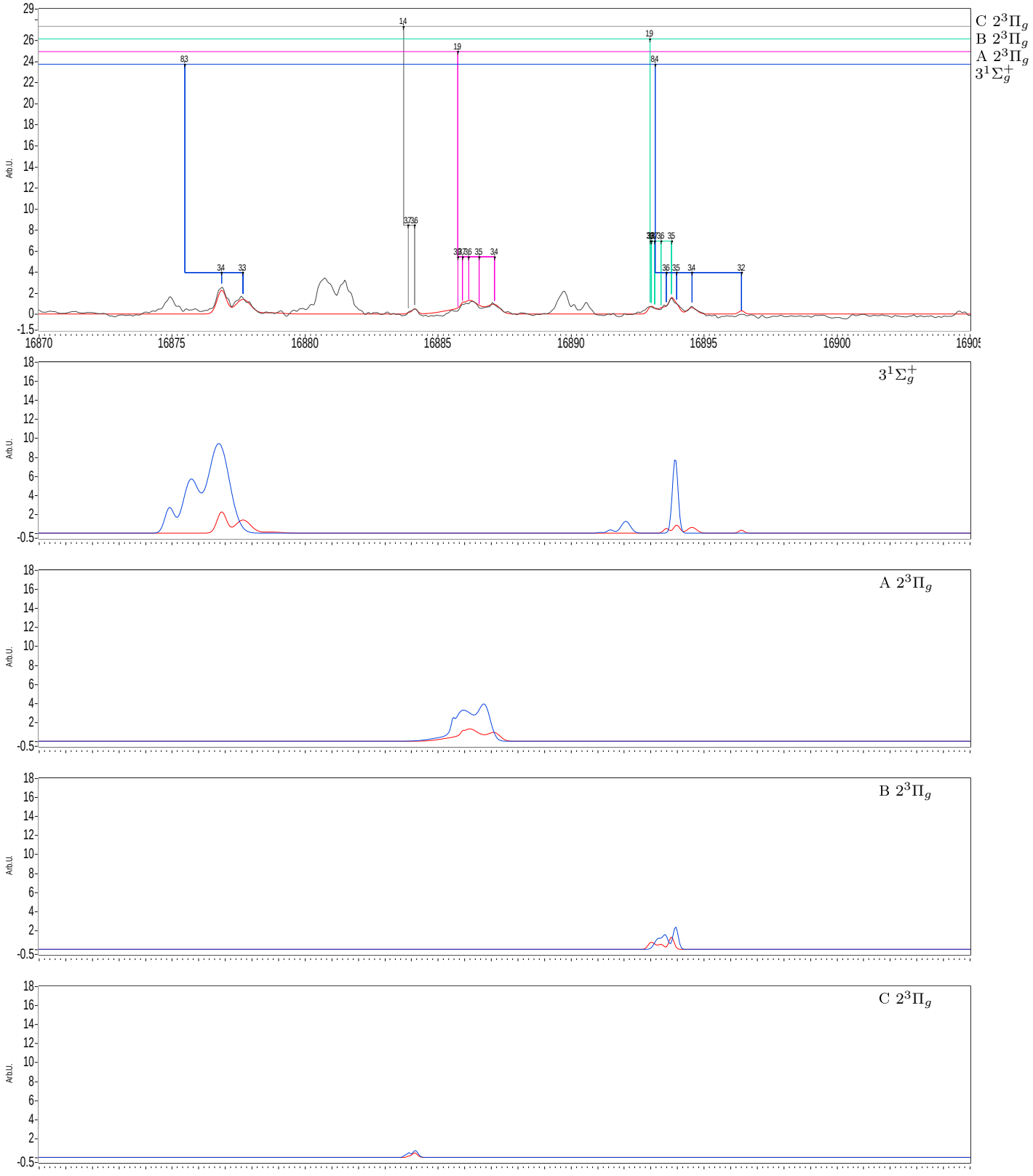
C $2^3\Pi_g$
B $2^3\Pi_g$
A $2^3\Pi_g$
$3^1\Sigma_g^+$
Arb.U.
16870
16875
16880
16885
16890
16895
16900
$3^1\Sigma_g^+$
A $2^3\Pi_g$
B $2^3\Pi_g$
C $2^3\Pi_g$

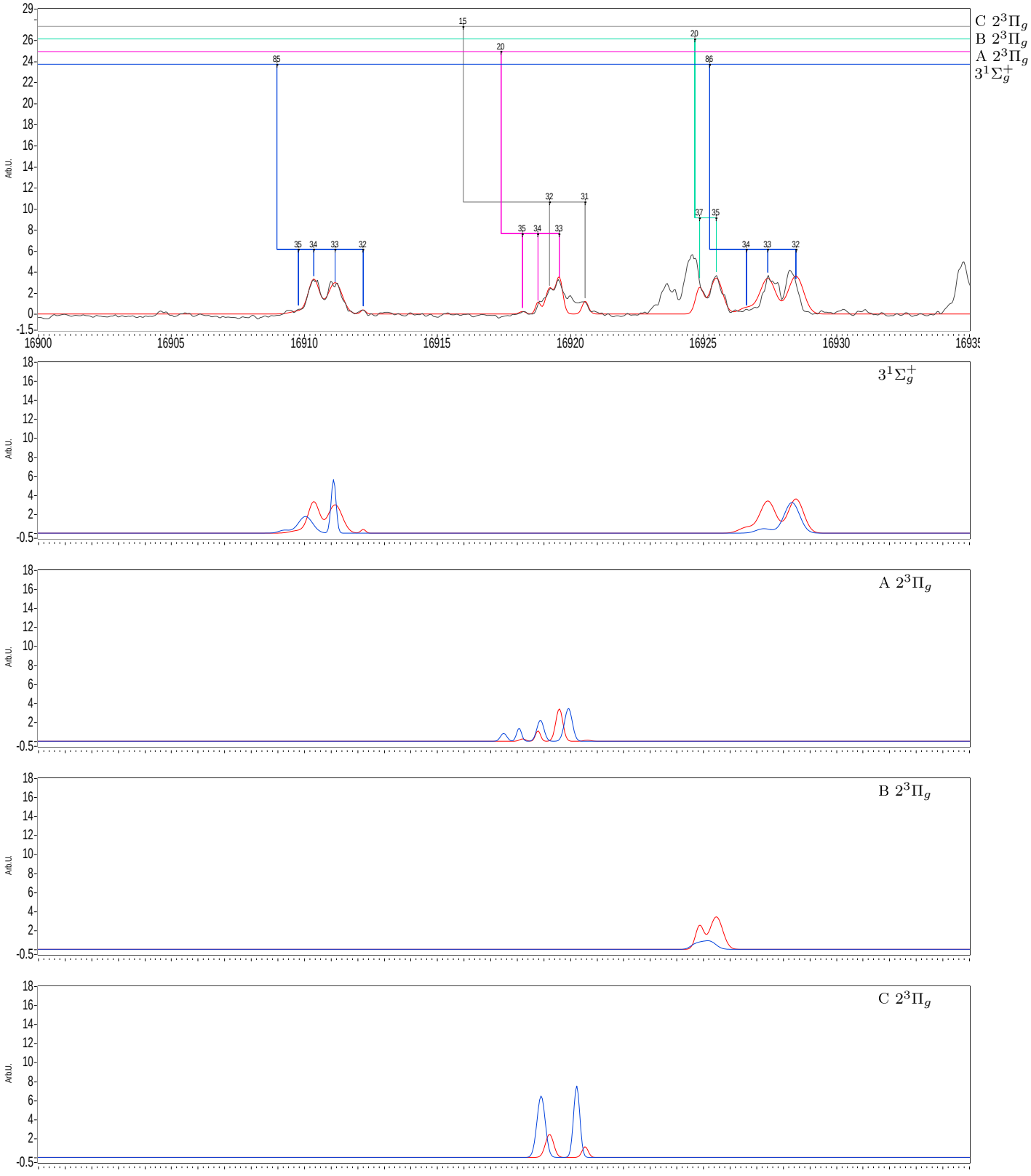
C $2^3\Pi_g$
B $2^3\Pi_g$
A $2^3\Pi_g$
$3^1\Sigma_g^+$
Arb.U.
16900
16905
16910
16915
16920
16925
16930
$3^1\Sigma_g^+$
A $2^3\Pi_g$
B $2^3\Pi_g$
C $2^3\Pi_g$

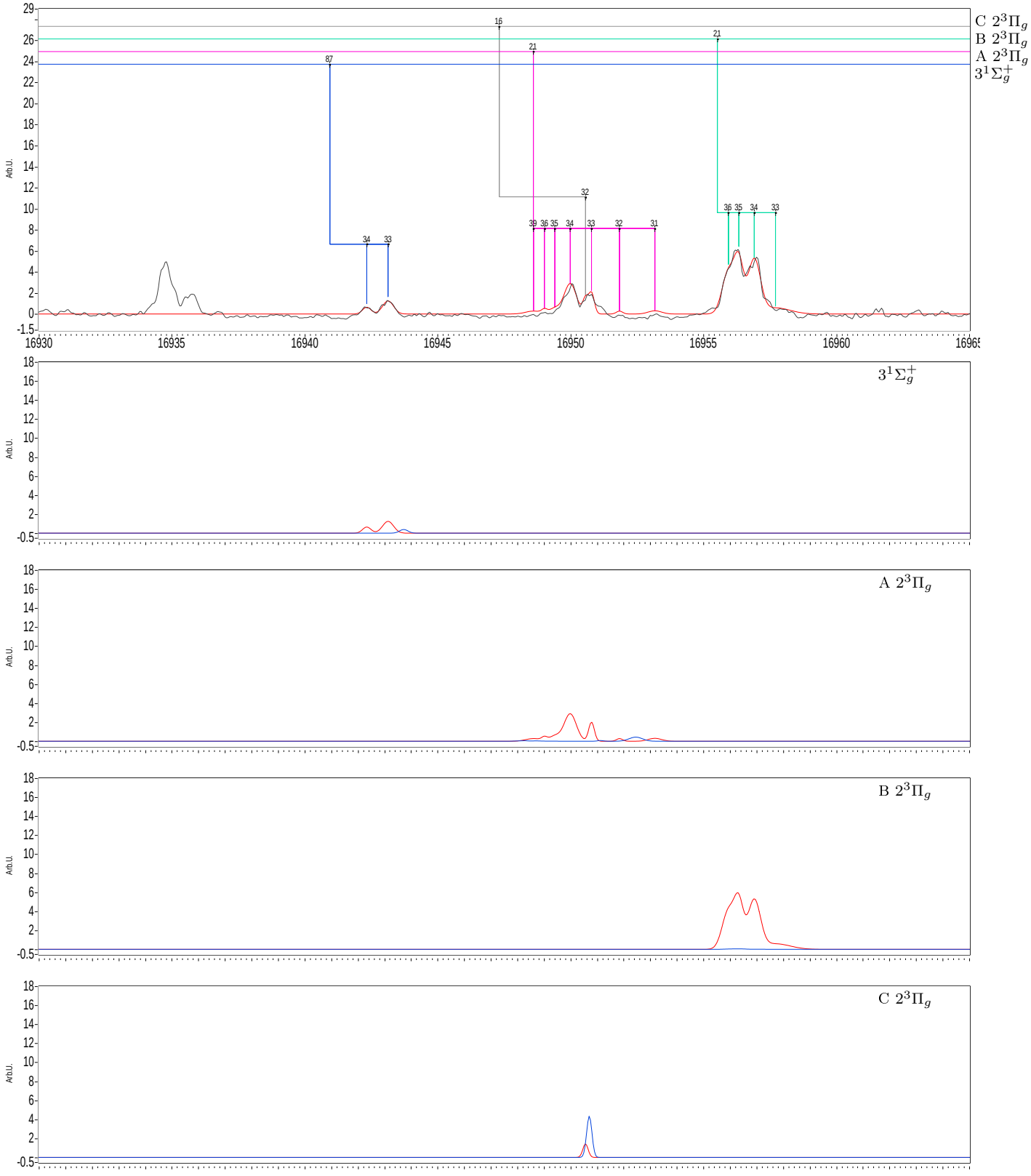
C $2^3\Pi_g$
B $2^3\Pi_g$
A $2^3\Pi_g$
$3^1\Sigma_g^+$
Arb.U.
16930
16935
16940
16945
16950
16955
16960
$3^1\Sigma_g^+$
A $2^3\Pi_g$
B $2^3\Pi_g$
C $2^3\Pi_g$

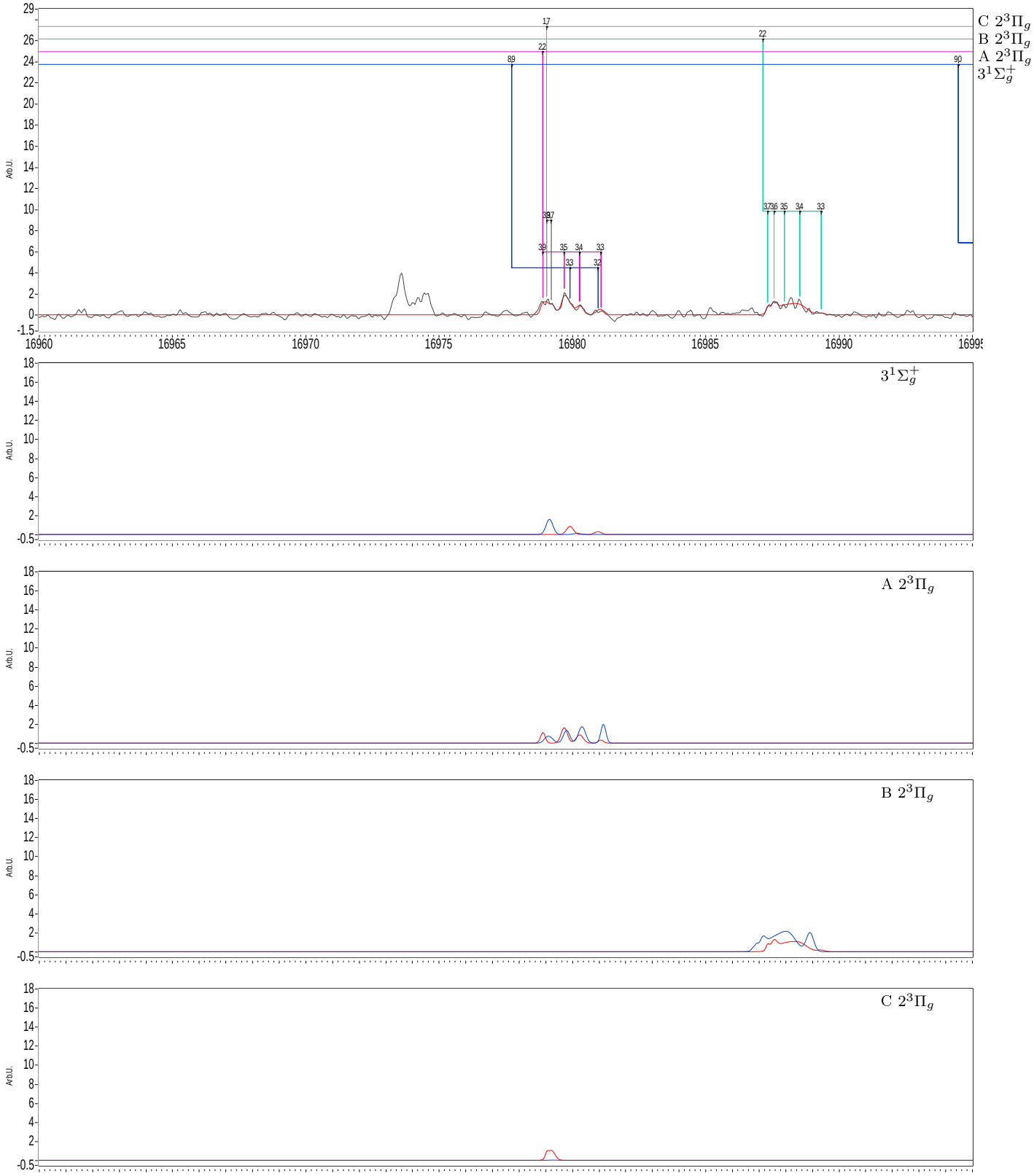
C $2^3\Pi_g$
B $2^3\Pi_g$
A $2^3\Pi_g$
$3^1\Sigma_g^+$
Arb.U.
16960
16965
16970
16975
16980
16985
16990
16995

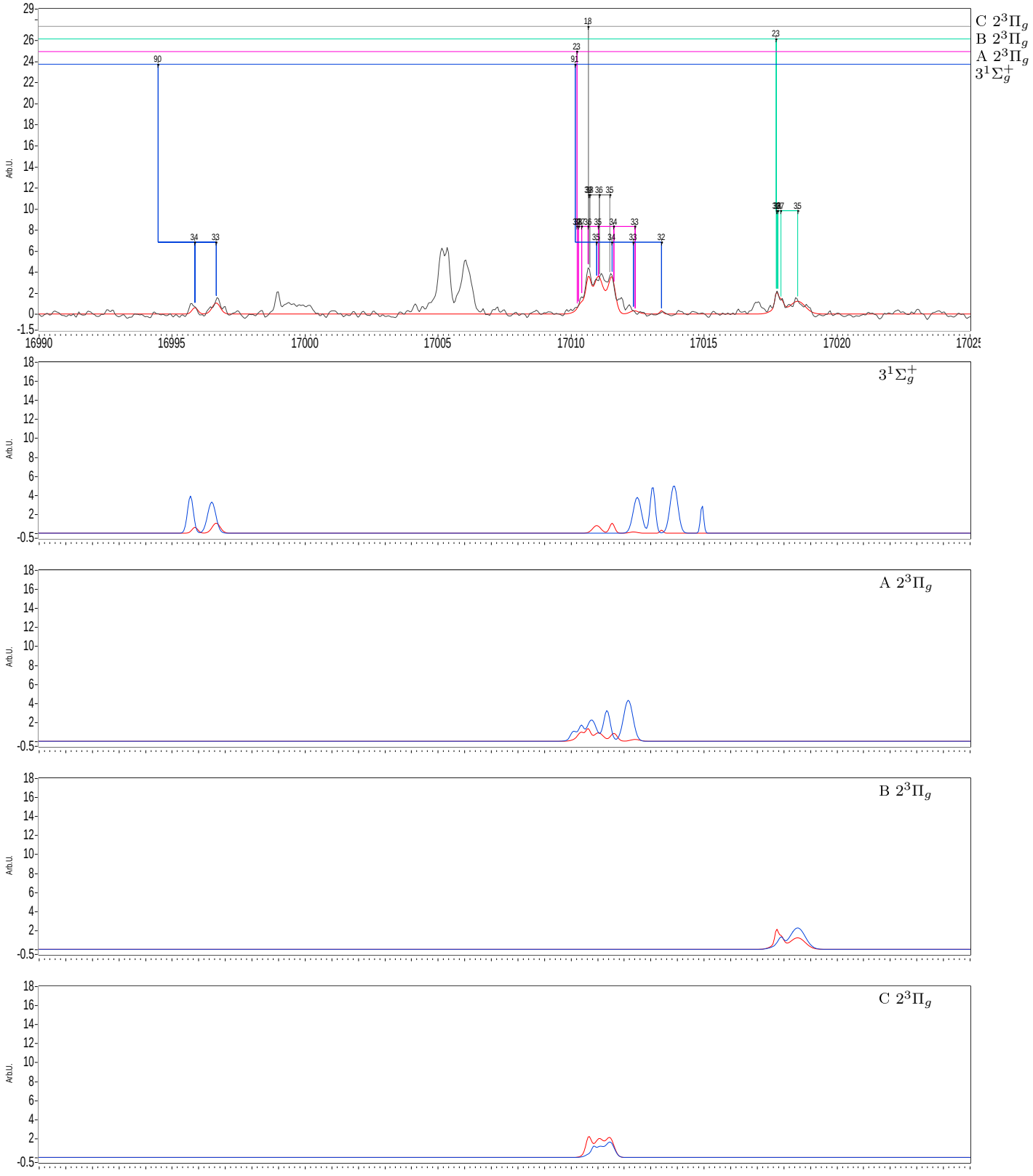
C $2^3\Pi_g$
B $2^3\Pi_g$
A $2^3\Pi_g$
$3^1\Sigma_g^+$
Arb.U.
16990
16995
17000
17005
17010
17015
17020
$3^1\Sigma_g^+$
A $2^3\Pi_g$
B $2^3\Pi_g$
C $2^3\Pi_g$

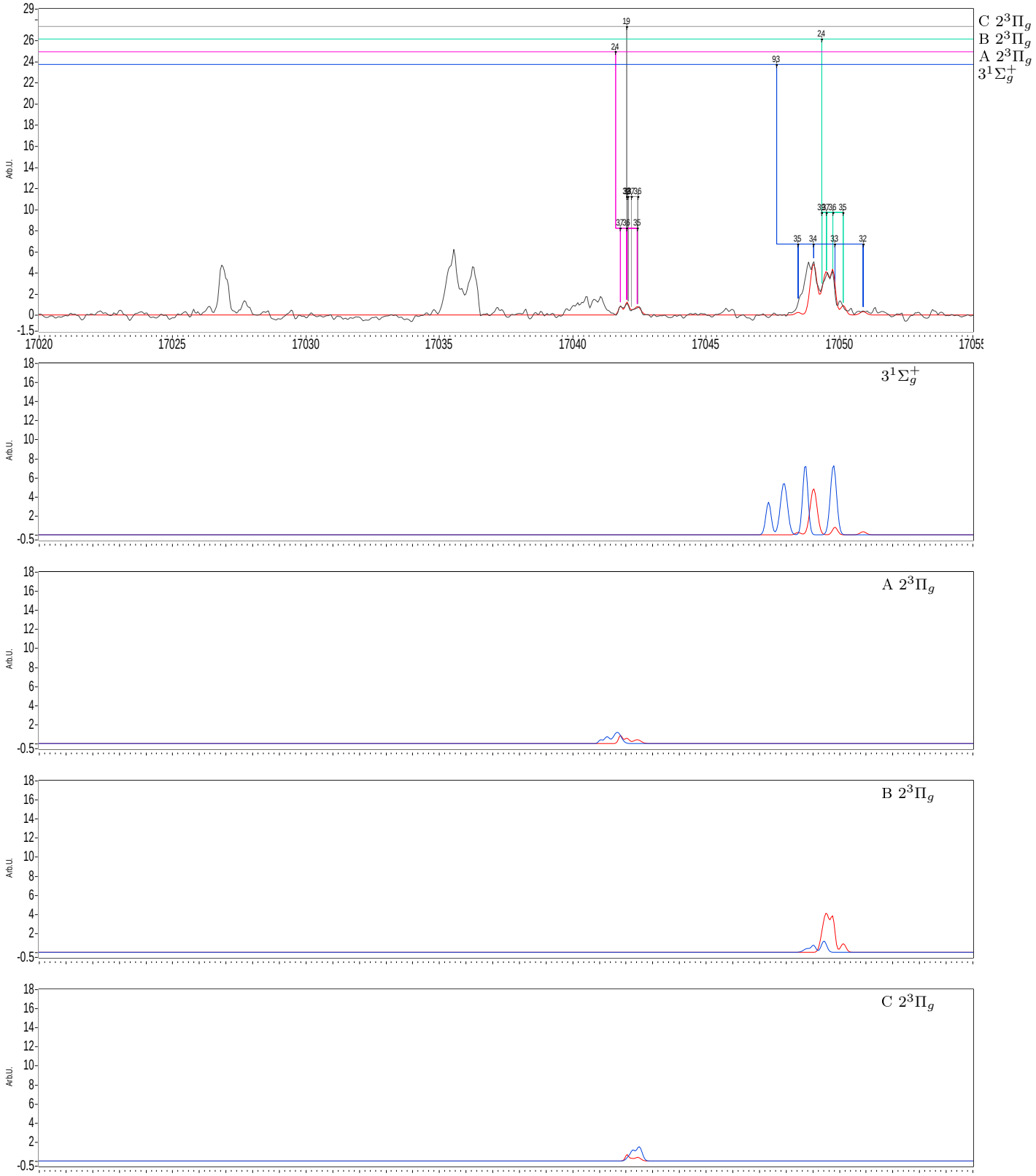
C $2^3\Pi_g$
B $2^3\Pi_g$
A $2^3\Pi_g$
$3^1\Sigma_g^+$
Arb.U.
17020
17025
17030
17035
17040
17045
17050
$3^1\Sigma_g^+$
A $2^3\Pi_g$
B $2^3\Pi_g$
C $2^3\Pi_g$

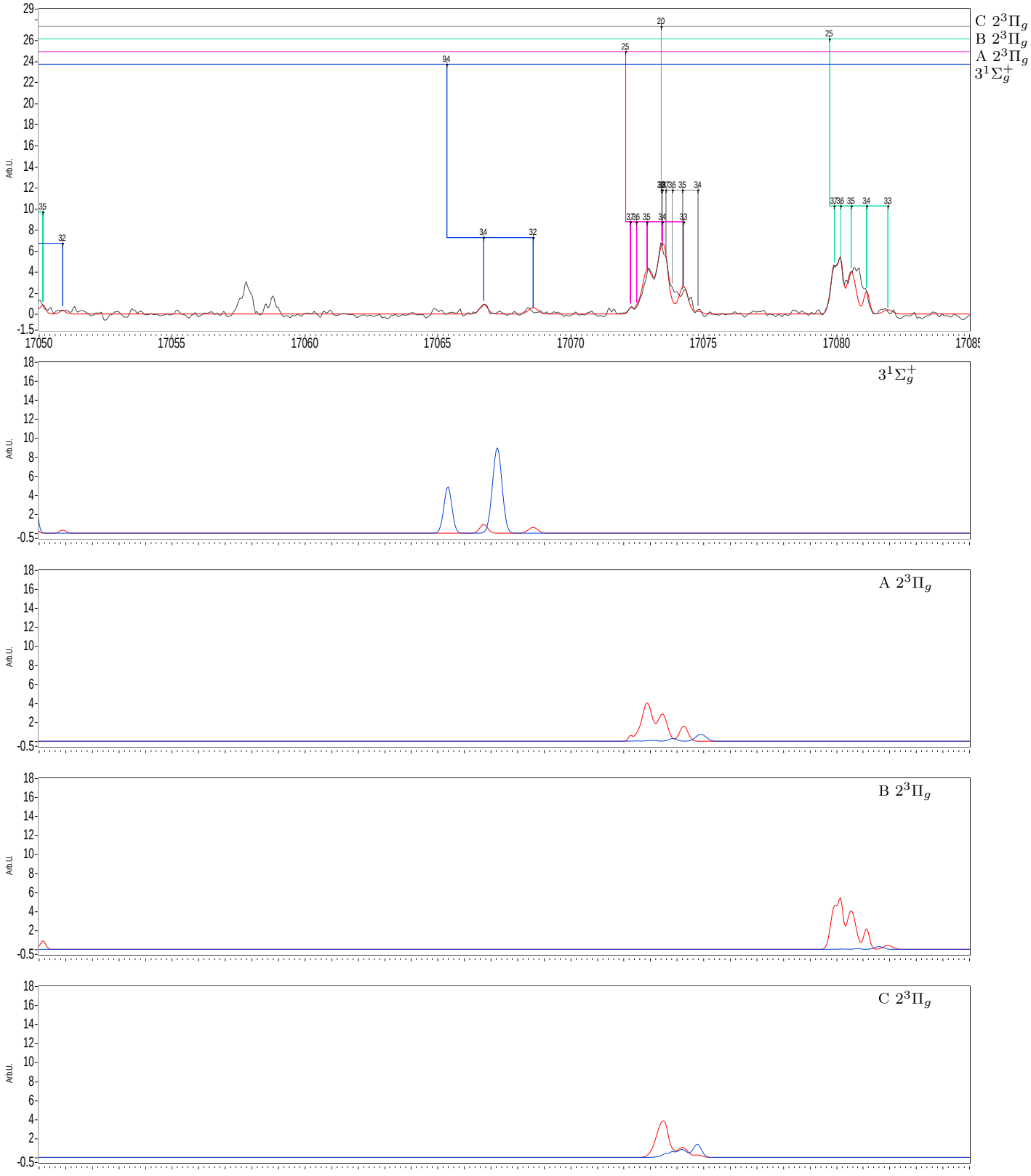
C $2^3\Pi_g$
B $2^3\Pi_g$
A $2^3\Pi_g$
$3^1\Sigma_g^+$
Arb.U.
17050
17055
17060
17065
17070
17075
17080
$3^1\Sigma_g^+$
A $2^3\Pi_g$
B $2^3\Pi_g$
C $2^3\Pi_g$

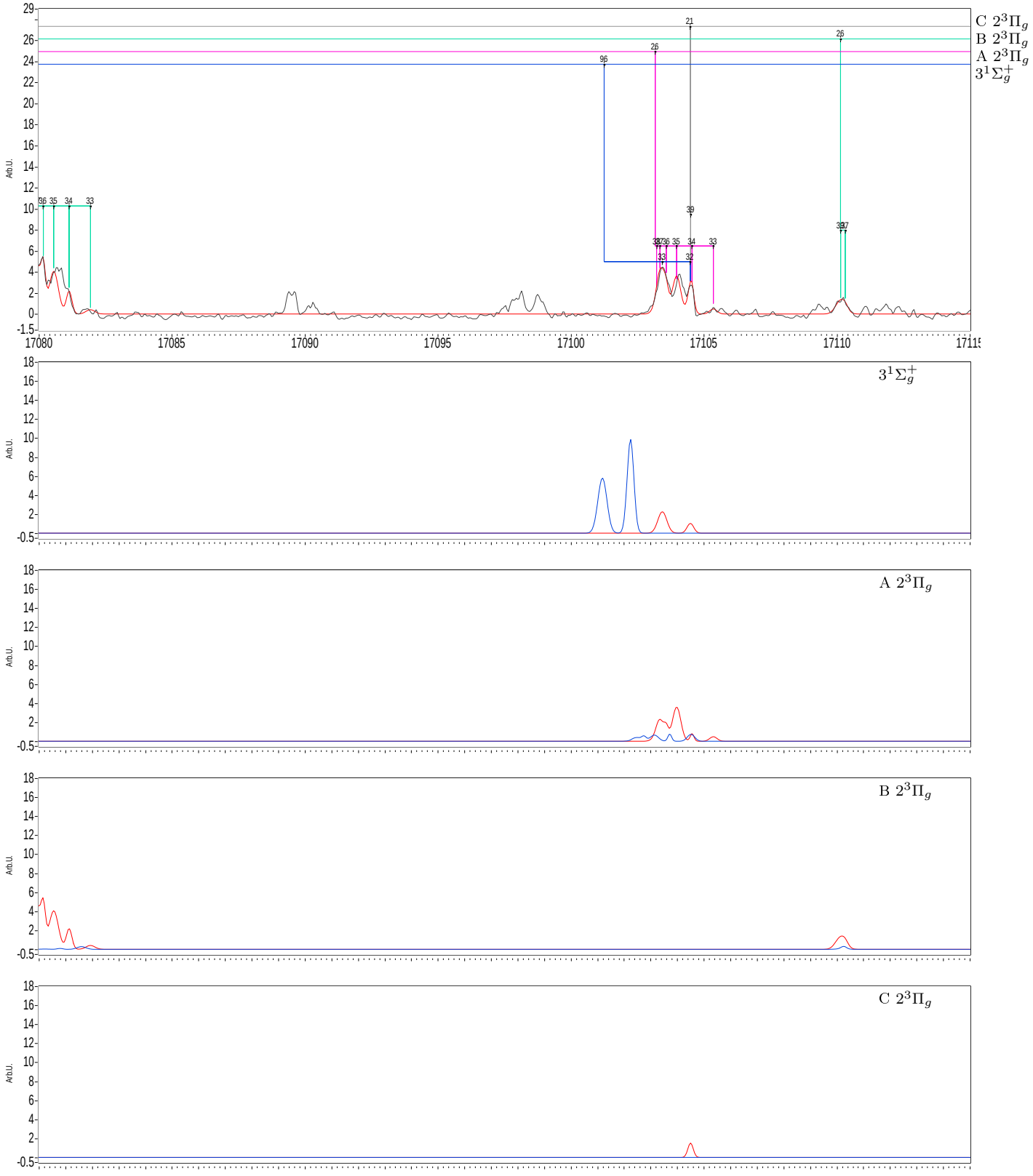
C $2^3\Pi_g$
B $2^3\Pi_g$
A $2^3\Pi_g$
$3^1\Sigma_g^+$
Arb.U.
17080
17085
17090
17095
17100
17105
17110
$3^1\Sigma_g^+$
A $2^3\Pi_g$
B $2^3\Pi_g$
C $2^3\Pi_g$

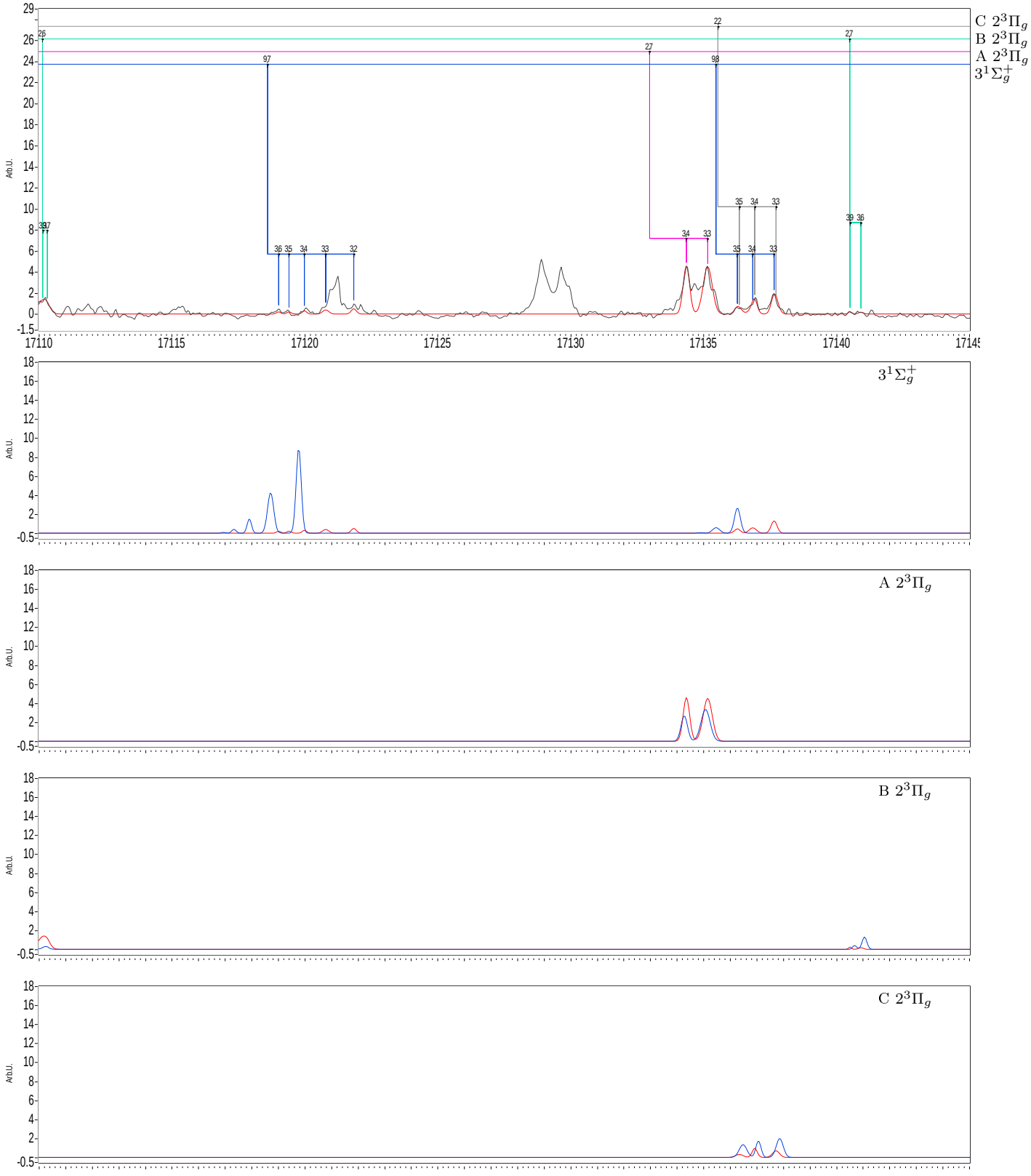
C $2^3\Pi_g$
B $2^3\Pi_g$
A $2^3\Pi_g$
$3^1\Sigma_g^+$
Arb.U.
17110
17115
17120
17125
17130
17135
17140
$3^1\Sigma_g^+$
A $2^3\Pi_g$
B $2^3\Pi_g$
C $2^3\Pi_g$

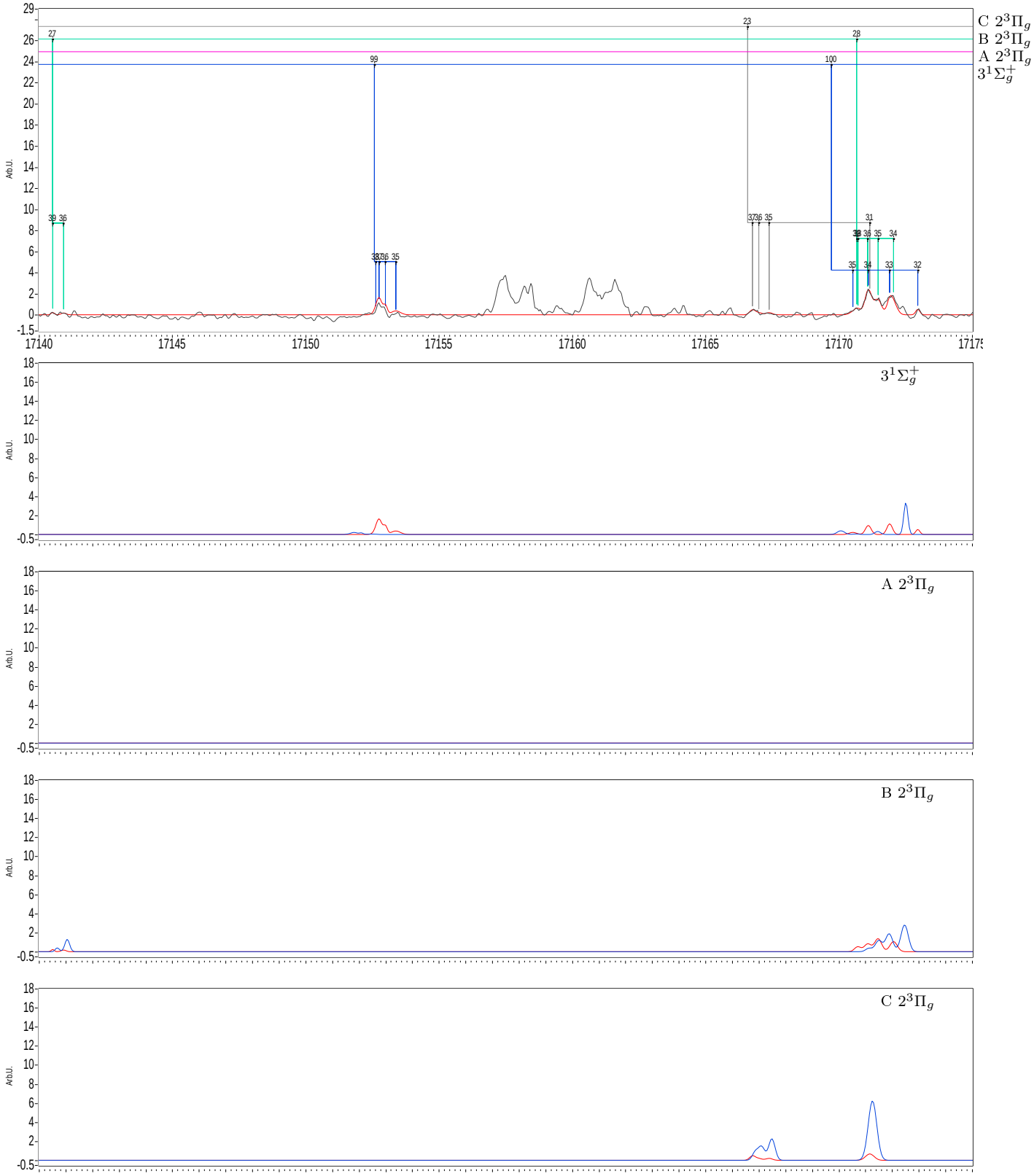
C $2^3\Pi_g$
B $2^3\Pi_g$
A $2^3\Pi_g$
$3^1\Sigma_g^+$
Arb.U.
17140
17145
17150
17155
17160
17165
17170

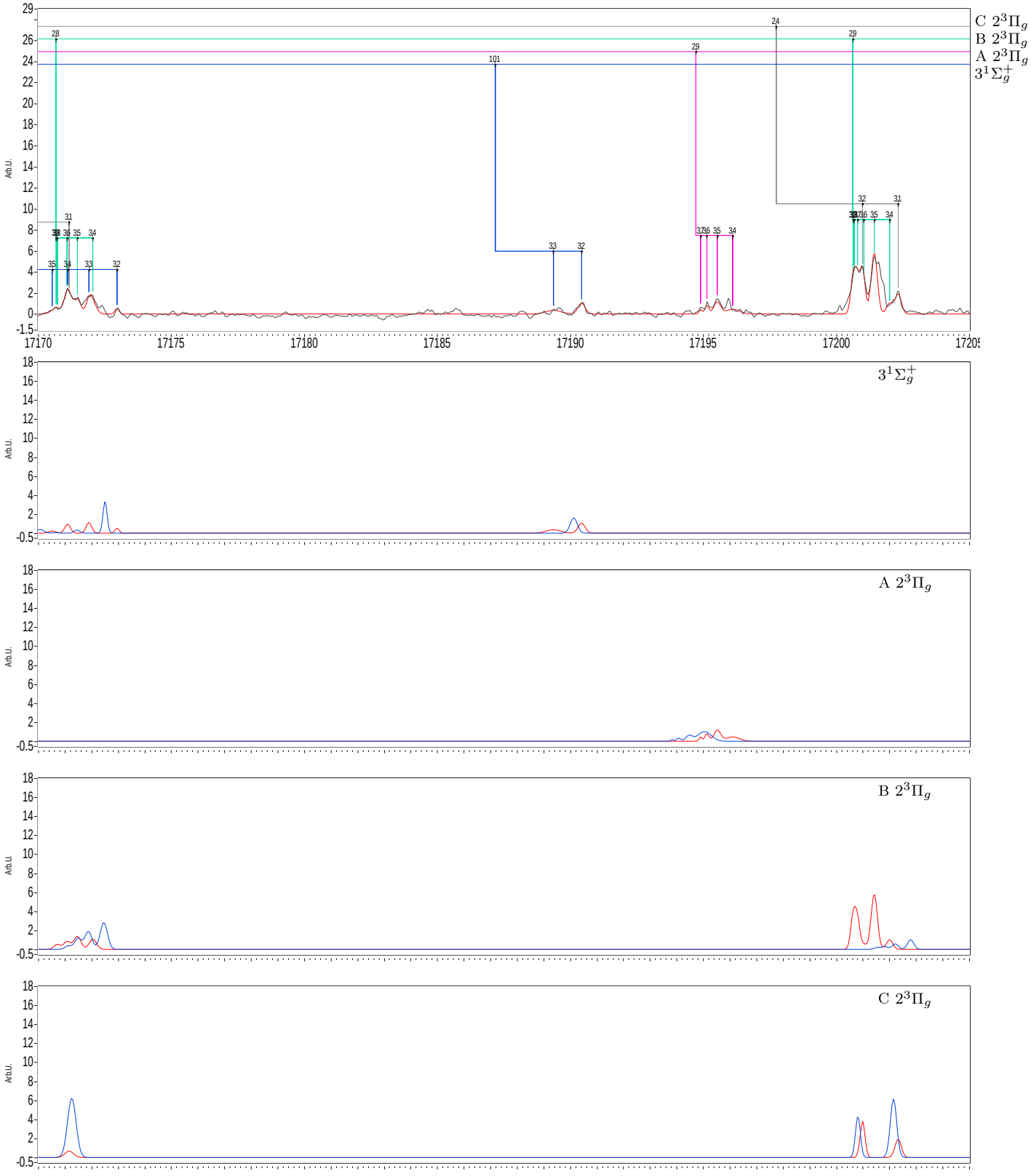
C $2^3\Pi_g$
B $2^3\Pi_g$
A $2^3\Pi_g$
$3^1\Sigma_g^+$
Arb.U.
17170
17175
17180
17185
17190
17195
17200
$3^1\Sigma_g^+$
A $2^3\Pi_g$
B $2^3\Pi_g$
C $2^3\Pi_g$

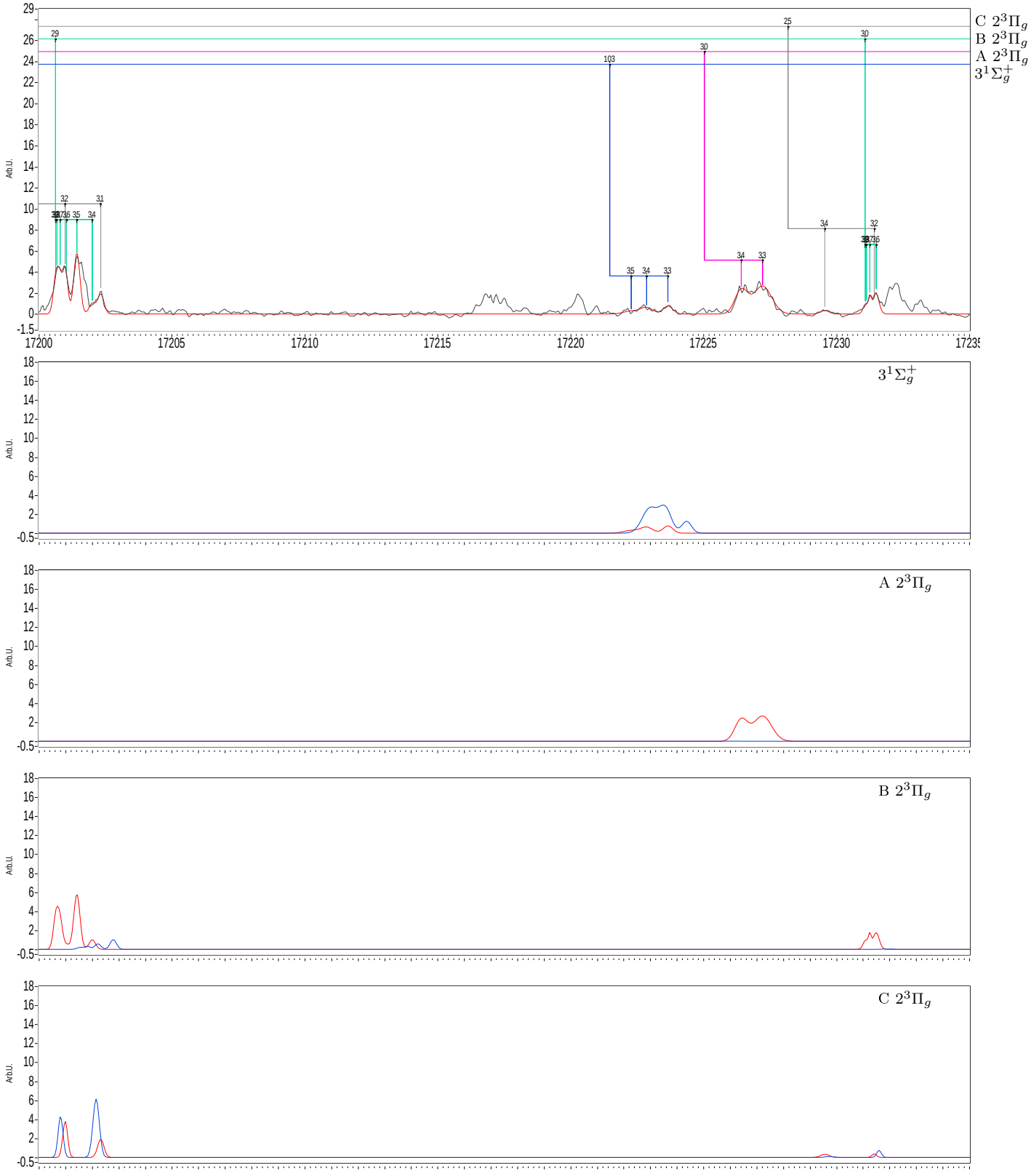
C $2^3\Pi_g$
B $2^3\Pi_g$
A $2^3\Pi_g$
$3^1\Sigma_g^+$
Arb.U.
17200
17205
17210
17215
17220
17225
17230
$3^1\Sigma_g^+$
A $2^3\Pi_g$
B $2^3\Pi_g$
C $2^3\Pi_g$

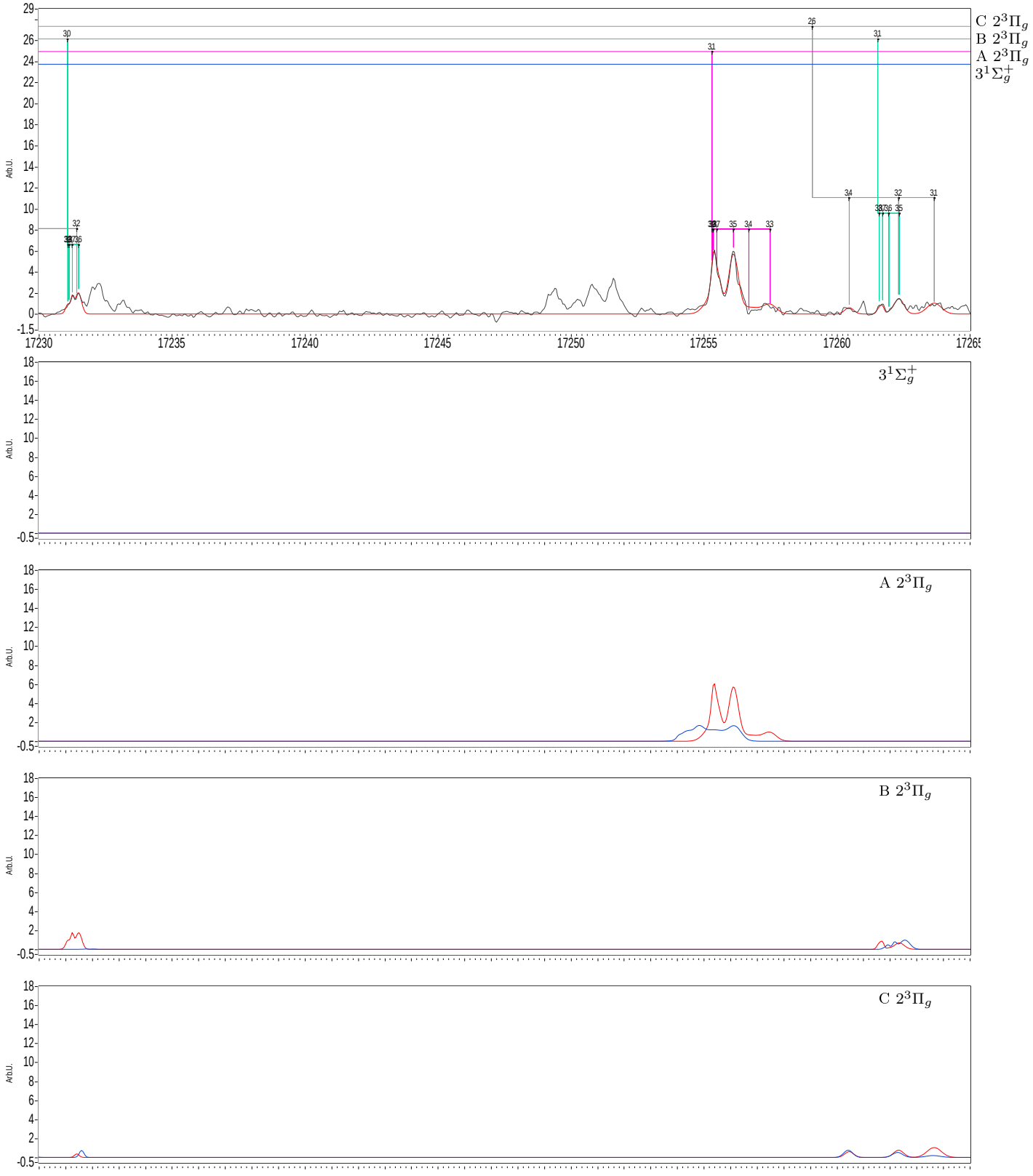
C $2^3\Pi_g$
B $2^3\Pi_g$
A $2^3\Pi_g$
$3^1\Sigma_g^+$
Arb.U.
17230
17235
17240
17245
17250
17255
17260
$3^1\Sigma_g^+$
A $2^3\Pi_g$
B $2^3\Pi_g$
C $2^3\Pi_g$

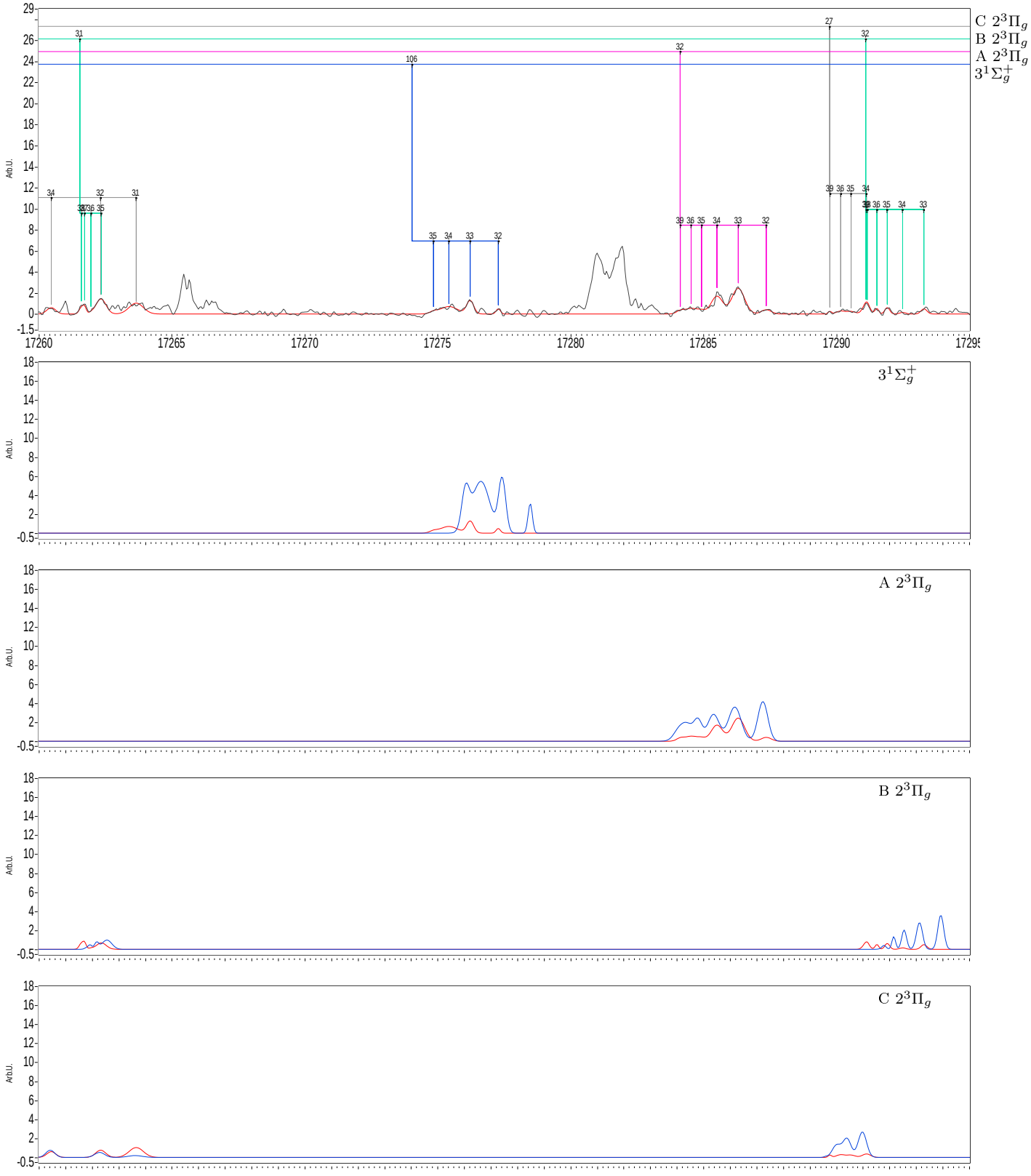
C $2^3\Pi_g$
B $2^3\Pi_g$
A $2^3\Pi_g$
$3^1\Sigma_g^+$
Arb.U.
17260
17265
17270
17275
17280
17285
17290
$3^1\Sigma_g^+$
A $2^3\Pi_g$
B $2^3\Pi_g$
C $2^3\Pi_g$

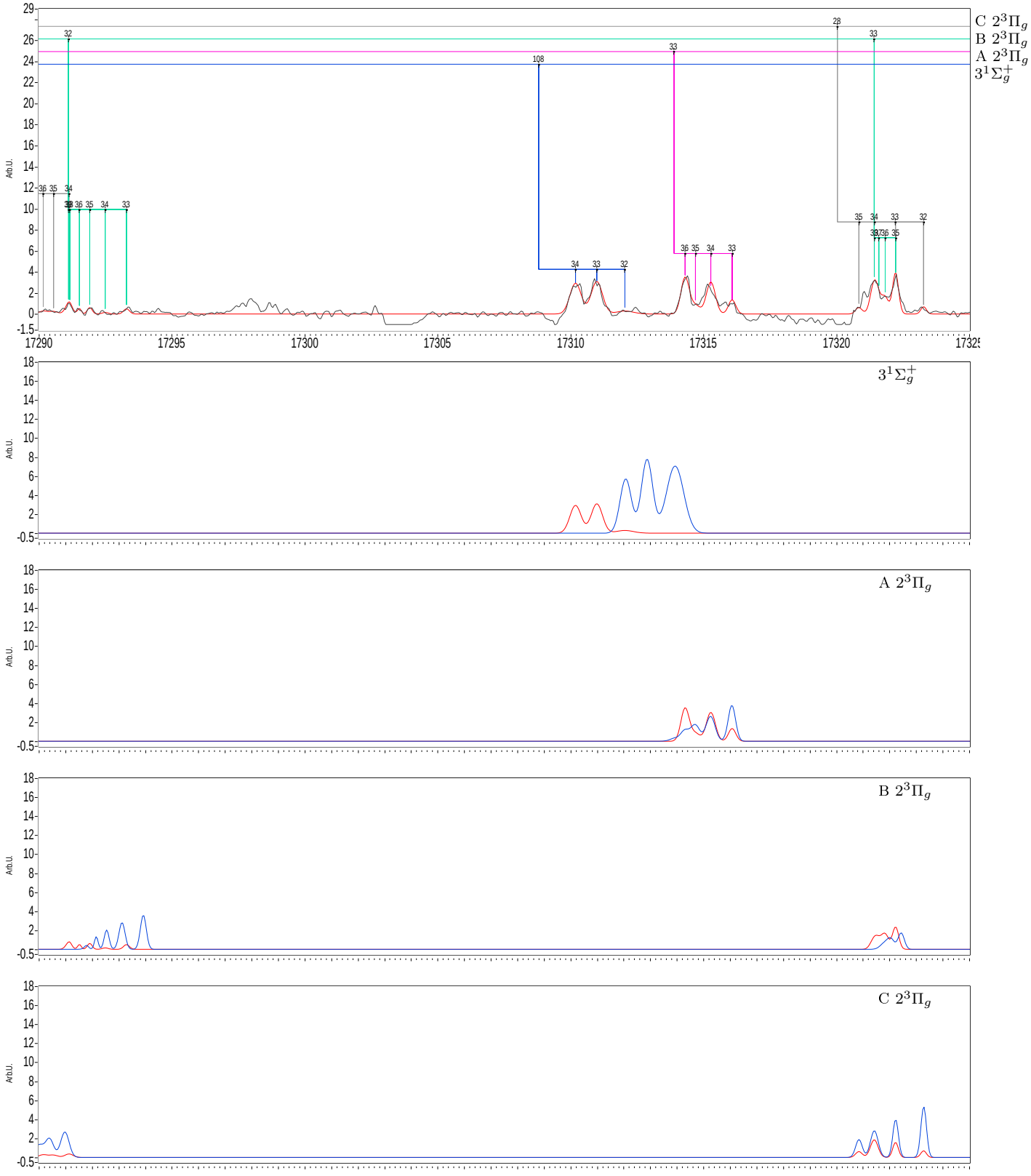
C $2^3\Pi_g$
B $2^3\Pi_g$
A $2^3\Pi_g$
$3^1\Sigma_g^+$
Arb.U.
17290
17295
17300
17305
17310
17315
17320
$3^1\Sigma_g^+$
A $2^3\Pi_g$
B $2^3\Pi_g$
C $2^3\Pi_g$

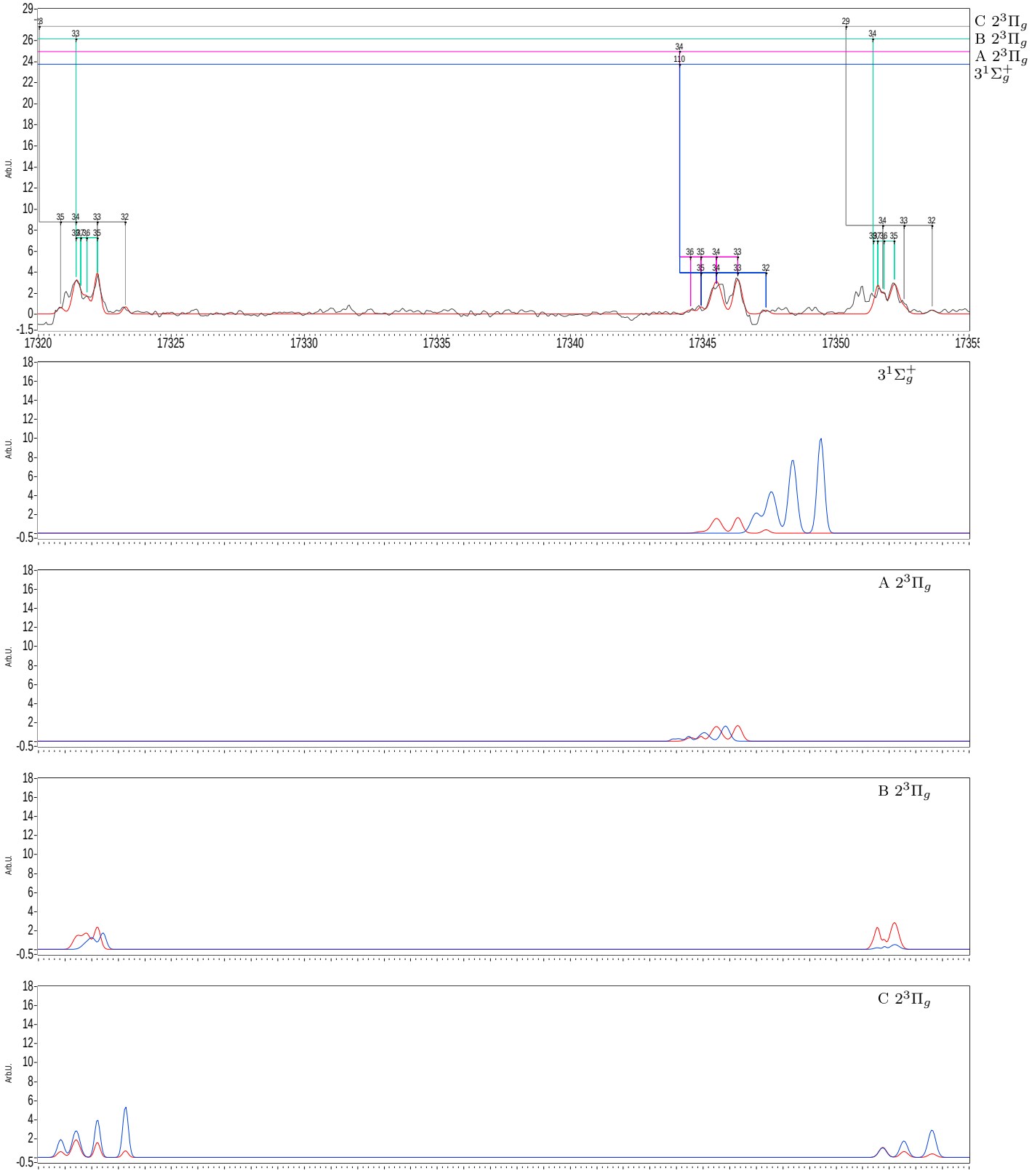
C $2^3\Pi_g$
B $2^3\Pi_g$
A $2^3\Pi_g$
$3^1\Sigma_g^+$
Arb.U.
17320
17325
17330
17335
17340
17345
17350
$3^1\Sigma_g^+$
A $2^3\Pi_g$
B $2^3\Pi_g$
C $2^3\Pi_g$

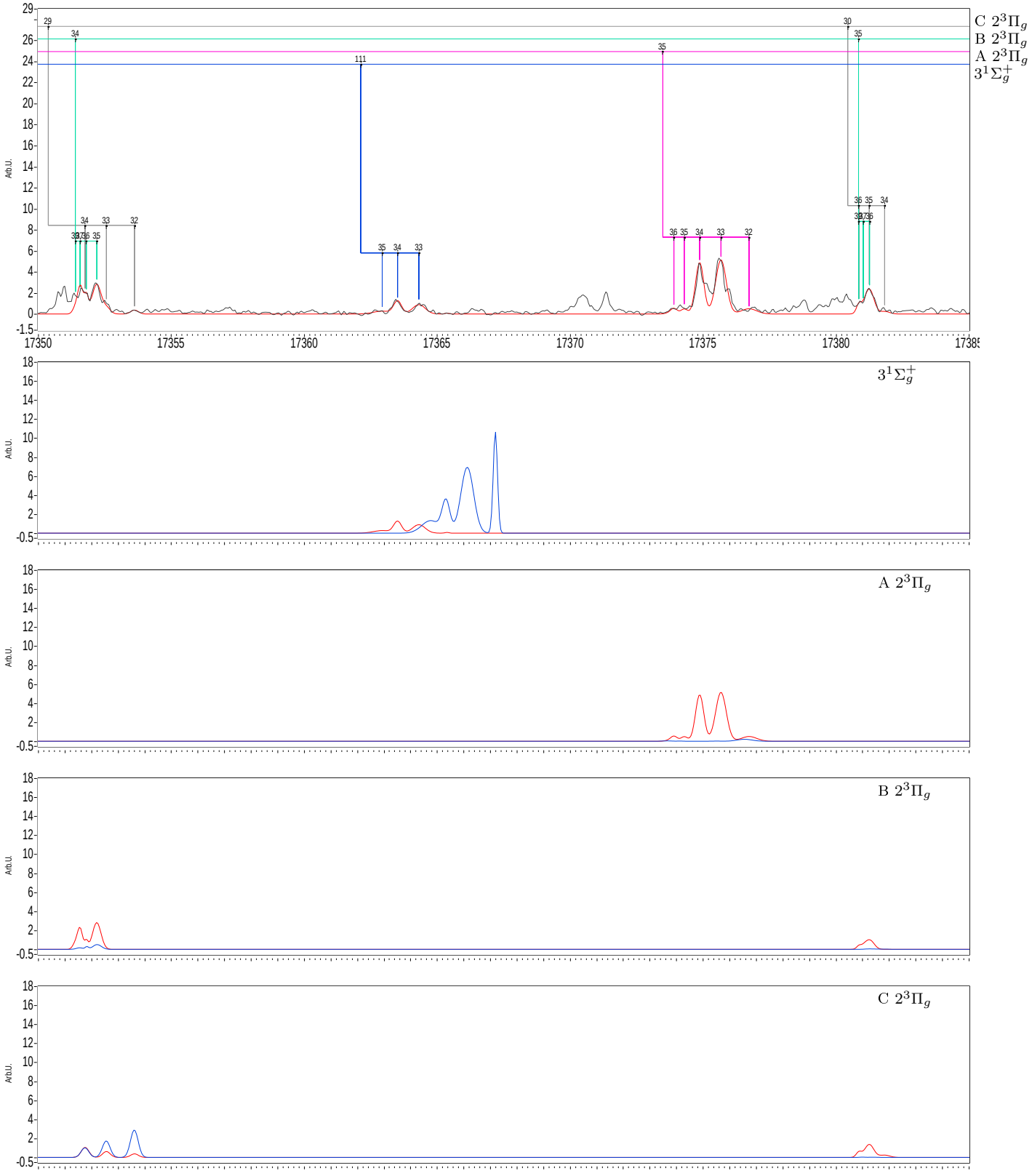
C $2^3\Pi_g$
B $2^3\Pi_g$
A $2^3\Pi_g$
$3^1\Sigma_g^+$
Arb.U.
17350
17355
17360
17365
17370
17375
17380
$3^1\Sigma_g^+$
A $2^3\Pi_g$
B $2^3\Pi_g$
C $2^3\Pi_g$

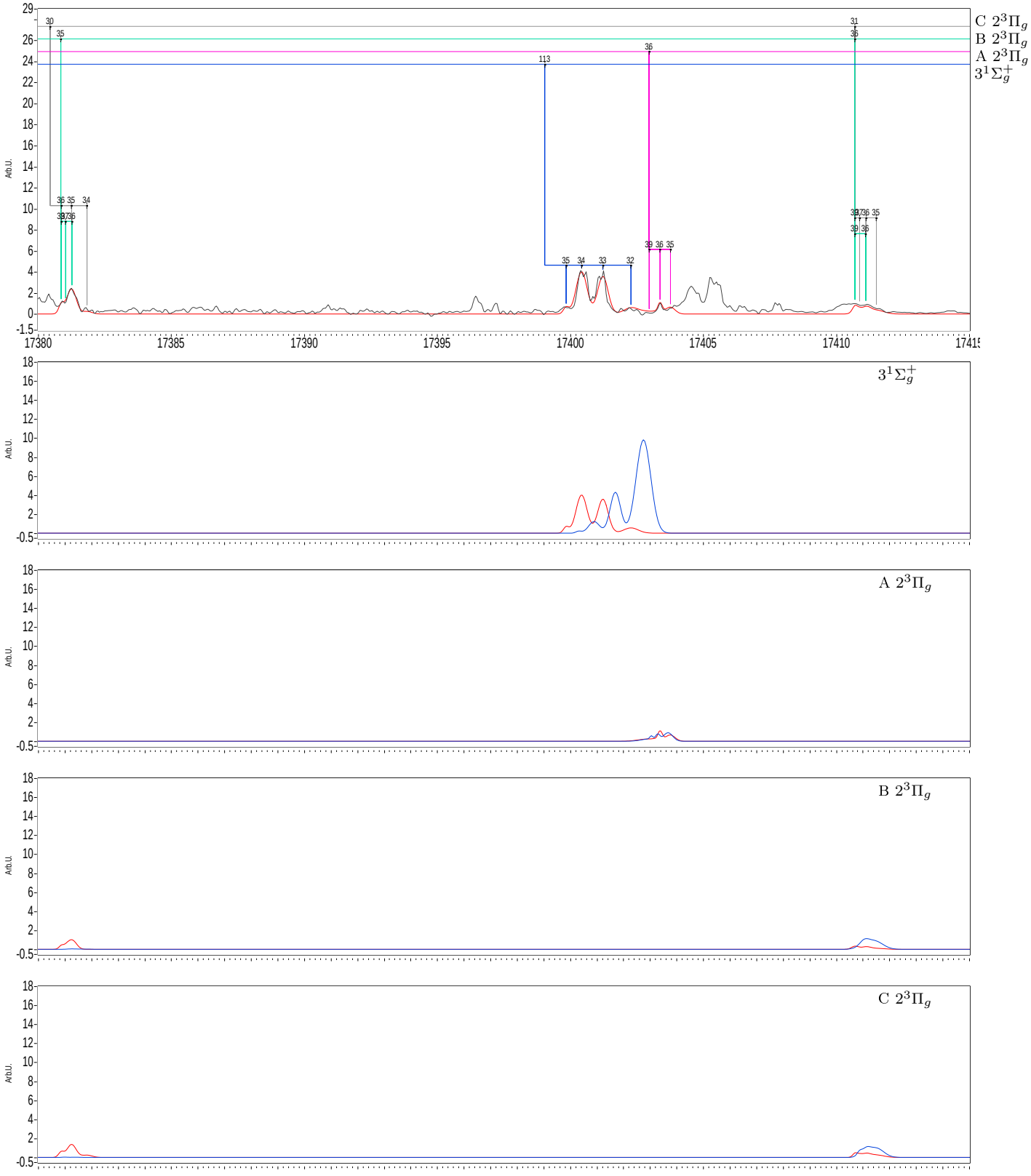
C $2^3\Pi_g$
B $2^3\Pi_g$
A $2^3\Pi_g$
$3^1\Sigma_g^+$
Arb.U.
17380
17385
17390
17395
17400
17405
17410
$3^1\Sigma_g^+$
A $2^3\Pi_g$
B $2^3\Pi_g$
C $2^3\Pi_g$

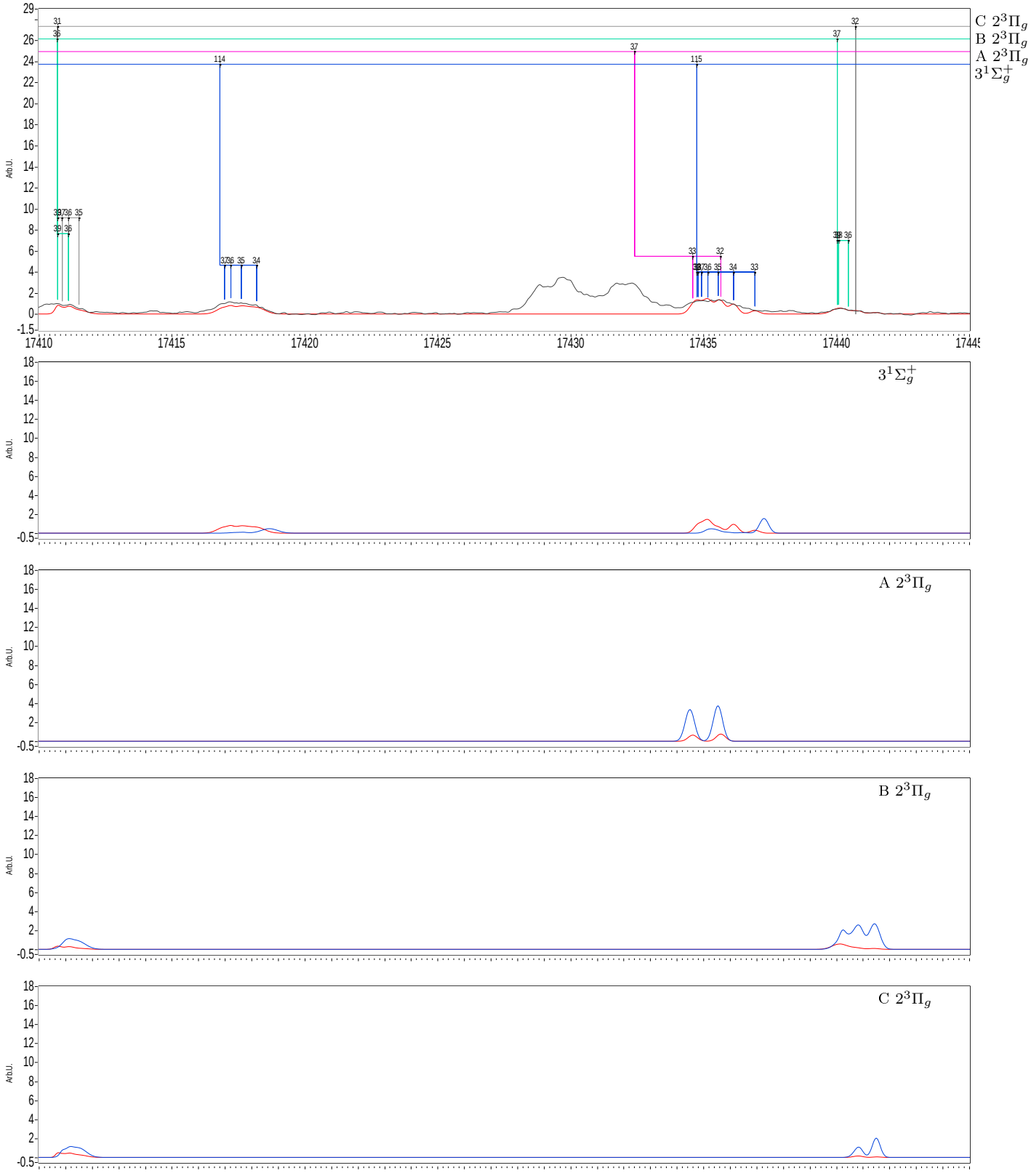
C $2^3\Pi_g$
B $2^3\Pi_g$
A $2^3\Pi_g$
$3^1\Sigma_g^+$
Arb.U.
17410
17415
17420
17425
17430
17435
17440

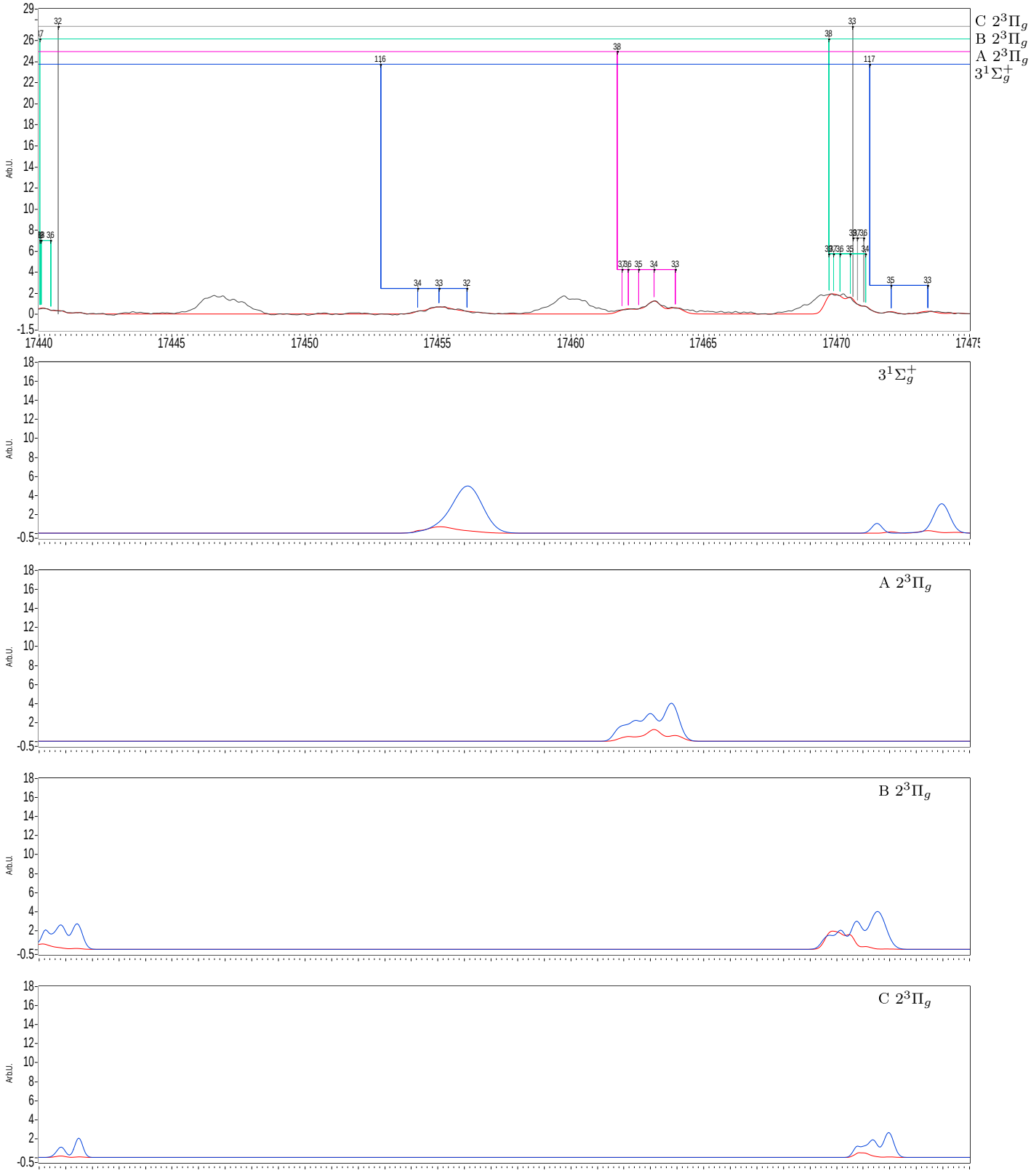
C $2^3\Pi_g$
B $2^3\Pi_g$
A $2^3\Pi_g$
$3^1\Sigma_g^+$
Arb.U.
17440
17445
17450
17455
17460
17465
17470
17475

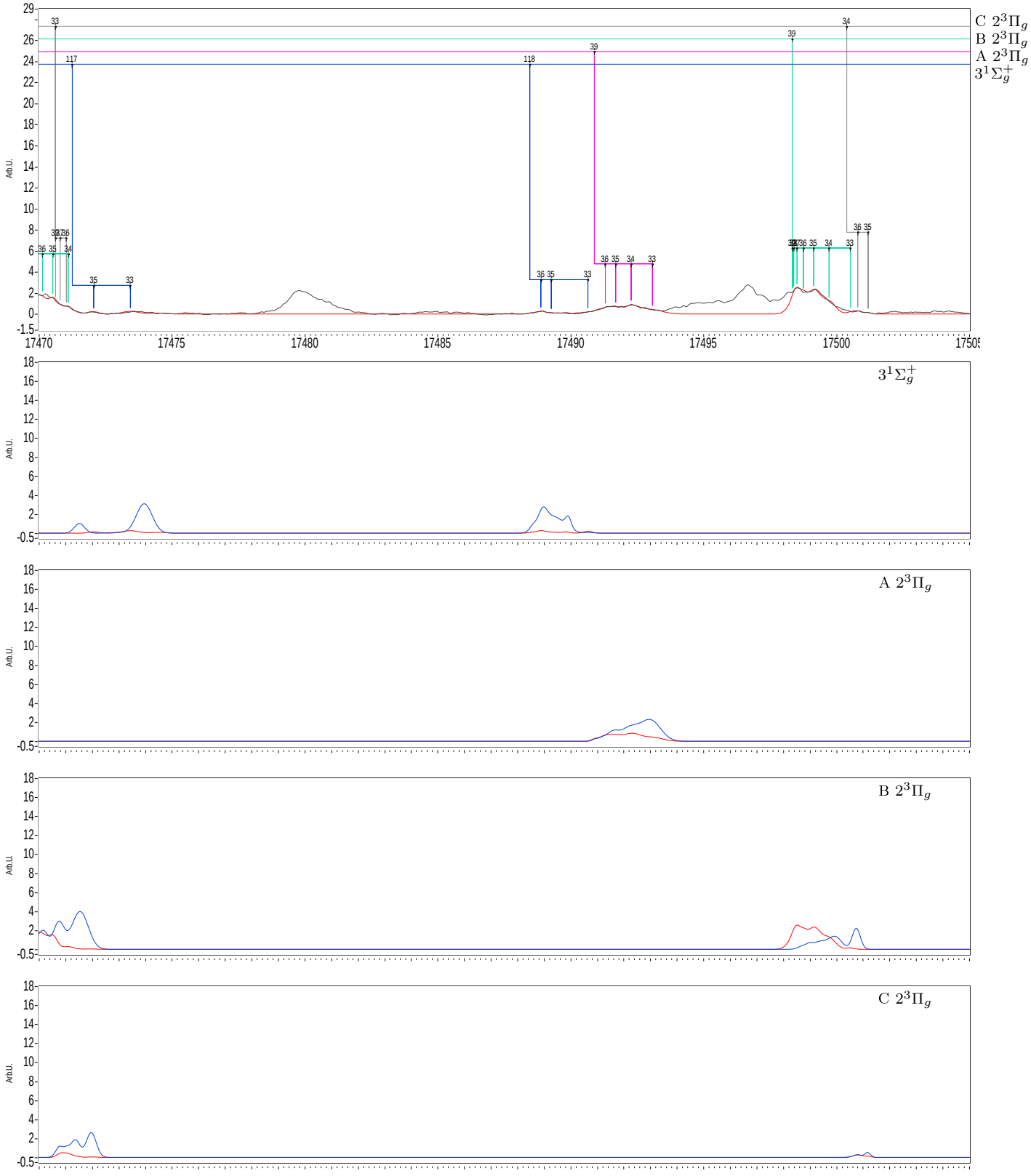
C $2^3\Pi_g$
B $2^3\Pi_g$
A $2^3\Pi_g$
$3^1\Sigma_g^+$
Arb.U.
17470
17475
17480
17485
17490
17495
17500
$3^1\Sigma_g^+$
A $2^3\Pi_g$
B $2^3\Pi_g$
C $2^3\Pi_g$

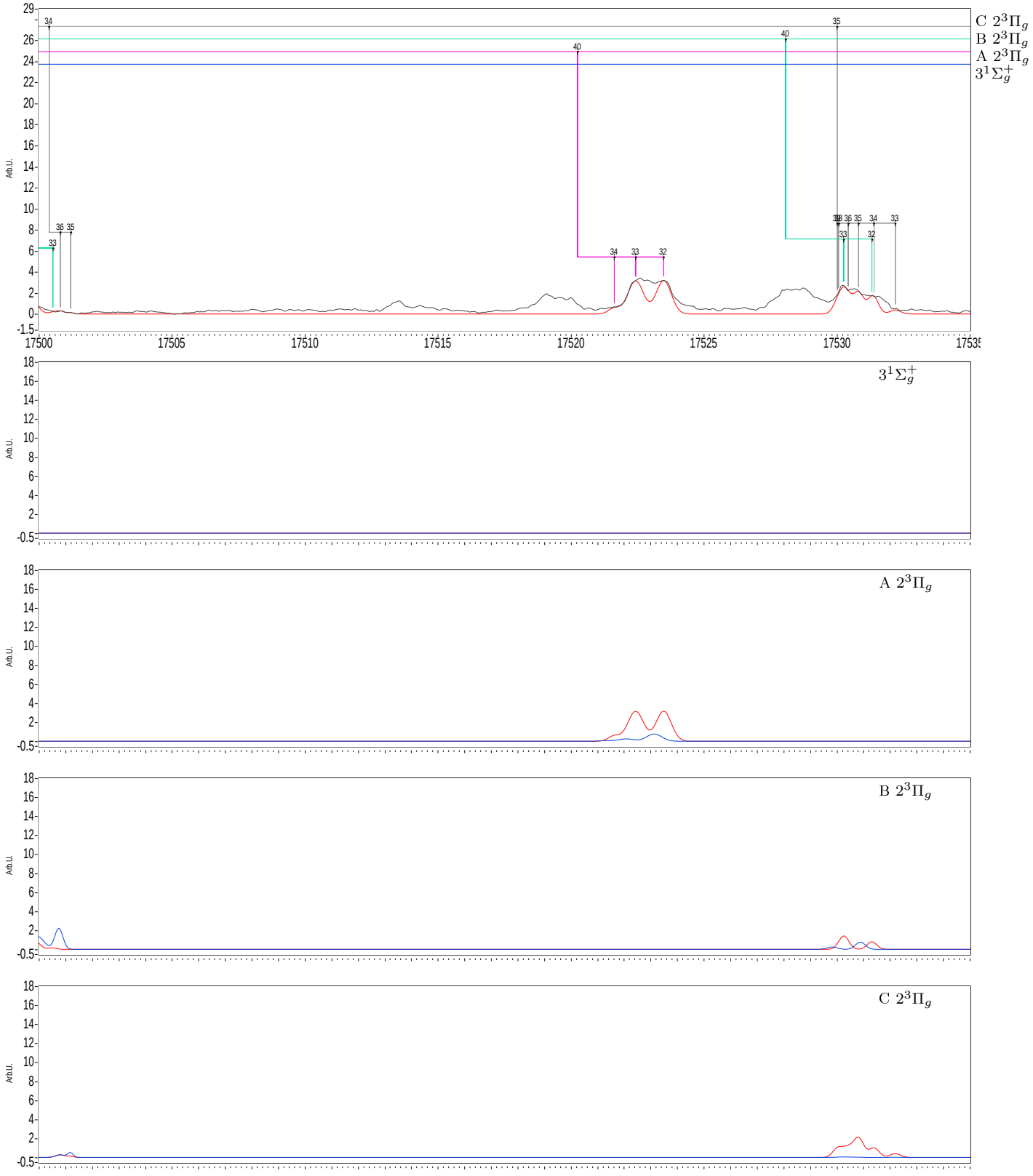
C $2^3\Pi_g$
B $2^3\Pi_g$
A $2^3\Pi_g$
$3^1\Sigma_g^+$
Arb.U.
17500
17505
17510
17515
17520
17525
17530
$3^1\Sigma_g^+$
A $2^3\Pi_g$
B $2^3\Pi_g$
C $2^3\Pi_g$

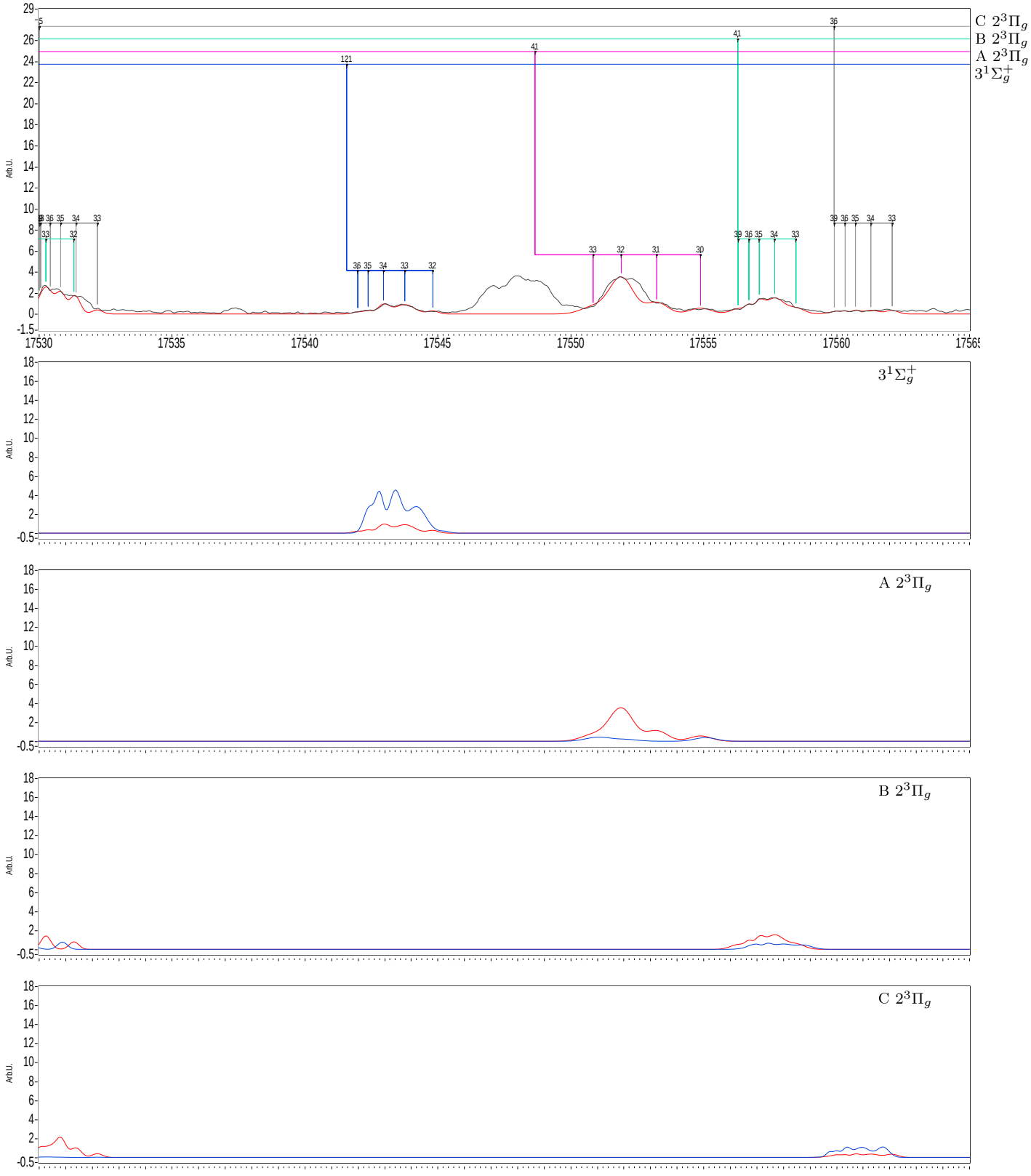
C $2^3\Pi_g$
B $2^3\Pi_g$
A $2^3\Pi_g$
$3^1\Sigma_g^+$
Arb.U.
17530
17535
17540
17545
17550
17555
17560

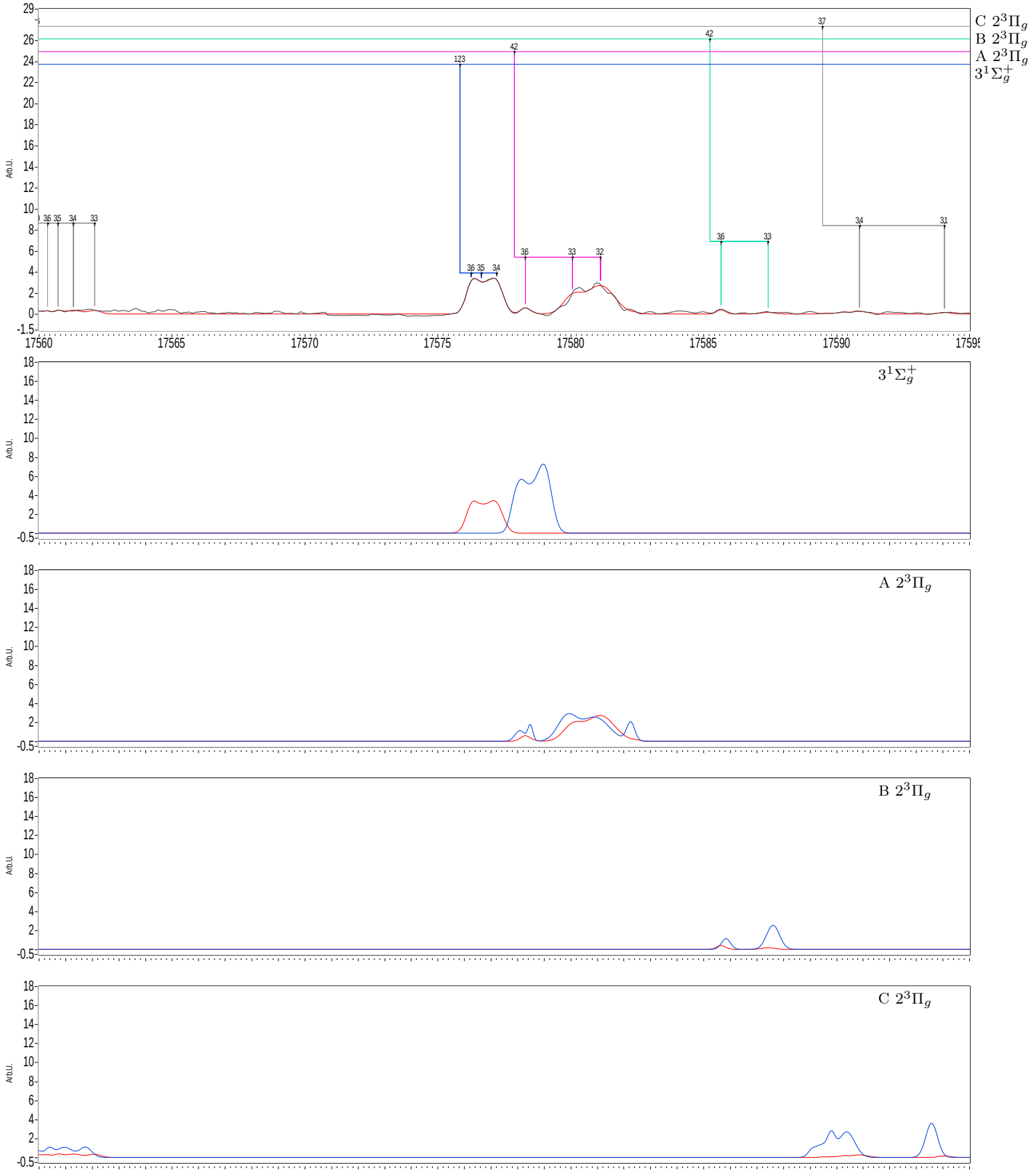
C $2^3\Pi_g$
B $2^3\Pi_g$
A $2^3\Pi_g$
$3^1\Sigma_g^+$
Arb.U.
17560
17565
17570
17575
17580
17585
17590
$3^1\Sigma_g^+$
A $2^3\Pi_g$
B $2^3\Pi_g$
C $2^3\Pi_g$

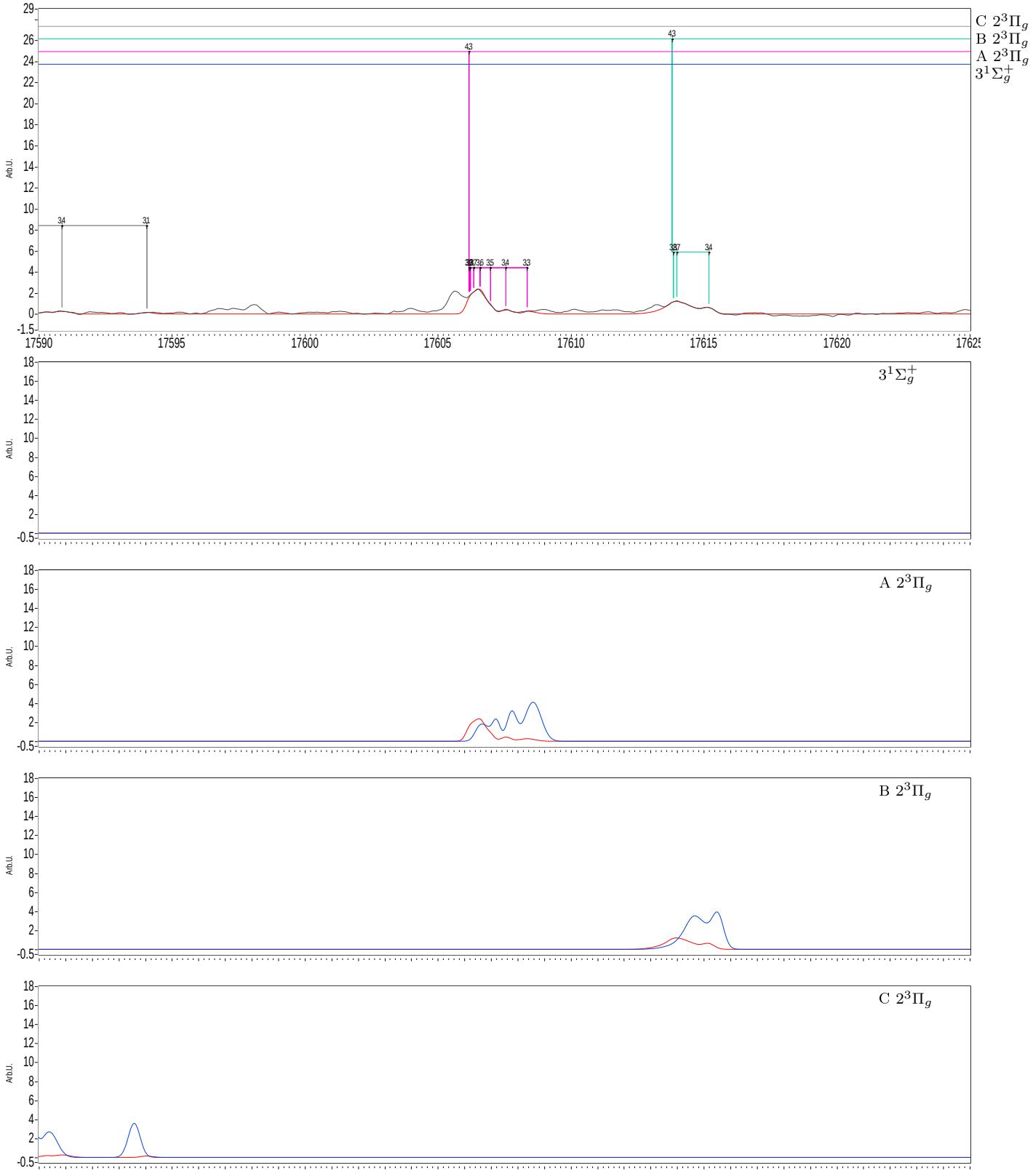
C $2^3\Pi_g$
B $2^3\Pi_g$
A $2^3\Pi_g$
$3^1\Sigma_g^+$
Arb.U.
17590
17595
17600
17605
17610
17615
17620
$3^1\Sigma_g^+$
A $2^3\Pi_g$
B $2^3\Pi_g$
C $2^3\Pi_g$

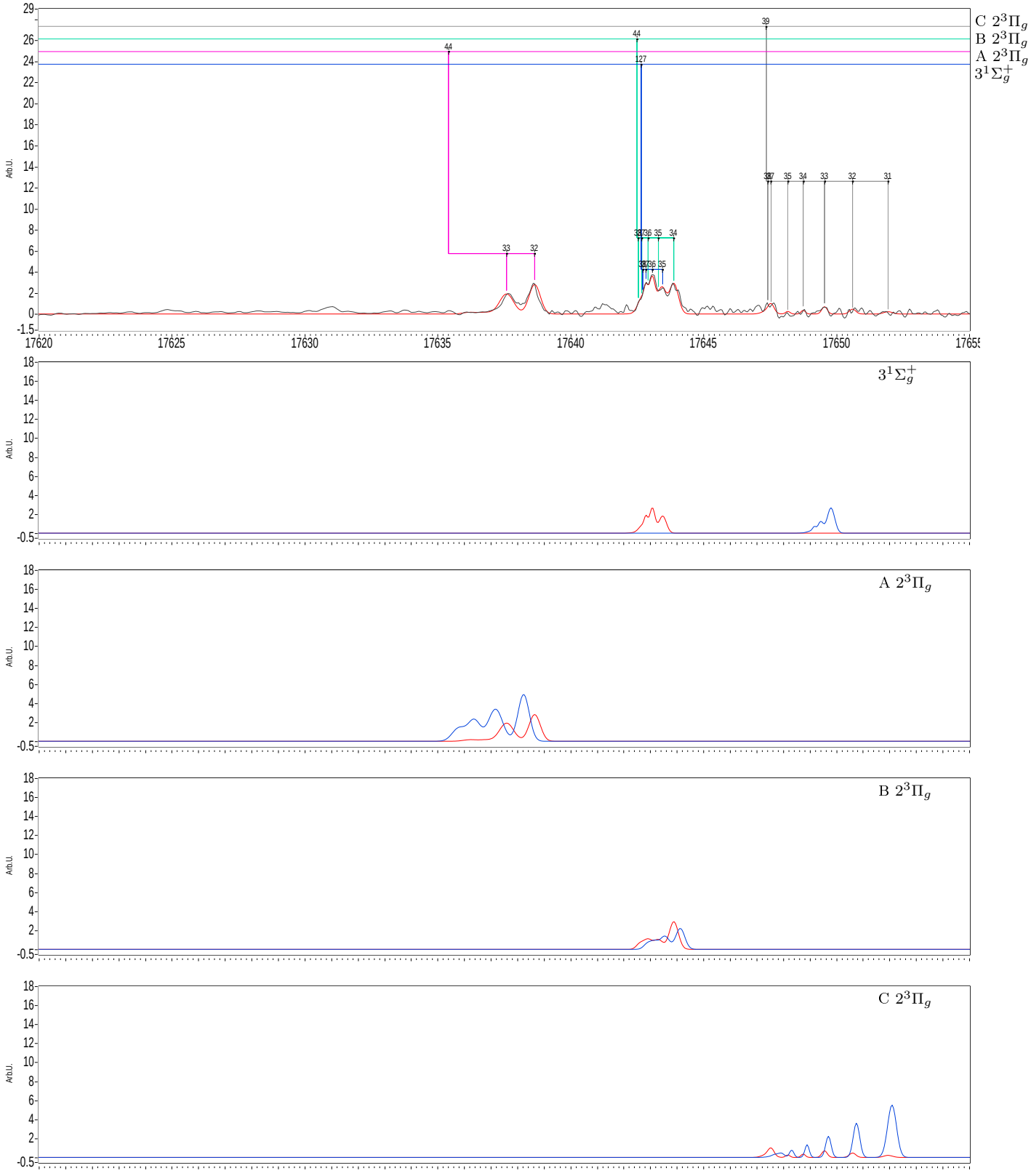
C $2^3\Pi_g$
B $2^3\Pi_g$
A $2^3\Pi_g$
$3^1\Sigma_g^+$
Arb.U.
17620
17625
17630
17635
17640
17645
17650
$3^1\Sigma_g^+$
A $2^3\Pi_g$
B $2^3\Pi_g$
C $2^3\Pi_g$

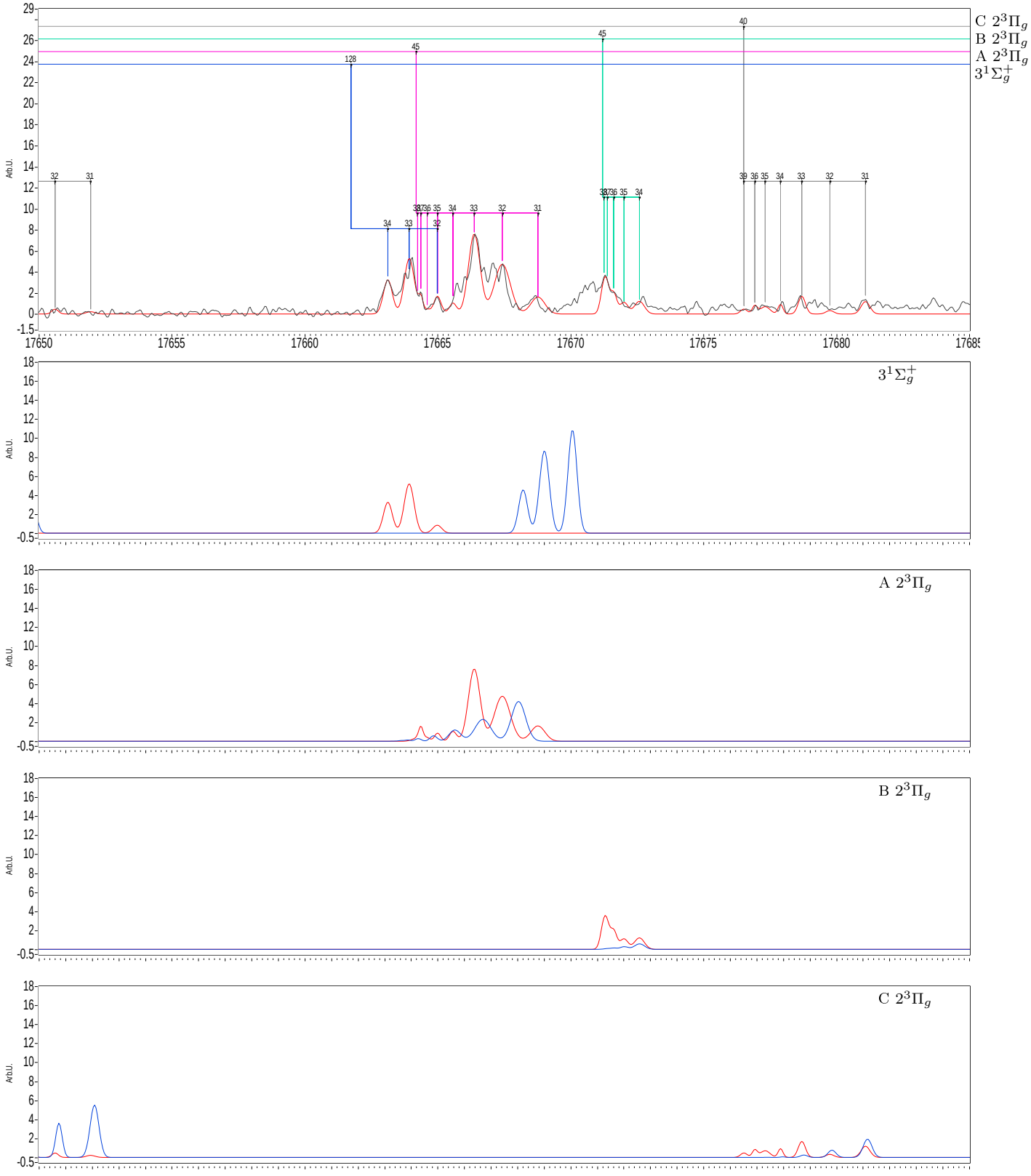
C $2^3\Pi_g$
B $2^3\Pi_g$
A $2^3\Pi_g$
$3^1\Sigma_g^+$
Arb.U.
17650
17655
17660
17665
17670
17675
17680
$3^1\Sigma_g^+$
A $2^3\Pi_g$
B $2^3\Pi_g$
C $2^3\Pi_g$

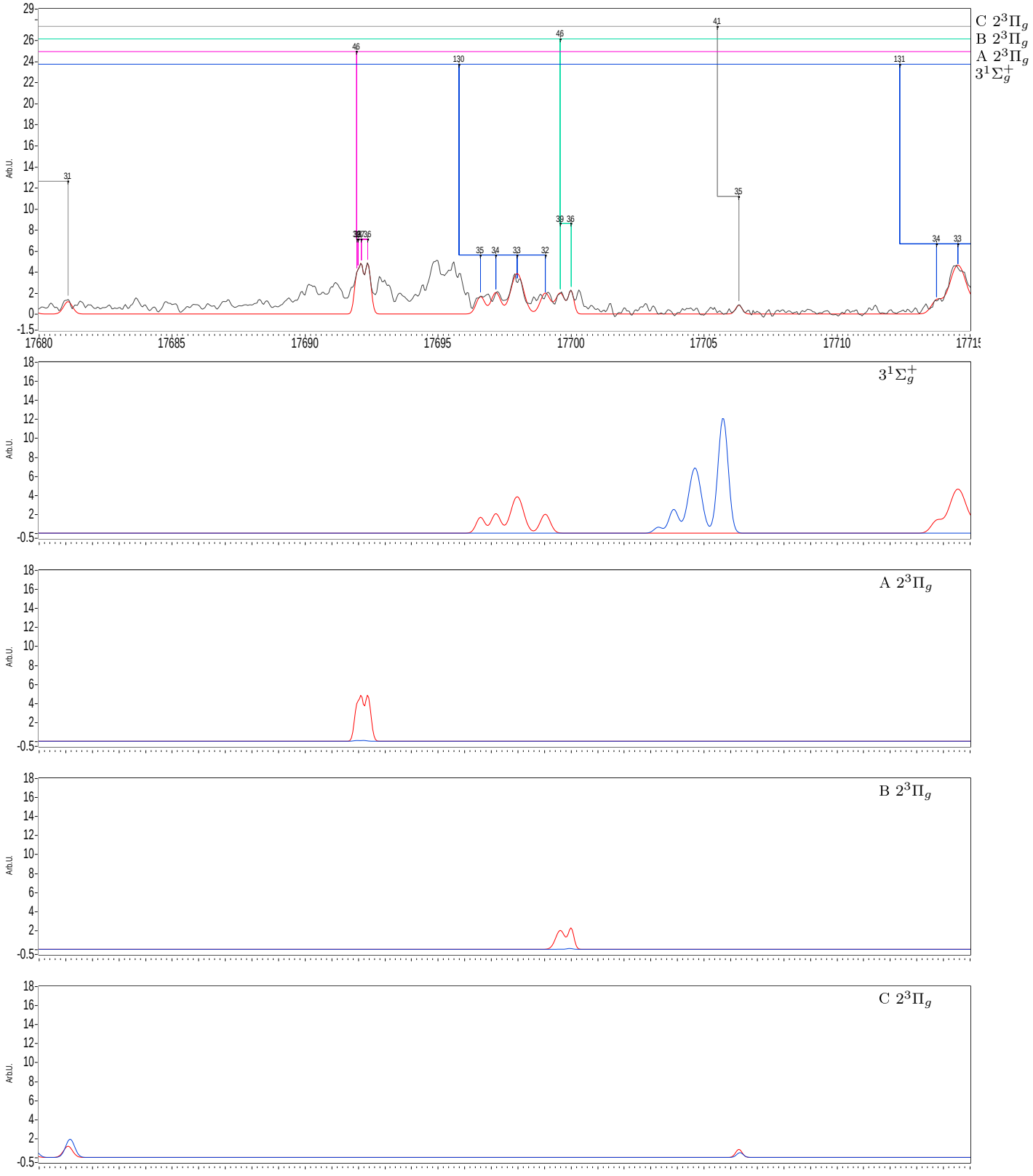
C $2^3\Pi_g$
B $2^3\Pi_g$
A $2^3\Pi_g$
$3^1\Sigma_g^+$
Arb.U.
17680
17685
17690
17695
17700
17705
17710
17715

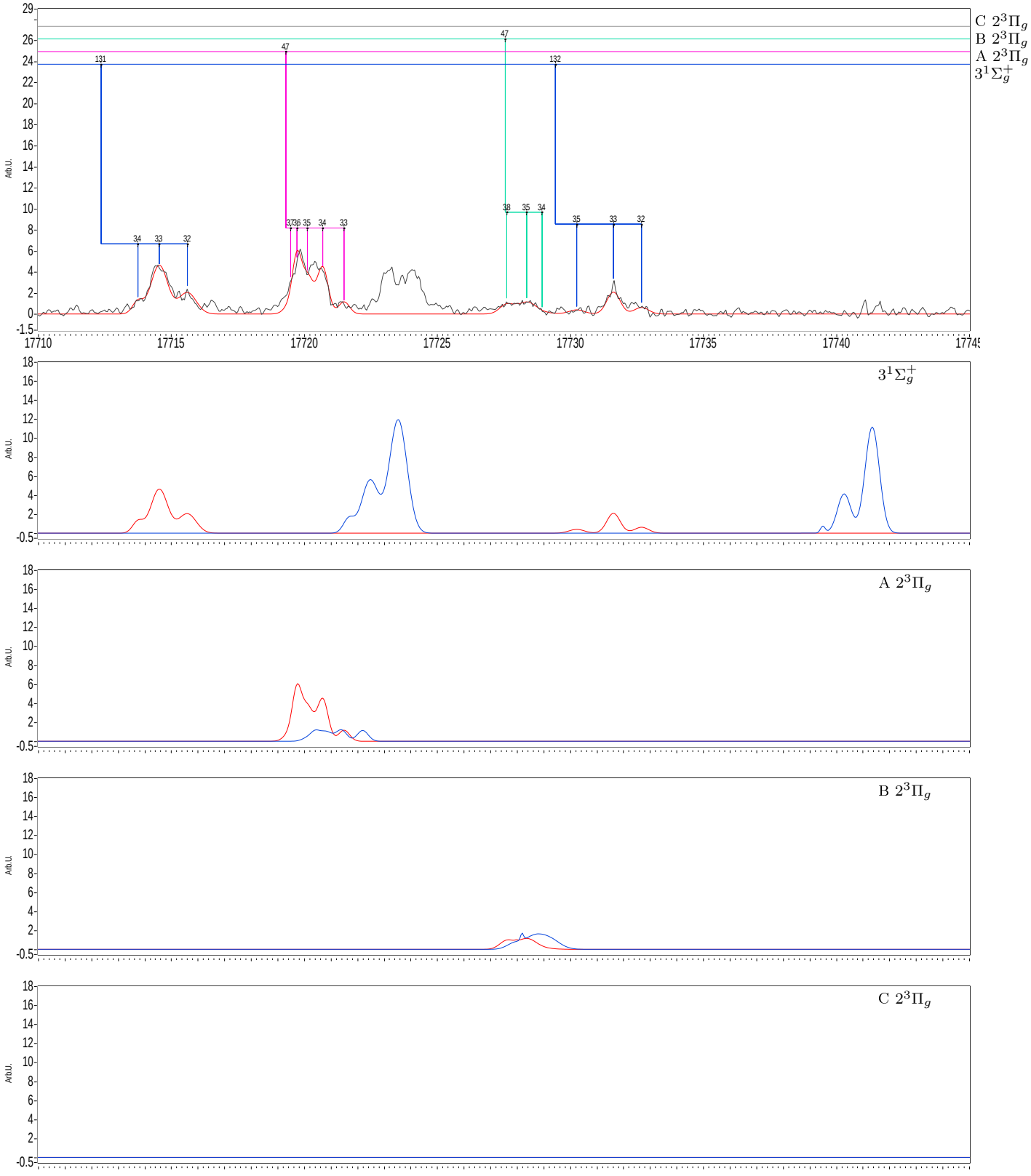
C $2^3\Pi_g$
B $2^3\Pi_g$
A $2^3\Pi_g$
$3^1\Sigma_g^+$
Arb.U.
17710
17715
17720
17725
17730
17735
17740
17745
131
47
47
132
34
33
32
37
36
35
34
33
38
35
34
35
33
32
$3^1\Sigma_g^+$
A $2^3\Pi_g$
B $2^3\Pi_g$
C $2^3\Pi_g$

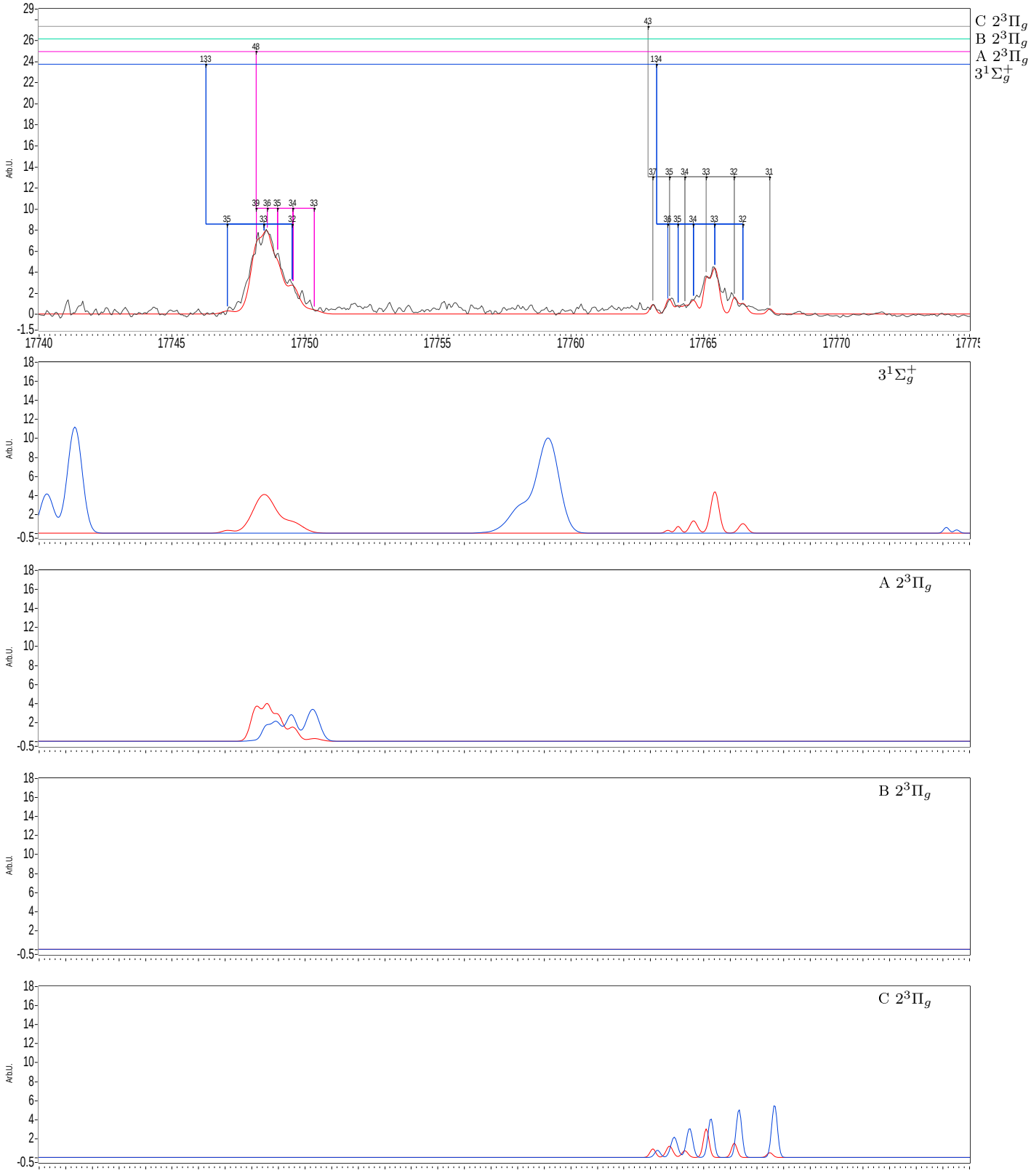
C $2^3\Pi_g$
B $2^3\Pi_g$
A $2^3\Pi_g$
$3^1\Sigma_g^+$
Arb.U.
17740
17745
17750
17755
17760
17765
17770
$3^1\Sigma_g^+$
A $2^3\Pi_g$
B $2^3\Pi_g$
C $2^3\Pi_g$

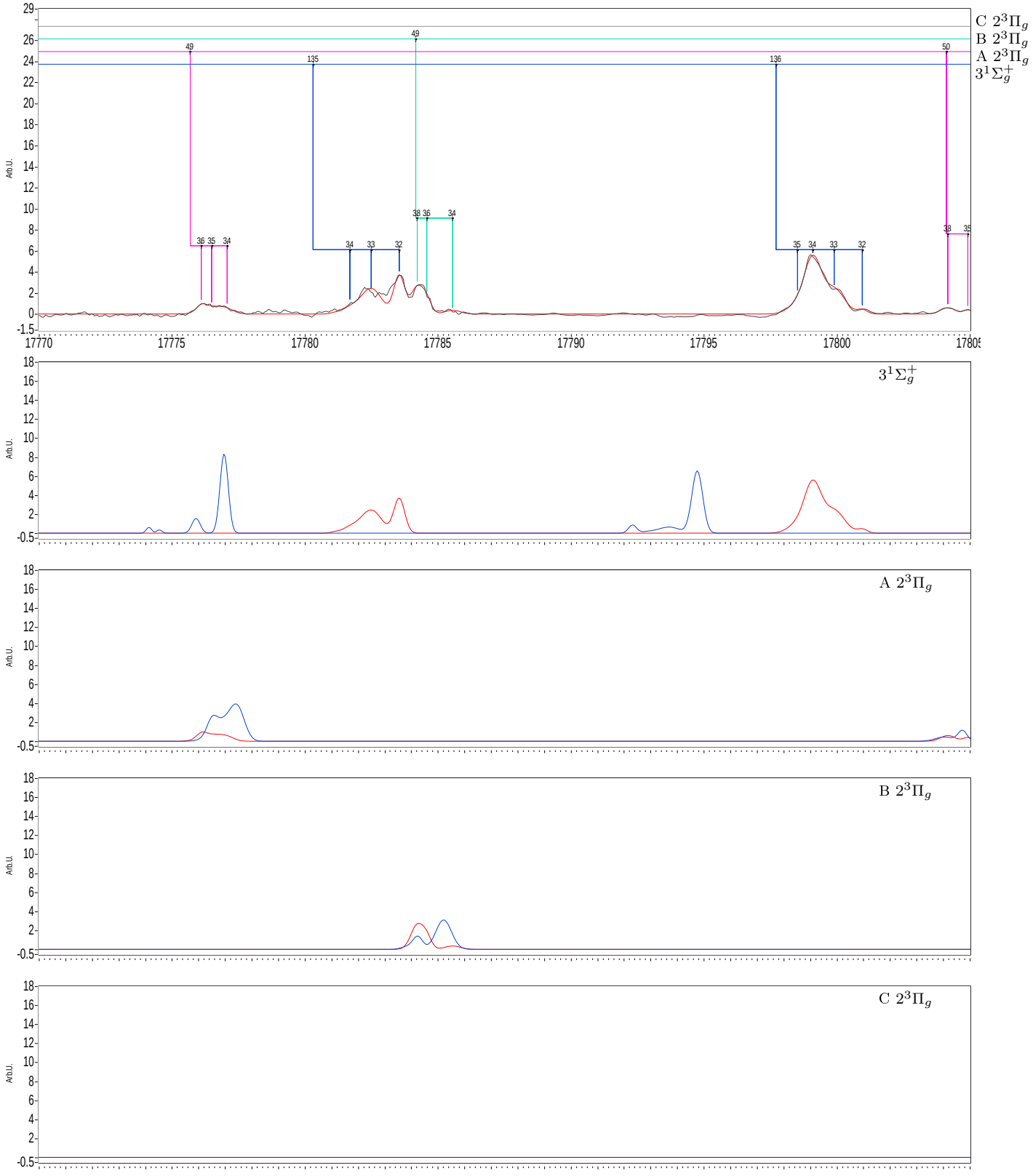
C $2^3\Pi_g$
B $2^3\Pi_g$
A $2^3\Pi_g$
$3^1\Sigma_g^+$
Arb.U.
17770
17775
17780
17785
17790
17795
17800
$3^1\Sigma_g^+$
A $2^3\Pi_g$
B $2^3\Pi_g$
C $2^3\Pi_g$

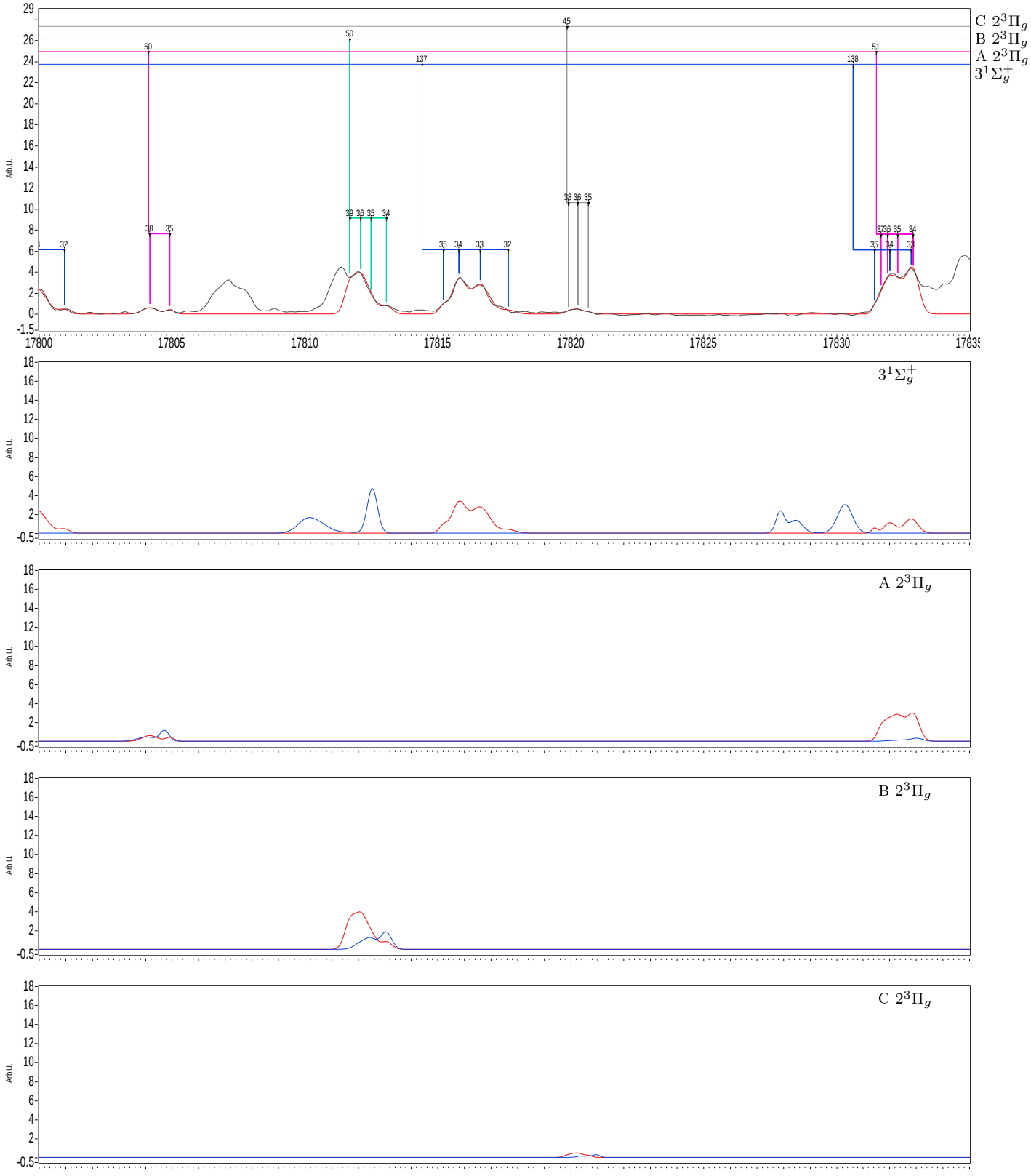
C $2^3\Pi_g$
B $2^3\Pi_g$
A $2^3\Pi_g$
$3^1\Sigma_g^+$
Arb.U.
17800
17805
17810
17815
17820
17825
17830
$3^1\Sigma_g^+$
A $2^3\Pi_g$
B $2^3\Pi_g$
C $2^3\Pi_g$

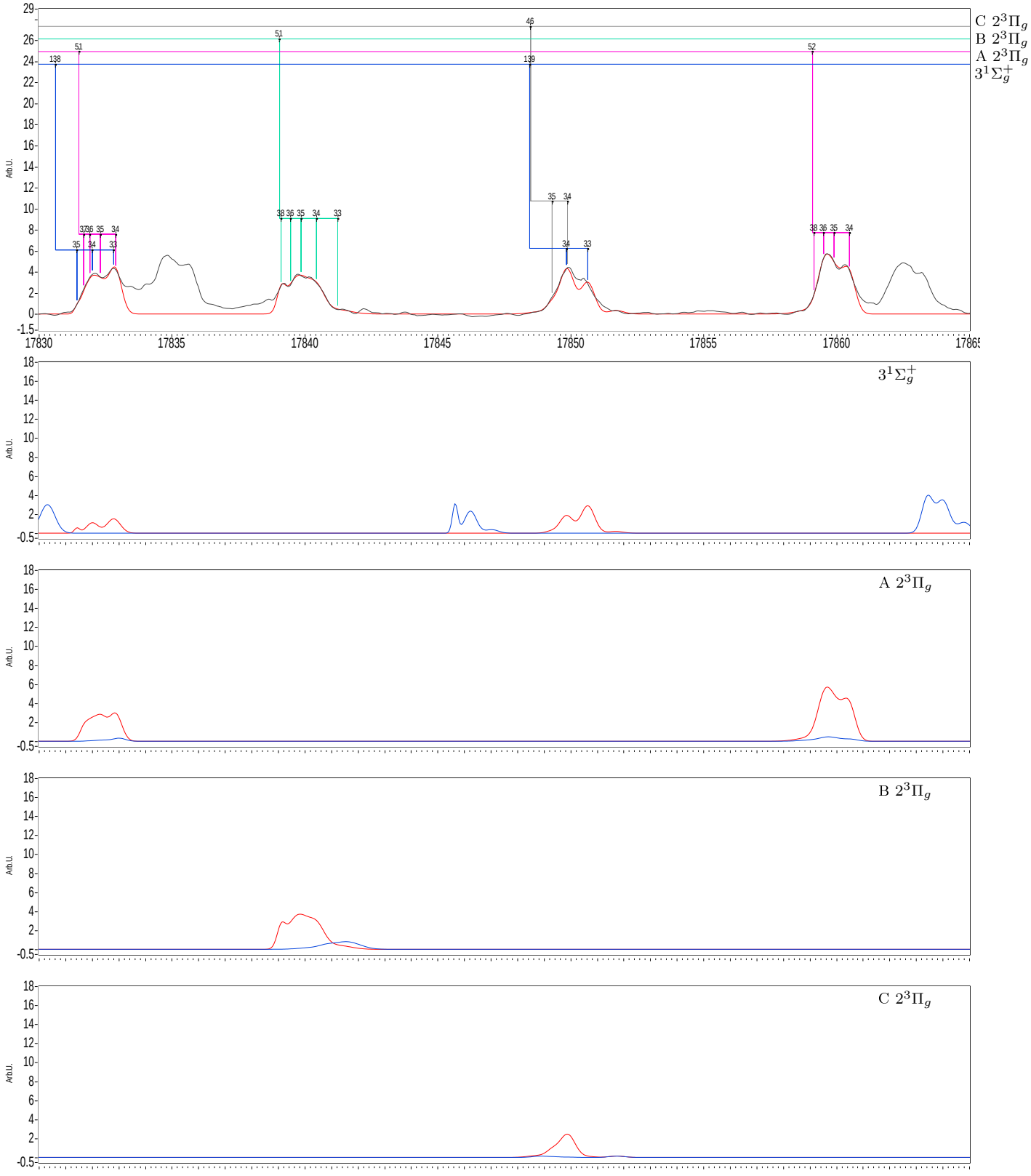
C $2^3\Pi_g$
B $2^3\Pi_g$
A $2^3\Pi_g$
$3^1\Sigma_g^+$
Arb.U.
17830
17835
17840
17845
17850
17855
17860
$3^1\Sigma_g^+$
A $2^3\Pi_g$
B $2^3\Pi_g$
C $2^3\Pi_g$

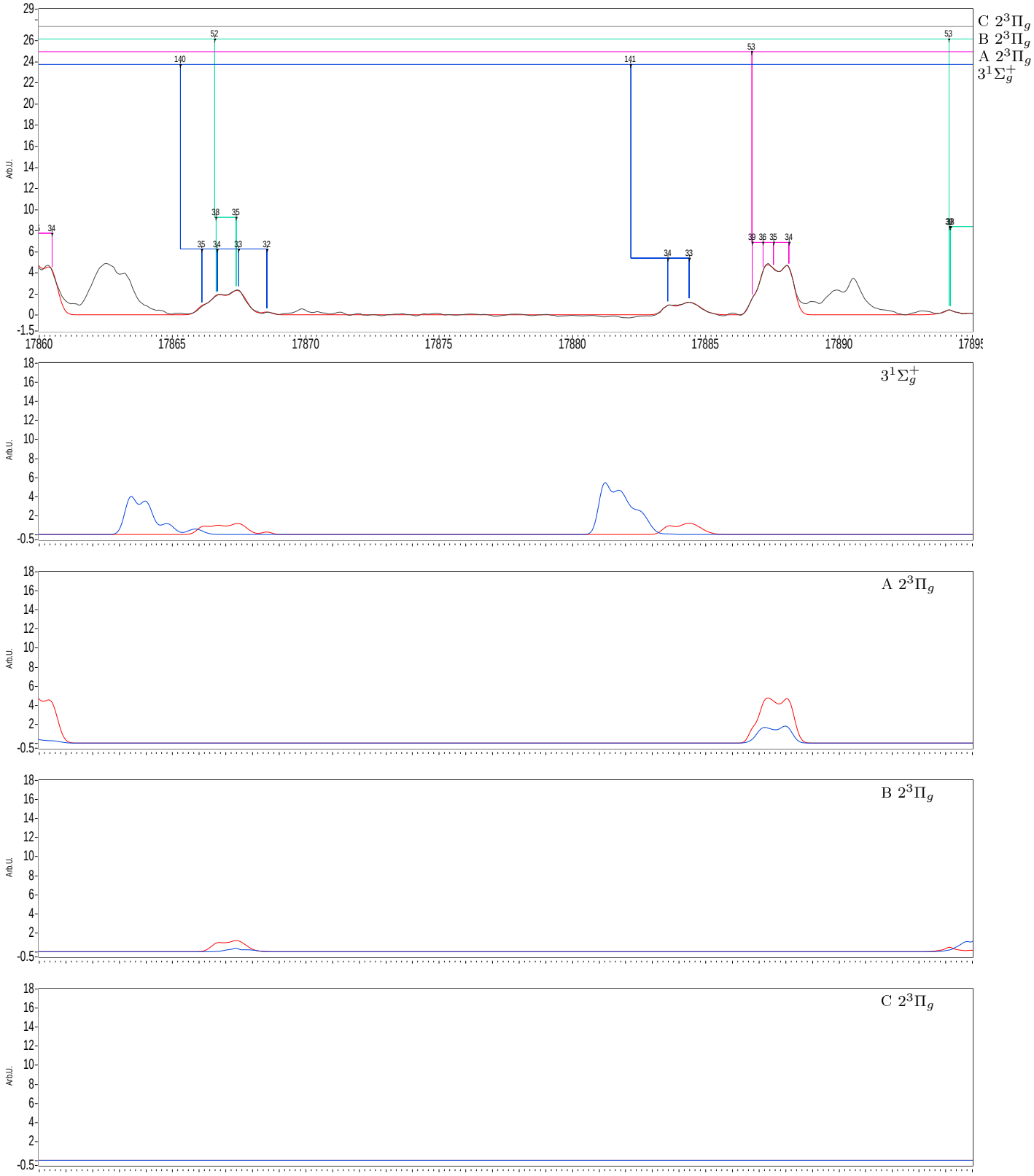
C $2^3\Pi_g$
B $2^3\Pi_g$
A $2^3\Pi_g$
$3^1\Sigma_g^+$
Arb.U.
17860
17865
17870
17875
17880
17885
17890
$3^1\Sigma_g^+$
A $2^3\Pi_g$
B $2^3\Pi_g$
C $2^3\Pi_g$

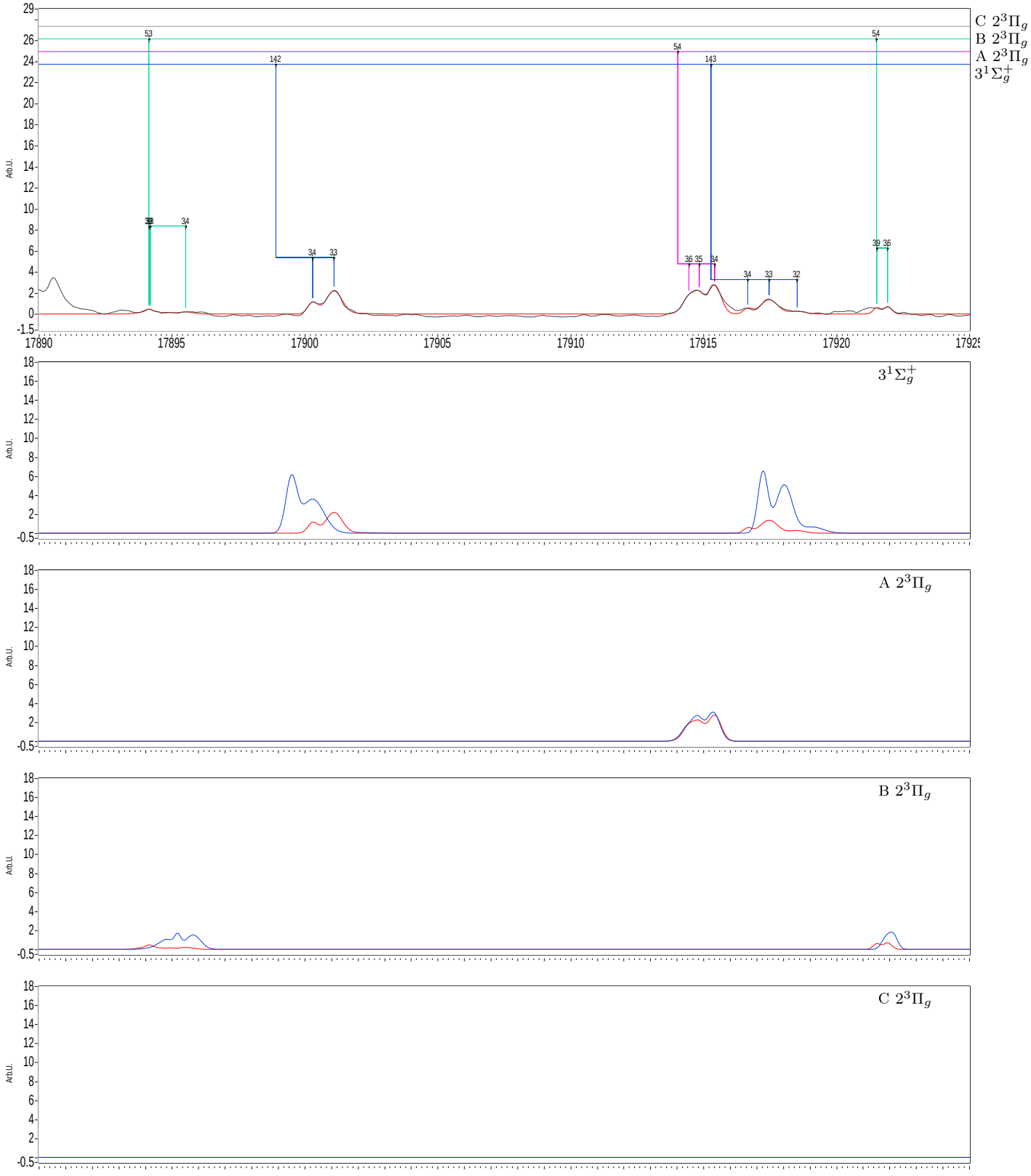
C $2^3\Pi_g$
B $2^3\Pi_g$
A $2^3\Pi_g$
$3^1\Sigma_g^+$
Arb.U.
17890
17895
17900
17905
17910
17915
17920
$3^1\Sigma_g^+$
A $2^3\Pi_g$
B $2^3\Pi_g$
C $2^3\Pi_g$

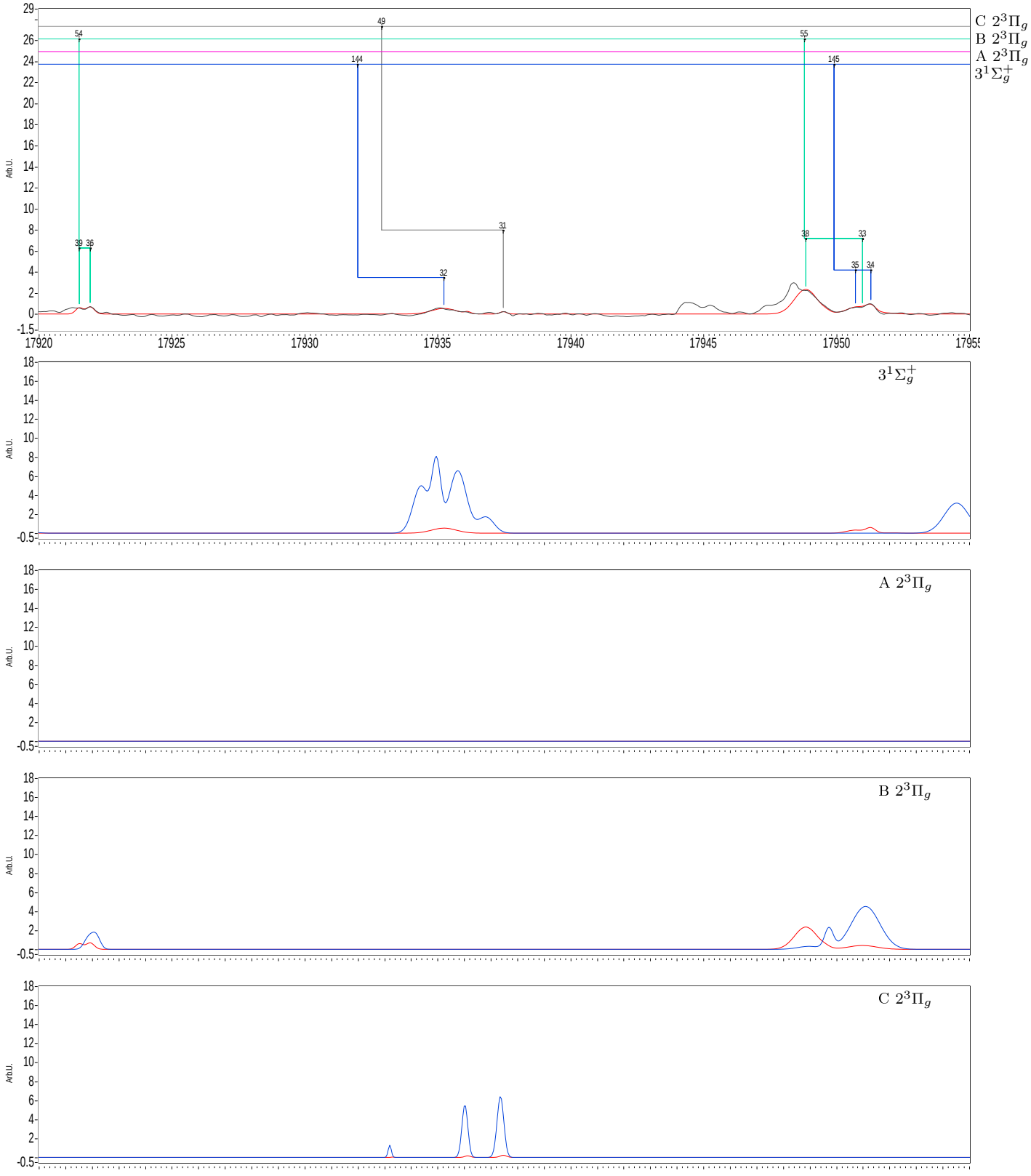
C $2^3\Pi_g$
B $2^3\Pi_g$
A $2^3\Pi_g$
$3^1\Sigma_g^+$
Arb.U.
17920
17925
17930
17935
17940
17945
17950
54
49
144
55
145
39
36
31
38
33
32
35
34
$3^1\Sigma_g^+$
A $2^3\Pi_g$
B $2^3\Pi_g$
C $2^3\Pi_g$

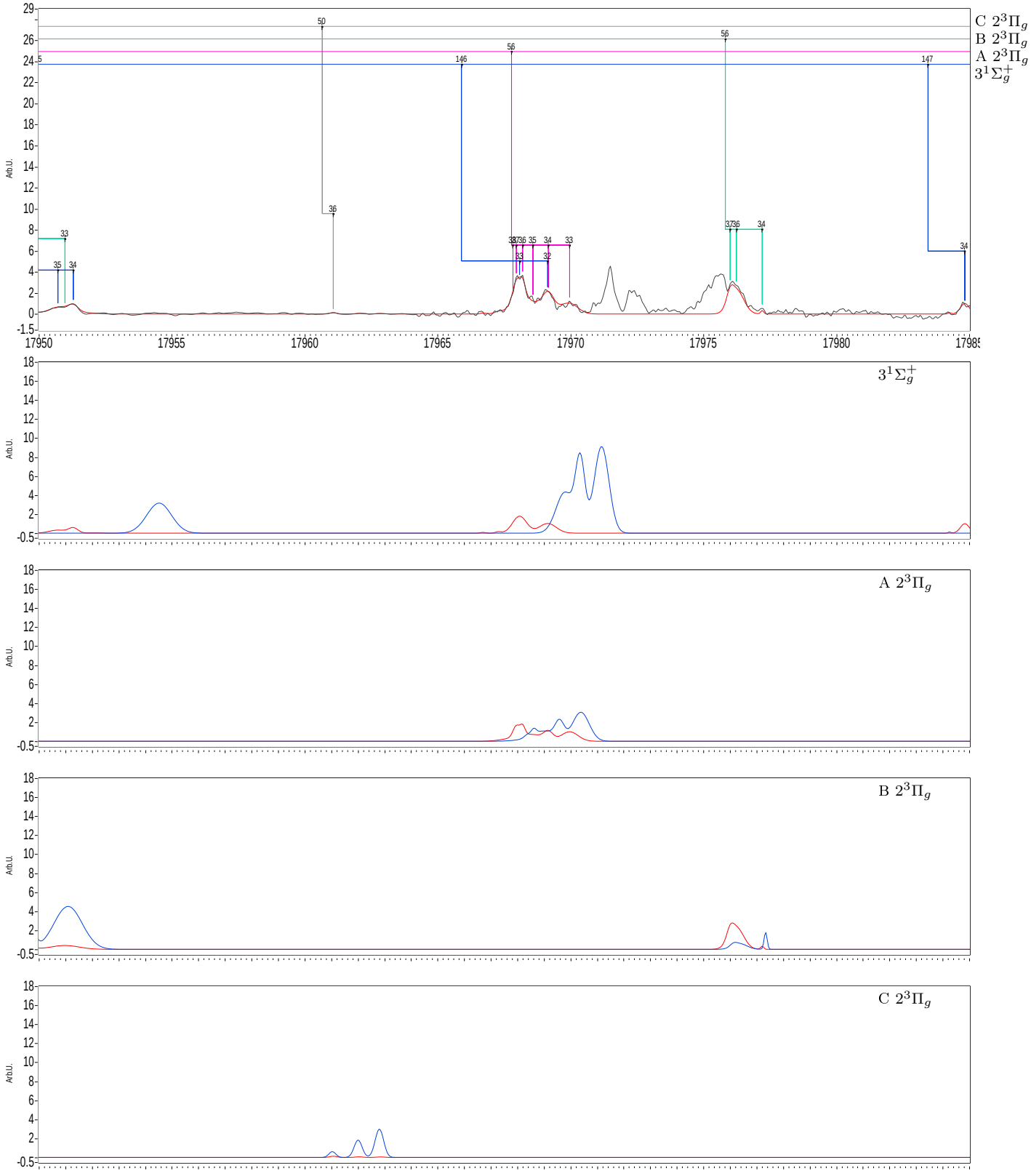
C $2^3\Pi_g$
B $2^3\Pi_g$
A $2^3\Pi_g$
$3^1\Sigma_g^+$
Arb.U.
17950
17955
17960
17965
17970
17975
17980
$3^1\Sigma_g^+$
A $2^3\Pi_g$
B $2^3\Pi_g$
C $2^3\Pi_g$

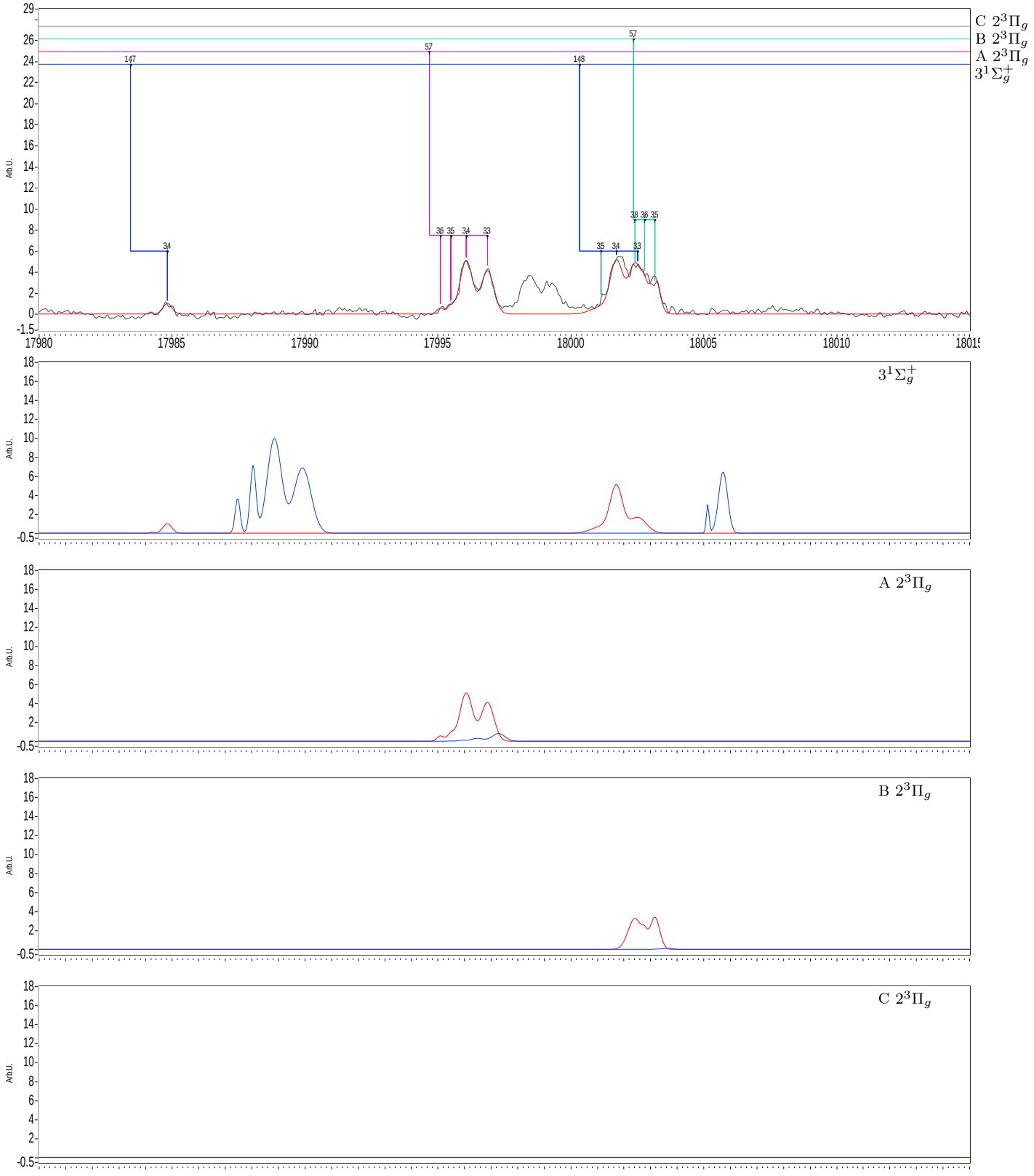
C $2^3\Pi_g$
B $2^3\Pi_g$
A $2^3\Pi_g$
$3^1\Sigma_g^+$
Arb.U.
17980
17985
17990
17995
18000
18005
18010
147
148
57
57
34
36 35 34 33
35 34 33
38 36 35

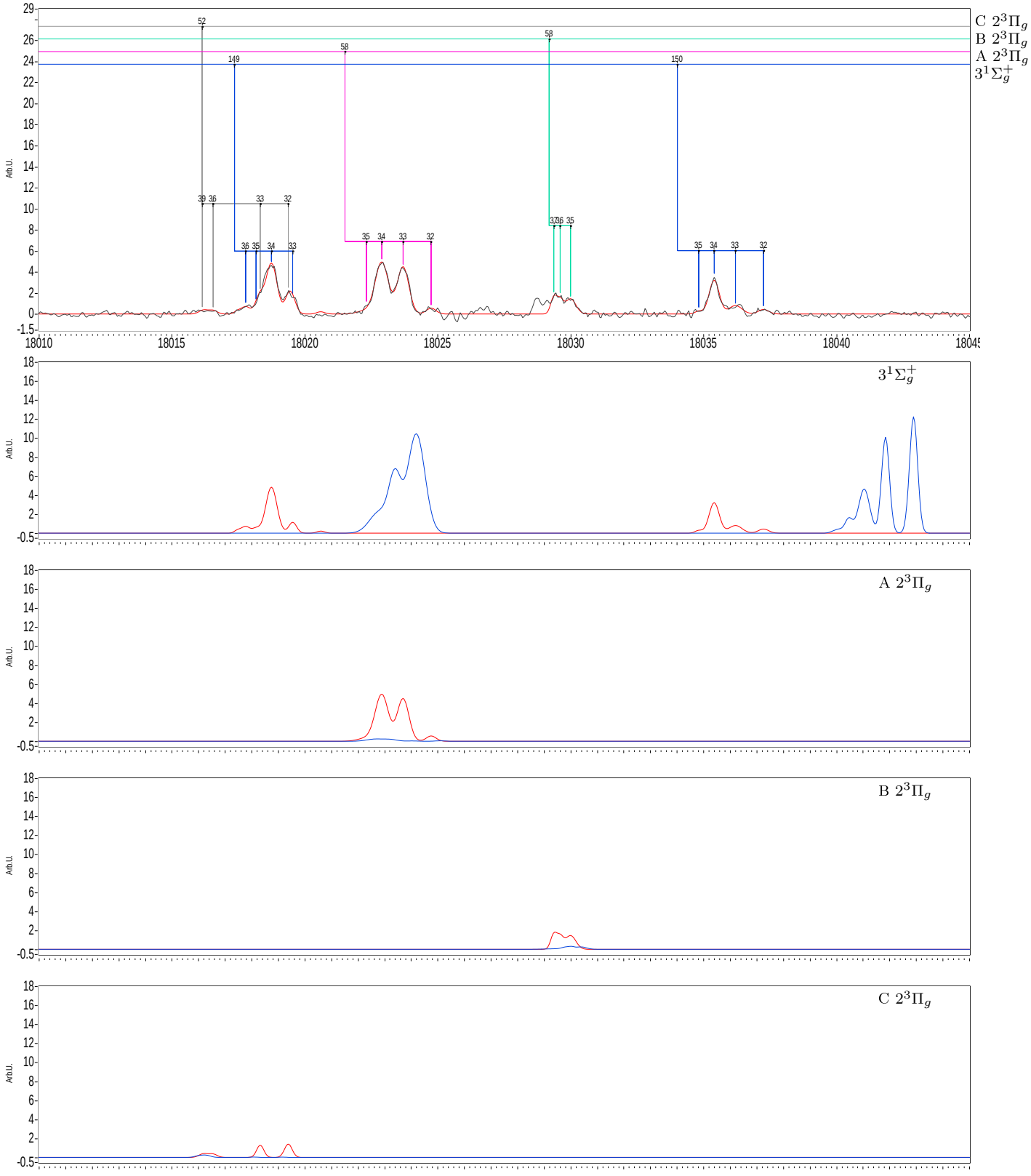
C $2^3\Pi_g$
B $2^3\Pi_g$
A $2^3\Pi_g$
$3^1\Sigma_g^+$
Arb.U.
18010
18015
18020
18025
18030
18035
18040
$3^1\Sigma_g^+$
A $2^3\Pi_g$
B $2^3\Pi_g$
C $2^3\Pi_g$

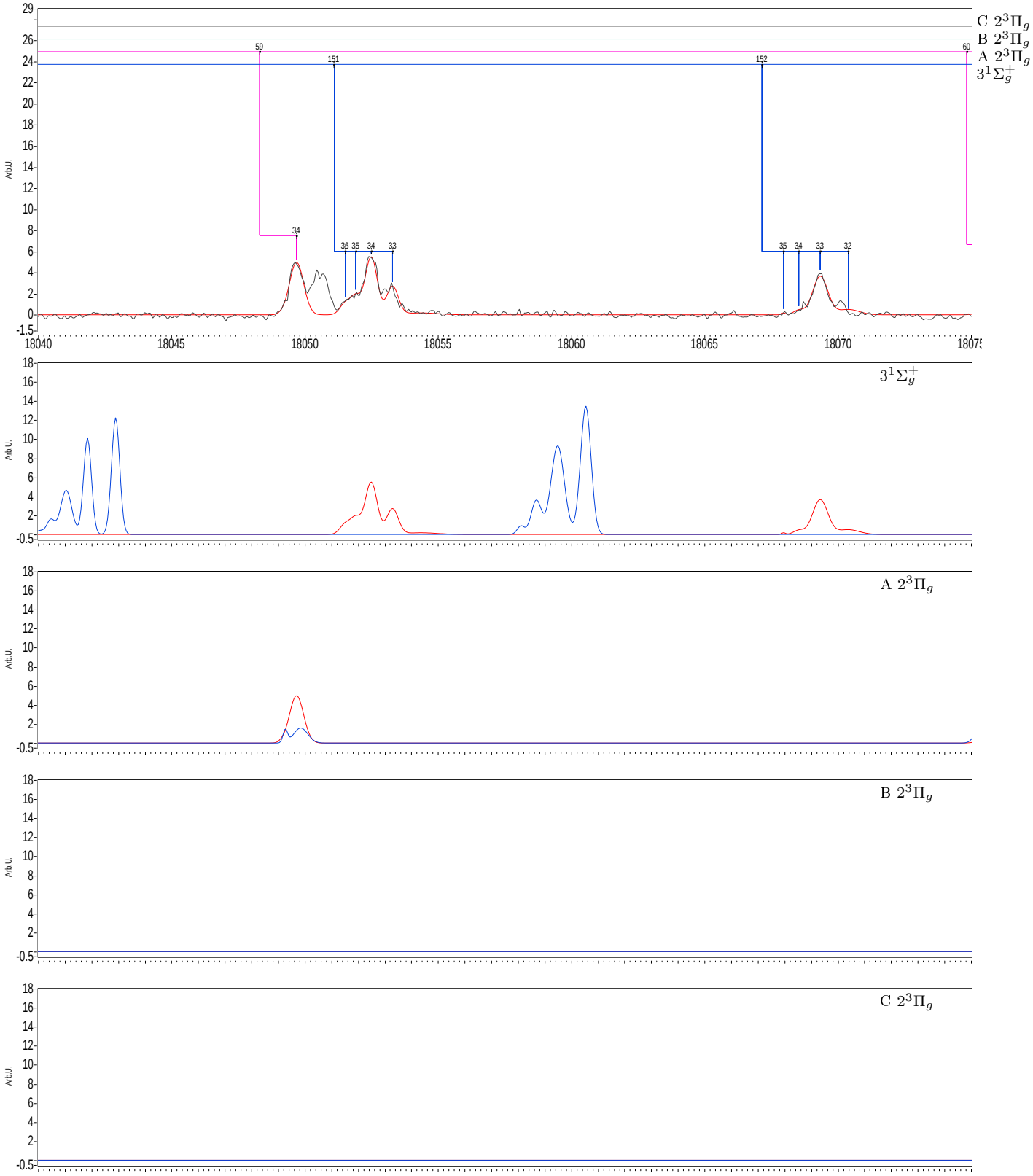
C $2^3\Pi_g$
B $2^3\Pi_g$
A $2^3\Pi_g$
$3^1\Sigma_g^+$
Arb.U.
59
151
152
60
34
36 35 34 33
35 34 33 32
18040
18045
18050
18055
18060
18065
18070
18075
$3^1\Sigma_g^+$
A $2^3\Pi_g$
B $2^3\Pi_g$
C $2^3\Pi_g$

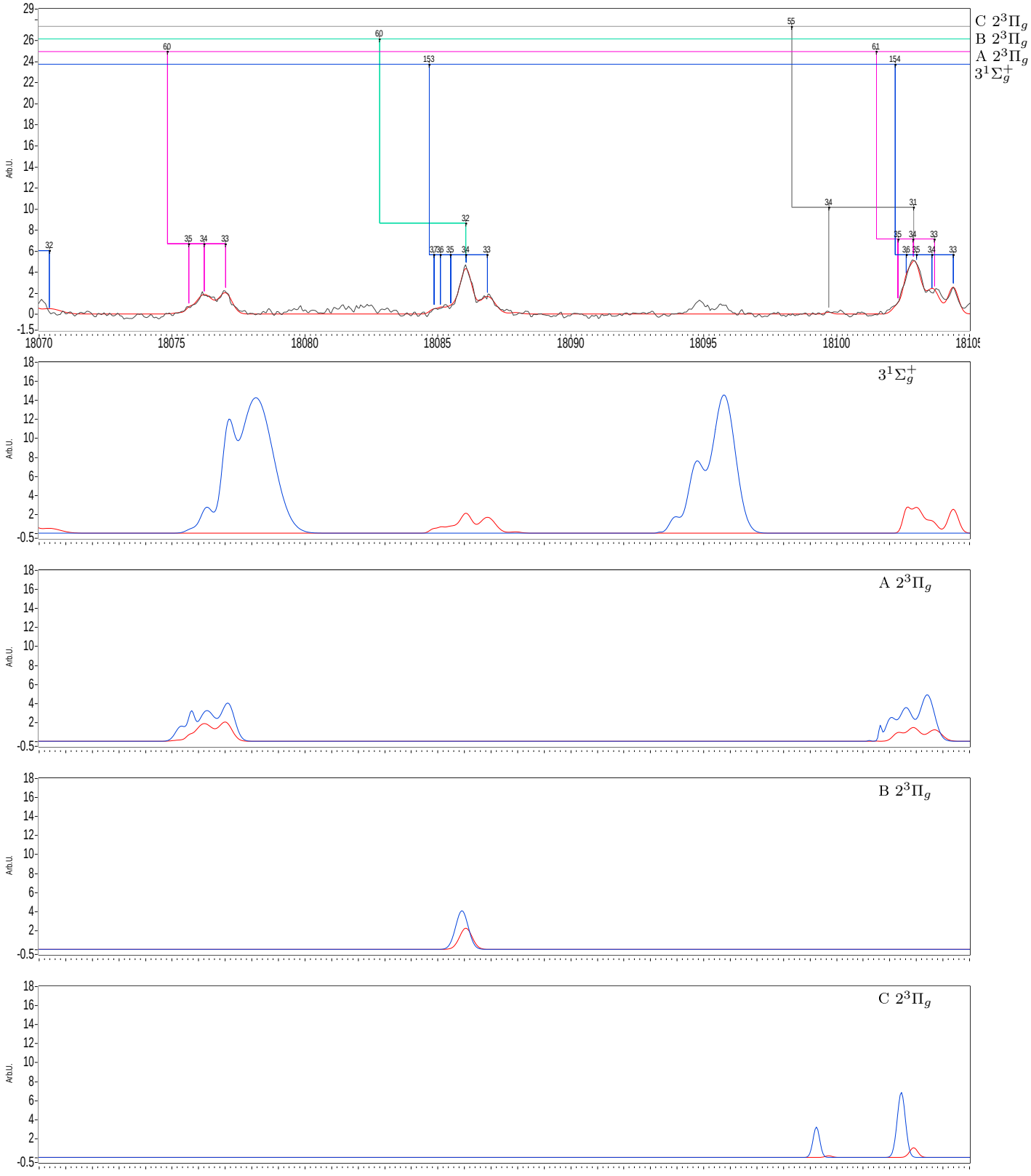
C $2^3\Pi_g$
B $2^3\Pi_g$
A $2^3\Pi_g$
$3^1\Sigma_g^+$
Arb.U.
18070
18075
18080
18085
18090
18095
18100
$3^1\Sigma_g^+$
A $2^3\Pi_g$
B $2^3\Pi_g$
C $2^3\Pi_g$

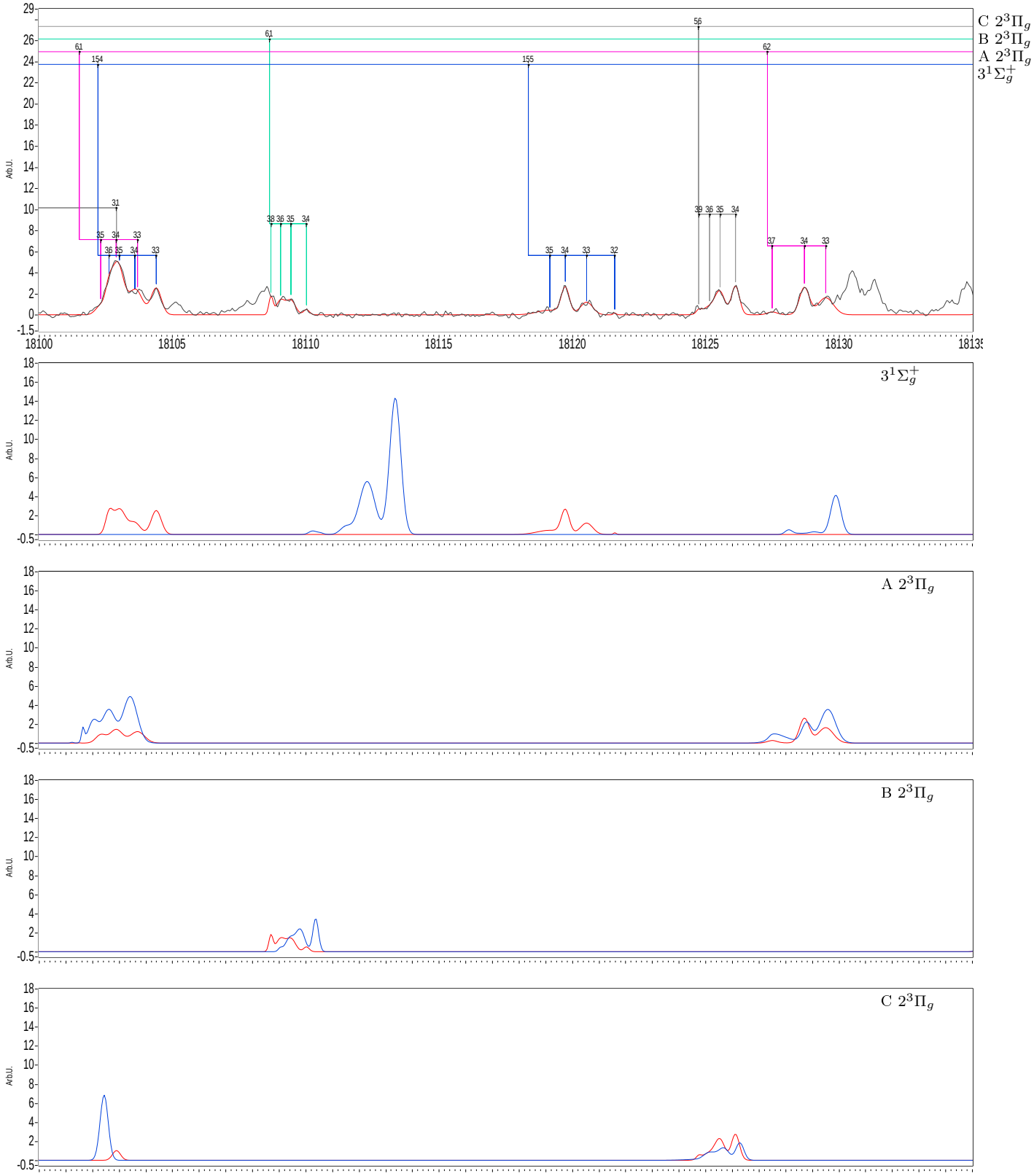
C $2^3\Pi_g$
B $2^3\Pi_g$
A $2^3\Pi_g$
$3^1\Sigma_g^+$
Arb.U.
18100
18105
18110
18115
18120
18125
18130
$3^1\Sigma_g^+$
A $2^3\Pi_g$
B $2^3\Pi_g$
C $2^3\Pi_g$

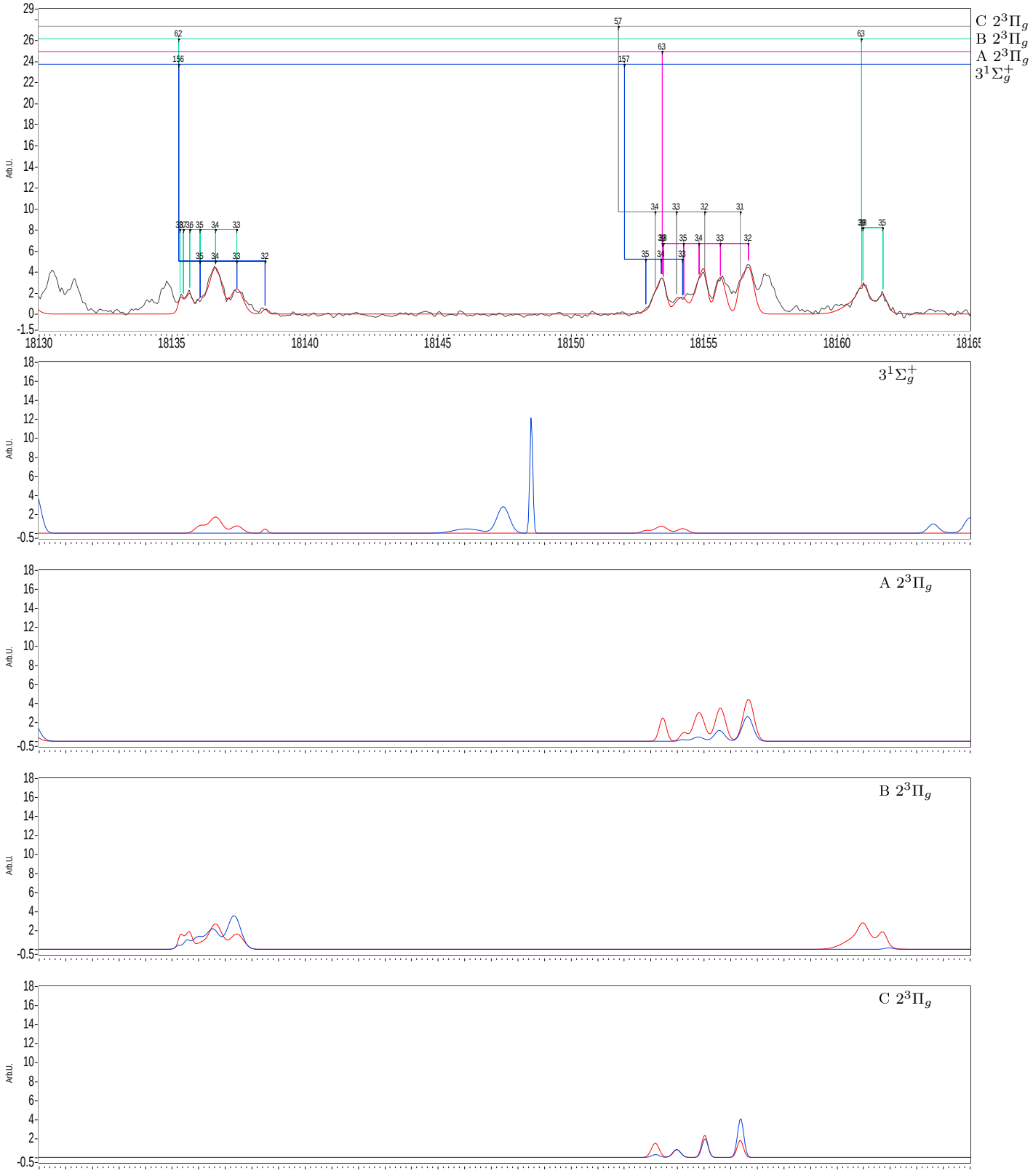
C $2^3\Pi_g$
B $2^3\Pi_g$
A $2^3\Pi_g$
$3^1\Sigma_g^+$
Arb.U.
18130
18135
18140
18145
18150
18155
18160
$3^1\Sigma_g^+$
A $2^3\Pi_g$
B $2^3\Pi_g$
C $2^3\Pi_g$

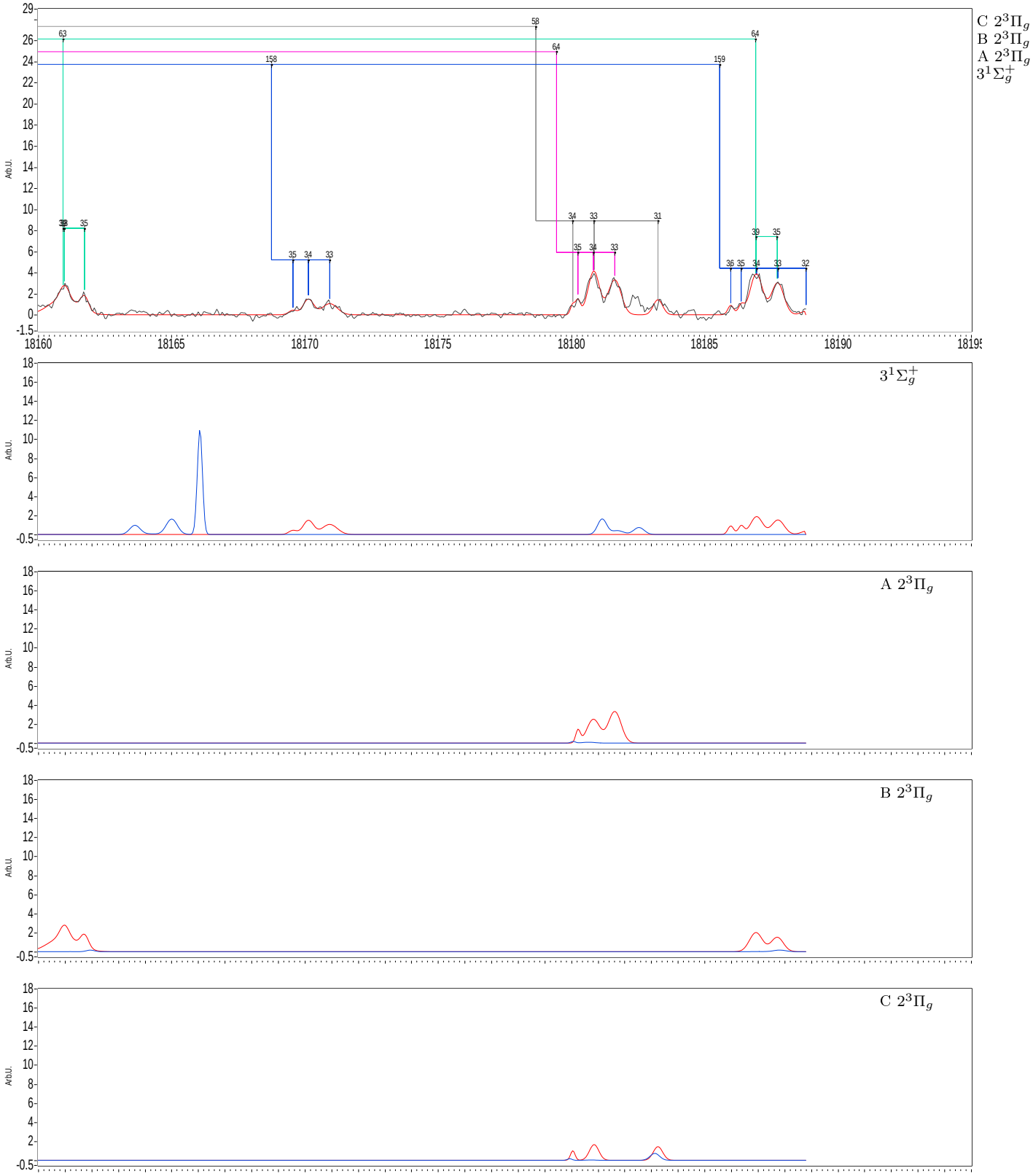
C $2^3\Pi_g$
B $2^3\Pi_g$
A $2^3\Pi_g$
$3^1\Sigma_g^+$
Arb.U.
18160
18165
18170
18175
18180
18185
18190
$3^1\Sigma_g^+$
A $2^3\Pi_g$
B $2^3\Pi_g$
C $2^3\Pi_g$

Bibliography

[1] J.M. Blatt, "Practical points concerning the solution of the Schrödinger equation", J. Comput. Phys. **1**, 382 (1967).

[2] T. F. Gallagher, "Rydberg Atoms" Cambridge University Press. Cambridge (1994).

[3] T. F. Gallagher,"Rydberg Atoms", Rep. Prog. Phys. **51**, 143 (1988).

[4] M. Saffman et al., "Quantum information with Rydberg atoms", Rev. Mod. Phys. **82**, 2313 (2010).

[5] S. Pan and F.H. Mies, "Rydberg-like properties of rotational-vibrational levels and dissociation continuum associated with alkali-halide charge-transfer states", J. Chem. Phys. **89**, 3096 (1988).

[6] J. D. D. Martin and J. W. Hepburn, "Electric Field Induced Dissociation of Molecules in Rydberg-like Highly Vibrationally Excited Ion-pair states", Phys. Rev. Lett. **79**, 3154 (1997).

[7] J. D. D. Martin and J. W. Hepburn, "Determination of bond dissociation energies by threshold ion pair production spectroscopy: An improved $D_0(HCl)$", J. Chem. Phys. **109**, 8139 (1998).

[8] L. Barbier, M.T. Djerad, and M. Chèret, "Collisional ion pair formation in an excited alkali-metal vapor", Phys. Rev. A **34**, 2710 (1986).

[9] E. Reinhold and W. Ubachs, "Observation of Coherent Wave Packets in a Heavy Rydberg System", Phys. Rev. Lett. **88**, 013001 (2002).

[10] R.C. Shiell, E. Reinhold, F. Magnus, and W. Ubachs, "Control of Diabatic versus Adiabatic Field Dissociation in a Heavy Rydberg System", Phys. Rev. Lett. **95**, 213002 (2005).

[11] E. Reinhold and W. Ubachs, "Heavy Rydberg states", Mol. Phys. **103**, 1329 (2005).

[12] R. Ekey and E. McCormack, "Spectroscopic observation of bound ungerade ion-pair states in molecular hydrogen", Phys. Rev. A **84**, 020501(R) (2011).

[13] M.I. Chibisov and R.K. Janev, "Asymptotic exchange interactions in ion-atom systems", Phys. Rep. **166**, 1 (1988).

[14] S. J. Park, S. W. Suh, Y. S. Lee, and G.-H. Jeung, "Theoretical Study of the Electronic States of the Rb_2 Molecule", J. Mol. Spectrosc. **207**, 129 (2001).

[15] I. I. Fabrikant, "Theory of negative ion decay in an external electric field", J. Phys. B **26**, 2533 (1993).

[16] H. Coker, "Empirical Free-Ion Polarizabilities of the Alkali Metal, Alkaline Earth Metal, and Halide Ions", J. Phys. Chem. **80**, 2078 (1976).

[17] Gwang-Hi Jeung, "Excited states of Na2 dissociating into 3d+3s, 4p+3s, and 5s+ 3s", Phys. Rev. A **35**, 26 (1987).

[18] He Wang et al., "Study of the $4^1\Sigma_g^+$ "shelf" state of Na_2 by optical-optical double resonance spectroscopy", J. Chem. Phys. **94**, 4756 (1991).

[19] T. Ban, R. Beuc, H. Skenderovič, and G. Pichler, "Rubidium pure long-range ion pair molecules", Europhys. Lett. **66**, 485 (2004).

[20] S. Wang, K.P. Lawley, T. Ridley, R.J. Donovan, "Field induced ion pair formation from ICl studied by optical triple resonance", Faraday Discuss. **115**, 345 (2000).

[21] T. Ridley et al., "The field-ionization of near-dissociation ion-pair states of I_2", J. Chem. Phys., **117**, 7117 (2002).

[22] Sandro Mollet and Frèdèric Merkt, "Dissociation dynamics of ion-pair states of Cl_2 at principal quantum numbers beyond 1500", Phys. Rev. A **82**, 032510 (2010).

[23] C. O. Reinhold, S. Yoshida, F. B. Dunning, "Electric-field-induced dissociation of heavy Rydberg ion-pair states" , J. Chem. Phys. **134**, 174305 (2011).

[24] H. Wang, X. T. Wang, P. L. Gould, and W. C. Stwalley, "Optical-Optical Double Resonance Photoassociative Spectroscopy of Ultracold ^{39}K Atoms near Highly Excited Asymptotes", Phys. Rev. Lett. **78**, 4173 (1997).

[25] Q. J. Hu, T. C. Melville, and J. W. Hepburn, "Threshold ion pair production spectroscopy of HCl/DCl: Born-Oppenheimer breakdown in HCl and HCl^+ and dynamics of photo ion pair formation", J. Chem. Phys. **119**, 8938 (2003).

[26] A.G. Suits and J.W. Hepburn, "Ion pair dissociation: Spectroscopy and Dynamics", Annu. Rev. Phys. Chem. **57**, 431 (2006).

[27] W. C. Stwalley and H. Wang ,"Photoassociation of Ultracold Atoms: A New Spectroscopic Technique", J. Mol. Spectrosc. **195**, 194 (1999).

[28] X. Wang, H. Wang, P. L. Gould, and W. C. Stwalley," Observation of the pure long-range 1_u state of an alkali-metal dimer by photoassociative spectroscopy", Phys. Rev. A **57**, 4600 (1998).

[29] A. Fioretti, C. Amiot, C. M. Dion, O. Dulieu, M. Mazzoni, G. Smirme, and C. Gabbanini, "Cold rubidium molecule formation through photoassociation: A spectroscopic study of the 0_g^- long-range state of $^{87}Rb_2$" Eur. Phys. J. D **15**, 189 (2001).

[30] Y. Huang, J. Qi, H K Pechkis, D. Wang, E. E. Eyler, P. L. Gould and W. C. Stwalley, "Formation, detection and spectroscopy of ultracold Rb_2 in the ground $X^1\Sigma_g^+$ state" J. Phys. B **39** S857 (2006)

[31] H. Wang, P. L. Gould, and W. C. Stwalley," Long-range interaction of the $^{39}K(4s)$+$^{39}K(4p)$ asymptote by photoassociative spectroscopy. I. The 0_g pure long-range state and the long-range potential constants" J. Chem. Phys. **106**, 7899 (1997).

[32] B. Bussery and M. Aubert-Frècon, "Potential Energy Curves and Vibration-Rotation Energies for the Two Purely Long-Range Bound States 1_u and O_g^- of the Alkali Dimers M2 Dissociating to M(ns2$S_{1/2}$) + M(np2$P_{3/2}$) with M = Na, K, Rb, and Cs", J. Mol. Spectrosc. **113**, 21 (1985).

[33] R. A. Cline, J. D. Miller, and D. J. Heinzen, "Study of Rb_2 long-range states by high-resolution photoassociation spectroscopy," Phys. Rev. Lett. **73**, 632 (1994).

[34] E. A. Shapiro, M. Shapiro, A. Pe'er and J. Ye, "Photoassociation adiabatic passage of ultracold Rb atoms to form ultracold Rb_2 molecules", Phys. Rev. A **75**, 013405 (2007).

[35] E. A. Shapiro, M. Shapiro, A. Pe'er and J. Ye, "Erratum: Photoassociation adiabatic passage of ultracold Rb atoms to form ultracold Rb_2 molecules", Phys. Rev. A **78** 02990 (2008).

[36] A. Vardi et al.," Theory of radiative recombination with strong laser pulses and the formation of ultracold molecules via stimulated photo-recombination of cold atoms" J. Chem. Phys. **107**, 6166 (1997).

[37] C. H. Greene, A. S. Dickinson, and H. R. Sadeghpour, "Creation of Polar and Nonpolar Ultra-Long-Range Rydberg Molecules", Phys. Rev. Lett. **85**, 2458 (2000).

[38] V. Bendkowksy et al., "Observation of ultralong-range Rydberg molecules", Nature **458**, 1005 (2009).

[39] D. L. Moores and D. W. Norcross, "Alkali-metal negative ions. I. Photodetachment of Li^-, Na^-, and K^-", Phys. Rev. A **10**, 1646 (1974).

[40] K. Bergmann et al., "Coherent population transfer among quantum states of atoms and molecules", Rev. Mod. Phys. **70**, 1003 (1998).

[41] M. Shapiro, "Theory of one and two photon dissociation with strong laser pulses" J. Chem. Phys. **101**, 3844 (1994).

[42] E. Kuznetsova, M. Gacesa, P. Pellegrini, S. F. Yelin, and R. CÃťtÃľ, "Efficient formation of ground-state ultracold molecules via STIRAP from the continuum at a Feshbach resonance", New. J. Phys. **11**, 055028 (2008).

[43] Huang, Ye, "Production, detection and trapping of ultracold molecular rubidium" (2006). Doctoral Dissertations. Paper AAI3231236. http://digitalcommons.uconn.edu/dissertations/AAI3231236/

[44] R.J. LeRoy, LEVEL8.0, http://scienide.uwaterloo.ca/~leroy/level/

[45] C. Strauss, T. Takekoshi, F. Lang, K. Winkler, R. Grimm, J. Hecker Denschlag, and E. Tiemann, "Hyperfine, rotational, and vibrational structure of the a $^3\Sigma_u^+$ state of $^{87}Rb_2$", Phys. Rev. A, **82**, 052514, (2010).

[46] R.H. Lipson and A.R. Hoy, "Vacuum ultraviolet laser spectra of ICl", J. Chem. Phys. **90** , 6821 (1989).

[47] Richard F.W. Bader . 2014. An Introduction to the Electronic Structure of Atoms and Molecules. [ONLINE] Available at: http://www.chemistry.mcmaster.ca/esam/. [Accessed 01 March 15].

[48] P. Atkins, R. Friedman, "Molecular Quantum Mechanics", Fourth Edition, Oxford University Press. Oxford (2005).

[49] M. Tomza, W. Skomorowski, M. MusiaÅĆ, R. GonzÃąlez-FÃľrez, C. P. Koch, and R. Moszynski, Mol. Phys. **111**, 1781 (2013).

[50] M. Cannon, Y. Liu, and F.B. Dunning, "Lifetime of K + -SF 6 - heavy Rydberg states formed by electron transfer in K(np)-SF 6 collisions", Chem. Phys. Lett. 458 , 35 (2008).

[51] K. Orlovsky, V. Grushevsky, and A. Ekers, "Theoretical study of energy transfer in Rb(7S) + Rb(5S) and Rb(5D) + Rb(5S) collisions", Eur. Phys. J. D **12** , 133 (2000).

[52] S Magnier, M Aubert-FrÃľcon,*J*Hanssen and C Le Sech, " Two-electron wavefunctions for the ground state of alkali negative ions", J. Phys. B: At. Mol. Opt. Phys. **32**, 5639-5643 (1999)

[53] H. K. Pechkis, D. Wang, Y. Huang, E. E. Eyler, P. L. Gould, W. C. Stwalley, and C. P. Koch, "Enhancement of the formation of ultracold $^{85}Rb_2$ molecules due to resonant coupling", Phys. Rev. A **76**, 022504 (2007)

[54] Predrag CvitanoviÄĞ, Roberto Artuso, Ronnie Mainieri, Gregor Tanner, GÃąbor Vattay, Niall Whelan and Andreas Wirzba. "CHAOS: CLASSICAL AND QUANTUM" Chapter 32. [ONLINE] Available at: http://chaosbook.org/version15/paper.shtml. [Accessed 01 March 15].

[55] Bellos, Michael A., "Short-Range Photoassociation and Trilobite-Like States of Ultracold Rb2" (2013). Doctoral Dissertations. Paper 51. Also available online http://digitalcommons.uconn.edu/dissertations/51/

[56] Pechkis, Hyewon K, "Utlracold Rb2 Molecules: Formation, Detection and Trapping in an Optical Dipole Trap" (2010). Doctoral Dissertations. Paper AAI3468083. Also available online: http://digitalcommons.uconn.edu/dissertations/AAI3468083/

[57] E.Raab et al.,"Trapping of Neutral Sodium Atoms with Radiation Pressure", Phys. Rev. Lett. **59**, (1987).

[58] Harold J. Metcalf, Peter van der Straten, "Laser Cooling and Trapping", Springer (November 9, 2001) ISBN-10: 0387987282, ISBN-13: 978-0387987286

[59] E. E. Eyler "A single-chip event sequencer and related microcontroller instrumentation for atomic physics research", Rev. Sci. Instrum. 82, 013105 (2011); http://dx.doi.org/10.1063/1.3523426

[60] E. E. Eyler "Instrumentation for laser physics and spectroscopy using 32-bit microcontrollers with an Android tablet interface", Rev. Sci. Instrum. 84, 103101 (2013); http://dx.doi.org/10.1063/1.4821986

[61] Ulrich Brackmann, "Lambdachrome laser dyes: data sheets", Lambda Physik Göttingen, Germany 1997 http://www.chem.ucla.edu\%7ecraigim/pdfmanuals/catalogs/

[62] L. Martinelli, "Dispense del corso di Esperimentazioni di Fisica I", ETS, Pisa 1991. Similar treatment also available online http://www.fci.unibo.it\%7eridolfi/fifa/stat.pdf

[63] W. Fuller, "Measurement Error Models", John Wiley & Sons, 1987.

[64] J. Fox, "Robust Regression Appendix to An R and S-PLUS Companion to Applied Regression", cran R-project contributed documentation, 2002. Available online: http://cran.r-project.org/doc/contrib/Fox-Companion/appendix-robust-regression.pdf

[65] "Overview of Curve Fitting Models and Methods in LabVIEW", National Instruments, 2009. Available online: http://www.ni.com/white-paper/6954/en/

[66] "Experimental data analyst documentation" Chapter 7: Robust Fitting, Wolfram, 2015. Available online http://reference.wolfram.com/applications/eda/

[67] P.F. Bernath, "Electronic Spectroscopy of Diatomic Molecules", in "Handbook of Molecular Physics and Quantum Chemistry", Wiley, U.K., 2002. http://bernath.uwaterloo.ca/media/DiatomicElectronic.pdf

[68] P.F. Bernath, "Notes on: Molecular Physics", Vrije Universiteit Amsterdam 2004. Available online: http://www.nat.vu.nl/~wimu/MolPhysDic_tot.fr.pdf

[69] Matthew P. Jacobson, "Extended cross correlation: A technique for spectroscopic pattern recognition", J. Chem. Phys., **107**, 20, 1997. Available online: https://molspect.chemistry.ohio-state.edu/institute/field3.pdf

[70] Dl Sprecher and F. Merkt, "Observation of g/u-symmetry mixing in the high-n Rydberg states of HD", J. Chem. Phys. **140**, 124313 (2014). Available online: http://scitation.aip.org/content/aip/journal/jcp/140/12/10.1063/1.4868024

[71] Townes and Schawlow, "Microwave Spectroscopy", McGraw Hill 1955. Partly available on googlebooks: http://scitation.aip.org/content/aip/journal/jcp/140/12/10.1063/1.4868024

[72] M. S. Safronova and U. I. Safronova, "Critically evaluated theoretical energies, lifetimes, hyperfine constants, and multipole polarizabilities in ^{87}Rb", Phys. Rev. A **83**, 052508 (2011)

[73] M. Marinescu and A. Dalgarno, "Dispersion forces and long-range electronic transition dipole moments of alkali-metal dimer excited states", Phys. Rev. A **52**, 311 (1995)

[74] M. C. McCarthy, C. A. Gottlieb, H. Gupta, and P. Thaddeus, "Laboratory and astronomical identification of the negative molecular ion C_6H^-", Astrophys. J. Lett. **652**, L141 (2006)

[75] A. G. G. M. Tielens, "The molecular universe", Rev. Mod. Phys. **85**, 1021 (2013)

[76] V.M. Bierbaum, Proc. Int. Astron. Union 7, 383 [The Molecular Universe , Proceedings of the IAU Symposium 280, Vol. 7 (Cambridge University Press, Cambridge, England, 2011), p. 383].

[77] C.A. Cole, N.J. Demarais, Zhibo Yang, T.P. Snow, V.M. Bierbaum "Heterocyclic Anions of Astrobiological Interest", Astrophys. J.**779** 181 (2013)

[78] F. Robicheaux, B.J. Bender, and M.A. Phillips, "Simulations of an ultracold, neutral plasma with equal mass for every charge", J. Phys. B **47**, 245701 (2014). http://www.physics.purdue.edu/~robichf/papers/jpb47_245701.pdf

[79] A. Dalgarno, R. A. McCray, "The Formation of Interstellar Molecules from Negative Ions", Astrophys. J. **181**, 95 (1973). http://adsabs.harvard.edu/doi/10.1086/152032

[80] E. Roueff, E. Herbst, "Molecular ions in astrophysics", J. Phys., Conf. Ser. **192**, 012008 (2009).

[81] I. S. Lim, J. K. Laerdahl, P. Schwerdtfeger, "The static electric dipole polarizability of Rb^+", J. Phys. B **33**, L91 (2000).

[82] C. Lupinetti, A. J. Thakkar, "Polarizabilities of the alkali anions: Li^- to Fr^- ", J. Chem. Phys. **125**, 194317 (2006).

[83] T.C. Killian, T. Pattard, T. Pohl, J.M. Rost, "Ultracold neutral plasmas", Phys. Rep. **449**, 77 (2007).

[84] Miriam Serena Vitiello, Giacomo Scalari, Benjamin Williams, Paolo De Natale "Quantum cascade lasers: 20 years of challenges", Opt. Express,**23**(4), 5167-5182 (2015). http://www.opticsinfobase.org/oe/fulltext.cfm?uri=oe-23-4-5167&id=312147

[85] D. Wang, J. T. Kim, C. Ashbaugh, E. E. Eyler, P. L. Gould, and W. C. Stwalley, "Rotationally resolved depletion spectroscopy of ultracold KRb molecules" Phys. Rev. A **75**, 032511 (2007).